



National Aeronautics and  
Space Administration

# BLADE LOSS TRANSIENT DYNAMICS ANALYSIS

VOLUME II

TASK II - THEORETICAL AND ANALYTICAL DEVELOPMENT  
TASK III - EXPERIMENTAL VERIFICATION

by

V.C. Gallardo  
A.S. Storace  
E.F. Gaffney  
L.J. Bach  
M.J. Stallone

GENERAL ELECTRIC COMPANY  
Aircraft Engine Business Group  
Cincinnati, OH 45215

June 1981

Prepared For

REPRODUCED BY  
NATIONAL TECHNICAL  
INFORMATION SERVICE  
U.S. DEPARTMENT OF COMMERCE  
SPRINGFIELD, VA. 22161

**National Aeronautics and Space Administration**

(NASA-CR-165373-Vol-2) BLADE LOSS TRANSIENT DYNAMICS ANALYSIS, VOLUME 2. TASK 2: THEORETICAL AND ANALYTICAL DEVELOPMENT. TASK 3: EXPERIMENTAL VERIFICATION Final Report (General Electric Co.) 250 p N81-27090  
Unclas  
G3/07 26802

NASA Lewis Research Center  
Contract NAS3-22053

250

## NOTICE

THIS DOCUMENT HAS BEEN REPRODUCED FROM THE BEST COPY FURNISHED US BY THE SPONSORING AGENCY. ALTHOUGH IT IS RECOGNIZED THAT CERTAIN PORTIONS ARE ILLEGIBLE, IT IS BEING RELEASED IN THE INTEREST OF MAKING AVAILABLE AS MUCH INFORMATION AS POSSIBLE.



## TABLE OF CONTENTS

<u>Section</u>	<u>Page</u>
1.0 INTRODUCTION	1
2.0 MODAL SYNTHESIS AND THE LAGRANGIAN IN THE DEVELOPMENT OF THE COMPONENT ELEMENT METHOD	3
2.1 Summary	3
2.2 Background and Introduction	3
2.3 Modal Synthesis	4
2.4 Lagrangian Dynamics	9
2.5 Damping and Other External Forces	11
2.5.1 Damping	11
2.5.2 External Forces	13
2.6 Application to Turbine Engine Dynamics	14
3.0 DETAILED ANALYTICAL DEVELOPMENT OF THE TETRA PROGRAM	30
3.1 Summary	30
3.2 Introduction	30
3.3 Analytical Development	31
3.3.1 Governing Differential Equations	31
3.3.2 Numerical Integration of the Governing Differential Equations	34
3.3.3 Modules and Structural Discretization	36
3.3.3.1 Modal Subsystems	37
3.3.3.2 Applied Physical Forces	42
3.3.3.3 Physical Connecting Elements	42
3.3.3.4 Generalized Spring-Damper Element	42
3.3.3.5 Space Link-Damper Element	45
3.3.3.6 Rub Element	47
3.3.3.7 Engine Support Element	50
3.3.3.8 Gyro Element	56
3.3.3.9 Unbalance Forces	59
3.3.3.10 Subsystem Internal Loads	63
3.4 Structure of the Computer Program	63
3.5 Turbine Engine Simulation	68
4.0 APPLICATION OF TETRA TO BLADE LOSS TRANSIENT RESPONSE ANALYSIS OF TWO TEST VEHICLES AND EXPERIMENTAL VERIFICATION	95
4.1 Summary	95
4.2 Introduction	95
4.3 Blade-Out Test Vehicle VAST Analysis	96
4.4 TETRA Analysis of the Blade-Out Test Vehicle	98
4.5 Blade-Out Engine VAST Analysis	104
4.6 TETRA Analysis of the Blade-Out Engine	104
4.7 Blade-Out Vehicle Test Description and Results	115

TABLE OF CONTENTS (Concluded)

<u>Section</u>	<u>Page</u>
4.8 Blade-Out Engine Test Description and Results	127
4.9 Comparison of TETRA Results for the Blade-Out Vehicle with Linear Analysis and Test	128
4.10 Comparison of TETRA Results for the Blade-Out Engine with Linear Analysis and Test	140
4.11 Discussion of TETRA Verification Results	147
5.0 CONCLUSIONS AND RECOMMENDATIONS	151
APPENDIX A BLADE-OUT VEHICLE SYSTEM NORMAL MODE SHAPES	155
APPENDIX B BLADE-OUT VEHICLE SUBSYSTEM NORMAL MODE SHAPES	159
APPENDIX C TETRA DATA FILE FOR THE BLADE-OUT VEHICLE LINEAR ANALYSIS	177
APPENDIX D BLADE-OUT VEHICLE TETRA RESULTS FOR MODERATE UNBALANCE	179
APPENDIX E BLADE-OUT ENGINE SUBSYSTEM NORMAL MODE SHAPES	192
APPENDIX F TETRA DATA FILE FOR THE ENGINE LINEAR ANALYSIS	225
APPENDIX G BLADE-OUT ENGINE TETRA RESULTS FOR NOMINAL UNBALANCE	227
REFERENCES	236

## LIST OF ILLUSTRATIONS

<u>Figure</u>		<u>Page</u>
1.	Schematic of a Turbine Engine.	15
2.	Geometry of Motion of a Rotating Element.	16
3.	Typical Subsystem and Physical Component Representation of an Engine System.	32
4.	Engine Rotor Subsystem Normal Modes in Two Orthogonal Planes.	38
5.	Typical Mounting Arrangement and Coordinate System.	40
6.	Vertical and Horizontal Planar Models.	44
7.	General Spring Damper Element.	46
8.	Space Link-Damper Element.	46
9.	Rub Force Model.	48
10.	Rub Element Model.	51
11.	An Example of an Aircraft Engine Mounting Arrangement.	52
12.	Engine Frame/Case Ovalization Effects Increase the Effective Flexibility at the Mounting Planes.	52
13.	Combined Engine Support Link Element - Multidirection, Multipoint Element Represents Case Distortion and Links Flexibility.	54
14.	Case Flexibility Represented by Multipoint/Direction Physical Spring Element (Which Defines a Portion of the Engine Support Element).	55
15.	Combined In-Plane and Out-of-Plane Stiffness Matrix for the Physical Spring Element Shown in Figure 14.	57
16.	Gyro Element.	58
17.	Diagram Used to Establish Accelerations Due to Disk Translation.	60
18.	Effect of Applied Physical Forces in the Fixed Frame.	62

LIST OF ILLUSTRATIONS (Continued)

<u>Figure</u>		<u>Page</u>
19.	TETRA Routines for Transformations and Numerical Integration.	64
20.	Finite-Element Model for Demonstrator, 40 DOF.	69
21.	Demonstrator Model 100 g-in. Sudden Unbalance at the Fan at 12,000 rpm.	72
22.	Demonstrator Model 100 g-in. Sudden Unbalance at the Fan at 12,000 rpm.	73
23.	Total System - Rotor Mode Shapes.	74
24.	Demonstrator Model 100 g-in. Sudden Unbalance at the Fan at 9908 rpm.	75
25.	Fan Response in Two Planes for NASA Demonstrator Model with Gyro 100 g-in. Sudden Fan Unbalance at 3000 rpm.	76
26.	Orbit Plots at the Fan for NASA Demonstrator Model with Gyro.	77
27.	Response in the Vertical Direction at the Case and Fan Rotor for the NASA Demonstrator Model for 5000 g-in. Sudden Fan Unbalance at 3000 rpm (No Rub).	78
28.	Response in the Vertical Direction at the Case and Fan Rotor for the NASA Demonstrator Model for 5000 g-in. Sudden Fan Unbalance at 3000 rpm (No Rub).	79
29.	Rotor and Case Orbit Plot for the NASA Demonstrator Model for 5000 g-in. Sudden Fan Unbalance at 3000 rpm (No Rub).	80
30.	Rotor and Case Orbit Plot for the NASA Demonstrator Model for 5000 g-in. Sudden Fan Unbalance at 3000 rpm (With Rub).	81
31.	Response in the Vertical Direction at the Case and Fan Rotor for the NASA Demonstrator Model for 5000 g-in. Sudden Fan Unbalance at 3624 rpm (No Rub).	82
32.	Response in the Vertical Direction at the Case and Fan Rotor for the NASA Demonstrator Model for 5000 g-in. Sudden Fan Unbalance at 3624 rpm (No Rub).	83

LIST OF ILLUSTRATIONS (Continued)

<u>Figure</u>		<u>Page</u>
33.	NASA Demonstrator Steady-State Frequency Response for 100 g-in. Fan Unbalance (No Gyro).	84
34.	NASA Demonstrator Steady-State Frequency Response for 100 g-in. Fan Unbalance (No Gyro).	85
35.	NASA Demonstrator Steady-State Frequency Response for 100 g-in. Fan Unbalance (Gyro at Fan and Turbine).	86
36.	NASA Demonstrator Steady-State Frequency Response for 100 g-in. Fan Unbalance (Gyro at Fan and Turbine).	87
37.	Response in the Vertical Direction of the Case and Fan Rotor for the NASA Demonstrator Model for 1000 to 3000 rpm Accel Segment; Radial-Displacement Dead Band Exceeds the Fan-Case Relative Displacement (No Rub).	88
38.	Response in the Vertical Direction of the Case and Fan Rotor for the NASA Demonstrator Model for 3000 to 5000 rpm Accel Segment; Radial-Displacement Dead Band Exceeds the Fan-Case Relative Displacement (No Rub).	89
39.	Response in the Vertical Direction of the Case and Fan Rotor for the NASA Demonstrator Model for 1000 to 3000 rpm Accel Segment; 10-mil Radial-Displacement Dead Band and $1 \times 10^6$ lb/in. Rub Spring at the Fan Rotor-Case (With Rub).	90
40.	Response in the Vertical Direction of the Case and Fan Rotor for the NASA Demonstrator Model for 3000 to 5000 rpm Accel Segment; 10-mil Radial-Displacement Dead Band and $1 \times 10^6$ lb/in. Rub Spring at the Fan Rotor-Case (With Rub).	91
41.	Force Exerted by the Forward Frame/Bearing (Spring 3) on the Rotor at Point 5 in the Vertical Direction for the NASA Demonstrator Model for 3000 to 5000 rpm Accel Segment; Radial Displacement Dead Band Exceeds the Fan Rotor-Case Relative Displacement (No Rub).	92
42.	Force Exerted by the Forward Frame/Bearing (Spring 3) on the Rotor at Point 5 in the Vertical Direction for the NASA Demonstrator Model for 3000 to 5000 rpm Accel Segment; 10-mil Radial Displacement Dead Band and $1 \times 10^6$ lb/in. Rub Spring at the Fan Rotor Case (With Rub).	93



LIST OF ILLUSTRATIONS (Continued)

<u>Figure</u>		<u>Page</u>
43.	Blade-Out Test Vehicle Schematic Model.	97
44.	Blade-Out Test Vehicle Schematic Model.	99
45.	Blade-Out Test Vehicle Rotor Subsystem.	100
46.	Blade-Out Test Vehicle TETRA Schematic.	101
47.	Test Vehicle Linear Analysis for Nominal Fan Rotor Unbalance - TETRA Results - No. 1 Bearing Load.	102
48.	Test Vehicle Linear Analysis for Nominal Fan Rotor Unbalance - TETRA Results - No. 1 Bearing Housing Deflection.	103
49.	Test Vehicle Blade-Out - TETRA Analysis - No. 1 Bearing Load.	105
50.	Test Vehicle Blade-Out - TETRA Analysis - No. 1 Bearing Velocity.	106
51.	TETRA Test Vehicle Blade-Out Analysis - Rub Element Included - No. 1 Bearing Loads at 4200 rpm.	107
52.	TETRA Test Vehicle Blade-Out Analysis - Rub Element Excluded - No. 1 Bearing Loads at 4200 rpm.	108
53.	Engine VAST Schematic.	109
54.	Engine Casing VAST Schematic.	110
55.	Engine Rotor VAST Schematic.	110
56.	Turbofan Engine TETRA Schematic.	112
57.	Engine Linear Analysis for Nominal Fan Unbalance - TETRA Results - No. 1 Bearing Load.	114
58.	Engine Linear Analysis for Nominal Fan Unbalance - TETRA Results - No. 1 Bearing Deflection.	114
59.	TETRA Engine Blade-Out Analysis - No. 1 Bearing Load.	116
60.	TETRA Engine Blade-Out Analysis - No. 1 Bearing Velocity.	117

LIST OF ILLUSTRATIONS (Continued)

<u>Figure</u>		<u>Page</u>
61.	Blade-Out Test Vehicle Instrumentation.	118
62.	Blade-Out Test Vehicle - No. 1 Bearing Load.	119
63.	Blade-Out Test Vehicle - No. 1 Bearing Deflections.	120
64.	Blade-Out Test Vehicle - Test Versus Predicted No. 1 Bearing Load Linear Pressure for Nominal Unbalance.	121
65.	Blade-Out Test Vehicle Decel Time History.	122
66.	Blade-Out Test Vehicle - No. 1 Bearing Housing 153° and 330° Strain Gages.	123
67.	Blade-Out Test Vehicle - Reconstituted No. 1 Bearing Housing Load Generated From 153° and 330° Strain Gages.	124
68.	Blade-Out Test Vehicle - Reconstituted No. 1 Bearing Housing Generated From 153° and 333° Strain Gages (Expanded).	125
69.	Blade-Out Test Vehicle - No. 1 Bearing Response.	126
70.	Blade-Out Test Vehicle - No. 1 Bearing Response (Expanded).	127
71.	Blade-Out Engine Test Decel Time History.	129
72.	Blade-Out Engine Test - No. 1 Bearing Housing Stress at 153°.	130
73.	Blade-Out Engine Test - No. 1 Bearing Housing Stress at 333°.	131
74.	Blade-Out Engine Test - Reconstituted No. 1 Bearing Load.	132
75.	Blade-Out Engine Test - No. 1 Bearing Response.	133
76.	Blade-Out Engine Test - No. 1 Bearing Response (Expanded).	134
77.	Test Vehicle Linear Analysis for Nominal Fan Rotor Unbalance - TETRA Versus VAST - No. 1 Bearing Load.	135

LIST OF ILLUSTRATIONS (Continued)

<u>Figure</u>		<u>Page</u>
78.	Test Vehicle Linear Analysis for Nominal Fan Rotor Unbalance - TETRA Versus VAST - No. 1 Bearing Housing Deflection.	136
79.	Test Vehicle Linear Analysis for Nominal Fan Rotor Unbalance - TETRA Versus Vast - Fan Stage Centerline Deflection.	137
80.	Blade-Out Test Vehicle - TETRA Versus Test for Blade-Out Condition - No. 1 Bearing Load.	138
81.	Blade-Out Test Vehicle - TETRA Versus Test for Blade-Out Condition - No. 1 Bearing Response.	139
82.	Blade-Out Test Vehicle - TETRA Versus Test for Blade-Out Condition - No. 1 Bearing Load.	141
83.	Blade-Out Test Vehicle - TETRA Versus Test for Blade-Out Condition - No. 1 Bearing Deflection.	142
84.	Engine Linear Analysis for Nominal Fan Unbalance - TETRA Versus VAST - No. 1 Bearing Load.	143
85.	Engine Linear Analysis for Nominal Fan Unbalance - TETRA Versus VAST - No. 1 Bearing Deflection.	144
86.	Blade-Out Engine - TETRA Versus Test for Blade-Out Condition - No. 1 Bearing Load.	145
87.	Blade-Out Engine - TETRA Versus Test for Blade-Out Condition - No. 1 Bearing Response.	145
88.	Blade-Out Engine Test Normalized Load Versus rpm.	146
89.	Blade-Out Engine Test Normalized Deflection.	148
90.	Blade-Out Test Vehicle Predicted Mode Shape at 387 rpm.	156
91.	Blade-Out Test Vehicle Predicted Mode Shape at 981 rpm.	157
92.	Blade-Out Test Vehicle Predicted Mode Shape at 4043 rpm.	158
93.	Blade-Out Test Vehicle, Subsystem 1 (Casing), 424 rpm.	160
94.	Blade-Out Test Vehicle, Subsystem 1 (Casing), 976 rpm.	161

LIST OF ILLUSTRATIONS (Continued)

<u>Figure</u>		<u>Page</u>
95.	Blade-Out Test Vehicle, Subsystem 1 (Casing), 5241 rpm.	162
96.	Blade-Out Test Vehicle, Subsystem 1 (Casing), 6535 rpm.	163
97.	Blade-Out Test Vehicle, Subsystem 1 (Casing), 11,539 rpm.	164
98.	Blade-Out Test Vehicle, Subsystem 1 (Casing), 16,258 rpm.	165
99.	Blade-Out Test Vehicle, Subsystem 1 (Casing), 18,878 rpm.	166
100.	Blade-Out Test Vehicle, Subsystem 1 (Casing), 36,388 rpm.	167
101.	Blade-Out Test Vehicle, Subsystem 1 (Casing), 39,995 rpm.	168
102.	Blade-Out Test Vehicle, Subsystem 1 (Casing), 41,284 rpm.	169
103.	Blade-Out Test Vehicle, Subsystem 1 (Casing), 53,107 rpm.	170
104.	Blade-Out Test Vehicle, Subsystem 1 (Casing), 69,016 rpm.	171
105.	Blade-Out Test Vehicle, Subsystem 1 (Casing), 75,867 rpm.	172
106.	Blade-Out Test Vehicle, Subsystem 2 (Rotor), 46 rpm.	173
107.	Blade-Out Test Vehicle, Subsystem 2 (Rotor), 146 rpm.	174
108.	Blade-Out Test Vehicle, Subsystem 2 (Rotor), 17,626 rpm.	175
109.	Blade-Out Test Vehicle, Subsystem 2 (Rotor), 78,001 rpm.	176
110.	Listing of TETRA Input Data File.	178
111.	No. 1 Bearing Load at 3500 rpm.	180
112.	No. 1 Bearing Deflection at 3500 rpm.	181
113.	No. 1 Bearing Load at 3800 rpm.	182
114.	No. 1 Bearing Deflection at 3800 rpm.	183
115.	No. 1 Bearing Load at 4000 rpm.	184
116.	No. 1 Bearing Deflection at 4000 rpm.	185
117.	No. 1 Bearing Load at 4050 rpm.	186

LIST OF ILLUSTRATIONS (Continued)

<u>Figure</u>		<u>Page</u>
118.	No. 1 Bearing Deflection at 4050 rpm.	187
119.	No. 1 Bearing Load at 4100 rpm.	188
120.	No. 1 Bearing Deflection at 4100 rpm.	189
121.	No. 1 Bearing Load at 4400 rpm.	190
122.	No. 1 Bearing Deflection at 4400 rpm.	191
123.	Subsystem 1 (Casing) Normalized Mode Shapes at 353 rpm.	193
124.	Subsystem 1 (Casing) Normalized Mode Shapes at 731 rpm.	194
125.	Subsystem 1 (Casing) Normalized Mode Shapes at 1703 rpm.	195
126.	Subsystem 1 (Casing) Normalized Mode Shapes at 2978 rpm.	196
127.	Subsystem 1 (Casing) Normalized Mode Shapes at 5110 rpm.	197
128.	Subsystem 1 (Casing) Normalized Mode Shapes at 5370 rpm.	198
129.	Subsystem 1 (Casing) Normalized Mode Shapes at 5655 rpm.	199
130.	Subsystem 1 (Casing) Normalized Mode Shapes at 6485 rpm.	200
131.	Subsystem 1 (Casing) Normalized Mode Shapes at 6815 rpm.	201
132.	Subsystem 1 (Casing) Normalized Mode Shapes at 7076 rpm.	202
133.	Subsystem 1 (Casing) Normalized Mode Shapes at 7852 rpm.	203
134.	Subsystem 1 (Casing) Normalized Mode Shapes at 8982 rpm.	204
135.	Subsystem 1 (Casing) Normalized Mode Shapes at 9644 rpm.	205
136.	Subsystem 1 (Casing) Normalized Mode Shapes at 10,379 rpm.	206
137.	Subsystem 1 (Casing) Normalized Mode Shapes at 11,632 rpm.	207
138.	Subsystem 1 (Casing) Normalized Mode Shapes at 12,665 rpm.	208
139.	Subsystem 1 (Casing) Normalized Mode Shapes at 13,354 rpm.	209
140.	Subsystem 1 (Casing) Normalized Mode Shapes at 15,130 rpm.	210

LIST OF ILLUSTRATIONS (Concluded)

<u>Figure</u>		<u>Page</u>
141.	Subsystem 1 (Casing) Normalized Mode Shapes at 15,469 rpm.	211
142.	Subsystem 1 (Casing) Normalized Mode Shapes at 18,172 rpm.	212
143.	Subsystem 1 (Casing) Normalized Mode Shapes at 18,845 rpm.	213
144.	Subsystem 1 (Casing) Normalized Mode Shapes at 19,480 rpm.	214
145.	Subsystem 1 (Casing) Normalized Mode Shapes at 21,616 rpm.	215
146.	Subsystem 1 (Casing) Normalized Mode Shapes at 22,085 rpm.	216
147.	Subsystem 1 (Casing) Normalized Mode Shapes at 23,181 rpm.	217
148.	Subsystem 1 (Casing) Normalized Mode Shapes at 24,268 rpm.	218
149.	Subsystem 2 (Rotor) Normalized Mode Shapes at 55 rpm.	219
150.	Subsystem 2 (Rotor) Normalized Mode Shapes at 73 rpm.	220
151.	Subsystem 2 (Rotor) Normalized Mode Shapes at 972 rpm.	221
152.	Subsystem 2 (Rotor) Normalized Mode Shapes at 2421 rpm.	222
153.	Subsystem 2 (Rotor) Normalized Mode Shapes at 5627 rpm.	223
154.	Subsystem 2 (Rotor) Normalized Mode Shapes at 11,081 rpm.	224
155.	TETRA Data File Listing for Engine.	226
156.	No. 1 Bearing Load at 2950 rpm.	228
157.	No. 1 Bearing Deflection at 2950 rpm.	229
158.	No. 1 Bearing Load at 3600 rpm.	230
159.	No. 1 Bearing Deflection at 3600 rpm.	231
160.	No. 1 Bearing Load at 3750 rpm.	232
161.	No. 1 Bearing Deflection at 3750 rpm.	233
162.	No. 1 Bearing Load at 4000 rpm.	234
163.	No. 1 Bearing Deflection at 4000 rpm.	235

LIST OF TABLES

<u>Table</u>		<u>Page</u>
I.	Modal Module - Static Structures.	24
II.	Modal Module - Rotating Structures.	25
III.	Connecting Elements.	28
IV.	Physical Global Degrees of Freedom and Directional Numbers for the Subsystems.	41
V.	Mode Shapes for the Six Rigid-Body Modes for a Subsystem.	43
VI.	Modal Subsystems.	65
VII.	Subsystem Identification.	66
VIII.	Frequencies for the Free-Free Modal Subsystems Used in the TETRA Analysis.	70
IX.	TETRA Model Complexity.	149

## 1.0 INTRODUCTION AND SUMMARY

The Blade Loss Transient Dynamic Analysis Program comprises three technical tasks, namely:

- Task I - Survey and perspective of problem areas in engine transient dynamics and selection of specific problem areas for analysis
- Task II - Analysis and development of analytical techniques of engine transient response from dynamic stimuli
- Task III - Experimental verification of the analytical method by correlation of analysis results with test data.

The ultimate objective is the development of a computer code for the analysis and prediction of turbine engine transient response from the loss of a blade. This has been necessitated by the growing awareness that engines must be lighter, more rugged, and run at higher speeds to achieve maximum efficiency and economy. The implications of blade loss, and subsequent dynamic loads, on engine integrity and performance become obvious. In order to tolerate unbalance loads, engine response must be predicted accurately so that an optimum structure can be designed with adequate bearings and dampers. Thus, damage will be minimized, in the event of a blade loss, without unduly penalizing the engine with regards to weight and fuel economy during normal operation.

From the results of Task I, a survey of field experience of blade loss and its consequences in turbine engines, critical problem areas were identified. The most critical problem areas with respect to probability of occurrence and subsequent damage to the engine were selected for analytical consideration in Task II.

The critical problem areas may be classified by fundamental mechanisms of resulting damage:

- Deflection Dominated - This is primarily a rub between rotor and casing or rotor-to-rotor
- High Loads and Stresses - Such as vibratory and transient loads.

The analytical approach chosen to develop a transient dynamic analysis computer program in Task II is the component element method. This method is essentially based on modal synthesis combined with a central, finite-difference, numerical-integration scheme. The methodology leads to a modular or building-block technique that is amenable to computer programming. It also presents a simple way to model engines of various structural configurations.



In order to verify the analytical method, Turbine Engine Transient Response Analysis (TETRA) developed in Task II, it was applied to two blade-out test vehicles that had been previously instrumented and tested. Comparison of the time-dependent test data with those predicted by TETRA is the subject of Task III. Finally, these comparisons led to recommendations for refinement or extension of the analytical method to improve its accuracy and overcome its shortcomings.

The subject contract has been completed, and the results are documented in the following reports:

- Volume I contains the results of Task I.
- Volume II contains the theoretical basis for the method of analysis of Task II as well as results of Task III. Included are the technical details of Task II (the application of the component element method to the development of TETRA). This includes the development of working equations, their discretization, numerical solution scheme, the modular concept of engine modeling, the program logical structure, and some illustrated results. It also contains the analytical predictions for two blade-out tests as well as the experimental verification required in Task III. Described are the blade-loss test vehicles (rig and full engine), the type of measured data, and the engine structural models. It also presents a comparison of the predicted response of these vehicles with sudden unbalance as calculated by TETRA with the appropriate measured dynamic data. Finally, the shortcomings, inadequacies, and recommendations for refinement or increased capability of program TETRA are reviewed.
- Volume III is a User's Manual for TETRA. It contains program logic, flow charts, error messages, input sheets, modeling instructions, option descriptions, input variable descriptions, and demonstration problems. The process of obtaining a NASTRAN 17.5 generated modal input file for TETRA is also described with a worked sample.

Each volume is divided into sections treating major topics in detail. In Volume II, for instance, Section 1.0 treats the fundamentals of the component element method in a clear and unified fashion and shows how physical elements and modal components combine to produce a representation of the whole engine. Section 2.0 of the same volume is much more detailed due to the many small items that must be coded in a computer program. Here the mathematical representations of the many modules are developed in detail: modal mass, modal stiffness, spring, dashpot, rub element, gyroscopic forces, unbalance-force excitation, time-integration scheme, total displacement, etc. Because of the modal approach, assembly of the engine is seen in the way one makes the input sheets to model the entire structure.

The volumes are written so that each is self-contained; therefore, some repetition is unavoidable.

## 2.0 MODAL SYNTHESIS AND THE LAGRANGIAN IN THE DEVELOPMENT OF THE COMPONENT ELEMENT METHOD

### 2.1 SUMMARY

The fundamental principles of the component element method are explained and illustrated. The component element method is based on the modal synthesis approach; the response of a complex structure is constructed in terms of the uncoupled normal modes of the main structural subsystems with appropriate connection forces introduced by physical connecting elements such as dashpots and springs. Lagrangian dynamics is introduced as a simple way to obtain the equations of the combined system. This approach also allows derivation of additional connecting forces such as those from squeeze films, rubs, and others in a general way.

The building block or modular approach follows directly from the logical structure of the modal synthesis approach. By representing the rotor motion with its nonrotating normal modes and the additional displacements and velocities due to rotation, it is found that the gyroscopic forces are reproduced and can be treated as "connection" forces which couple the motions in two orthogonal planes.

It is also shown that the classical rotor equations neglect so-called parametric excitation introduced by unbalance. These parametric terms are contained in the harmonic or time-dependent coefficients of rotor angular displacement, velocity, and acceleration at locations where there is an unbalance; they are comparable to harmonic variations in rotor moments of inertia. Omission of these terms is found to be justified since they are proportional to the square of the unbalance eccentric radius.

This section mainly clarifies the component element method so that its fundamentals are more easily understood. The actual working equations used in the development of the TETRA program are given in Volume III.

### 2.2 BACKGROUND AND INTRODUCTION

Carpenters build houses with 2 x 4's, rafters, concrete slab, and nails; we make turbine engines with blades, disks, combustors, rotors, and casings. Therefore, it is necessary to develop a method for predicting the dynamic stresses and vibrations of a complex structure in terms of the behavior of individual component parts. Modal synthesis is such a method of calculating structural dynamic response. Under various appellations such as transfer function (Reference 1), impedance (Reference 2), admittance (Reference 2), component mode (References 2, 3, and 4), or component element (Reference 5), which are esoteric in different technical disciplines, modal synthesis is an elegant but simple concept that may have been developed as far back as the 19th century. Mathematicians associate it with the solution of partial

differential equations by expansion in orthogonal functions, such as Fourier Series, and call it Rayleigh-Ritz (Reference 6), or Galerkin's Method when the functions are not orthogonal (Reference 6).

The principle is that the dynamic response of a complex structure is constructed by the ordered concatenation of the characteristic responses of its parts. These characteristic responses are also called the normal modes of that component and are calculated independent of the influence of other components. A component may be one simple beam, or it may be a conglomeration of several elements. An example of the latter is a compressor rotor which is made up of rotor, disks, blades and seals; the normal mode would be that of the complete compressor rotor behaving as a single entity.

These various components are assembled to form the complete engine with connecting elements at bearings and other support points. These connections not only couple the components but also modify their boundary conditions. Because the modal characteristics follow the same form and connecting elements are expressed by their damping and spring characteristics, the basis for a modular representation of complex structures is a natural consequence.

To obtain the proper and ordered concatenation of the components modes through the connecting elements, as well as to assure the correctness of the dynamic equations, Lagrangian dynamics is employed. By starting from the fundamental concepts of energy and Euler-Lagrange variational principle, the equations of each component and the proper connecting terms can be derived without ambiguity.

The resulting equations of the assembly can be solved by several techniques such as Runge-Kutta or the "difference" methods for transient response calculations. The marriage of the modular representation of the modal synthesis method with the central-difference, numerical-integration solution is the essence of the component element method.

This report will detail the fundamentals of modal synthesis and the Lagrangian approach for the analysis of structural dynamic response in general and turbine engine dynamic response in particular.

### 2.3 MODAL SYNTHESIS

It is known that any function which satisfies a linear partial differential equation (PDE) and the appropriate boundary conditions is a solution, and the linear combination of such functions is also a solution. These functions have been obtained by intuition, trial and error, and (more directly) from the solution of the homogeneous PDE (e.g., with the right-hand side equal to zero). The latter is called the Eigen value or characteristic-value problem. In dynamics and vibrations, the Eigen values or characteristic roots are called the natural frequencies or critical speeds; the deflection shape corresponding to each natural frequency is the mode shape or Eigen vector. The

solution of the full PDE from a combination of these modes is called the method of superposition of normal modes or modal expansion.

Modal synthesis carries modal expansion one step further by utilizing the normal modes to calculate the response of the structure when additional constraints are imposed.

These mode shapes are also called normal or orthogonal modes because the product of any two mode shapes when multiplied by the mass and integrated over the volume is zero when the modes are not identical and not zero when they are. This is the principle of orthogonality of normal modes. This principle is especially interesting because a purely mathematical concept leads to the principle of the conservation of energy.

The modal synthesis with a simply supported beam under an impulse load and with a spring at  $z = z^*$  is illustrated. The PDE and appropriate boundary conditions are

$$EIu^{iv}(z,t) + \mu\ddot{u}(z,t) = -Ku(z^*,t) + F_0(z,t)\delta(z - z_0)\delta(t)$$

$$u(0,t) = u(L,t) = u''(0,t) = u''(L,t) = 0$$

where the Dirac delta functions describe the force to act at a point  $z_0$  and at a time zero.

The homogeneous equation is obtained with the right-hand side equal to zero, and the well known Eigen values or frequencies and mode shapes are:

$$\omega_n = n\pi^2 \sqrt{EI/\mu L^4}$$

$$u_n(z) = \sin n\pi z/L$$

Now, assume the solution to be:

$$u(z,t) \equiv \sum_i u_i(z)q_i(t)$$

$q_i(t)$  = unknown participation of  $i$ -th mode or generalized coordinate

Substituting these into the full PDE and simplifying gives:

$$\sum_n \left[ EI \left( \frac{n\pi}{L} \right)^4 q_n + \mu \ddot{q}_n \right] \sin \frac{n\pi z}{L} = -K \sum_n q_n \sin \frac{n\pi z^*}{L} + F_0(z_0, t)$$

Multiply this with  $u_k \delta q_k \equiv \sin \frac{k\pi z}{L} \delta q_k$  and integrate over the span, then obtain the partial derivative with respect to  $\delta q_m$ . Thus,

$$\sum_n \left[ EI \left( \frac{n\pi}{L} \right)^4 q_n + \mu \ddot{q}_n \right] \int \sin \frac{n\pi z}{L} \sin \frac{m\pi z}{L} dz = -K \sum_n \sin \frac{n\pi z}{L}^* \sin \frac{m\pi z}{L}^* q_n + F_0(z_0, t) \sin \frac{m\pi z_0}{L}$$

By using the principle of orthogonality, the summation sign in the left-hand side is dropped. However, the summation in the right-hand side does not vanish. Thus,

$$q_m EI \left( \frac{n\pi}{L} \right)^4 \int_0^L \sin^2 \frac{n\pi z}{L} dz + \ddot{q}_n \int_0^L \mu \sin^2 \frac{n\pi z}{L} dz = -K \sum_n \sin \frac{n\pi z}{L}^* \sin \frac{m\pi z}{L}^* q_n + F_0(z_0, t) \sin \frac{m\pi z_0}{L}$$

The first integral is the  $n$ -th modal stiffness, and the second integral is the  $n$ -th modal or generalized mass. In the more standard notation, we have the set of ordinary differential equations (ODE) with "t" the only independent variable:

$$M_{mn} \ddot{q}_n + K_{mn} q_n + \bar{K}_{mn} q_n = F_0 \sin \frac{m\pi z_0}{L}$$

$$M_{mn} = \int \mu u_m u_n dz = \int \mu \sin \frac{n\pi z}{L} \sin \frac{m\pi z}{L} dz ; M_{mn} \begin{cases} \neq 0, i = j \\ = 0, i \neq j \end{cases}$$

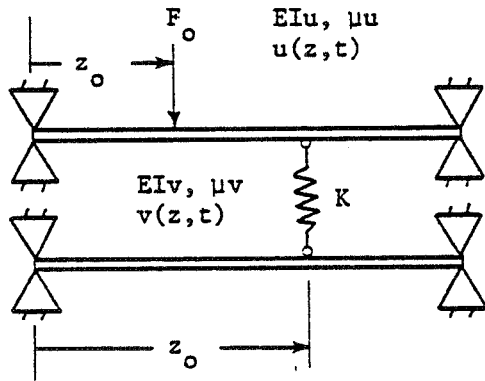
where:

$$K_{mn} = \int EI \left( \frac{n\pi}{L} \right)^4 \sin \frac{n\pi z}{L} \sin \frac{m\pi z}{L} dz \equiv \omega_{(nm)}^2 M_{mn}$$

$$\bar{K}_{mn} = K \sin \frac{m\pi z}{L}^* \sin \frac{n\pi z}{L}^*$$

It can be seen that these modal equations have coupling terms through the support spring. This spring actually alters the whole beam. The normal modes of this new beam with the spring at  $z = z^*$  can be obtained in terms of the modes of the original beam by solving the homogeneous equation of the new beam equation.

This example is a simple illustration of modal synthesis. Now suppose we have two simply supported beams that are parallel to each other and connected by a spring. This is illustrated below:



$$\begin{aligned}
 u(0,t) &= u(L,t) = u''(0,t) = u''(L,t) = 0 \\
 v(0,t) &= v(L,t) = v''(0,t) = v''(L,t) = 0
 \end{aligned}$$

The governing equation of each beam is similar to that of the single beam. The difference is that the spring force at the connection points is proportional to the relative deflection and, hence, mode shapes of both beams. The PDE of both beams are:

$$EI_u u^{iv} + \mu_u \ddot{u} = F_0(z_0, t) - K [u(z^*, t) - v(z^*, t)]$$

$$EI_v v^{iv} + \mu_v \ddot{v} = K [u(z^*, t) - v(z^*, t)]$$

Now writing the beam displacements in terms of their simply supported normal modes

$$u(z,t) = \sum u_i(z) q_i(t)$$

$$v(z,t) = \sum v_i(z) p_i(t)$$

and multiplying the first by  $u_k \delta q_k$  (virtual modal displacement of the first beam), the second by  $v_k \delta P_k$  (virtual modal displacement of second beam), then integrating over  $z$  we get:

$$\delta q_k \left\{ \ddot{q}_n \bar{M}_{kn} + q_n \bar{K}_{m_n} + k u_k \sum [(u_1^* q_1 + \dots u_n^* q_n) - (v_1^* P_1 + \dots v_n^* P_n)] \right\} = F_0 u_k \delta q_k$$

$$\delta P_k \left\{ \ddot{P}_n \bar{M}_{kn} + q_n \bar{K}_{m_n} - k v_k \sum [(u_1^* q_1 + \dots u_n^* q_n) - (v_1^* P_1 + \dots v_n^* P_n)] \right\} = 0$$

Taking the derivative of the first with respect to  $\delta q_m$  and the second with respect to  $\delta P_m$ , we have the ODE of the connected beams; thus:

$$M_{m_n} \ddot{q}_{m_n} + K_{m_n} q_n + k_{m1} q_1 + k_{m2} q_2 + \dots k_{m_n} q_n - \bar{k}_{m1} P_1 - \bar{k}_{m2} P_2 \dots \bar{k}_{mn} P_{1n} =$$

$$F_0 u_m(z_0).$$

$$\bar{M}_{m_n} \ddot{P}_{m_n} + \bar{k}_{m_n} P_n + \tilde{k}_{m1} P_1 + \tilde{k}_{m2} P_2 + \dots \tilde{k}_{m_n} P_{m_n} - \tilde{k}_{m1} q_1 - \tilde{k}_{m2} q_2 -$$

$$\dots \tilde{k}_{m_n} q_n = 0$$

where

$$k_{m_n} = \omega_{m_n}^2 M_{m_n} \quad M_{m_n} = \int_0^L \mu_u u_m u_n dz \quad \omega_{m_n} = (r\pi)^2 \sqrt{\frac{EI_u}{\mu_u L^4}}$$

$$\bar{k}_{m_n} = \omega_{m_n}^{-2} \bar{M}_{m_n} \quad \bar{M}_{m_n} = \int_0^L \mu_v v_m v_n dz \quad \bar{\omega}_{m_n} = (r\pi)^4 \sqrt{\frac{EI_v}{\mu_v L^4}}$$

$$M_{m_n}, K_{m_n}, \bar{M}_{m_n}, \bar{K}_{m_n}, \omega_{m_n}, \bar{\omega}_{m_n} \begin{cases} \neq 0, & m=n \\ = 0, & m \neq n \end{cases}$$

$$k_{m_n} = k u_m^* u_n^* \equiv k u_m(z^*) u_n(z^*)$$

$$\tilde{k}_{m_n} = K v_m^* v_n^*; \quad \tilde{k}_{m_n} = K v_m^* u_n^*; \quad \bar{k} = K u_m^* v_n^*$$

One can see that the modal equations of each beam have coupling terms involving other modes of that same beam and also modes of the other beam.

The last example illustrates the modal synthesis approach using the normal modes of the component beams and the characteristic of the spring connection. From this illustration, the analysis can be easily extended to more complex structures.

However, in application to structures with rotating components as well as static elements, formation of the generalized equations is not clear and sometimes ambiguous. To avoid this difficulty, the concept of the Lagrangian will be described.

#### 2.4 LAGRANGIAN DYNAMICS

It is called Lagrange's equation in the U.S.; however, it is known as Euler-Lagrange in Western Europe and in Moscow as the Euler-Ostrogradski equation. For consolidation, it will be referred to as the Euler-Lagrange-Ostrogradski (ELO) variational equation in this report.

The ELO is a relationship that must be satisfied in order to minimize the kinetic and potential energies of a system. It is written thus:

$$\frac{d}{dt} \frac{\partial L}{\partial \dot{\xi}} - \frac{\partial L}{\partial \xi} = F_{\xi}$$

where:

L = T - V, Lagrangian; T = Kinetic energy, V = potential energy

$\xi(t)$  = Dependent variable or generalized coordinate

$F_{\xi}$  = Generalized force in  $\xi(t)$

t = Time;  $\dot{\xi} = d\xi/dt$

This is another statement of Newton's Law that force equals mass times acceleration. It is a more general relation since it allows the force relations to be obtained in nonphysical space such as the space of the modal or generalized coordinates we have mentioned earlier.

In the section on modal synthesis, we began with the equation of motion of the structure, the PDE, and proceeded to obtain solutions. By contrast, the ELO begins with displacements, proceeds to obtain the kinetic and potential energies, and finally develops the equations of motion or PDE.

One can approach the Lagrangian using the physical displacements which would result in the PDE with the spatial coordinates and time as independent variables. This is the standard procedure for obtaining the PDE of fluids or elasticity such as those in plates and shells and the simple beam discussed



earlier. Or the Lagrangian can be expressed directly in terms of generalized modal coordinates (e.g., write the physical displacements and velocities in terms of the normal modes). The latter is the typical approach to analysis of complex structures or problems which involve the interaction of a structure with a fluid, as in aeroelasticity.

A simplification can also be made on the ELO operation on kinetic energy. This is particularly helpful for an articulated structure with a complex motion and for rotating structures such as rotors or propeller blades. Recall that the kinetic energy is the sum of the squares of the physical velocity components in the three cartesian axes and that these physical displacements may be expressed in terms of modal coordinates or other coordinates fixed to the structure.

It can be shown that the physical displacements measured from a fixed reference frame can be written as:

$$\begin{aligned}x &= x[\xi(t)] \\y &= y[\xi(t)] \\z &= z[\xi(t)]\end{aligned}$$

where  $\xi$  assumes all the generalized coordinates and  $x(\xi)$ , say, means a function of all the generalized coordinates. Then, the kinetic energy for a body is:

$$T = 1/2 \int (\dot{x}^2 + \dot{y}^2 + \dot{z}^2) dm$$

The ELO operation on the kinetic energy can be shown to reduce to:

$$\frac{d}{dt} \frac{\partial T}{\partial \dot{\xi}} - \frac{\partial T}{\partial \xi} = \left( \ddot{x} \frac{\partial x}{\partial \xi} + \ddot{y} \frac{\partial y}{\partial \xi} + \ddot{z} \frac{\partial z}{\partial \xi} \right) dm$$

When the final equations of motion will be linearized, the above relation will allow separate linearization of the accelerations and directional derivatives. This will drastically reduce algebraic manipulation and the chances of errors in reaching the final result.

The potential energy of connecting elements can be formulated for each configuration in terms of displacements at its ends: A, B. For example, a simple linear spring has the energy:

$$\frac{1}{2} k \left[ (z_a(x^*)) - z_b(x^*) \right]^2$$

The modal energy is much simpler. From the conservation of energy, the modal potential energy is simply:

$$\frac{1}{2} \omega_{(ij)}^2 M_{ij}$$

$$M_{ij}; \omega_{(ij)} \begin{cases} \neq 0, & i=j \\ = 0, & i \neq j \end{cases}$$

In the case of rotating structures such as a turbine rotor, the normal modes can be obtained with or without the effects of rotation. With the latter, the effects of rotation can be added separately by constructing the equations of the rotating rotor with the static normal modes in two perpendicular planes and the additional displacements due to rotation. Following the Lagrangian approach discussed above, the physical displacement of a point on the rotor can be written down by considering the geometry of motion. The ELO operation on the kinetic energy will yield the inertial equations of motion with the additional gyroscopic terms. Neither modal potential energy nor the potential energy of the connecting elements are affected by the rotation.

## 2.5 DAMPING AND OTHER EXTERNAL FORCES

So far, we have shown derivations of the equations of a conservative system without external forces. Damping and external forces or even other springs can be derived in a similar manner from physical forces with the principle of virtual work. The principle of virtual work may also be considered a special variational principle like the ELO.

### 2.5.1 Damping

In the case of viscous damping, Rayleigh's dissipation function can be constructed. It is normally written:

$$D = \frac{1}{2} C \dot{z}^2$$

where:

D = Dissipation function

C = Viscous damping coefficient

$\dot{z} = \frac{dz}{dt}$ , Physical relative velocity between ends of the damper or dashpot.

If the dashpot connects two structures, a and b, whose normal modes are known, one can write the dissipation function, say for damping in the z direction:

$$D = \frac{1}{2} C (\dot{z}_a(x^*) - \dot{z}_b(x^*))^2 \equiv \frac{1}{2} C (\dot{z}_a^* - \dot{z}_b^*)^2$$

and the modal force is:

$$F = \frac{\partial D}{\partial \dot{\xi}} = C(\dot{z}_a^* - \dot{z}_b^*) \frac{\partial}{\partial \dot{\xi}} (\dot{z}_a^* - \dot{z}_b^*)$$

where  $\dot{\xi}$  takes on all the possible generalized velocities. The terms  $z_a$  and  $z_b$  are expressed as the sum of the normal modes of structures a and b whose modal participations are denoted by  $\xi(t)$ .

A separate dissipation function is, of course, defined for each dashpot. These damping forces introduce coupling between modes as well as between components.

Distributed damping may also be constructed, although this is not always practical. However, modal damping has been used frequently. It is an especially distributed damping proportional to either the mass or the stiffness distribution or both. This proportionality to either of these two distributions allows one to take advantage of the orthogonality of normal modes. Therefore, the modal dissipation function may be written simply as:

$$D_m = \frac{1}{2} \zeta M_{ij} \dot{q}_i \dot{q}_j \quad \text{Mass-proportional dissipation function}$$

$$D_k = \frac{1}{2} \zeta K_{ij} \dot{q}_i \dot{q}_j \quad \text{Stiffness-proportional dissipation function}$$

and the damping forces are:

$$\frac{\partial D_m}{\partial \dot{q}_i} = \zeta M_{ij} \dot{q}_j$$

$$\frac{\partial D_k}{\partial \dot{q}_i} = \zeta K_{ij} \dot{q}_j$$

noting that  $M_{ij}$  and  $K_{ij}$  are nonzero for  $ij$  only.

### 2.5.2 External Forces

Physical external forces which are functions of location and time act along directions with respect to the fixed reference frame. To obtain the generalized forces which act on the generalized coordinate equations of motion, the principle of virtual work is employed. This principle was used earlier in the exposition of the concept of the modal synthesis. The virtual work of a physical force is the product of that force times the virtual displacement along the action line of that force. Consider a force  $F_z$  parallel to the  $z$  axis. The virtual displacement is  $\delta z$ , and the virtual  $\delta W$  work is:

$$\delta W = - F_z \delta z$$

The generalized force in the generalized coordinate is then:

$$F_\xi = \frac{\partial(\delta W)}{\partial(\delta \xi)} = - F_z \frac{\partial(\delta z)}{\partial(\delta \xi)} = - F_z \frac{\partial z}{\partial \xi}$$

A physical spring or dashpot may be also considered as an external force. Applying the virtual work principle will yield a generalized spring force identical to that obtained in the ELO operation on the spring potential energy.

Recalling the Lagrangian and the ELO and combining these with the dissipation function and the virtual work principle, the complete equations of motion of any complex structure may be obtained with a variational principle. Thus:

$$F_\xi = \frac{d}{dt} \frac{\partial L}{\partial \dot{\xi}} - \frac{\partial L}{\partial \xi} + \frac{\partial D}{\partial \dot{\xi}} - \frac{\partial(\delta W)}{\partial(\delta \xi)}$$

where:  $L$ ,  $D$ , and  $\delta W$  contain all the total energies, dissipation functions, and virtual work in the whole system, and  $\xi$  assumes all the generalized coordinates.

The resulting fully coupled equations define a matrix whose order is the total number of all the generalized coordinates of all the component structures, and the only independent variable is time.

We have shown a method for deriving the equations of motion of single structures and more complex structures made up of many components. From these governing equations, one can establish the ordered concatenation of the individual elements and the proper treatment of the interconnections. Each mode represented by modal mass, stiffness, and mode shape is a module, and a single component which is a physical module can be represented by its modal modules. With the modal building blocks and the modules of connecting elements and external forces, the model of a complex structure can be constructed. The solution is the response of the entire system given in terms of the response of the normal modes of its components.





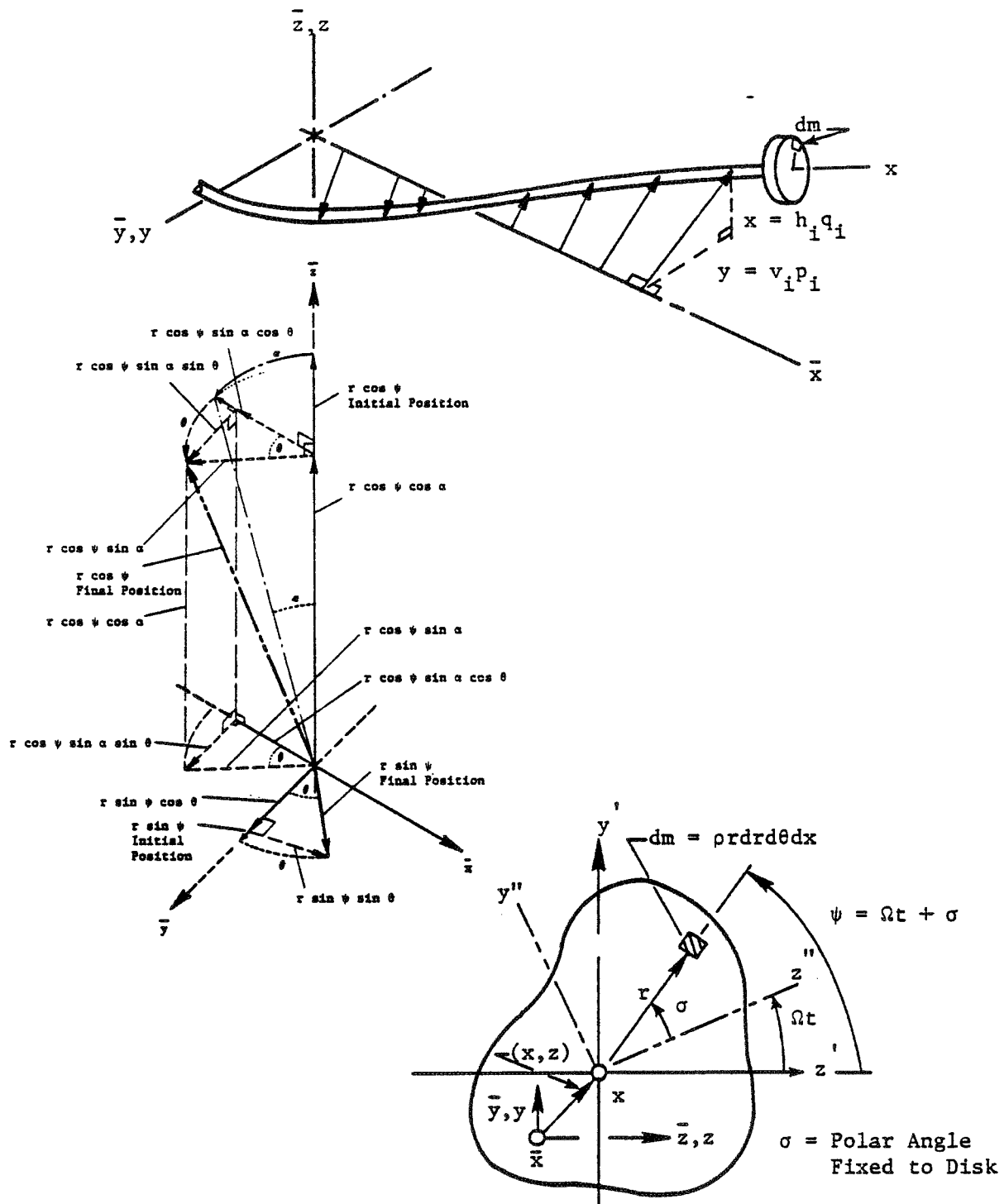


Figure 2. Geometry of Motion of a Rotating Element.

where:

$$z_c^* = \sum_i h_i(x^*) q_i \quad y_c^* = \sum_i v_i(x^*) P_i$$

$$z_r^* = \sum_i h_i(x^*) q_i \quad y_r^* = \sum_i u_i(x^*) P_i$$

Since we are using nonrotating modes for the rotor, which have no gyroscopic effect, we will first write down the displacement components of a point on the rotor which is  $r$  from the centerline. These consist of the stationary mode displacements and those induced by the rotor speed as well as the small rotations from bending slope. Let:

- $\bar{z}(x,t)$  = Total displacement with respect to ground-horizontal plane
- $\bar{y}(x,t)$  = Total displacement with respect to ground-vertical plane
- $\bar{x}(x,t)$  = Total displacement with respect to ground induced by bending in both planes
- $\psi = (\Omega t + \sigma)$  = Angular displacement about axis
- $\Omega$  = Rotor speed, assumed constant
- $h_i q_i$  = Stationary modes - horizontal plane
- $v_i P_i$  = Stationary modes - vertical plane
- $\alpha = \partial \bar{z} / \partial x = \partial z / \partial x$  ;  $\theta = \partial \bar{y} / \partial x = \partial y / \partial x$

We have not shown the subscript, for brevity. Also, for conciseness, we will express the stationary modes as  $z$  and  $y$ ;  $\alpha$  and  $\theta$  are the  $x$  derivatives. It should be understood that these are made up of sums of the normal modes  $h_i q_i$  and  $v_i P_i$ .

From the figure of the geometry of motion given below, we can write down the total displacement components with this sequence of rotations:

1. Rotor rotation:  $\psi, \dot{\psi}$
2. Slope rotation about the horizontal fixed axis:  $\alpha, \dot{\alpha}$
3. Slope rotation about the vertical fixed axis:  $\theta, \dot{\theta}$



thus:

$$\begin{aligned}\bar{z} &= z + r \cos \alpha \cos \psi \\ \bar{y} &= y + r \sin \alpha \sin \theta \cos \psi + r \cos \theta \sin \psi \\ \bar{x} &= -r \sin \alpha \cos \theta \cos \psi + r \sin \theta \sin \psi\end{aligned}$$

The modal potential energy is not affected by the rotor revolution. So, the rotor Lagrangian (exclusive of connecting elements which were already considered with the casing) is:

$$L_r = \frac{1}{2} \int_r \left\{ \dot{\bar{x}}^2 + \dot{\bar{y}}^2 + \dot{\bar{z}}^2 \right\} dm - \frac{1}{2} \left\{ \omega_{(ij)}^2 M_{ij} q_i q_j \right\}_{r_v} - \frac{1}{2} \left\{ \omega_{(ij)}^2 M_{ij} p_i p_j \right\}_{r_v}$$

To obtain the kinetic or inertial terms, we operate with the ELO on the rotor kinetic energy:

$$f_\beta = \frac{d}{dt} \frac{\partial T_r}{\partial \dot{\beta}} - \frac{\partial T_r}{\partial \beta} = \int_r \left\{ \ddot{x} \frac{\partial x}{\partial \beta} + \ddot{y} \frac{\partial y}{\partial \beta} + \ddot{z} \frac{\partial z}{\partial \beta} \right\} dm$$

with  $\beta = z, y, \alpha, \theta$ . This is done so the results can be compared with those normally derived for rotor critical speed. And to obtain the equation in the modal generalized coordinates ( $\xi = q_i, p_i$ ), we proceed as follows

$$\frac{d}{dt} \frac{\partial T_r}{\partial \dot{\xi}} - \frac{\partial T_r}{\partial \xi} = \sum_\beta \left( \frac{d}{dt} \frac{\partial T_r}{\partial \dot{\beta}} - \frac{\partial T_r}{\partial \beta} \right) \frac{d\beta}{d\xi} = \sum_\beta f_\beta \frac{d\beta}{d\xi}$$

and:

$$\begin{aligned}z &= \sum_i h_i q_i & y &= \sum_i v_i p_i \\ \alpha &= \sum_i \frac{\partial h_i}{\partial x} q_i & \theta &= \sum_i \frac{\partial v_i}{\partial x} p_i\end{aligned}$$

Proceeding in this manner, the kinetic or inertial rotor equations in the  $\beta = x, y, \alpha, \theta$  coordinates and then the modal generalized coordinates  $P_i, q_i$  are found to be:

In Physical Displacements

$$f_z = \int \{ \ddot{z} - \Omega^2 r \cos \psi \} dm$$

$$f_y = \int \{ \ddot{y} - \Omega^2 r \sin \psi \} dm$$

$$f_\alpha = \int \{ \ddot{\alpha} r^2 \cos^2 \psi - 2\dot{\alpha} \Omega r^2 \sin \psi \cos \psi - \ddot{\theta} r^2 \sin \psi \cos \psi - 2\dot{\theta} \Omega r^2 \cos^2 \psi \} dm$$

$$f_\theta = \int \{ \ddot{\theta} r^2 \sin^2 \psi + 2\dot{\theta} \Omega r^2 \sin \psi \cos \psi - \ddot{\alpha} r^2 \sin \psi \cos \psi + 2\dot{\alpha} \Omega r^2 \sin^2 \psi \} dm$$

In Modal Generalized Coordinates

$$f_{q_i} = \int \{ (h_i h_j + r^2 h_i' h_j' \cos^2 \psi) \ddot{q}_j - 2h_i h_j \dot{q}_j \Omega r^2 \sin \psi \cos \psi - h_i v_j' \ddot{P}_j r^2 \sin \psi \cos \psi - 2h_i v_j' \dot{P}_j \Omega r^2 \cos^2 \psi - \Omega^2 h_i r \cos \psi \} dm$$

$$f_{P_i} = \int \{ (v_i v_j + r^2 v_i' v_j' \sin^2 \psi) \ddot{P}_j + 2v_i v_j' \dot{P}_j \Omega r^2 \sin \psi \cos \psi - v_i h_j' \ddot{q}_j r^2 \sin \psi \cos \psi + 2v_i h_j' \dot{q}_j \Omega r^2 \sin^2 \psi - \Omega^2 v_i r \sin \psi \} dm$$

The integrals are evaluated over the volume of the rotor. In cylindrical coordinates, the differential mass is:

$$dm = r dr d\psi dz$$

noting that:

$$\psi = \Omega t + \sigma ; \int [ ] dm = \int_x \int_{r=0} \int_{\sigma=0}^{2\pi} [ ] \rho r dx dr d\sigma$$

For brevity, let us perform the integration over disks (neglecting the mass of the rotor) only so that the  $dz$  just becomes " $z$ ," the axial thickness of the disk. So, now examine the integration with respect to the face of the disk, e.g.,  $dA = r dr d\sigma$ . For the case where the disk has no unbalance so that the neutral axis, centerline, center of rotation, and centroidal axis are coincident, it can be seen that:\*

$$g(x) \int r \begin{pmatrix} \cos \psi \\ \sin \psi \end{pmatrix} dm = G(x) \int_r \int_{\sigma=0}^{2\pi} r^2 \begin{pmatrix} \cos(\Omega t + \sigma) \\ \sin(\Omega t + \sigma) \end{pmatrix} dr d\sigma = \begin{pmatrix} 0 \\ 0 \end{pmatrix}$$

similarly

$$g(x) \int r \sin \psi \cos \psi dm = G(x) \int_r \int_0^{2\pi} \sin(\Omega t + \sigma) \cos(\Omega t + \sigma) dr d\sigma = 0$$

and that

$$\begin{aligned} g(x) \int \begin{pmatrix} \cos^2 \psi \\ \sin^2 \psi \end{pmatrix} r^2 dm &= G(x) \int_r \int_0^{2\pi} \rho \begin{pmatrix} \cos^2(\Omega t + \sigma) \\ \sin^2(\Omega t + \sigma) \end{pmatrix} r^3 dr d\sigma \\ &= G(x) \frac{\rho \pi r^4}{4} \end{aligned}$$

When the values of these integrals are substituted into the kinetic terms in the equations of motion, we obtain the classical rotor equations.

However, when the disk center of gravity (CG) is no longer coincident with the axis of rotation, centerline, or rotor neutral axis, the integrals over the face of the disk are no longer simple constants. For example:

$$h_i \int r \cos \psi dm = h_i(x_0) \Delta x m e \Omega^2 \cos \Omega t = F_{unb},$$

$F_{unb}$ , the rotating unbalance, as "seen" by a stationary coordinate or support where  $m e$  = unbalance.

---

\*Note that the mode shapes are functions only of  $x$ , the axial distance. Let these functions be  $g(x)$  and  $\int_x g(x) dx = G(x)$ .

When the other  $\sin \psi$ ,  $\cos \psi$ ,  $\sin \psi \cos \psi$ ,  $\sin^2 \psi$ ,  $\cos^2 \psi$  integrals are evaluated over an unbalanced disk, so-called secular terms are obtained - terms multiplied by:

$$\begin{aligned} & \sin \Omega t, \cos \Omega t \\ & \sin 2\Omega t, \cos 2\Omega t \end{aligned}$$

If we recall that these integrals are coefficients of the generalized coordinates, the equations of motion will have terms like these:

$$q_i \sin \Omega t, q_i \cos \Omega t, \ddot{q}_i \cos 2 \Omega t, \ddot{q}_i \sin 2 \Omega t, \dot{q}_i \sin 2 \Omega t$$

$$P_i \sin \Omega t, P_i \cos \Omega t, \bar{P}_i \cos 2 \Omega t, \bar{P}_i \sin 2 \Omega t, \dot{P}_i \cos 2 \Omega t$$

These terms are sometimes called parametric terms because they imply a harmonic variation in a parameter. In this case, these would be time-varying moments of inertia and mass moments.

However, since these "unbalance" integrals are dependent only on the square of the unbalance, eccentricity, or noncongruency of the CG from the axis of rotation, the values are small and may be neglected. Of course, where the eccentric radius is no longer small, these parametric terms become important.

Combining the terms from the casing, the connecting elements, and the rotor, the equations of motion of the entire turbine engine can be written down:

$$\begin{aligned} (1) \quad \left( F_{q_i} \right)_c = 0 = & \left\{ M_{ij} (\ddot{q}_j + \omega_{(ij)}^2 q_j) \right\}_c + \sum_{x^*} K_h(x^*) (z_c^* - z_r^*) \frac{\partial}{\partial q_i} (z_c^* - z_r^*) \\ & + \left\{ C_{ij} \dot{q}_j \right\}_c + \sum_{x^*} C_h(x^*) (\dot{z}_c^* - \dot{z}_r^*) \frac{\partial}{\partial q_i} (z_c^* - z_r^*) \end{aligned}$$

(1) We assume that the rotor is symmetric so that the horizontal and vertical modes are the same and therefore all orthogonal.

$$(1) \quad \left( \sum_{P_i} \right)_c = 0 = \left\{ M_{ij} (P_j + \omega^2 (ij) q_j) \right\}_c + \sum_{z^*} K_v(x^*) (y_c^* - y_r^*) \frac{\partial}{\partial q_i} (y_c^* - y_r^*)$$

$$+ \left\{ C_{ij} \dot{P}_j \right\}_c + \sum_{z^*} C_v(x^*) (\dot{y}_c^* - \dot{y}_r^*) \frac{\partial}{\partial \dot{P}_i} (\dot{y}_c^* - \dot{y}_r^*)$$

$$(2) \quad \sum_{x_o} \Omega^2 h_i(x_o) e_r(x_o) \cos \Omega t = \left\{ M_{ij} (\ddot{q}_j + \omega^2 (ij) q_j) \right\}_r$$

$$- \sum_{x^*} K_h(x^*) (z_c^* - z_r^*) \frac{\partial}{\partial q_i} (z_c^* - z_r^*) + \left\{ C_{ij} \ddot{q}_j \right\}_r$$

$$- \sum_{x^*} C_h(x^*) (\dot{z}_c^* - \dot{z}_r^*) \frac{\partial}{\partial \dot{q}_i} (\dot{z}_c^* - \dot{z}_r^*) + \Omega \sum_{P_j} G_{q_i P_j} \dot{P}_j$$

$$(2) \quad \sum_{z_o} \Omega^2 v_i(x_o) e_r(x_o) \sin \Omega t = \left\{ M_{ij} (\ddot{P}_i + \omega^2 (ij) P_j) \right\}_v - \sum_{x^*} K_v(x^*) (y_c^* - y_r^*)$$

$$- \sum_{x^*} K_v(x^*) (y_c^* - y_r^*) \frac{\partial}{\partial P_i} (y_c^* - y_r^*) + \left\{ C_{ij} \dot{P}_j \right\}_v$$

$$- \sum_{x^*} C_v(x^*) (\dot{y}_c^* - \dot{y}_r^*) \frac{\partial}{\partial \dot{P}_i} (\dot{y}_c^* - \dot{y}_r^*) - \Omega \sum_{q_j} G_{q_j P_i} \dot{q}_j$$

(2) Location of unbalance (s) =  $x_o$

$$G_{q_i P_j} = -G_{q_i P_i} = 2 \int v_i' h_j' r^2 \begin{pmatrix} \sin^2 \psi \\ \cos^2 \psi \end{pmatrix} r^2 dm$$

Recall that:  $M_{ij}$ 's are nonzero only for  $i = j$ :

$$z_c^* = z_c(x^*, t) = \sum h_{i_c}(x^*) q_{i_c}$$

$$y_c^* = y_c(x^*, t) = \sum v_{i_c}(x^*) P_{i_c}$$

$$z_r^* = z_r(x^*, t) = \sum h_{i_r}(x^*) q_{i_r}$$

$$y_r^* = y_r(x^*, t) = \sum v_{i_r}(x^*) P_{i_r}$$

Therefore, the resulting matrix of equations will have an order equal to the number of all modes.

The only excitations in this model (since we ignored the parametric excitation) are those from the simple unbalances acting on the rotor:

$$f_{q_{i_r}} = \Omega^2 \sum_{x_0's} m(x_0) e(x_0) h_i(x_0) \cos \Omega t$$

$$f_{P_{i_r}} = \Omega^2 \sum_{x_0's} m(x_0) e(x_0) v_i(x_0) \sin \Omega t$$

As described in Volume III, interference loads such as rubs can also be modeled and included in the TETRA computer code. The numerical solution for the transient response of a turbine engine with a sudden unbalance is also discussed in Volume III. Briefly, a central-difference integration approach is used to solve the governing equations. This consists of rewriting each ODE such that the generalized acceleration is on the left-hand side and the rest are to the right. The central-difference technique then calculates the current values of the acceleration, velocity, and displacement of each coordinate in terms of three previous values. With these values, the value of the forces (right-hand side) is updated, and the calculation is repeated at each time step.


Examples of typical structural and connecting modules are given in Tables I through III. In TETRA, such modules and others are used to model an entire engine as well as its supporting structure.

Table I. Modal Module - Static Structures.

Horizontal Plane


$$\begin{pmatrix} M_{ij} & 0 & \dots & 0 \\ 0 & M_{22} & & 0 \\ \vdots & \vdots & \ddots & \vdots \\ 0 & 0 & \dots & M_{nn} \end{pmatrix}_H \begin{pmatrix} \ddot{q}_1 \\ \ddot{q}_2 \\ \vdots \\ \ddot{q}_n \end{pmatrix} = \begin{pmatrix} F_{q1} \\ F_{q2} \\ \vdots \\ F_{qn} \end{pmatrix}$$

Generalized Mass



$$\begin{pmatrix} K_{11} & 0 & \dots & 0 \\ 0 & K_{22} & \dots & 0 \\ \vdots & \vdots & \ddots & \vdots \\ 0 & 0 & \dots & K_{nn} \end{pmatrix}_H \begin{pmatrix} q_1 \\ q_2 \\ \vdots \\ q_n \end{pmatrix} = \begin{pmatrix} F_{q1} \\ F_{q2} \\ \vdots \\ F_{qn} \end{pmatrix}$$

Generalized Sp'g.




Same for: P<sub>i</sub>, Vertical Plane.

Vertical Plane

$$\begin{pmatrix} M_{11} & 0 & \dots & 0 \\ 0 & M_{22} & & 0 \\ \vdots & \vdots & \ddots & \vdots \\ 0 & 0 & \dots & M_{mm} \end{pmatrix}_V \begin{pmatrix} \ddot{P}_1 \\ \ddot{P}_2 \\ \vdots \\ \ddot{P}_m \end{pmatrix} = \begin{pmatrix} F_{P1} \\ F_{P2} \\ \vdots \\ F_{Pm} \end{pmatrix}$$

Generalized Mass



$$\begin{pmatrix} K_{11} & 0 & \dots & 0 \\ 0 & K_{22} & \dots & 0 \\ \vdots & \vdots & \ddots & \vdots \\ 0 & 0 & \dots & K_{mm} \end{pmatrix}_V \begin{pmatrix} P_1 \\ P_2 \\ \vdots \\ P_m \end{pmatrix} = \begin{pmatrix} F_{P1} \\ F_{P2} \\ \vdots \\ F_{Pm} \end{pmatrix}$$

Generalized Stiffness




Table II. Modal Module - Rotating Structures.

Horizontal Plane

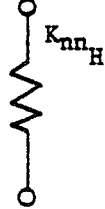
$$\begin{Bmatrix} M_{11} & 0 & \dots & 0 \\ 0 & M_{22} & \dots & 0 \\ \vdots & \vdots & \ddots & \vdots \\ 0 & 0 & \dots & M_{nn} \end{Bmatrix}_H \begin{Bmatrix} \ddot{q}_1 \\ \ddot{q}_2 \\ \vdots \\ \ddot{q}_n \end{Bmatrix} = \begin{Bmatrix} F_{q1} \\ F_{q2} \\ \vdots \\ F_{qn} \end{Bmatrix}$$

Horizontal Generalized Mass



$$\begin{Bmatrix} K_{11} & 0 & \dots & 0 \\ 0 & K_{22} & \dots & 0 \\ \vdots & \vdots & \ddots & \vdots \\ 0 & 0 & \dots & K_{nn} \end{Bmatrix}_H \begin{Bmatrix} q_1 \\ q_2 \\ \vdots \\ q_n \end{Bmatrix} = \begin{Bmatrix} F_{q1} \\ F_{q2} \\ \vdots \\ F_{qn} \end{Bmatrix}$$

Horizontal Generalized Stiffness



Vertical Plane

$$\begin{Bmatrix} M_{11} & 0 & \dots & 0 \\ 0 & M_{22} & \dots & 0 \\ \vdots & \vdots & \ddots & \vdots \\ 0 & 0 & \dots & M_{mm} \end{Bmatrix}_V \begin{Bmatrix} \ddot{P}_1 \\ \ddot{P}_2 \\ \vdots \\ \ddot{P}_m \end{Bmatrix} = \begin{Bmatrix} F_{P1} \\ F_{P2} \\ \vdots \\ F_{Pm} \end{Bmatrix}$$

Vertical Generalized Mass



$$\begin{Bmatrix} K_{11} & 0 & \dots & 0 \\ 0 & K_{22} & \dots & 0 \\ \vdots & \vdots & \ddots & \vdots \\ 0 & 0 & \dots & K_{mm} \end{Bmatrix}_V \begin{Bmatrix} P_1 \\ P_2 \\ \vdots \\ P_m \end{Bmatrix} = \begin{Bmatrix} F_{P1} \\ F_{P2} \\ \vdots \\ F_{Pm} \end{Bmatrix}$$

Vertical Generalized Stiffness

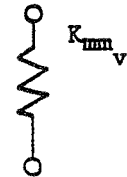




Table II. Modal Module - Rotating Structure (Continued).

Gyroscopic: Horizontal-Vertical Planes Coupling

$\dot{q}_1$	$\dot{q}_2$	..	$\dot{q}_n$	$\dot{P}_1$	$P_2$	..	$\dot{P}_m$		
$[0]$				$-G_{q_1 P_1}$	$-G_{q_1 P_2}$	..	$-G_{q_1 P_m}$	$\begin{Bmatrix} \dot{q}_1 \\ \dot{q}_2 \\ \vdots \\ \dot{q}_n \end{Bmatrix}$	$\begin{Bmatrix} F_{q_1} \\ F_{q_2} \\ \vdots \\ F_{q_n} \end{Bmatrix}$
				$-G_{q_2 P_1}$	$-G_{q_2 P_2}$	..	$-G_{q_2 P_m}$		
				$\vdots$	$\vdots$		$\vdots$		$\vdots$
				$-G_{q_n P_1}$	$-G_{q_n P_2}$	..	$-G_{q_n P_m}$	$\begin{Bmatrix} \dot{P}_1 \\ \dot{P}_2 \\ \vdots \\ \dot{P}_m \end{Bmatrix}$	$\begin{Bmatrix} F_{P_1} \\ F_{P_2} \\ \vdots \\ F_{P_m} \end{Bmatrix}$
$G_{q_1 P_1}$	$G_{q_2 P_1}$	..	$G_{q_n P_1}$	$[0]$					
$G_{q_1 P_2}$	$G_{q_2 P_2}$	..	$G_{q_n P_2}$						
$\vdots$	$\vdots$		$\vdots$						
$G_{q_1 P_m}$	$G_{q_2 P_m}$	..	$G_{q_n P_m}$						

$$G_{q_n P_m} = 2\Omega \int_{\text{volume}} h_n(x) v_m(x) r^2 \begin{pmatrix} \cos^2 \psi \\ \text{or} \\ \sin^2 \psi \end{pmatrix} dm$$

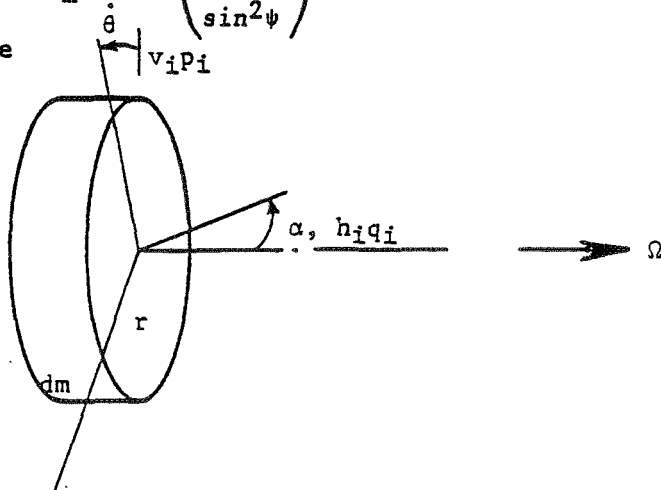


Table II. Modal Module - Rotating Structure (Concluded).

Unbalance Load - At Each Unbalance Location,  $x = x_0$ .

$$\Omega_m^2 \begin{Bmatrix} \epsilon h_1 \cos \Omega t \\ \epsilon h_2 \cos \Omega t \\ \vdots \\ \epsilon h_n \cos \Omega t \\ \epsilon v_1 \sin \Omega t \\ \epsilon v_2 \sin \Omega t \\ \vdots \\ \epsilon v_m \sin \Omega t \end{Bmatrix} = \begin{Bmatrix} F_{q1} \\ F_{q2} \\ \vdots \\ F_{qn} \\ F_{p1} \\ F_{p2} \\ \vdots \\ F_{pm} \end{Bmatrix}$$

N.B.  $h_i(x_0)$   $v_i(x_0)$

$x = x_0$ , Unbalance Location

$m\epsilon$  = Unbalance Magnitude

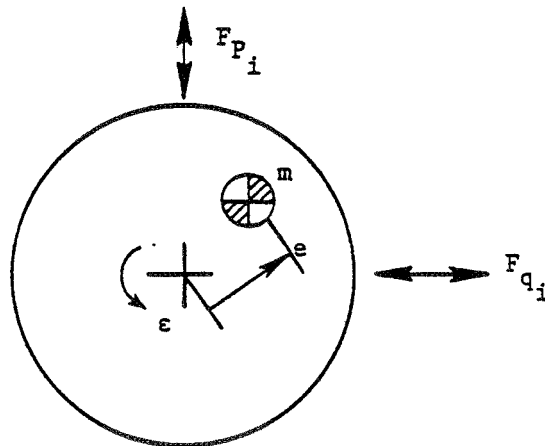
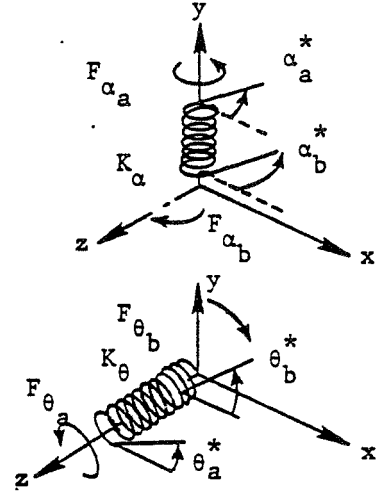




Table III. Connecting Elements (Concluded).

Rotation Spring

$$\left( \begin{array}{cc|c} K_\alpha & -K_\alpha & [0] \\ -K_\alpha & K_\alpha & [0] \\ \hline & & K_\theta & -K_\theta \\ & & -K_\theta & K_\theta \end{array} \right) \begin{pmatrix} \alpha_a^* \\ \alpha_b^* \\ \theta_a^* \\ \theta_b^* \end{pmatrix} = \begin{pmatrix} F_{\alpha_a} \\ F_{\alpha_b} \\ F_{\theta_a} \\ F_{\theta_b} \end{pmatrix}$$



$$F_{q_{ja}} = F_{\alpha_a} \frac{\partial \alpha_a^*}{\partial q_{ja}} = h'_{ja} K_\alpha \left\{ h'_{1a} q_{1a} - h'_{1b} q_{1b} + h'_{2a} q_{2a} h'_{2b} q_{2b} + \dots \right\} = h'_{ja} F_{\alpha_a}$$

$$F_{q_{jb}} = F_{\alpha_b} \frac{\partial \alpha_b^*}{\partial q_{jb}} = -h'_{jb} F_{\alpha_b}$$

$$F_{p_{ja}} = F_{\theta_a} \frac{\partial \theta_a^*}{\partial p_{ja}} = u'_{ja} F_{\theta_a} = u'_{ja} K_\theta \left\{ u'_{1a} p_{1a} - u'_{1b} p_{1b} + u'_{2a} p_{2a} - u'_{2b} p_{2b} + \dots \right\}$$

$$F_{p_{jb}} = F_{\theta_b} \frac{\partial \theta_b^*}{\partial p_{jb}} = -u'_{jb} F_{\theta_b}$$

### 3.0 DETAILED ANALYTICAL DEVELOPMENT OF THE TETRA PROGRAM

#### 3.1 SUMMARY

This section contains the detailed application of the component element method to Task II analyses for the transient dynamic response of a turbine engine. The component element approach results in a single independent variable, time, and reduces the number of differential equations required to obtain the essential dynamic characteristics of a turbine engine. The component elements consist of elastic and rigid-body elements, described by generalized coordinates obtained by coordinate transformations, and physical connecting elements that model bearing/frame springs and dampers, rotor-case rub springs, and gyroscopic crossaxis coupling effects.

The generalized coordinates are based on the free-free modes and partially constrained modes associated with engine subsystem structures (rotor, casing, and pylon). The method extends conventional modal analysis procedure to account for physical damping, asymmetric stiffness terms, and rotor-case rubs including the effects of the dead band associated with the structural clearance.

An efficient, numerical, time-integration scheme - the central finite-difference method - is used to obtain the solution through an explicit, step-by-step calculation.

A description of a computer code that was developed to implement the transient analysis method is also provided.

#### 3.2 INTRODUCTION

This section is the detailed development of the application of the component element synthesis method described in the previous section for the transient dynamic analysis of turbine engine systems in three dimensions. In addition, the structure and major program modules of a computer code that was developed to implement the transient analysis method is presented along with some computed results.

The analysis method presented is conceptually similar to that described by Levy and Wilkinson (Reference 6) and clarified in Section 2.0 of this document. However, the method and the mathematical modeling approach described in this report have been specifically developed for the analysis of flexible turbine engine systems and include features needed to predict the response produced by suddenly applied loads such as those caused by blade loss.

The turbine engine is described by a reduced system of second-order differential equations, and a solution for the transient response is obtained through an explicit numerical-integration scheme: the central finite-difference method. Global stiffness and damping matrices are not assembled, and only

the right-hand side of the system of equations (i.e., the forces) is updated at each time step. The differential equations are formulated in terms of generalized coordinates and modal elastic and rigid-body elements that represent physical connections. In the former case, the elements are obtained through the coordinate transformations associated with the free-free modes and partially constrained modes computed for engine subsystem structures (rotors, case, and pylon). In the latter case, the elements describe the physical connections between the subsystem structures. These connections can be nonlinear and are defined with bearing/frame springs and dampers, engine support elements, link elements, rotor-case rub springs or stop elements, and gyroscopic crossaxis coupling elements. The rotor-case rub springs are used to model the additional load path, between the rotor and the case, that exists for the large rotor excursions caused by high rotor unbalance. For this element, the effect of the force dead band associated with the structural clearance is included in the formulation for the effective restoring forces.

The representation of the entire engine in terms of these components is achieved by a rational concatenation of the corresponding equations by application of Newton's Law or the principle of virtual work and the Lagrangian as described in Section 2.0.

### 3.3 ANALYTICAL DEVELOPMENT

#### 3.3.1 Governing Differential Equations

The turbine engine system is described in terms of generalized coordinates and physical connecting elements. The generalized coordinates are obtained through coordinate transformations from the real space coordinates. Through the principle of virtual work, these generalized coordinates are the modal participation of specified engine subsystems. These modes and their generalized coordinates are associated with subsystems that typically include the high and low pressure rotors, the engine case, and the pylon. Subsystem normal modes may be calculated from finite-element analyses or determined experimentally. Figure 3 shows a schematic of a subsystem and physical component element definition for an engine system. The nonlinearities can be treated with the physical connecting elements, and the subsystem natural modes are used to define regions of the engine system which are expected to remain linear. As long as the nonlinearities are not severe enough to induce operating regimes where the original modes are totally unrepresentative, the use of the natural modes is effective.

Following the technique of the component element method, an ordinary differential equation is formulated for each generalized coordinate. These are written so that the acceleration is on the left-hand side and the rest are on the right, thus:

$$m_1 \ddot{q}_1 = -K_1 q_1 = -C_1 \dot{q}_1 + F_1(t) = Q_1 \quad (1)$$



The notation of Section 2.0 has been altered here to standard matrix notation in order to take advantage of matrix manipulation in the program coding. However, the principles are the same.

$q_i$  are the generalized or modal coordinates that describe the subsystem modes. The  $q_i$  is the participation of the  $i$ -th mode of that subsystem. These are the principal dependent variables.

$m_i$  are the generalized or modal masses.

$k_i$  are the generalized stiffnesses that exist only for the distortion energy modes.

$$k_i = \{\phi_i\}_T [K] \{q_i\} \quad (2)$$

$[K]$  is the physical stiffness matrix for the subsystem, and  $\{\phi_i\}$  is the Eigen vector or mode shape of the  $i$ -th mode.

$C_i$  are generalized damping coefficients proportionate to the modal masses

$$C_i = \frac{1}{Q_{Fi}} \frac{k_i}{\omega_i} \quad (3)$$

where  $Q_{Fi}$  = the modal Q-factor, and  $\omega_i$  is the undamped natural frequency for the  $i$ -th mode.

$F_i$  are the generalized forces that are associated with applied physical forces. These physical forces include rotor unbalance forces, user-specified forces, crossaxis forces due to Coriolis acceleration, spring forces, damping forces, and rub forces.

$Q_i$  are the total generalized forces which include the generalized restoring forces  $-k_i q_i$ , the generalized forces  $-C_i \dot{q}_i$ , and the generalized forces  $F_i$  associated with the applied physical forces. The total generalized forces are updated at each time step.

It is useful to introduce the concept of a coupling ratio in formulating the generalized forces  $F_i$  in terms of the physical forces.

$$F_i = F_{r,d} B_{i,r,d} \quad (4)$$

The coupling ratio  $B_{i,r,d}$  forms the elements of  $\{Q_i\}$  and is the deflection at point  $r$  in the direction  $d$  for a unit value of the  $i$ -th generalized coordinate. The term  $F_{r,d}$  defines the applied physical force at point  $r$  in the direction  $d$ . Then the total generalized forces can be written as:

$$Q_i = \sum_r \sum_d F_{r,d} B_{i,r,d} - k_i q_i - C_i \dot{q}_i \quad (5)$$



and the equations of motion can be arranged into the form:

$$\ddot{q}_i = \frac{Q_i}{m_i} \quad i = 1, 2, 3, \dots \quad (6)$$

### 3.3.2 Numerical Integration of the Governing Differential Equations

The transient response solution for Equation 6 is obtained with an explicit numerical-integration scheme: the central finite-difference method. In this scheme, the accelerations of each of the generalized coordinates associated with the component modes are computed at each time step using the current values of the applied forces. The accelerations are directly used to compute the future generalized displacements, and no iteration is required. The future displacements then allow the calculation of updated forces, and the procedure is repeated until the desired number of time-step solutions has been obtained. As discussed in Reference 5, this concept has also been used in the prediction of crash response of vehicle structural systems. Global stiffness and damping matrices are never assembled. Local stiffness and damping matrices are defined, and it is only necessary to update those physical connecting element stiffness and damping matrices which are nonlinear. The forces are then determined by multiplication at the element level. This explicit scheme requires much less computer time and core storage than would be required in an implicit scheme where nonlinear system or global matrices must be redefined at each time step.

Each of the equations of motion described by Equation 6 appears to be uncoupled. However, they are actually coupled through the physical constituent forces of  $F_i$  that relate to the displacement and velocity-dependent load paths between the modal subsystems that are used to define the linear regions in the engine system.

In the central finite-difference method, the current total generalized forces in Equation 6 can be expressed in terms of the current and previous values of the generalized displacements  $q_i$ :

$$Q_i^0 = f(q_i^0, q_i^{-1}, q_i^{-2}) \quad (7)$$

The superscripts 0, -1, -2 pertain to the current and two previous values of the generalized displacements (present value, value one time step earlier, and value two steps earlier). Then, the current generalized accelerations are obtained from:

$$\ddot{q}_i^0 = \frac{Q_i^0}{m_i} \quad (8)$$

The following finite-difference equation is used to solve for the new or future generalized displacements:

$$q_i^1 = 2q_i^0 - q_i^{-1} + \ddot{q}_i^0 (\Delta T)^2 \quad (9)$$

The superscript 1 pertains to the future values of the generalized displacements.

For convergent or stable solutions, the time step  $\Delta T$  must be less than

$$2 \sqrt{\frac{m_i}{K_i^T}}$$

where  $K_i^T$  is the total effective stiffness that includes all product terms relating to  $q_i$  in Equation 1. While not immediately apparent from inspection of Equation 1, the effects of  $q_i$  are included in  $F_i$ . It will be noted that for nonlinear problems  $K_i^T$  values are not known prior to the solution. In practice,  $\Delta T$  should be made equal to about 1/40 of the smallest period of oscillation for the subsystem modes, assuming that there are no connection points, or:

$$\Delta T = \frac{2\pi}{40} \sqrt{\frac{m_i}{k_i}} = 0.157 \sqrt{\frac{m_i}{k_i}}$$

The initial conditions are accounted for by setting for the initial time interval:

$$q_i^1 = q_i^0 + \dot{q}_i^0 \Delta T + \frac{1}{2} \ddot{q}_i^0 (\Delta T)^2$$

$$q_i^0 = q_i$$

$$q_i^{-1} = q_i^0 - \dot{q}_i^0 \Delta T + \frac{1}{2} \ddot{q}_i^0 (\Delta T)^2 \quad (10)$$

$$q_i^{-2} = 2 q_i^{-1} - q_i^0 + \ddot{q}_i^0 (\Delta T)^2$$

The latter condition arises from the assumption that the acceleration prior to time  $t_0$  is  $\ddot{q}_i^0$ .

The major task in the implementation of the method is the computation of the current total generalized forces  $Q_i^0$ . From Equation 5,

$$Q_i^0 = \sum_r \sum_d F_{r,d}^0 B_{i,r,d} - k_i q_i^0 - C_i \dot{q}_i^0 \quad (11)$$

The current generalized velocities are obtained from the following backward difference approximation:

$$\dot{q}_i^0 = \frac{3 q_i^0 - 4 q_i^{-1} + q_i^{-2}}{2 \Delta T} \quad (12)$$

Hence, in Equation (11), the force terms involving the generalized stiffness and damping can be readily defined. Conceptually, these force terms can be associated with scalar springs and dashpots connecting the generalized masses  $m_i$  directly to ground. The generalized force term

$$\sum_r \sum_d F_{r,d}^0 B_{i,r,d}$$

includes coupling force terms between the generalized masses that are dependent on the current physical displacements and velocities of the physical connecting elements at the attachment points to the modal subsystems. In addition,  $F_{r,d} B_{i,r,d}$  includes nondisplacement and velocity-dependent terms that do not couple the generalized masses. These terms are associated with rotor unbalance and user-specified forces.

The current physical displacements  $X_{r,d}$  and velocities  $\dot{X}_{r,d}$  needed to establish the coupling forces are obtained from the summation of the modal participations of the generalized displacements. In other words, at each time step the modal displacements are transformed into real space (Equations 13 and 14) so that the physical displacements can be obtained:

$$X_{r,d} = \sum_i q_i^0 B_{i,r,d} \quad (13)$$

$$\dot{X}_{r,d} = \sum_i \dot{q}_i^0 B_{i,r,d} \quad (14)$$

$X_{r,d}$  and  $\dot{X}_{r,d}$  are the physical displacements and velocities, respectively, at the point  $r$  in the direction  $d$ .

The displacement and velocity-dependent terms of the  $F_{r,d}^0$  forces associated with a given connecting element are then determined at the local level by multiplying the connecting-element stiffness matrix into the physical displacements, the connecting-element damping matrix into the physical velocities, and then adding the two results as depicted by Equation 15. It will be noted that in the case of the Coriolis acceleration forces only an effective local damping matrix exists for each station where this effect is included.

$$F_{r,d}^0 = \sum_d \sum_r X_{r,d} K_{r,d} + \sum_d \sum_r \dot{X}_{r,d} C_{r,d} \quad (15)$$

$K_{r,d}$  and  $C_{r,d}$  are the current stiffness and damping coefficients for the connecting element.

### 3.3.3 Modules and Structural Discretization

The concept of the modal synthesis and the component element method naturally lead to modules or building blocks. These modules reflect physical as well as mathematical components. With the first, the structure of the entire engine may be constructed with physical subsystems as one may

sketch a schematic of the structure, and in the other a mathematical representation is built of the complete engine structure in terms of mathematical modules that mimic the response of the physical system. For example, it had been shown in Section 3.3.1, as well as in Section 2.0, that expansion of the physical displacement of each structural subsystem into its normal modes and application of Newton's Law or the Lagrangian results in modules of modal or generalized masses and stiffnesses analogous to the structural mass and stiffness of a simple spring-mass system. In addition, modal or generalized exciting forces can be constructed from the physical and external forces by multiplying these with the modal displacement at the point and line of action of the physical force. Rotation of a component also introduces gyroscopic modules that couple motions in two orthogonal planes. Similarly, the connecting forces have their own modules. In the following sections, the mathematical models of these modules are derived and written in forms amenable to computer coding.

### 3.3.3.1 Modal Subsystems

Modal representations obtained by transforming the degrees-of-freedom from real space to modal space are used to define the structural dynamic properties of the subsystems. This transformation can be made with the concept of the Lagrangian or virtual work principle as described in Section 2. The concept of using modal coordinates to reduce the dimensionality of the model and to clarify the dynamics of the model has historically been exploited in vibration analysis. Childs (Reference 7) and Lund (Reference 8) have reported success in using this approach for flexible rotor transient analysis.

The equation describing the coordinate transformation for a given subsystem follows:

$$\{X\} = \sum_i q_i \{\phi_i\} \quad (16)$$

$\{X\}$  is the physical displacement vector whose elements are the  $X_{r,d}$  values

$q_i$  are the generalized coordinates

$\{\phi_i\}$  is the mode shape vector whose elements are the  $B_{i,r,d}$  values.

The real-space formulations are based on beam-like, finite-element (discrete mass and stiffness), subsystem models of the engine rotor(s) and case and a three-dimensional, finite-element model of the pylon, all described with respect to a ground-fixed coordinate system. Figure 4 shows typical subsystem normal modes and coupling ratios for a rotor finite-element model. The flexural vibration characteristics of equivalent nonrotating shaft(s) are used to define the rotor(s). The whirl phenomenon is addressed by using Euler's law for angular motions to establish crossaxis coupling forces that are dependent

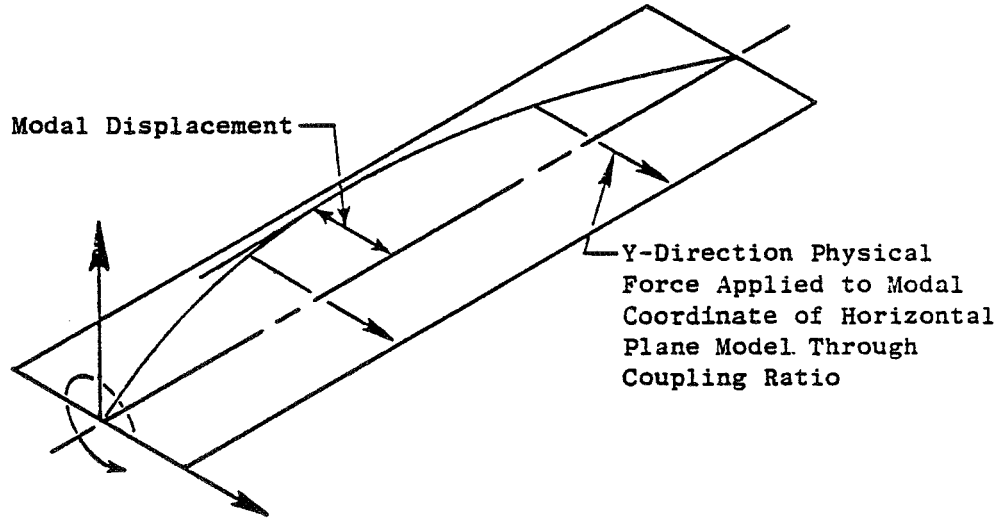
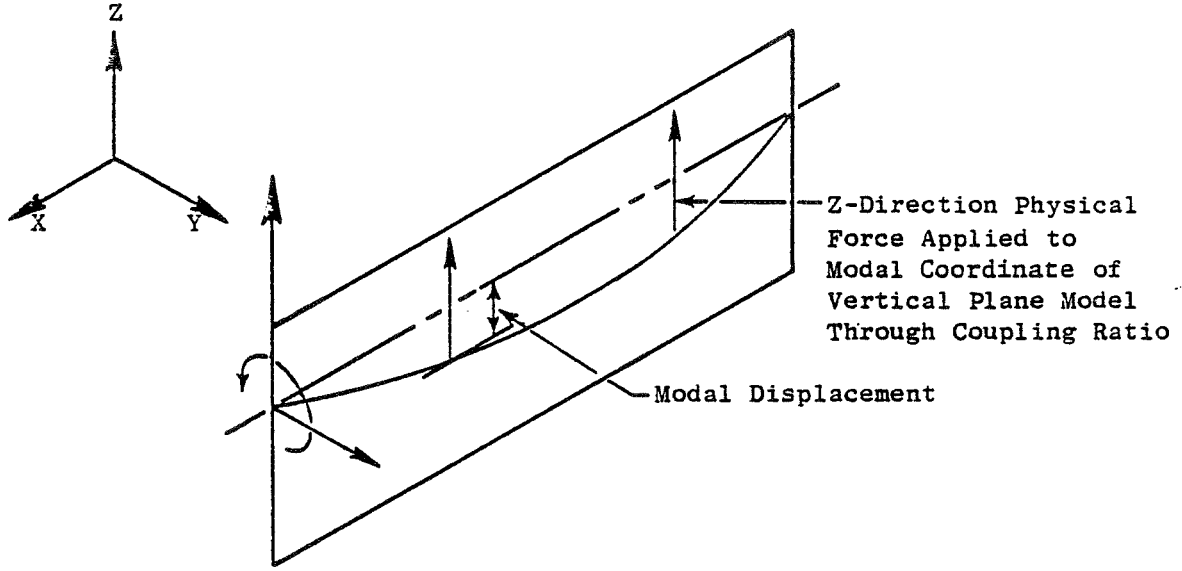


Figure 4. Engine Rotor Subsystem Normal Modes in Two Orthogonal Planes.

on angular velocities in two planes and proportional to the polar inertia; these forces are applied as external forces (contributors to the  $F_i$  forces described in Equation 1) to the modal coordinates that represent the rotor in two planes.

The free-free undamped modes in both the vertical and the horizontal plane for the rotor(s) and the case are derived from planar finite-element models. In addition, a single-dimension (single degree-of freedom at each station) torsional model is also used to model the case. The rigid-body modes for the rotor(s) and case in the vertical and horizontal directions can be defined either with the "soft spring" rigid-body modes or with separate modal subsystems representing computed rigid-body modes based on mass properties and geometry. The torsional-direction, rigid-body modes for the case are represented either with the soft-spring, rigid-body modes or with a rigid-body modal subsystem. It will be noted that the case torsional direction is important for modeling the engine mounting system load paths. The fore-and-aft motions are represented with rigid-body modal subsystems for both the rotor(s) and the case. The pylon finite-element model is used to define a set of three-dimensional, cantilevered modes. Figure 5 shows the global coordinate system, direction numbers, and a typical engine mounting arrangement. Table IV identifies the physical degrees-of-freedom associated with each subsystem. Relative to defining the rigid-body mode shapes for separate rigid-body subsystems, it will be noted that, in general, an unconstrained rigid-body is free to move in space in six directions. Such rigid-body motion corresponds, in rectilinear coordinates, to translations in X, Y, and Z and rotations in  $\theta_x$ ,  $\theta_y$ ,  $\theta_z$ . The equations describing these motions are as follows:

$$\begin{pmatrix} F_x \\ F_y \\ F_z \\ M_x \\ M_y \\ M_z \end{pmatrix} = \begin{bmatrix} m & 0 & 0 & 0 & 0 & 0 \\ 0 & m & 0 & 0 & 0 & 0 \\ 0 & 0 & m & 0 & 0 & 0 \\ 0 & 0 & 0 & I_x & 0 & 0 \\ 0 & 0 & 0 & 0 & I_y & 0 \\ 0 & 0 & 0 & 0 & 0 & I_z \end{bmatrix} \cdot \begin{pmatrix} \ddot{X} \\ \ddot{Y} \\ \ddot{Z} \\ \ddot{\theta}_x \\ \ddot{\theta}_y \\ \ddot{\theta}_z \end{pmatrix} \tag{17}$$

Applied Physical Forces
Inertia Matrix
Physical Acceleration of the Center of Gravity

These equations are included in the set defined by Equation 1. In this special case,  $m_i$  corresponds to the physical mass properties  $m$ ,  $I_x$ ,  $I_y$ , or  $I_z$ ,  $q_i$  corresponds to the physical coordinates  $X$ ,  $Y$ ,  $Z$ ,  $\theta_x$ ,  $\theta_y$ , or  $\theta_z$  of the center of gravity, and the  $k_i$  terms are equal to zero. Note that for a general (nonprincipal) set of axes, the inertia matrix of Equation 17 would include off-diagonal terms. For a three-dimensional body where the planes of symmetry

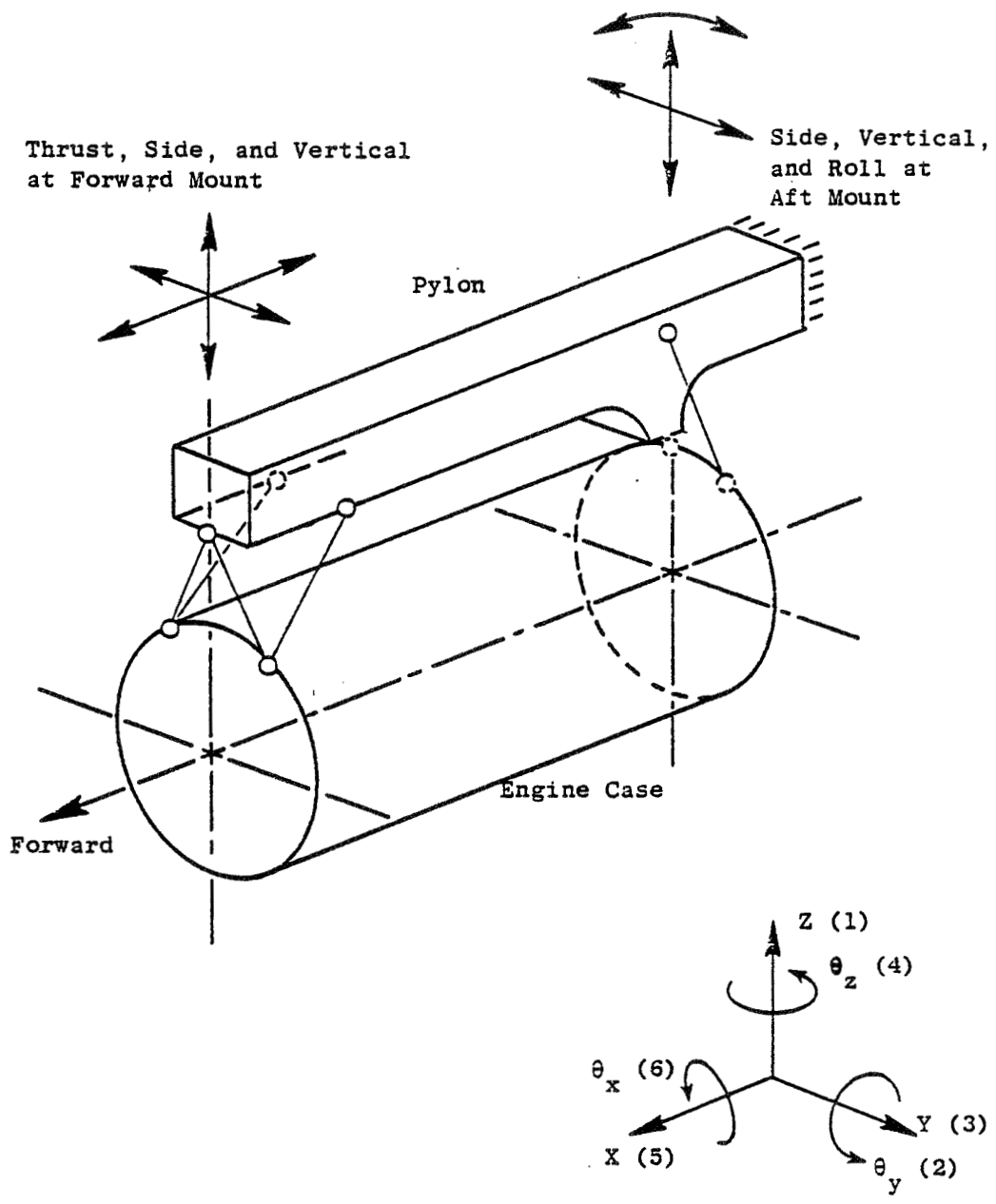
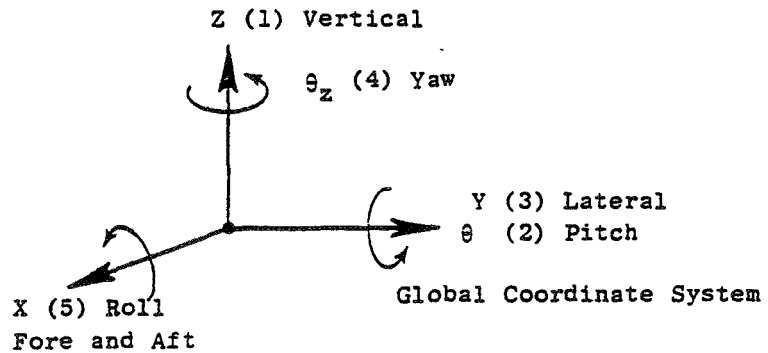


Figure 5. Typical Mounting Arrangement and Coordinate System.

Table IV. Physical Global Degrees of Freedom and Direction Numbers for the Subsystem.

Subsystems	Global Degrees of Freedom					
	Z	$\theta_y$	Y	$\theta_x$	X	$\theta_x$
	1	2	3	4	5	6
Vertical-Plane-Flexible Rotor(s)	X	X				
Horizontal-Plane-Flexible Rotor(s)			X	X		
Rigid-Body Rotor(s)	X	X	X	X	X	
Vertical-Plane-Flexible Case	X	X				
Horizontal-Plane-Flexible Case			X	X		
Rigid-Body Case	X	X	X	X	X	X
Torsional-Flexible Case						X
Three-Dimensional-Flexible Pylon	X		X		X	





pass through the center of mass, there is no inertia coupling, and the inertia matrix corresponds to that of Equation 17. The Eigen vectors for the six rigid-body modes are shown in Table V.

In general the flexible, beam-like rotor and case finite-element models will be used to generate modal data for a single plane, say the vertical plane. These modal data can also be used to represent the horizontal plane. However, it will be noted that the sign of the modal data in either the Y or the  $\theta_z$  direction must be changed in order to maintain a sign convention that is consistent with a right-hand, global-coordinate system. This is shown in Figure 6.

### 3.3.3.2 Applied Physical Forces

In addition to the rotor unbalance and user-specified forces, applied physical forces include forces that are displacement and velocity dependent. The applied physical forces communicate with the generalized coordinates that represent the subsystems through the coupling ratios,  $B_{i,r,d}$ . The displacement and velocity-dependent forces act through the interconnections between the modal subsystems, and the load paths for these interconnections are defined with the physical connecting elements.

### 3.3.3.3 Physical Connecting Elements

The force/displacement and force/velocity relationships for the physical connecting elements will be expressed in terms of the stiffness and damping matrices shown in Equation 18.

$$\{F\} = - [K_e] \{X\} - [C_e] \{\dot{X}\} \quad (18)$$

The elements of  $\{F\}$ ,  $\{X\}$ , and  $\{\dot{X}\}$  define the terms  $\dot{F}_{r,d}$ ,  $X_{r,d}$ , and  $\dot{X}_{r,d}$  respectively of Equation 15.

Equation 18 defines the physical forces exerted by the physical connecting element on the modal subsystems to which it is connected.

### 3.3.3.4 Generalized Spring-Damper Element

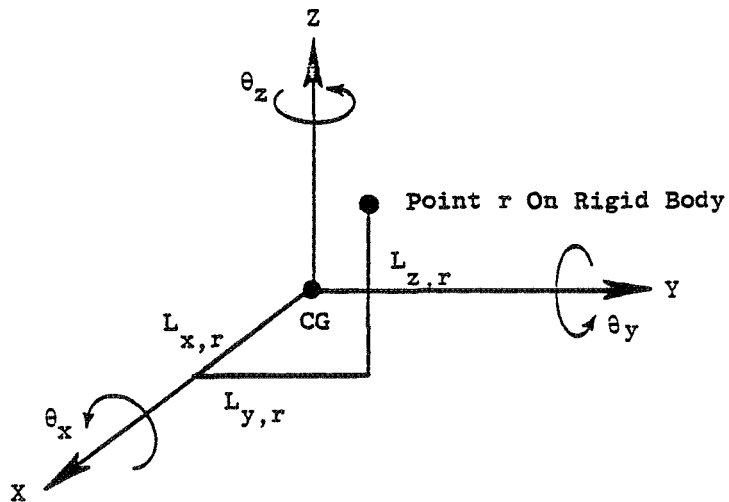
This element is associated with two physical points located at arbitrary locations in global space. Each of these points is assigned six degrees of freedom - three translational displacements (or velocities) and three rotational displacements (or velocities). Thus, the dimension for either the stiffness or the damping matrix is equal to 12.

This element can be used to represent simple, uncoupled, point springs and dampers that are useful in modeling rolling-element bearings. Among the other load-path configurations this element can be used to model are engine frame/sump structures, hydrodynamic bearing definitions with direct and cross

Table V. Mode Shapes for the Six Rigid-Body Modes for a Subsystem.

Physical Direction and Coordinate for Point r		Generalized Coordinate $q_i$					
Direction Number	Coordinate	X	Y	Z	$\theta_x$	$\theta_y$	$\theta_z$
5	Xr, 5	1.0	0	0	0	$L_{z,r}$	$-L_{y,r}$
3	Xr, 3	0	1.0	0	$-L_{z,r}$	0	$L_{x,r}$
1	Xr, 1	0	0	1.0	$L_{y,r}$	$-L_{x,r}$	0
6	Xr, 6	0	0	0	1.0	0	0
2	Xr, 2	0	0	0	0	1.0	0
4	Xr, 4	0	0	0	0	0	1.0
		$\phi_1$	$\phi_2$	$\phi_3$	$\phi_4$	$\phi_5$	$\phi_6$

Columns Correspond to Rigid-Body Mode Shapes



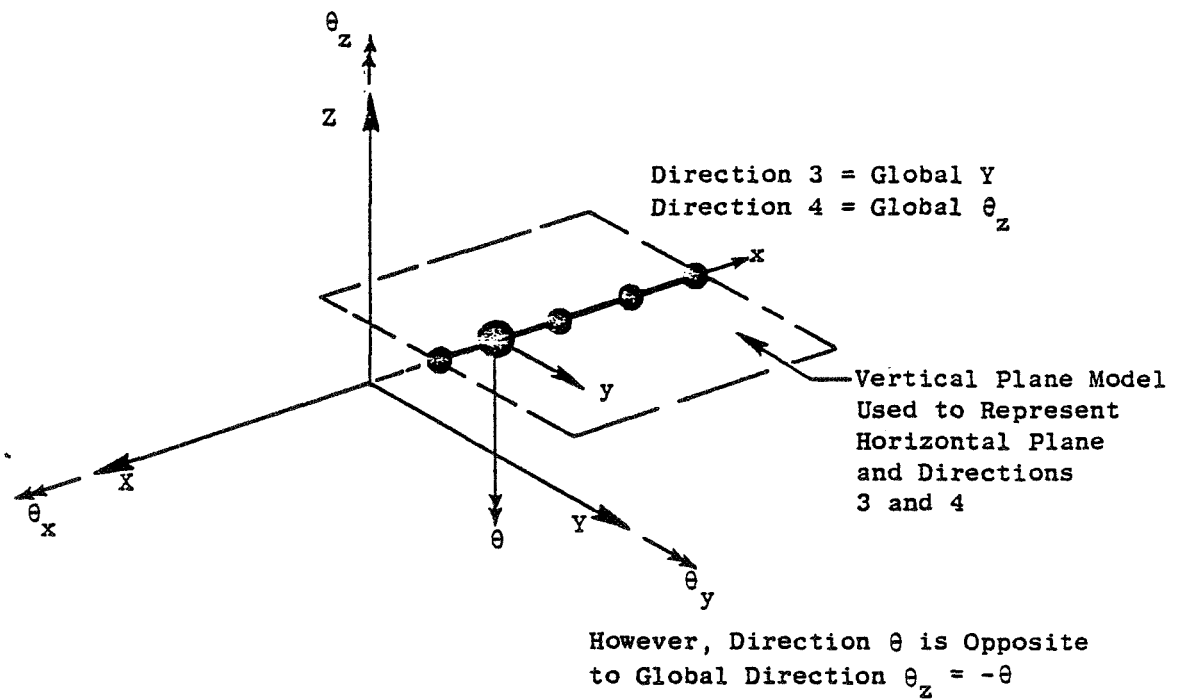
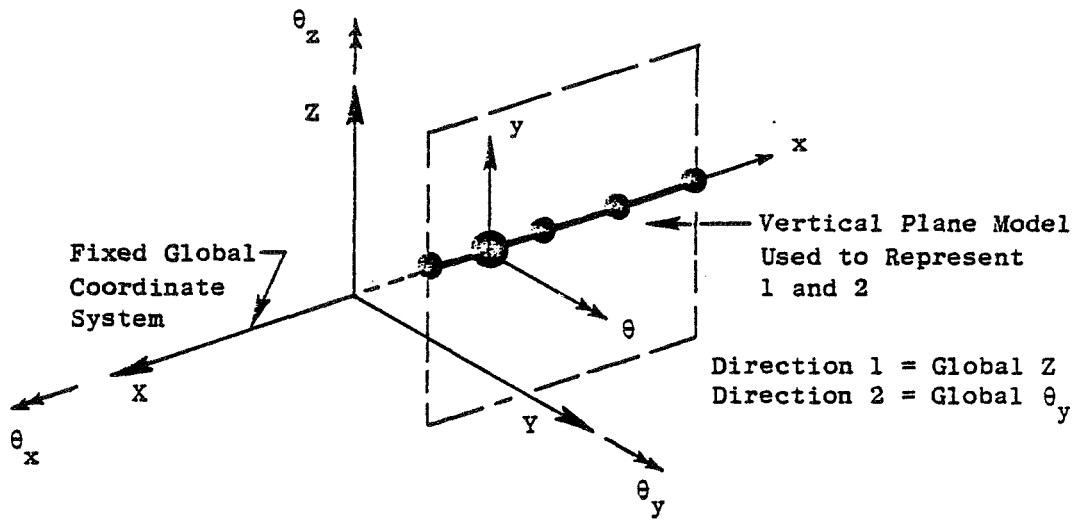


Figure 6. Vertical and Horizontal Planar Models.

stiffness and damping, and crossaxis stiffness coupling arising from aerodynamic effects. A sketch of this element is shown in Figure 7.

Typically, the stiffness elements in  $[K_e]$  are computed via a finite-element program, or with a closed-form solution for an idealized model, or are obtained from static or dynamic testing. The damping elements in  $[C_e]$  are computed if analytical expressions are available, or are obtained from dynamic testing, or are based on the assumption that the damping is proportional to the stiffness. In this latter case  $[C_e] = \alpha [K_e]$ , and the proportionality can be based on a specified percent of critical damping at a selected frequency as shown in Equation 19.

$$[C_e] = \frac{1}{\omega Q_f} [K_e] \quad (19)$$

$$Q_f = \text{Specified Q-factor} = \frac{1}{2 C/C_c}$$

$\omega$  = Selected frequency, radians/second.

### 3.3.3.5 Space Link-Damper Element

The space link-damper element sketched in Figure 8 is described by sixth-order stiffness and damping matrices.

$$[K_e] = \frac{AE}{L} \begin{bmatrix} n^2 & nm & nl & -n^2 & -nm & -nl \\ nm & m^2 & ml & -nm & -m^2 & -lm \\ nl & ml & l^2 & -ln & -lm & -l^2 \\ -n^2 & -nm & -ln & n^2 & nm & nl \\ -nm & -m^2 & -lm & nm & m^2 & ml \\ -nl & -lm & -l^2 & ln & ml & l^2 \end{bmatrix} \quad (20)$$

$n$ ,  $m$ , and  $l$  are the direction cosines, and the column and row order correspond to directions 1, 3, and 5 at points I and J, respectively.

$A$  = cross-sectional area, in.<sup>2</sup>

$E$  = Young's modulus

$L$  = length

The damping matrix  $[C_e]$  can be defined either in terms of translational (dashpot) damping directed along the axis of the link or by proportional damping.

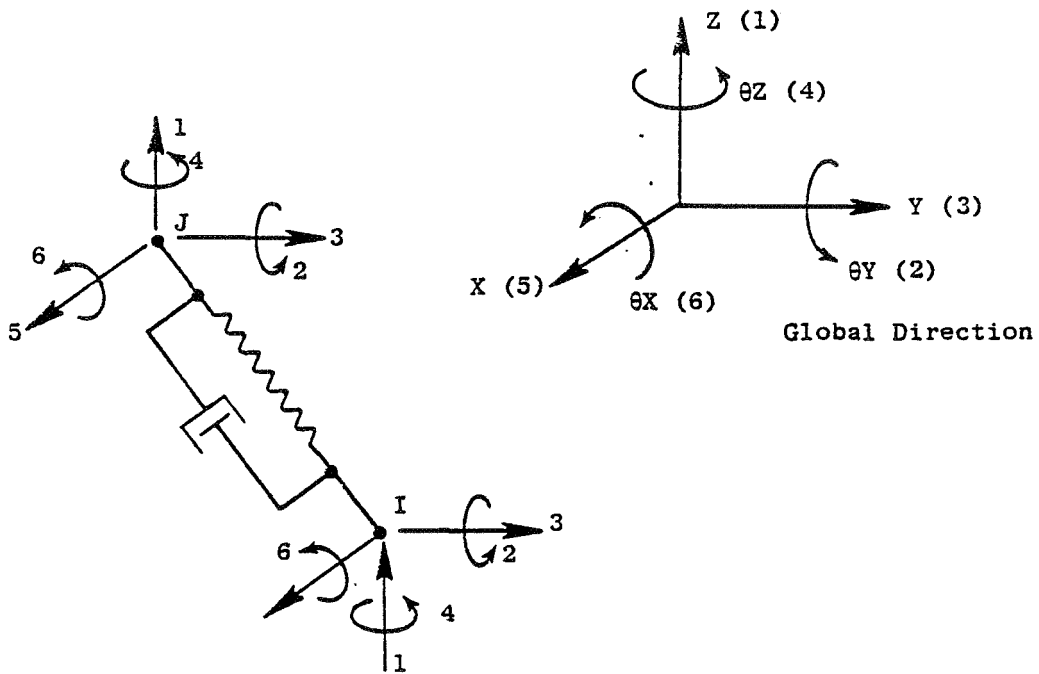


Figure 7. General Spring Damper Element.

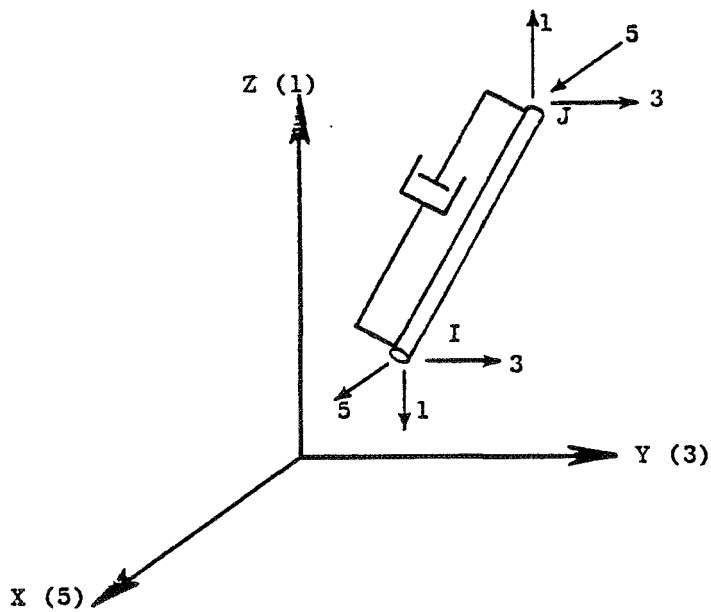


Figure 8. Space Link-Damper Element.

In the former case,

$$[C_e] = \frac{L}{AE} C [K_e] \quad (21)$$

$C \frac{\text{lb-sec}}{\text{in.}}$  is a specified scalar damping value.

In the latter case, the form of the damping matrix is that shown in Equation 19.

### 3.3.3.6 Rub Element

The large rotor amplitudes associated with blade loss cause heavy rotor-case rubs that are usually accompanied by severe local damage to blades and case. It is to some degree fortunate that this local damage does occur, because the loads acting on the bearings and frames are reduced by the action of the additional load path between the rotor and case that is provided through the mechanism of the heavy rubs. As a consequence of this action, the engine may be capable of withstanding, without catastrophic structural failure, the transient loading induced by the blade loss.

The rub element allows the mathematical modeling of the nonlinear tip rub that includes the dead-band displacement interval prior to closure between the rotor and case. Upon closure, an equivalent linear spring, representing the local case distortion and blade compliance, is used to define the rotor-to-case load path. The net result is a bilinear spring with zero slope over the dead band and a finite slope over the region of interference.

Figure 9 shows the relationships between the rub force and the position vectors of the rotor and case centers. Neglecting friction, the rub force can be defined as a force that acts in the direction defined by the line of centers. The vector rub force acting on the rotor can be written as:

$$F_r = - \frac{\Delta}{|\Delta|} (|\Delta| - \epsilon_0) K - (V_r - V_c) C \quad \text{for } |\Delta| > \epsilon_0 \quad (22)$$

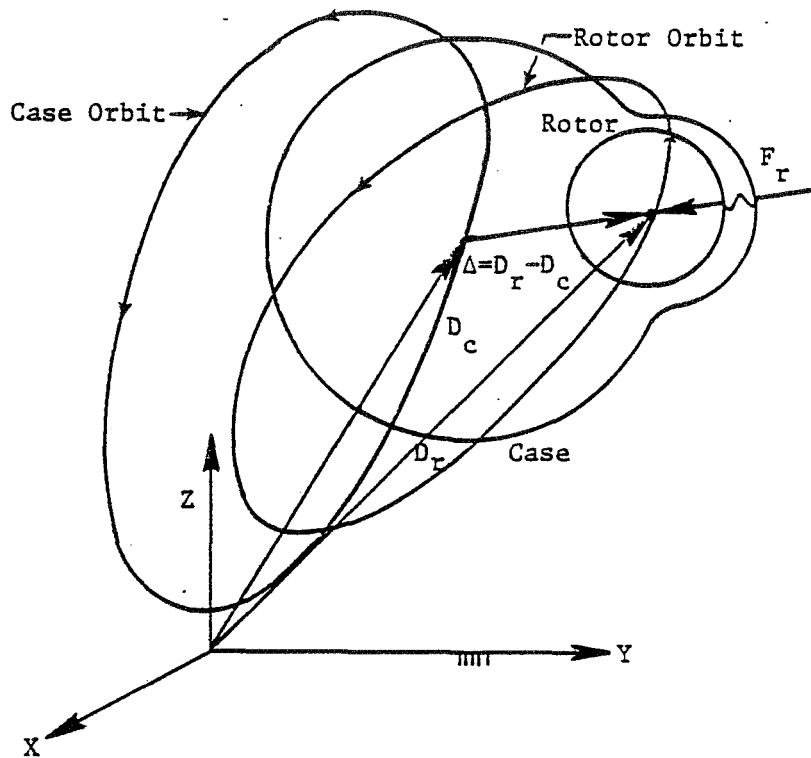
$$F_r = 0 \quad \text{for } |\Delta| \leq \epsilon_0$$

Where  $K$  = Radial spring rate representing the local case distortion (represented by the bulge shown in Figure 9 and the blade compliance.

$\epsilon_0$  = Structural clearance

$\Delta$  =  $(D_r - D_c)$  = vector difference between the position vectors of the rotor and case centers.

$\frac{\Delta}{|\Delta|}$  = unit vector in the direction of vector  $\Delta$ .



At Time =  $t$ , Vectors,  $D_c$  and  $D_r$  Define Positions of Case and Rotor Centers.

Vector Difference =  $\Delta = D_r - D_c$

If  $|\Delta| > \epsilon_o$ , A Rub Will Occur

$\epsilon_o$  = Structural Clearance

$$F_r = \text{Vector Rub} = - \frac{\Delta}{|\Delta|} (|\Delta| - \epsilon_o)K$$

$K$  = Spring Rate Representing The Local Case Distortion and Blade Compliance

Figure 9. Rub Force Model.

$V_R$  and  $V_C$  are the vector velocities of the rotor and case centers, respectively.

$C$  is the damping rate.

In complex notation,  $\Delta$  can be written as:

$$\Delta = D_R - D_C = (y_R + j Z_R) - (y_C + j Z_C) = (y_R - y_C) + j (Z_R - Z_C)$$

Where  $j$  = unit vector in the  $z$ -direction.

$$|\Delta| = \text{amplitude of } \Delta = \sqrt{(y_R - y_C)^2 + (Z_R - Z_C)^2} \quad (23)$$

$$F_R = - [(y_R - y_C) + j (Z_R - Z_C)] [1.0 - \epsilon_0/|\Delta|] K - (V_R - V_C) C$$

$$F_R = - (y_R - y_C) [1.0 - \epsilon_0/|\Delta|] K - j (Z_R - Z_C) [1.0 - \epsilon_0/|\Delta|] K \\ - C[(\dot{y}_R - \dot{y}_C)] - j C [\dot{Z}_R - \dot{Z}_C]$$

Defining

$$A = 1.0 - \frac{\epsilon_0}{\sqrt{(y_R - y_C)^2 + (Z_R - Z_C)^2}} K \quad (24)$$

as an effective spring coefficient which is dependent on the initial structural clearance and the rotor-case relative displacement and case-blade local spring rate. A stiffness matrix can be defined as follows:

$$\begin{Bmatrix} F_R^Z \\ F_R^Y \\ F_C^Z \\ F_C^Y \end{Bmatrix} = \begin{bmatrix} -A & 0 & A & 0 \\ 0 & -A & 0 & A \\ A & 0 & -A & 0 \\ 0 & A & 0 & -A \end{bmatrix} \begin{Bmatrix} Z_R \\ Y_R \\ Z_C \\ Y_C \end{Bmatrix} \quad (25)$$

Where  $F_R^Z$  and  $F_R^Y$  are the forces acting on the rotor center in the  $z$  and  $y$  directions, respectively.

$F_C^Z$  and  $F_C^Y$  are the forces acting on the case center in the  $z$  and  $y$  directions, respectively.

$Z_R$ ,  $Y_R$ ,  $Z_C$ ,  $Y_C$  are the absolute displacements of the rotor and case center.



The stiffness matrix in Equation 25 is also shown in Figure 10 and represents the  $[K_e]^*$  matrix in Equation 18. The damping forces can be written in matrix form as:

$$\begin{pmatrix} F_c^z \\ F_r^y \\ F_c^z \\ F_c^y \end{pmatrix} = \begin{bmatrix} -C & 0 & C & 0 \\ 0 & -C & 0 & C \\ C & 0 & -C & 0 \\ 0 & C & 0 & -C \end{bmatrix} \begin{pmatrix} z_r \\ r\dot{y} \\ c\dot{z} \\ c\dot{y} \end{pmatrix} \quad (26)$$

$\dot{z}_r$ ,  $\dot{y}_r$ ,  $\dot{z}_c$ ,  $\dot{y}_c$  are the absolute velocities of the rotor and case centers. The damping matrix in Equation 26 represents the  $[C_e]^*$  matrix in Equation 18. It will be noted that the rub element defined by Equations 25 and 26 can be used to model rotor-to-rotor rubs as well as rotor-to-case rubs. In this case the inside rotor is identified with the subscript r, and the outside rotor is identified with subscript c.

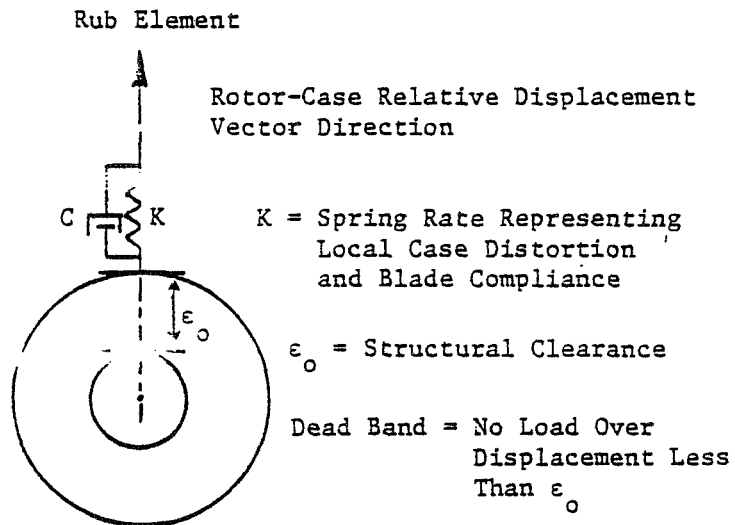
### 3.3.3.7 Engine Support Element

Real aircraft engine mounting systems are quite complex and must be modeled three-dimensionally if accurate simulation is to be obtained. Figure 11 shows an example of an aircraft engine mounting arrangement where three mounting planes are utilized. The forward mounting plane takes vertical, side, and axial loads. The midmounting plane takes side and roll loads. The aft mounting plane takes vertical loads only.

The engine support element is a multipoint, multidirection element that provides the capability to model the complex load paths between the engine case and the pylon and thus allows for the direct modeling of actual engine mount structures. In addition, this element couples the flexible- and rigid-body-centerline modal subsystems that represent the engine case to the support links that comprise the mounting system. Thus, this element is really a combined engine/support-case flexibility element that couples the beam-like casing model to the three-dimensional pylon subsystem (3-D). Figure 12 shows typical engine case-link attachment points. The loads at these attachment points induce frame/case distortions that increase the effective flexibility at the engine centerline. In this example, the side-direction flexibility at the forward mounting plane would be increased by the fan frame/case ovalization effect, and the vertical direction flexibility at the aft mounting plane would be increased by the turbine frame/case ovalization effect.

---

\*Equations 25 and 26 represent the forces acting on the connecting subsystems and already incorporate the minus signs shown in Equation 18. Hence, in this case, the  $[K_e]$  and  $[C_e]$  matrices shown in Equations 25 and 26 should be multiplied by -1 to conform to the form of Equation 18.



$$\begin{bmatrix} F_R^1 \\ F_R^3 \\ F_C^1 \\ F_C^3 \end{bmatrix} = \begin{bmatrix} -A & 0 & A & 0 \\ 0 & -A & 0 & A \\ A & 0 & -A & 0 \\ 0 & A & 0 & -A \end{bmatrix} \cdot \begin{bmatrix} X_R^1 \\ X_R^3 \\ X_C^1 \\ X_C^3 \end{bmatrix}$$

Spring Rub Forces  
Acting on Rotor and  
Case When  $|\Delta| > \epsilon_0$

$$A = \left[ 1.0 - \frac{\epsilon_0}{\sqrt{(X_R^1 - X_C^1)^2 + (X_R^3 - X_C^3)^2}} \right] K = \left[ 1.0 - \frac{\epsilon_0}{|\Delta|} \right] K$$

Superscripts 1 and 3 Represent Directions Z and Y.

Figure 10. Rub Element Model.

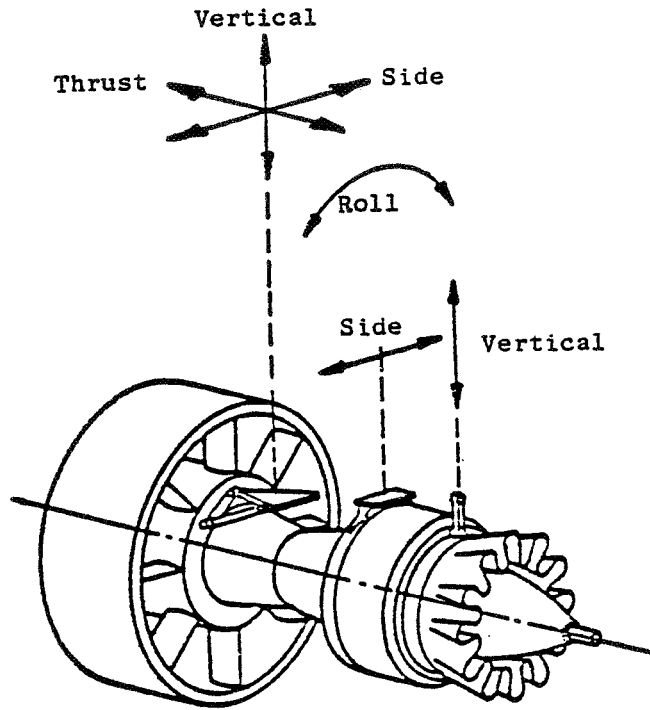
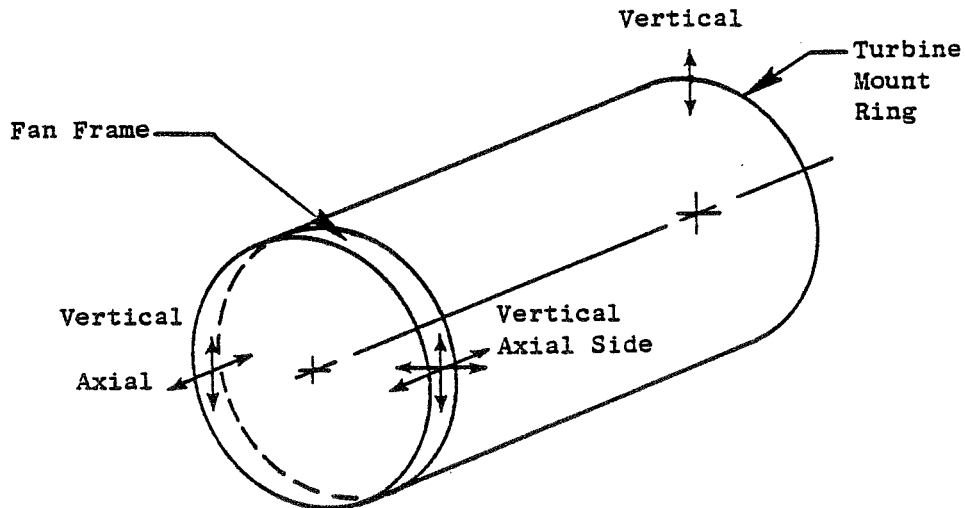


Figure 11. An Example of an Aircraft Engine Mounting Arrangement.



In this illustration, the local loads at the attachment points result in additional mounting flexibility at the forward plane, in the side direction, and at the aft plane, in the vertical.

Figure 12. Engine Frame/Case Ovalization Effects Increase the Effective Flexibility at the Mounting Planes.

Figure 13 shows the attachment and centerline points in global space and the load directions for the two mounting planes corresponding to the typical mounting arrangement shown in Figure 5. At the forward mounting plane, points L, M, and N are the attachment points on the pylon, and point I is at the engine centerline. The two attachment points on the engine case are identified by J and K. In this case, the engine support element is represented with the stiffness matrix relating to the points I, L, M, and N. The displacement terms associated with points J and K are reduced out. Point I has six degrees of freedom, and points L, M, and N each have three degrees of freedom. It is necessary to eliminate points J and K because the physical connecting elements are only used to define the load paths between modal subsystems or between modal subsystems and ground.

The model definition for the portion of the engine support element that pertains to the case flexibility (flexibility between the engine centerline and the case-attachment points) is shown in Figure 14. In this representation, all of the case flexibility is lumped at the case-attachment points (Points J and K), and rigid members are used to transfer the loads to the centerline point (Point I). The case flexibility is described by three spring rates  $K_v$ ,  $K_h$ , and  $K_a$ . These rates are reciprocals of the case flexibility values obtained by either calculation or measurement. In the former case, a finite-element model of the frame is typically used to define the flexibility values. For example,  $K_v$  would be defined by applying an  $n = 1$  shear flow and restraining the frame model at the case-attachment point locations. The vertical displacement of a horizontal diameter would then be used to establish the spring rate  $K_v$ . Figure 15 shows the twelfth-order stiffness matrix that describes the case flexibility. The terms a, b, c, d, e, and f are multipliers used to proportion the spring rates, and the associations between the spring rates  $K_v$ ,  $K_h$ ,  $K_a$ , and the lumped spring location points J and K are shown below.

Spring Rates (lb/in.)	Point	
	J	K
$K_v$	a	c
$K_h$	b	d
$K_a$	e	f

Case Distortion Spring Rates

$K_v$  = Vertical Spring Rate

$K_h$  = Horizontal Spring Rate

$K_a$  = Axial Spring Rate

In conjunction with this scheme, the following restraints must be followed.

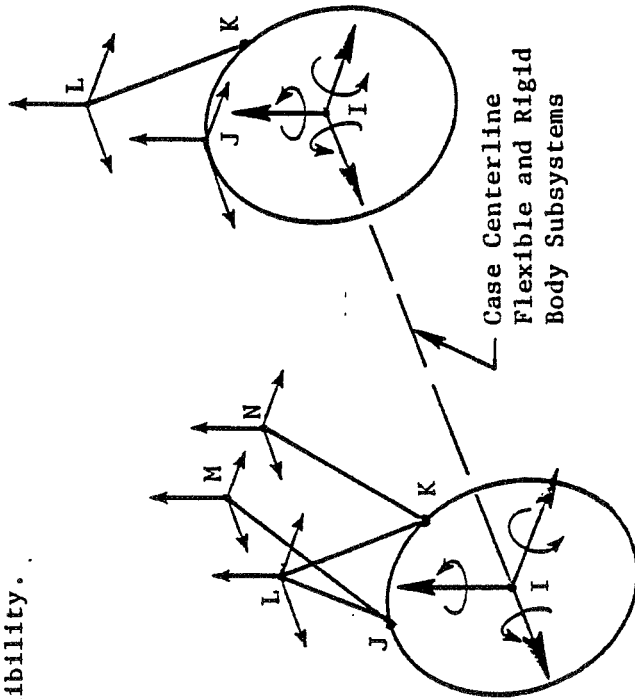
$$a + c = 1.0$$

$$b + d = 1.0$$

$$e + f = 1.0$$

$$\text{For symmetrical mounting, } a = b = c = d = e = f = 0.5.$$

Combined Engine Support-Link Element -  
 Multidirection, Multipoint Element  
 Represents Case Distortion and Links  
 Flexibility.



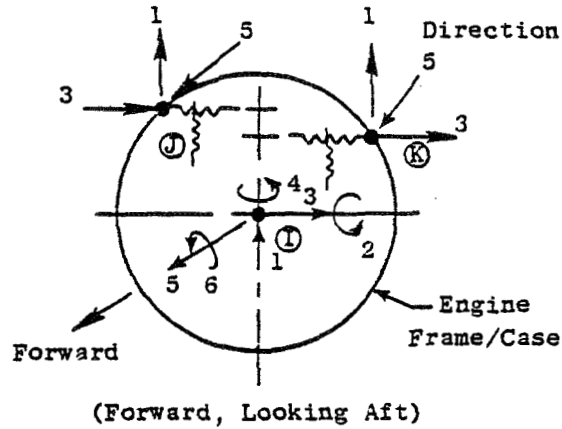
Example of Combined  
 Engine Support Link  
 Element At The Aft  
 Mounting Plane With  
 Associated Points  
 I, J, K, L.

Example of Combined  
 Engine Support Link  
 Element At The Forward  
 Mounting Plane With  
 Associated Points I,  
 J, K, L, M, N.

In This Example, At The  
 Forward Plane Modal Sub-  
 Systems Attach to Points  
 I, L, M, and N. The Displacements  
 At Points J and K are Reduced  
 Out.

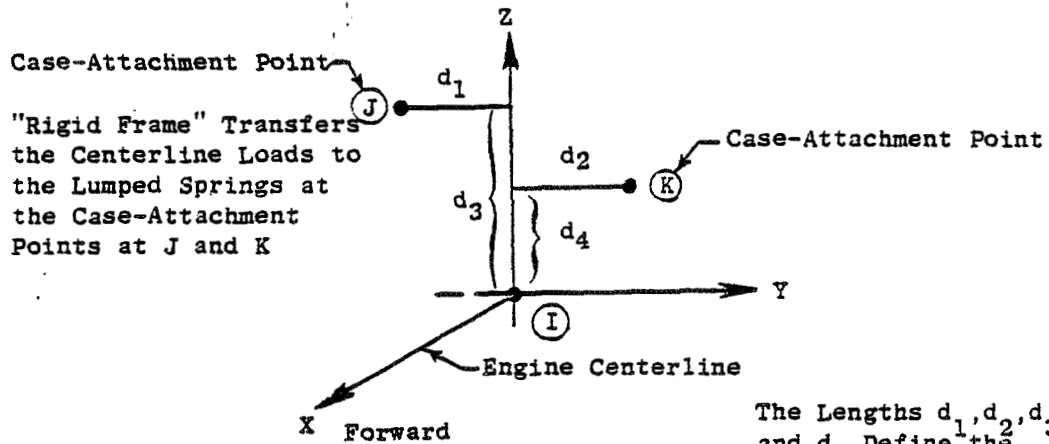
At The Aft Plane, Modal  
 Subsystems Attach To Points  
 I, J, and L. The Displacements  
 At Point K Are Reduced Out.

Figure 13. Combined Engine Support Link Element - Multidirection, Multipoint Element  
 Represents Case Distortion and Links Flexibility.



This Spring Element Couples the Flexible and Rigid-Body Centerline Subsystems That Represent the Engine Case to the Case-Attachment Points

The Locations of the Case-Attachment Points Are Arbitrary At the Mounting Station



Case-Attachment Point J  
"Rigid Frame" Transfers the Centerline Loads to the Lumped Springs at the Case-Attachment Points at J and K

The Lengths  $d_1, d_2, d_3,$  and  $d_4$  Define the Case-Attachment Points Relative to the Engine Centerline Located at Point I

Figure 14. Case Flexibility Represented by Multipoint/Direction Physical Spring Element (Which Defines a Portion of the Engine Support Element).

The engine support element is a variable-geometry element formed by combining the spring element stiffness matrix  $[K_f]$  of Figure 15 with the stiffness matrices of the connecting link elements. The stiffness matrices for the individual link elements have the same form as the stiffness matrix shown in Equation 20.

$$[K_c] = [K_f] + [K_L] = \begin{bmatrix} K_{11} & K_{12} \\ K_{21} & K_{22} \end{bmatrix} \quad (27)$$

$$[K_e] = [K_{11} - K_{12} K_{22}^{-1} K_{21}] \quad (28)$$

$[K_f]$  = Spring element stiffness matrix representing the case

$[K_L]$  = Stiffness matrix for the links

$[K_c]$  = Total unreduced stiffness matrix for the assembly

$[K_e]$  = Reduced stiffness matrix for the engine support element

The matrix  $[K_c]$  in Equation 27 represents the total unreduced stiffness matrix and includes the case Points J and K. Equation 28 represents the matrix reduction that is performed to eliminate Points J and K. Figure 13 shows two examples of engine support element configurations. It will be noted that there are no local moment load paths at Points J and K or at the link attachments at the pylon.

The damping matrix  $[C_e]$  for the engine support element is defined in terms of proportional damping and has the form of the damping matrix shown in Equation 19.

### 3.3.3.8 Gyro Element

The gyro element models the crossaxis forces due to Coriolis acceleration and addresses general whirl motion defined by the response in two planes. These crossaxis forces are mathematically treated as "right-hand-side forces," or externally applied forces, and couple the vertical and horizontal-plane rotor subsystem models. Figure 16 shows the damping matrix used to define the gyro forces acting on the connecting subsystems. This matrix represents -1 times the  $[C_e]$  matrix in Equation 18 and is derived from Euler's equations for rotational motion. For a spinning disk on a whirling shaft, Euler's equations of motion in a fixed frame can be written as:

$$\begin{bmatrix} I_y & 0 \\ 0 & I_z \end{bmatrix} = \begin{Bmatrix} \ddot{\theta}_y \\ \ddot{\theta}_z \end{Bmatrix} + \begin{bmatrix} 0 & I_x \omega \\ I_x \omega & 0 \end{bmatrix} \begin{Bmatrix} \ddot{\theta}_y \\ \ddot{\theta}_z \end{Bmatrix} = \begin{Bmatrix} M_y \\ M_z \end{Bmatrix} \quad (29)$$

	$x_1^1$	$x_1^2$	$x_1^3$	$x_1^4$	$x_1^5$	$x_1^6$	$x_J^1$	$x_J^3$	$x_J^5$	$x_K^1$	$x_K^3$	$x_K^5$
$F_1^1$	$K_V (asc)$	0	0	0	0	$cK_V d_2$ $-aK_V d_1$	$-aK_V$	0	0	$-cK_V$	0	0
$F_1^2$	0	$K_a^* (d_4^2 f + d_3^2 e)$	0	$K_a^* (d_1 d_1 e - d_2 d_4 f)$	$K_a^* (d_4 f + d_3 e)$	0	0	0	$-d_3 e K_a$	0	0	$-d_4 f K_a$
$F_1^3$	0	0	$K_h (b + d)$	0	0	$-K_h (d_3 b + d_4 d)$	0	$-bK_h$	0	0	$-dK_h$	0
$F_1^4$	0	$K_a^* (d_1 d_1 e - d_2 d_4 f)$	0	$K_a^* (e d_1^2 + f d_2^2)$	$K_a^* (d_1 e - d_2 f)$	0	0	0	$-e d_1 K_a$	0	0	$f d_2 K_a$
$F_1^5$	0	$K_a^* (d f + d_3 e)$	0	$K_a^* (d_1 e - d_2 f)$	$K_a (e + f)$	0	0	0	$-e K_a$	0	0	$-f K_a$
$F_1^6$	$cK_V d_2$ $-aK_V d_1$	0	$-K_h^* (d_3 b + d_4 d)$	0	0	$K_V (c d_2^2 + a d_1^2)$ $K_h (b d_3^2 + d d_4^2)$	$aK_2 d_1$	$b d_3 K_h$	0	$-c d_2 K_V$	$d d_4 K_h$	0
$F_J^1$	$-aK_V$	0	0	0	0	$a d_1 K_V$	$aK_V$	0	0	0	0	0
$F_J^3$	0	0	$-bK_h$	0	0	$b d_3 K_h$	0	$bK_h$	0	0	0	0
$F_J^5$	0	$-d_3 e K_a$	0	$-e d_1 K_a$	$-e K_a$	0	0	0	$e K_a$	0	0	0
$F_K^1$	$-cK_V$	0	0	0	0	$-c d_2 K_V$	0	0	0	$cK_V$	0	0
$F_K^3$	0	0	$-dK_h$	0	0	$d d_4 K_h$	0	0	0	0	$dK_h$	0
$F_K^5$	0	$-d_4 f K_a$	0	$f d_2 K_a$	$-f K_a$	0	0	0	0	0	0	$f K_a$

$$= [K] f$$

The subscripts and superscripts for the forces and displacements pertain to the point numbers and the direction numbers, respectively.

Figure 15. Combined In-Plane and Out-of-Plane Stiffness Matrix for the Physical Spring Element Shown in Figure 14.





$M_y$  and  $M_z$  are the applied moments.

$$\begin{bmatrix} I_y & 0 \\ 0 & I_z \end{bmatrix} = \text{The inertia matrix that defines the uncoupled rotary inertia moments acting in the two planes.}$$

$$\begin{bmatrix} 0 & I_{x\omega} \\ -I_{x\omega} & 0 \end{bmatrix} = \text{The damping matrix that defines the coupled-velocity dependent gyroscopic moments.}$$

The effects of the uncoupled rotary inertia are implicitly included in the rotor subsystem modal data, and the velocity-dependent moments are treated as the applied physical forces shown in Figure 16.

### 3.3.3.9 Unbalance Forces

At a given rotor mass station, the unbalance forces are related to the radial separation of the geometric and mass centers associated with the specified unbalance. The unbalance forces are inertia-type forces of a translational nature contrasted to the rotary and gyroscopic forces which are of a rotational nature. This allows us to make use of an important theorem in analytical mechanics which states that translational motions of the center of gravity of a rigid body are not coupled by inertia forces to the rotations of the body about its center of gravity. This theorem is attributed to Euler. Consequently, we may separate the translational and rotational inertia forces into two groups and treat them independently. The effects of the rotational inertia forces are incorporated via the subsystem modal data and through the gyro elements as mentioned previously. The unbalance forces associated with the translational motions of the center of gravity are identical in form to those acting on a mass particle.

Figure 17 will be used in the development of the acceleration forces due to disk translation.

Defining:  $\epsilon_u$  = Radial separation of geometric center and the mass center of the disk.

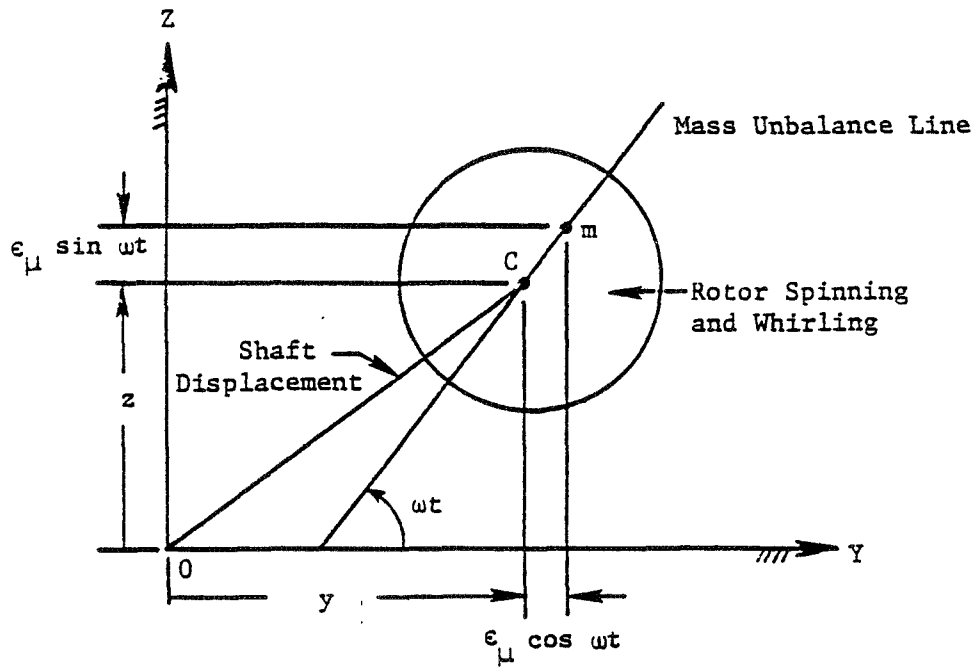
$\vec{n}_z$  = Unit vector in Z direction of fixed reference frame.

$\vec{n}_y$  = Unit vector in Y direction of fixed reference frame.

The vector velocity of the mass center can be written:

$$\text{Velocity of mass center} = \vec{V}_T = \frac{d}{dt} (Y + \epsilon_u \cos \omega t) \vec{n}_y + \frac{d}{dt} (Z + \epsilon_u \sin \omega t) \vec{n}_z$$

$$\text{Replace } \omega t \text{ with } \theta \quad \vec{V}_T = \frac{d}{dt} (Y + \epsilon_u \cos \theta) \vec{n}_y + \frac{d}{dt} (Z + \epsilon_u \sin \theta) \vec{n}_z$$



$\omega$  = Spin speed

O = Bearing Center

C = Shaft Center

m = Gravity center

$\epsilon_{\mu}$  = Radial separation of geometric center and mass center of disk

Figure 17. Diagram Used to Establish Acceleration Due to Disk Translation.

$$\dot{\vec{V}}_c = (\dot{Y} - \epsilon_u \dot{\theta} \sin \theta) \vec{n}_y + (\dot{Z} + \epsilon_u \dot{\theta} \cos \theta) \vec{n}_z$$

$\vec{A}_c$  = vector acceleration of mass center.

$$\vec{A}_c = \frac{d}{dt} (\dot{Y} - \epsilon_u \dot{\theta} \sin \theta) \vec{n}_y + \frac{d}{dt} (\dot{Z} + \epsilon_u \dot{\theta} \cos \theta) \vec{n}_z$$

$$\vec{A}_c = (\ddot{Y} - \epsilon_u \ddot{\theta} \sin \theta - \epsilon_u \dot{\theta}^2 \cos \theta) \vec{n}_y \\ + (\ddot{Z} + \epsilon_u \ddot{\theta} \cos \theta - \epsilon_u \dot{\theta}^2 \sin \theta) \vec{n}_z$$

The  $\ddot{Y}$  and  $\ddot{Z}$  acceleration terms are already included in the modal subsystem representation of the rotor. The remaining accelerations are as follows:

<u>Acceleration Term</u>	<u>Z Direction</u>	<u>Y Direction</u>
Centripetal Acceleration	$-\epsilon_u \dot{\theta}^2 \sin \theta$	$-\epsilon_u \dot{\theta}^2 \cos \theta$
Angular Acceleration	$\epsilon_u \ddot{\theta} \cos \theta$	$-\epsilon_u \ddot{\theta} \sin \theta$

The fixed frame reversed effective or D'Alembert forces applied to the mass stations of the modal subsystems representing unbalanced rotors are of the following form:

Z Direction (Vertical-Plane Subsystem)

$$F_z = M \epsilon_u \dot{\theta}^2 \sin \theta - M \epsilon_u \ddot{\theta} \cos \theta = U \omega^2 \sin \omega t - U \alpha \cos \omega t$$

Y Direction (Horizontal-Plane Subsystem)

$$F_y = M \epsilon_u \dot{\theta}^2 \cos \theta + M \epsilon_u \ddot{\theta} \sin \theta = U \omega^2 \cos \omega t + U \alpha \sin \omega t$$

M = disk mass

U = M  $\epsilon_u$  = mass unbalance

$\alpha = \ddot{\theta} = \frac{d}{dt} (\omega) = \text{angular acceleration}$

Including the effect of unbalance phase, as shown in Figure 18, the applied physical forces in the fixed frame due to unbalance at Point r are written as follows:

$F_{r,z}$  = force at point r in Z direction

$$= U_r \omega^2 \sin (\omega t + \phi_r) - U_r \alpha \cos (\omega t + \phi_r) \quad (30)$$

$F_{r,y}$  = force at point r in Y direction

$$= U_r \omega^2 \cos (\omega t + \phi_r) + U_r \alpha \sin (\omega t + \phi_r) \quad (31)$$

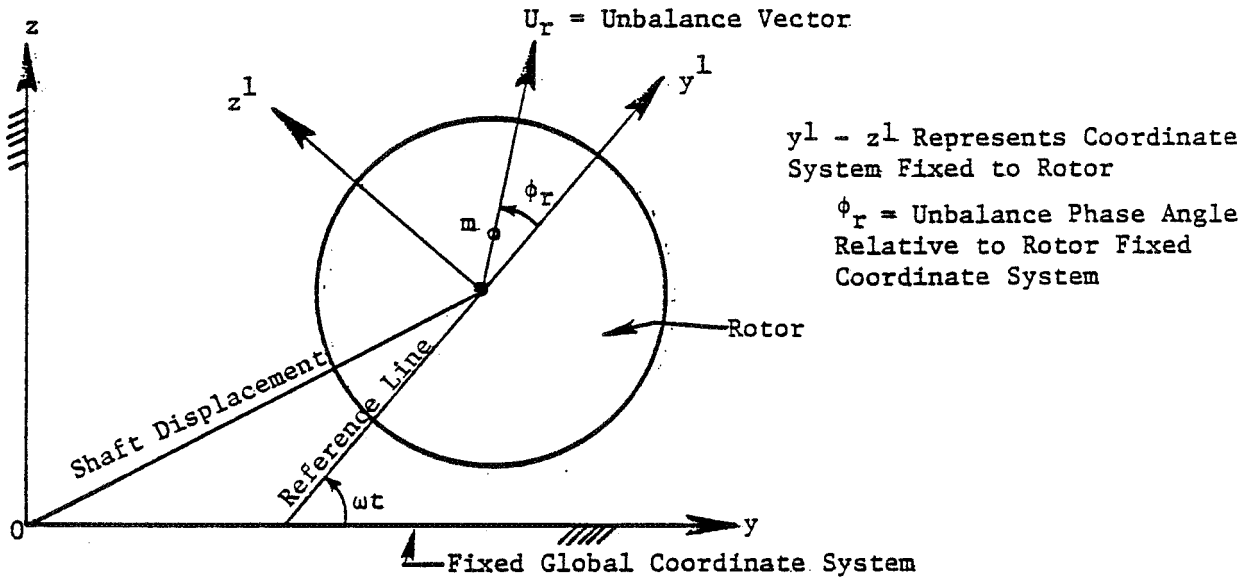


Figure 18. Effect of Applied Physical Forces in the Fixed Frame.

In order to define the unbalance forces, the current angular velocity  $\dot{\theta}$  and angular acceleration  $\ddot{\theta}$  of the unbalanced rotor must be known. In addition, the current angular velocity of the rotor is needed to calculate the gyro moments. The angular position, velocity, and acceleration of the unbalanced rotor are treated independent of the time-transient, system-response values. The speed history of the rotor is defined in terms of an accel/decel rate and an ending time for a series of speed segments.

$\theta_0$  = current angular position of rotor.

$\theta_1$  = future angular position at time  $t_1$ .

$t_0$  = current time

$\Delta t$  = time step

$t_1$  = future time =  $t_0 + \Delta t$

$\alpha_{\Delta t}$  = angular acceleration for time interval  $\Delta t$

$\dot{\theta}_1$  = future angular velocity

$$\theta_1 = \theta_0 + \dot{\theta}_0 (\Delta t) + \frac{1}{2} \alpha_{\Delta t} (\Delta t)^2 \quad (32)$$

$$\dot{\theta}_1 = \dot{\theta}_0 + \alpha_{\Delta t} (\Delta t) \quad (33)$$

### 3.3.3.10 Subsystem Internal Loads

The internal loads for a given subsystem are determined by superposing the effects of the applied physical forces that are displacement or velocity dependent and the physical forces derived from the modal contributions. In the former case, the physical forces are related to changes in the boundary conditions to the original modal subsystems; in the latter case, the physical forces are associated with transformations from modal to real space.

Total internal loads:

$$f_{r,d} = f(F_{r,d}, P_{r,d})$$

where  $F_{r,d}$  = contribution of applied physical force

$P_{r,d}$  = contribution of modal forces

$$P_{r,d} = \sum_i (F_{i,r,d}) (q)$$

where  $F_{i,r,d}$  represents the force at Point  $r$  in the Direction  $d$  for a unit value of the  $i$ -th generalized coordinate.

It will be noted that the values of the generalized coordinates  $q_i$  are dependent on the applied physical forces that are displacement and velocity dependent as well as the applied physical forces that are not dependent on displacement and velocity.

Examples of the internal bearing forces are given in Figures 41 and 42 in Section 3.5.

## 3.4 STRUCTURE OF THE COMPUTER PROGRAM

The TETRA computer program automatically combines subsystem modal data and physical connecting element data to form the governing differential equations described in Equation 6 for each of the generalized coordinates and performs the numerical integration. The major subroutines where the transformations and the numerical integration of the generalized differential equations are performed are identified in Figure 19.

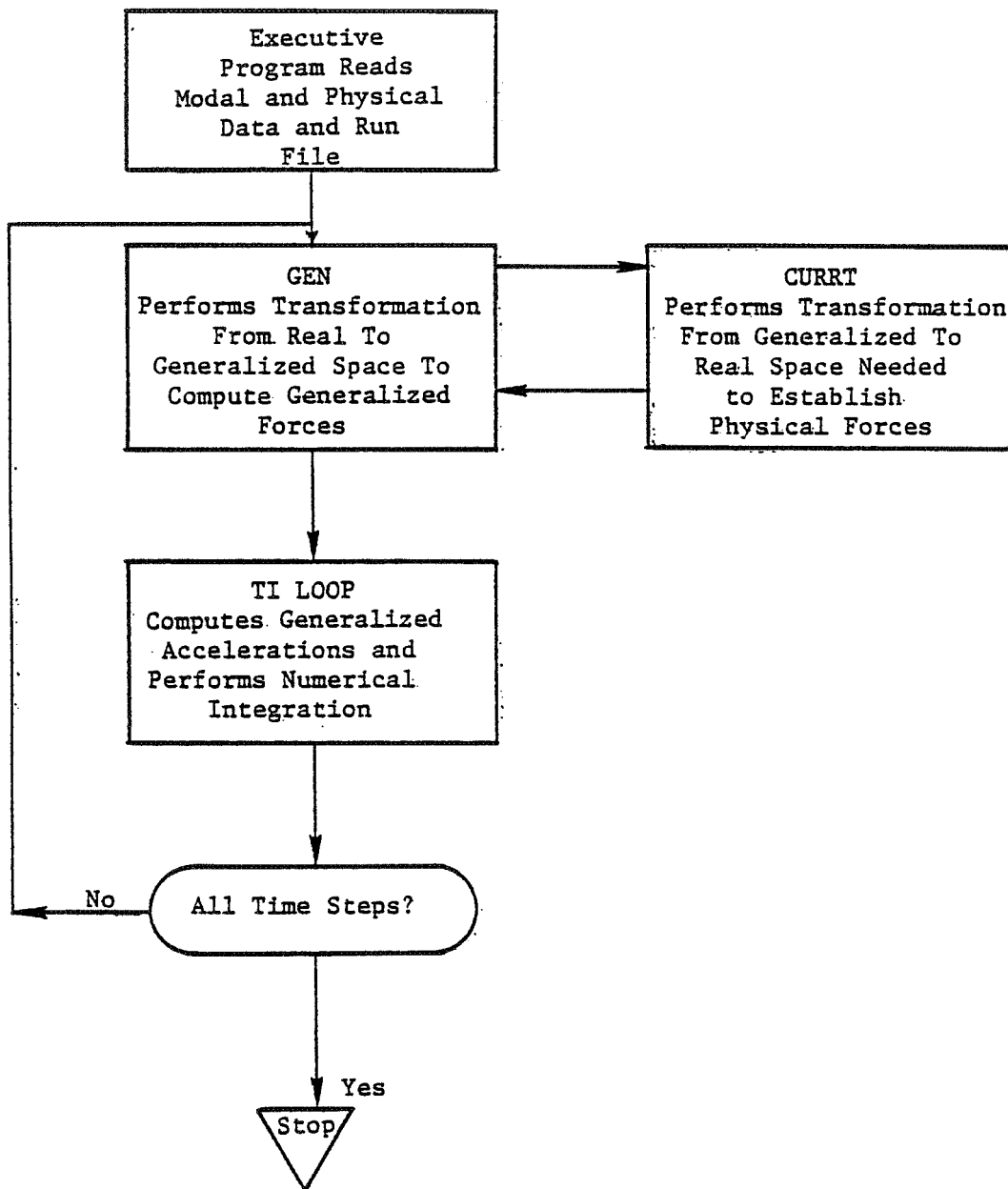


Figure 19. TETRA Routines for Transformations and Numerical Integration.

The task of establishing the current total generalized forces  $Q_i^0$  acting on each of the generalized coordinates  $q_i$  is accomplished in the subroutine GEN. The current physical displacements and velocities, needed to establish the physical coupling forces used by GEN in the formation of the generalized forces, are determined in subroutine CURRT which transforms the modal displacements  $q_i$  into real space at each time step. It will be noted that, in computing the generalized forces from the physical displacements and velocities, a transformation from real space to generalized space is performed by subroutine GEN for each time step. The generalized forces also include the effects of applied physical forces which are not displacement or velocity dependent, such as unbalance forces. The generalized forces and the generalized masses are utilized in subroutine TILoop to compute the generalized accelerations using Equation 18 and to compute the future values of the generalized displacements using the central finite-difference method as shown in Equation 9.

The modal subsystem numbers and the types and the regions they represent are identified in Table VI. The number of directions (physical degrees of freedom, DOF) and the direction numbers associated with these degrees of freedom are listed in Table VII.

Table VI. Modal Subsystems.

<u>No.</u>	<u>Subsystem</u>	<u>Type</u>
1	Vertical Plane Rotor - 1 Model	Flexible-Planar
2	Horizontal Plane Rotor - 1 Model	Flexible-Planar
3	3-D Rigid Body Rotor - 1 Model	Rigid with 5 DOF
4	Vertical Plane Rotor - 2 Model	Flexible-Planar
5	Horizontal Plane Rotor - 2 Model	Flexible-Planar
6	3-D Rigid Body Rotor - 2 Model	Rigid with 5 DOF
7	Vertical Plane Case Model	Flexible-Planar
8	Horizontal Plane Case Model	Flexible-Planar
9	3-D Rigid Body Case Model	Rigid with 6 DOF
10	Torsional Case Model	Flexible-Twist
11	3-D Flexible Pylon (Wing) Model	Flexible-3-D



Table VII. Subsystem Identification.

Subsystem Model		Directions	
Subsystem	Description	Number	Direction Numbers
1	Rotor-1 Vertical Plane Flexible Model	2	K=1 K=2
2	Rotor-1 Horizontal Plane Flexible Model	2	K=3 K=4
3	Rotor-1 Rigid Body Model	5	K=1 K=2 K=3 K=4 K=5
4	Rotor-2 Vertical Plane Flexible Model	2	K=1 K=2
5	Rotor-2 Horizontal Plane Flexible Model	2	K=3 K=4
6	Rotor-2 Rigid Body Model	5	K=1 K=2 K=3 K=4 K=5
7	Case Vertical Plane Flexible Model	2	K=1 K=2
8	Case Horizontal Plane Flexible Model	2	K=3 K=4
9	Case Rigid Body Model	6	K=1    K=4 K=2    K=5 K=3    K=6
10	Case-Torsional Flexible Model	1	K=6
11	Pylon 3-D Flexible Model	3	K=1    K=5 K=3

Eleven triple-subscripted arrays are used to store the subsystem mode shape data:

$S_i(I,J,K)$  = Mode shape modal displacements for the  
i-th modal subsystem.

$i = 1, 2, 3, \dots, 11$  (Table VI)

$I$  identifies the generalized coordinate

$J$  identifies the location or point on the mode shape

$K$  identifies the direction (Table VII)

The  $S_i$  array data are used to define the coupling ratios  $B_{i,r,d}$  needed to perform the transformations between real and generalized space.

The physical displacement and velocity data for the current time step are stored in the arrays  $X(I,J)$  and  $VEL(I,J)$ , respectively:

$I$  = point number

$J$  = direction number (1 - 6)

The generalized coordinate values are stored in the array  $Z(I,J)$ :

$Z(I,J)$  = Present and previous values for the generalized coordinates

$I$  = Generalized coordinate number

$J = 1$  for current time (0),  $2$  for one previous time step  
(-1),  $3$  for two previous time steps (-2).

The generalized masses, stiffnesses, and damping coefficients for the governing differential equations are stored in the arrays  $ZM$ ,  $ZK$ , and  $ZC$ :

$ZM(I)$  = Generalized masses

$ZK(I)$  = Generalized stiffnesses

$ZC(I)$  = Generalized damping coefficients

The physical coupling forces used in the formation of the generalized forces are computed by multiplying the physical displacements and velocities into the connecting element stiffness and damping matrices, respectively, and then adding the results. The current values for the physical connecting element data are stored in the arrays,  $AKE_i$  and  $ADE_i$ .

$AKE_i(I,J,K)$  = Stiffness array for the i-th physical connecting  
element type.

$ADE_i(I,J,K)$  = Damping array for the i-th physical connecting  
element type.

- $i = 1, 2, \dots$  = Identifies the physical connecting element type. For example, the generalized spring-damper element, the rub element, etc.
- I = Identifies the physical connecting element number.
- J = Identifies the row number associated with a force for a given point and direction.
- K = Identifies the column number associated with a displacement for a given point and direction.

The information needed to identify the locations of the AKE and ADE array elements is provided in the following arrays:

- ICOMPJ (I) = Number of points for Element I.
- ICOMPE (I,J) = The global point numbers for Element I associated with the J-th point.
- ICOMPD (I,J) = The number of directions for Element I associated with the J-th point.
- ICOMPNI(I,J,K) = The direction numbers for Element I associated with the J-th point and the K-th direction.

### 3.5 TURBINE ENGINE SIMULATION

The results obtained with a demonstrator model based on a VAST simulation of the single-spool engine system in Figure 20 will now be presented. The straight lines shown for the rotor and case in this figure represent segment beam-centerline elements that include both stiffness and mass properties. Free-free modal data for the rotor and case subsystems along with physical spring-damper connecting element data were input to the TETRA time-transient computer program, and solutions were obtained for various rotor speed and rotor unbalance conditions.

Modal data based on planar finite-element models of the total system shown in Figure 20 and on the free-free rotor and casing subsystems were computed with the VAST program. In the former case, a frequency-domain modal analysis was used to establish the steady-state frequency response of the total system: In the latter case, the TETRA program was used to synthesize the free-free modal data and the physical connecting element data and predict the time-domain response for the combined system.

Spectral analysis and a comparison of the TETRA and frequency-domain solutions indicated that TETRA had correctly synthesized the modal and physical data to predict the time-transient response for the combined system.

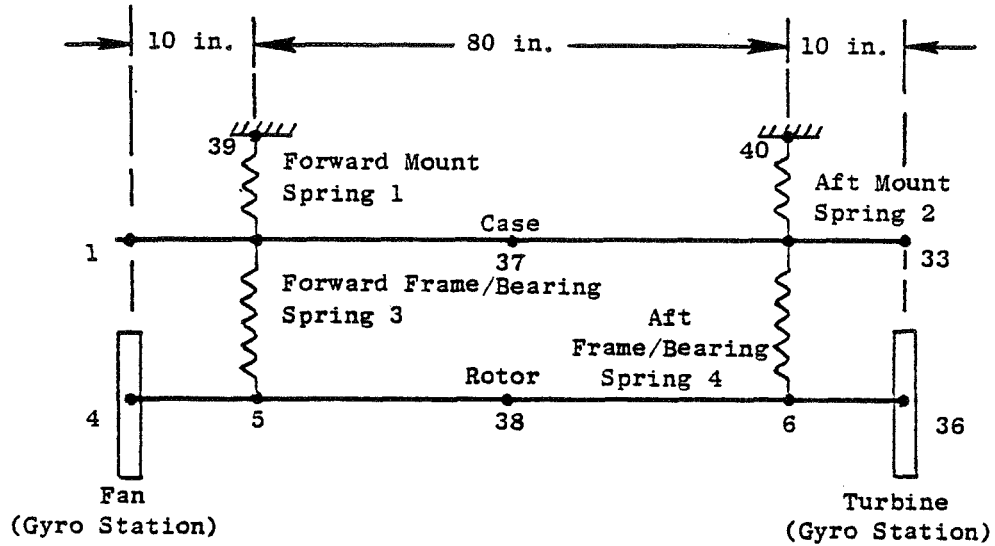


Figure 20. Finite-Element Model for Demonstrator, 40 DOF.

The frequencies for the free-free subsystem modes used in the TETRA analysis are shown in Table VIII. Eight generalized coordinates, corresponding to these frequencies, were used to define the time response for the total system which has 40 degrees of freedom. Therefore, the dimensionality of the model has been reduced by 80%.

Table VIII. Frequencies\* for the Free-free Modal Subsystems Used in the TETRA Analysis.

Rotor		Case	
cpm	Hz	cpm	Hz
99.3	1.655	125.1	2.085
120.8	2.013	159	2.65
10065	167.75	30367	510.62
16851	280.85		
26425	440.42		

\*Free-free modal data obtained with the following boundary conditions. The rotor was supported at each end with 300 lb/in. spring, and the case was supported at each end with a 100 lb/in. spring.

Inspection of Table VIII shows that the smallest period of oscillation for the subsystem modes is equal to  $1.0/510.62 = 0.001958$  second. Accounting for the stiffening effect of the physical connecting springs, a time step value that is considerably less than 0.001958 second must be used for the numerical integration that will be performed with the TETRA program. In practice,  $\Delta T$  should be made equal to about  $1/40$  of the smallest period of oscillation for the subsystem modes:

$$\frac{1}{40} \times 0.001958 = 4.895 \times 10^{-5}$$

On this basis, a time step of  $\Delta T = 50$  microseconds was selected.

The free-free modal data were used in the TETRA program to represent both the vertical and the horizontal plane, and uncoupled springs (in the Z and Y directions) were used to connect the modal subsystems to each other and to

the ground to model the configuration shown in Figure 20. The rigid-body modes for the rotor and the case were approximated with the soft-spring, rigid-body modes at 1.655, 2.013, 2.085, and 2.65 Hz. In addition, they were defined in subsequent analyses with the true representations based on the mass properties. The results obtained with the two approaches were in good agreement. A modal Q-factor equal to 15 (3.33% critical damping) was used to represent the damping of each of the casing subsystem modes. The rotor subsystem modes were undamped. Proportional damping based on a physical Q-factor equal to 15, a selected frequency of 3624 rpm, and corresponding to one of the critical speeds was used to represent the damping for the connecting spring elements.

For constant-speed running, the following time-step and total-time parameters were used in the TETRA time-integration analysis:

$$\Delta T = 50 \text{ } \mu\text{sec}$$

Number of time integration points = 10,240.

$$\text{Time frame} = 10,240 \times 50 \times 10^{-6} = 0.512 \text{ seconds.}$$

Figure 21 shows the TETRA computed displacement-time history at the middle of the rotor (Point 38) in the vertical direction corresponding to a sudden 100 g-in. fan unbalance at a constant 12,000 rpm speed. The number of computed values was decimated so that 1024 points are shown, and the time increment between points is equal to 5 microseconds. The 12,000-rpm speed corresponds to supercritical-speed operation relative to a rotor-dominated mode computed at 9908 rpm for the total system. Overshoot is clearly in evidence for the transient response shown in Figure 21. The fast Fourier transform of this time response, shown in Figure 22, indicates that four modes are contributing to the response. The peak at 200 Hz (12,000 rpm) is associated with the driving force. The VAST predicted mode shapes for the total system sketched in Figure 23 show that the modes at 3,617, 9,908, 13,983, and 26,473 rpm should be responsive at the middle of the rotor for fan unbalance. This indicates that TETRA has correctly synthesized the modal and physical data to predict the time-transient response for the total system. Figure 24 shows the displacement-time history at the middle of the rotor in the vertical direction corresponding to a sudden 100 g-in. fan unbalance at 9908-rpm critical speed operation. In this case there is no overshoot, and the transient response builds up to the steady-state level. This response is characteristic of operation at a critical speed.

The results presented in Figures 21 and 24 do not include gyroscopic stiffening. Figure 25 shows the off-resonant response in two planes at the fan that reflects the effects of gyroscopic stiffening at both the fan and turbine. Figure 26 shows orbit plots of the data presented in Figure 25. Inspection of Figure 26 shows that the initial response is a noncircular whirl. This noncircular whirl transitions into a circular whirl after steady-state conditions are reached. Figures 27 through 32 show response plots at the fan and case that include both the effects of gyroscopic stiffening and the rub load path. Figures 33 through 36 show the steady-state frequency

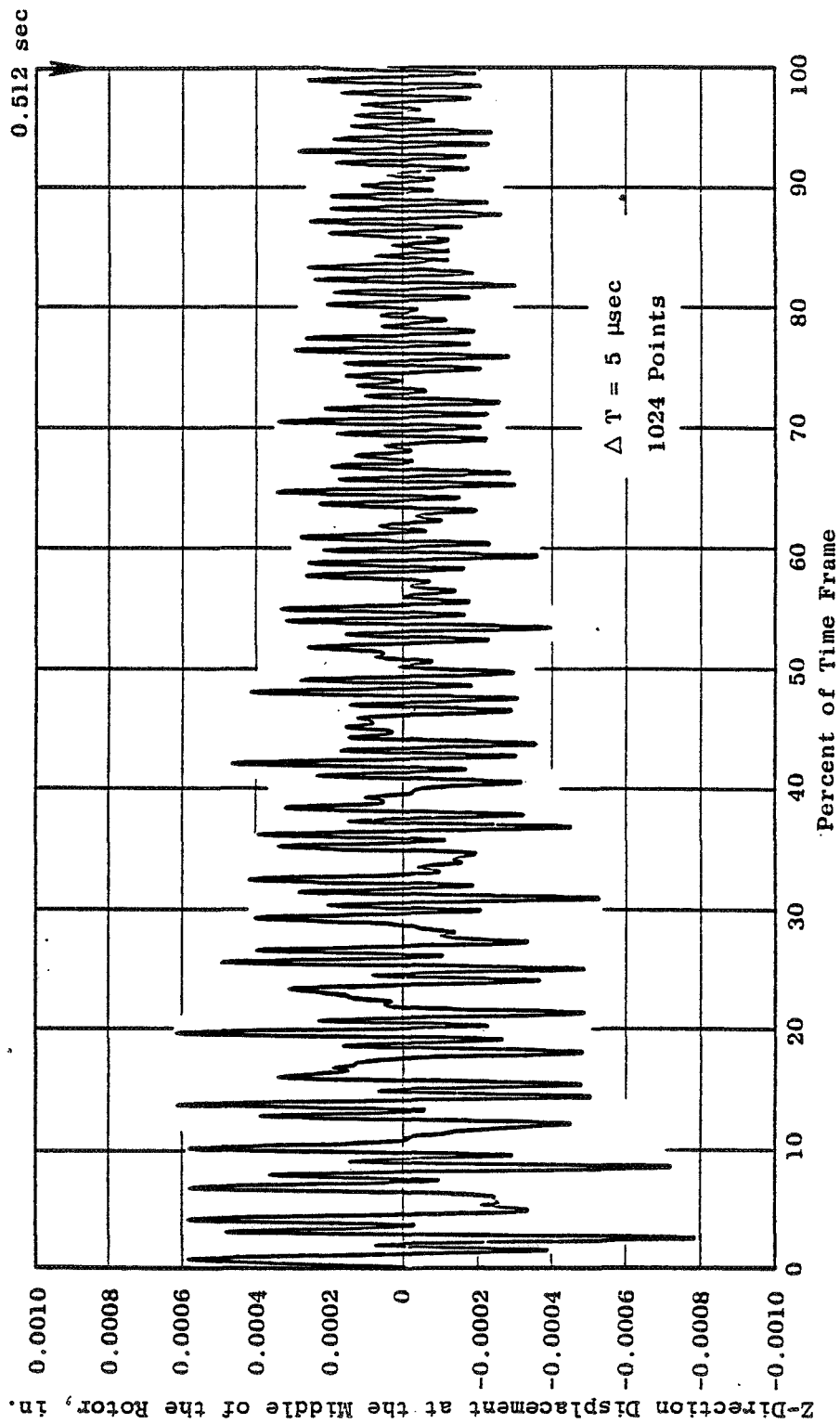


Figure 21. Demonstrator Model 100 g-in. Sudden Unbalance at the Fan at 12,000 rpm.

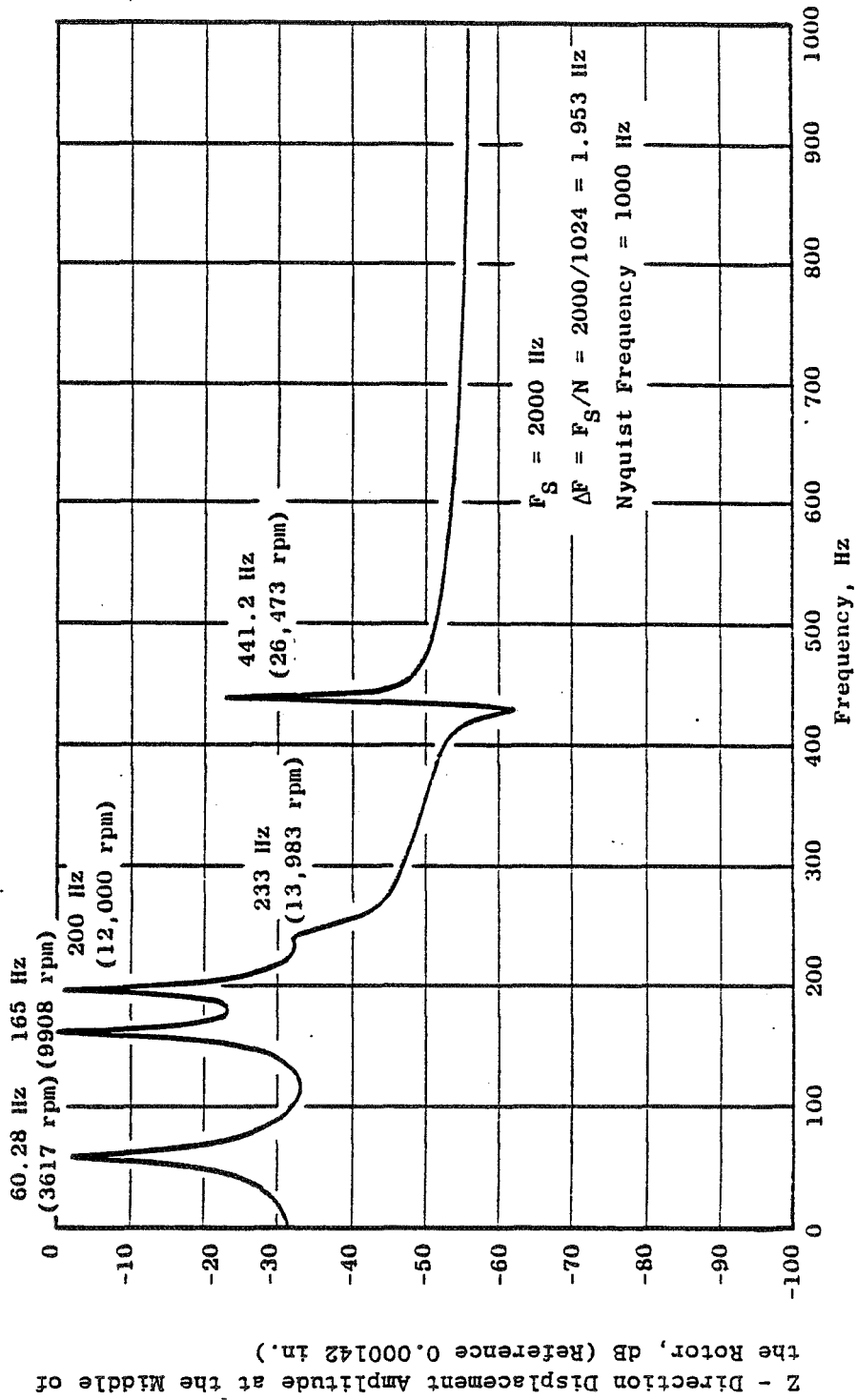


Figure 22. Demonstrator Model 100 g-in. Sudden Unbalance at the Fan at 12,000 rpm.



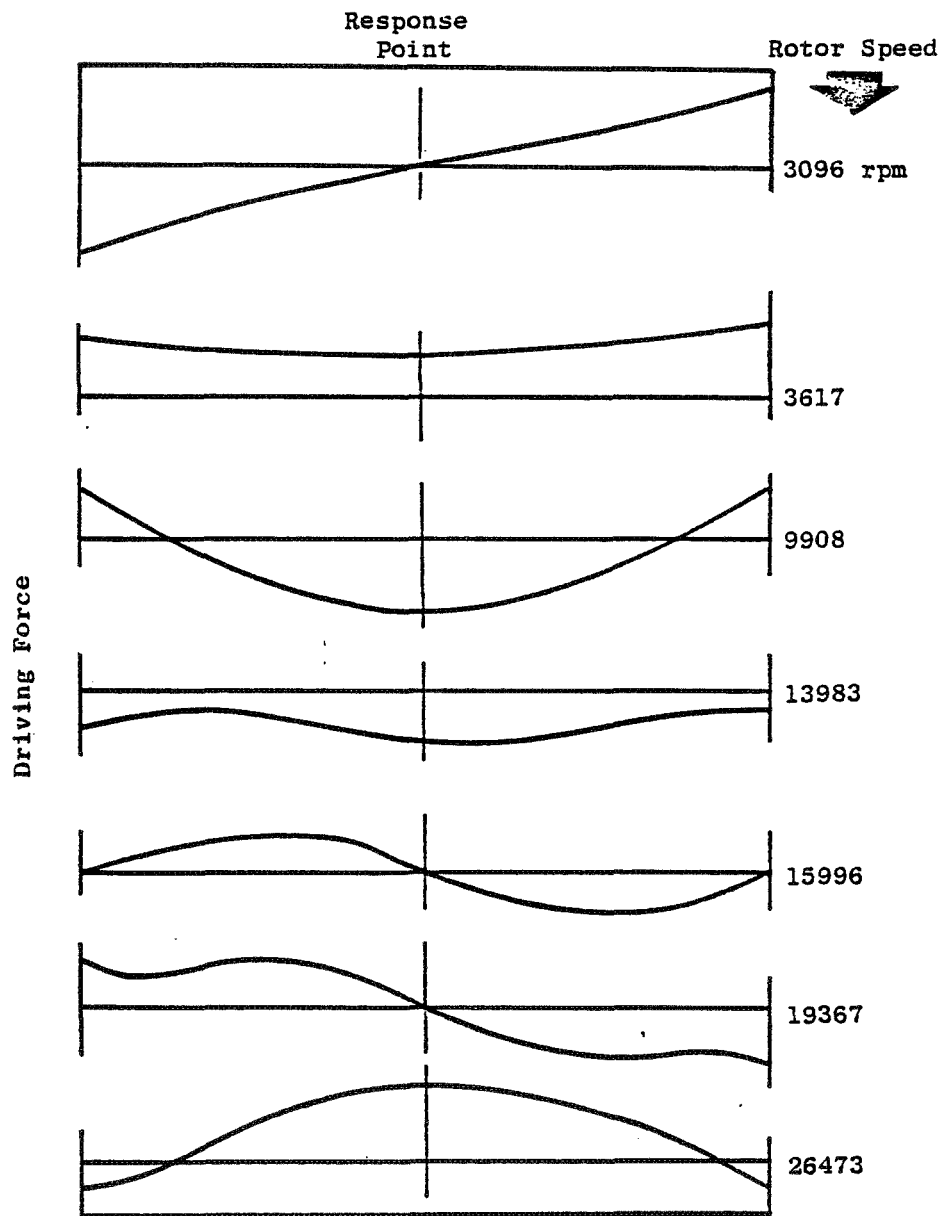


Figure 23. Total System - Rotor Mode Shapes.

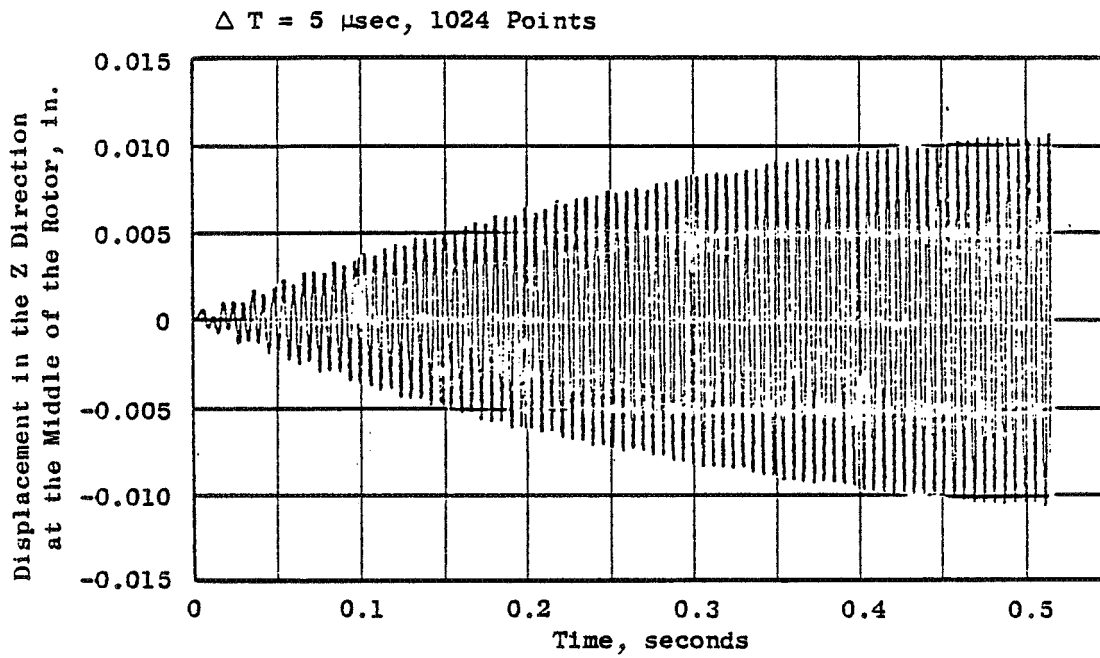


Figure 24. Demonstrator Model 100 g-in. Sudden Unbalance at the Fan at 9908 rpm.

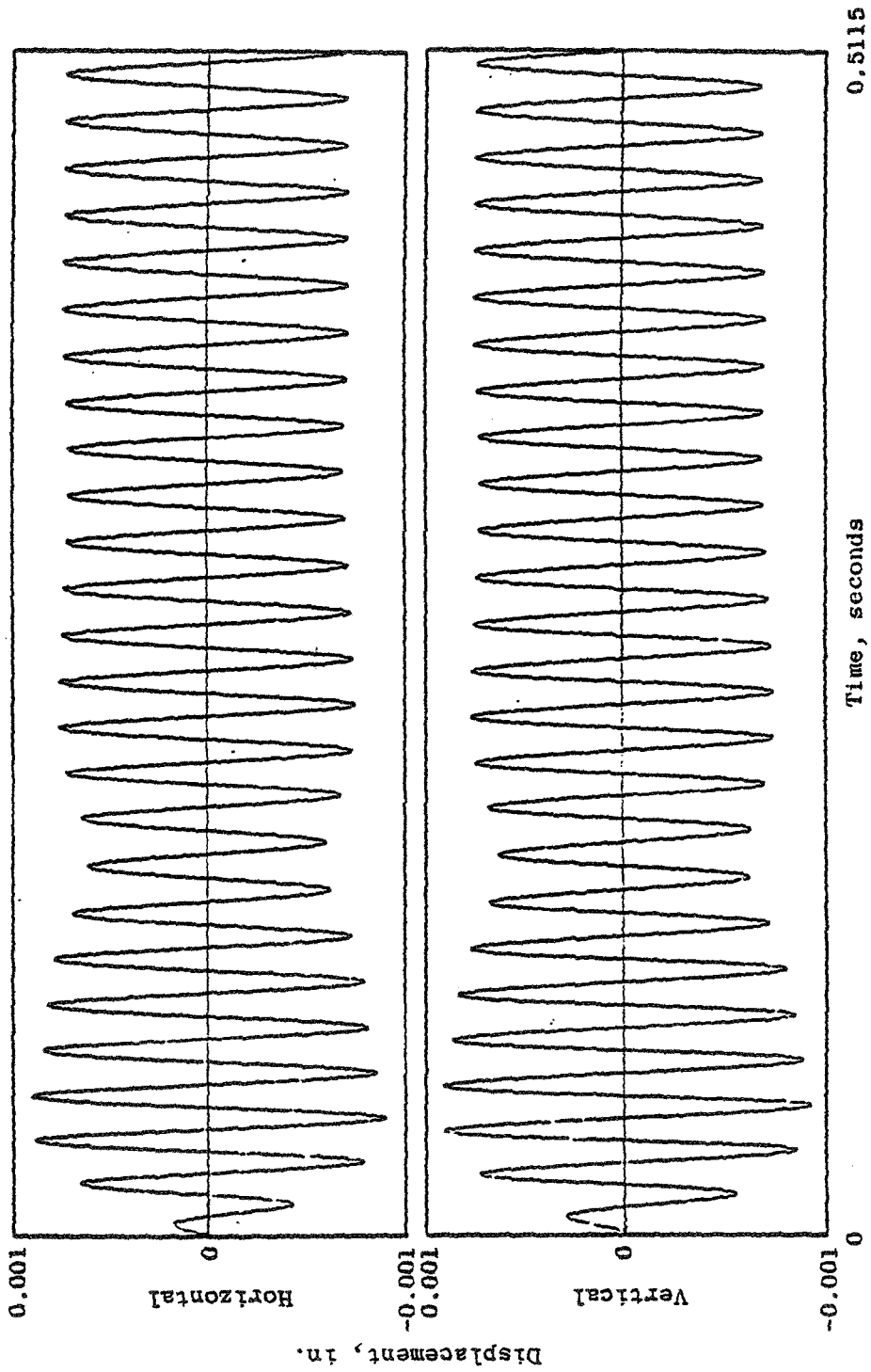


Figure 25. Fan Response in Two Planes for NASA Demonstrator Model with Gyro 100 g-in. Sudden Fan Unbalance at 3000 rpm.

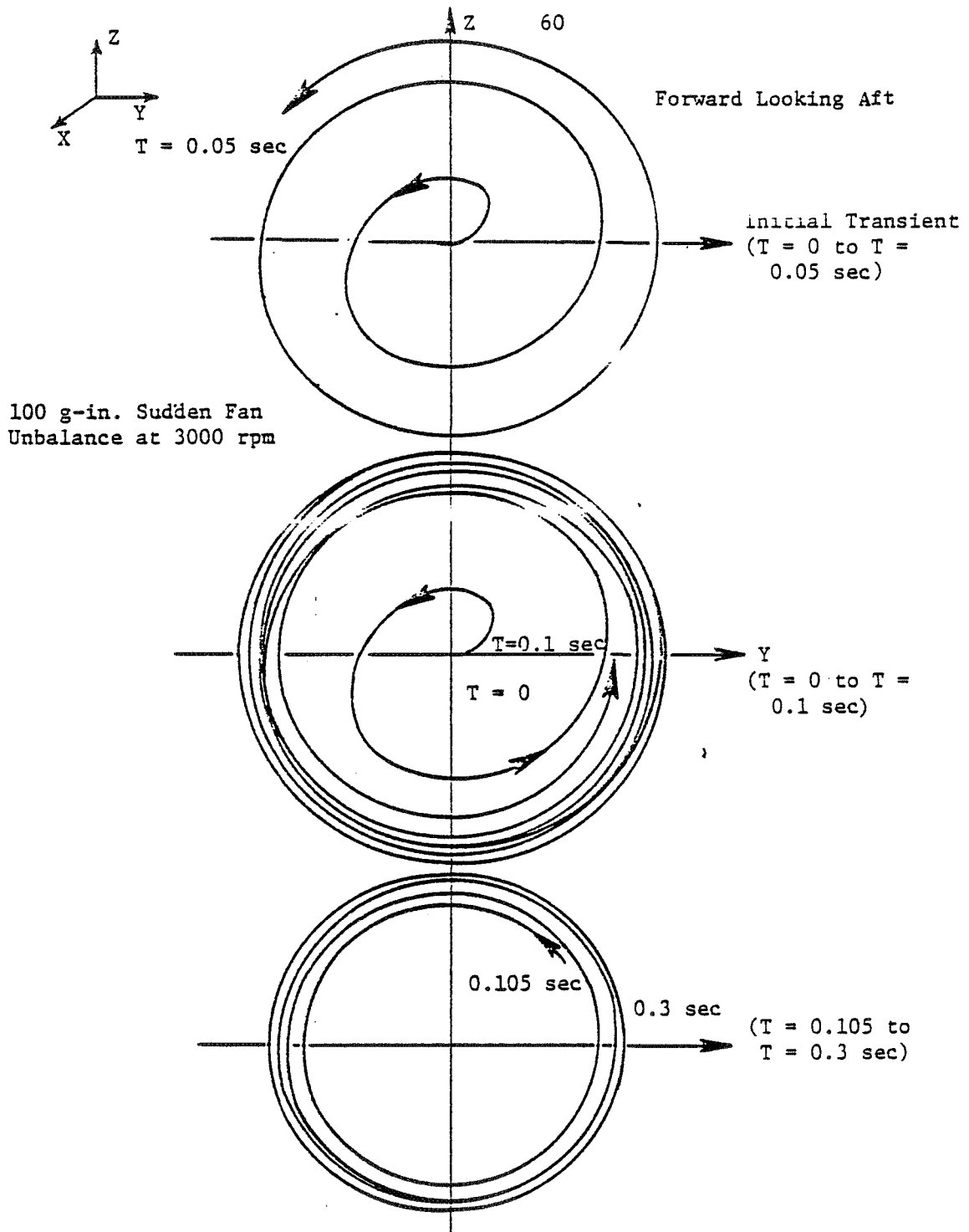


Figure 26. Orbit Plots at the Fan for NASA Demonstrator Model with Gyro.

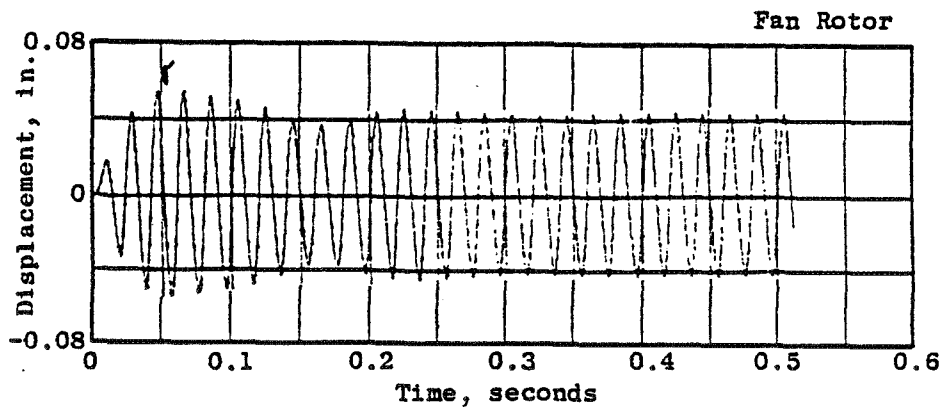
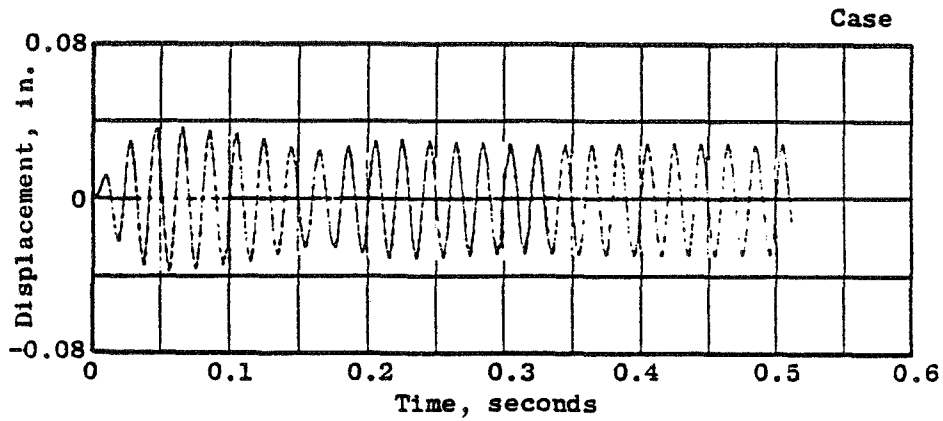


Figure 27. Response in the Vertical Direction at the Case and Fan Rotor for the NASA Demonstrator Model for 5000 g-in. Sudden Fan Unbalance at 3000 rpm (No Rub).

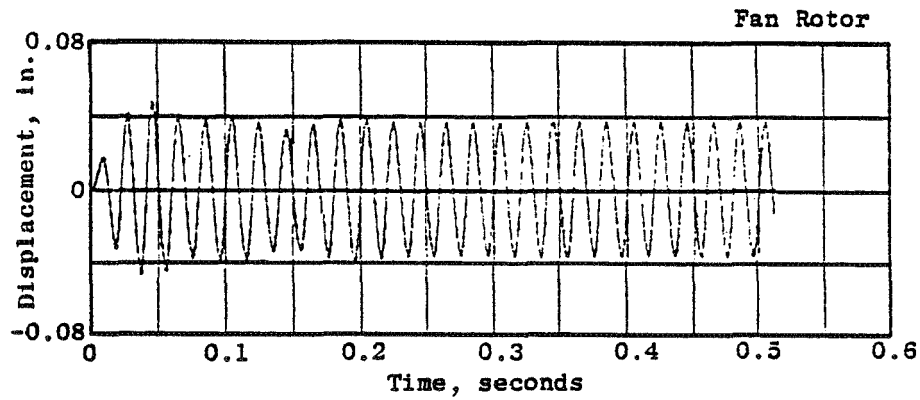
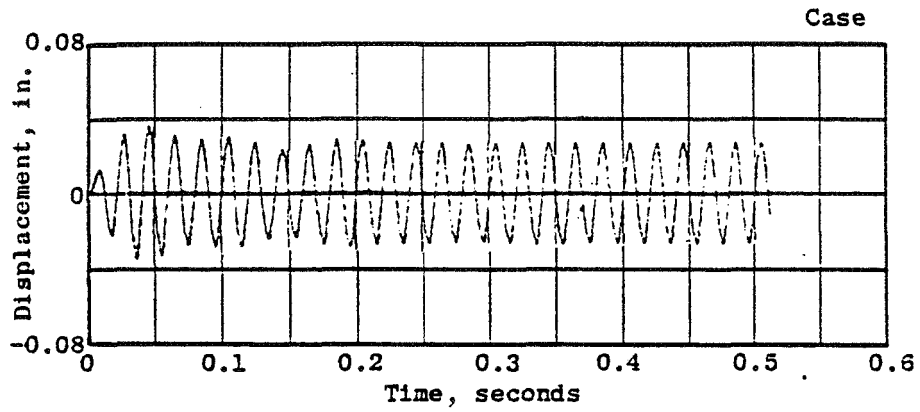


Figure 28. Response in the Vertical Direction at the Case and Fan Rotor for the NASA Demonstrator Model for 5000 g-in. Sudden Fan Unbalance at 3000 rpm (With Rub).

Shown to Time 0.05 seconds; Radial-Displacement Dead Band Exceeds the Fan Rotor-Case Relative Displacement.

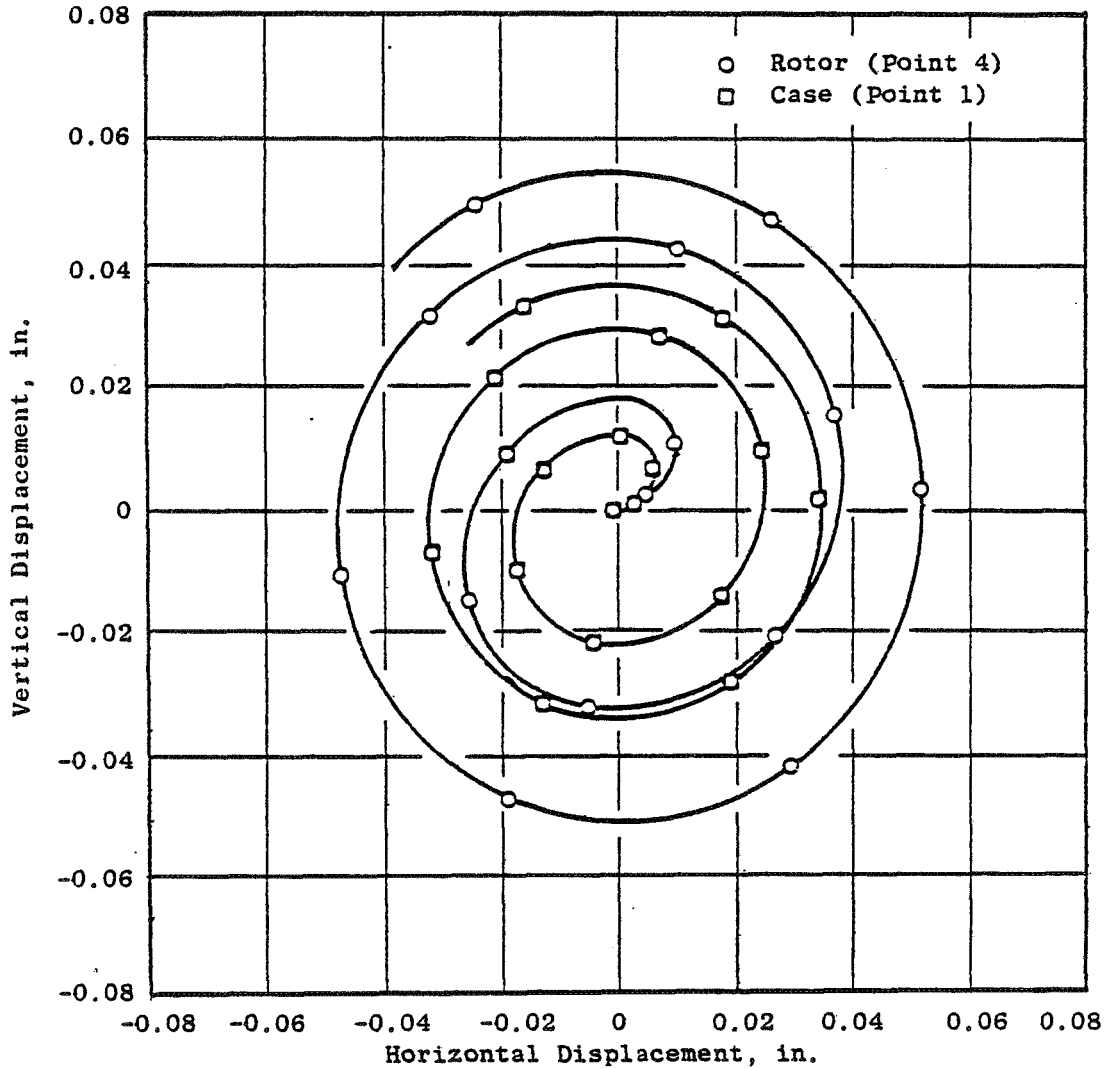


Figure 29. Rotor and Case Orbit Plot for the NASA Demonstrator Model for 5000 g-in. Sudden Fan Unbalance at 3000 rpm (No Rub).

Shown to Time 0.05 seconds; 10-mil, Radial-Displacement Dead Band and  $1 \times 10^6$  lb/in. Rub Spring at the Fan Rotor Case.

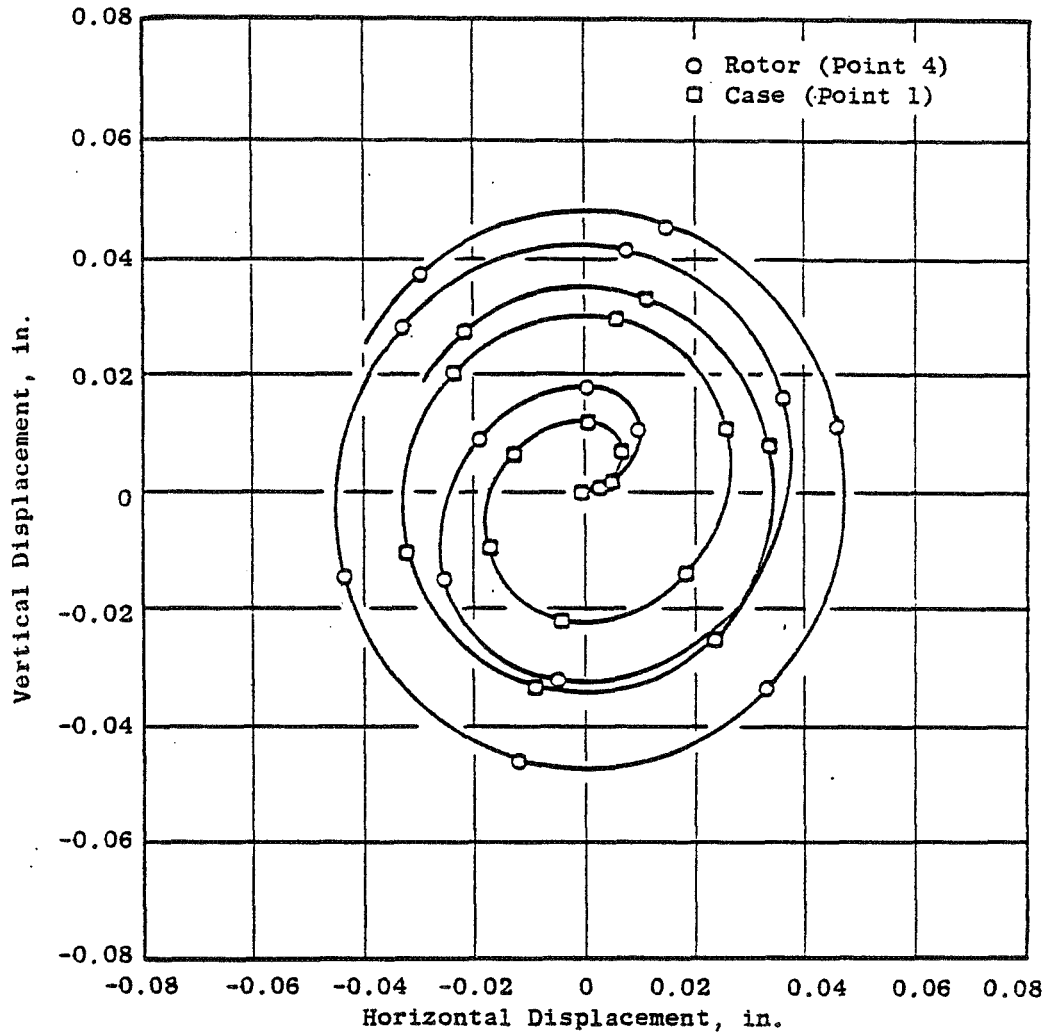


Figure 30. Rotor and Case Orbit Plot for the NASA Demonstrator Model for 5000 g-in. Sudden Fan Unbalance at 3000 rpm (With Rub).



Radial displacement dead band exceeds the fan rotor/case relative displacement.

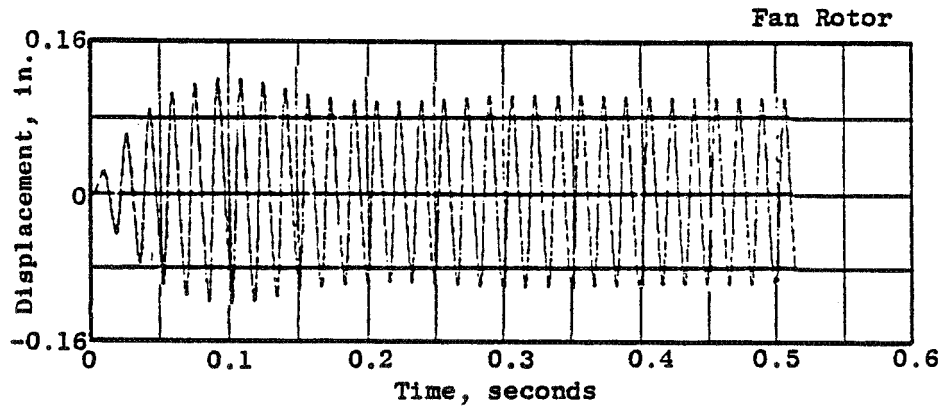
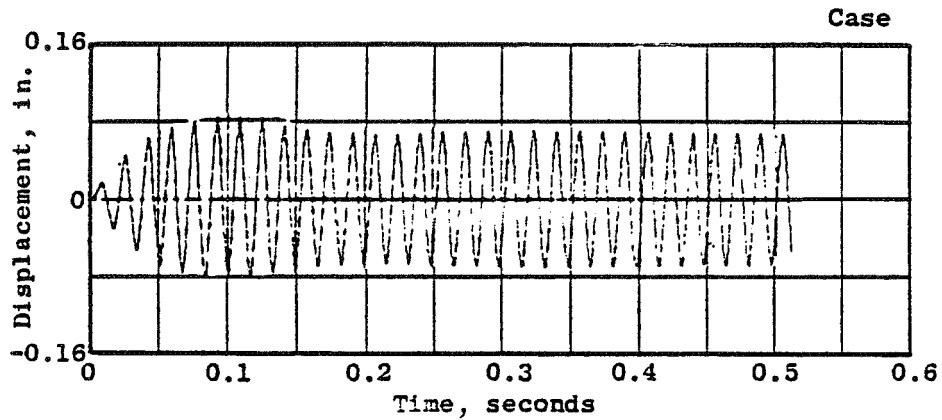


Figure 31. Response in the Vertical Direction at the Case and Fan Rotor for the NASA Demonstrator Model for 5000 g-in. Sudden Fan Unbalance at 3624 rpm (No Rub).

Ten-mil radial displacement dead band and  $1 \times 10^6$  lb/in. rub spring at the fan rotor/case.

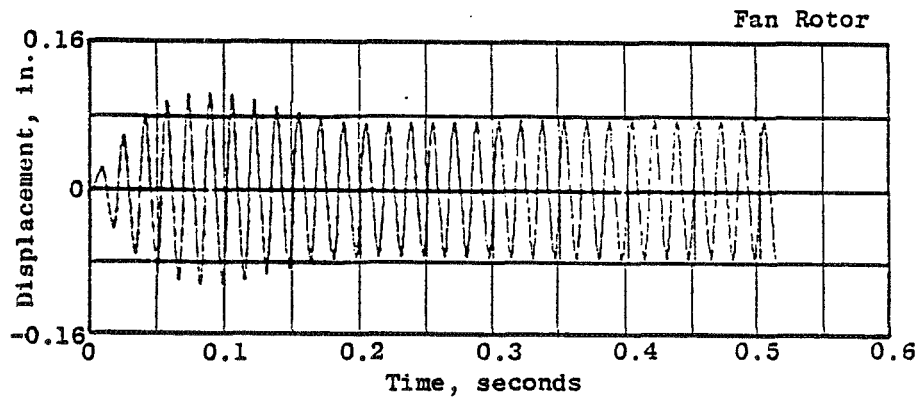
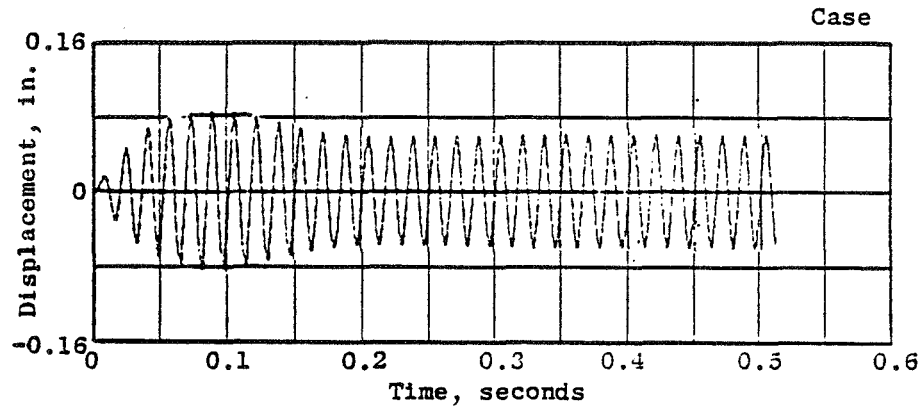


Figure 32. Response in the Vertical Direction at the Case and Fan Rotor for the NASA Demonstrator Model for 5000 g-in. Sudden Fan Unbalance at 3624 rpm (With Rub).

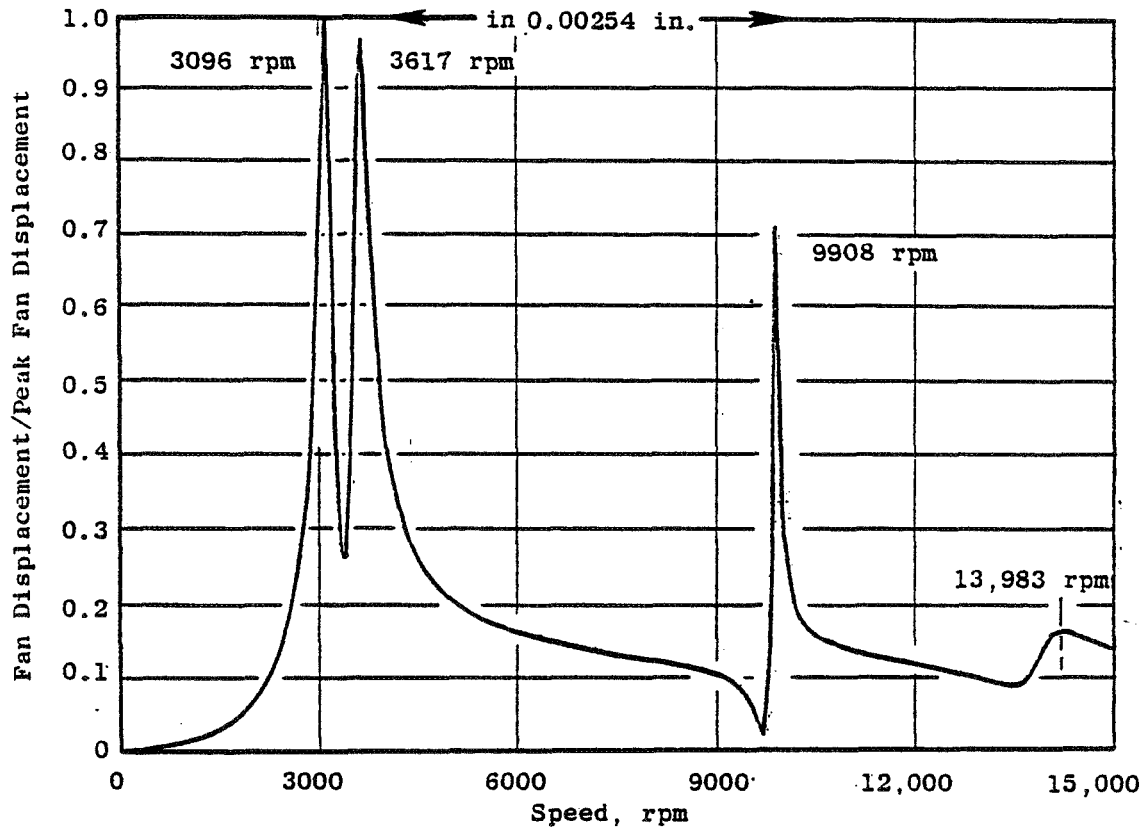


Figure 33. NASA Demonstrator Steady-State Frequency Response for 100 g-in. Fan Unbalance (No Gyro).

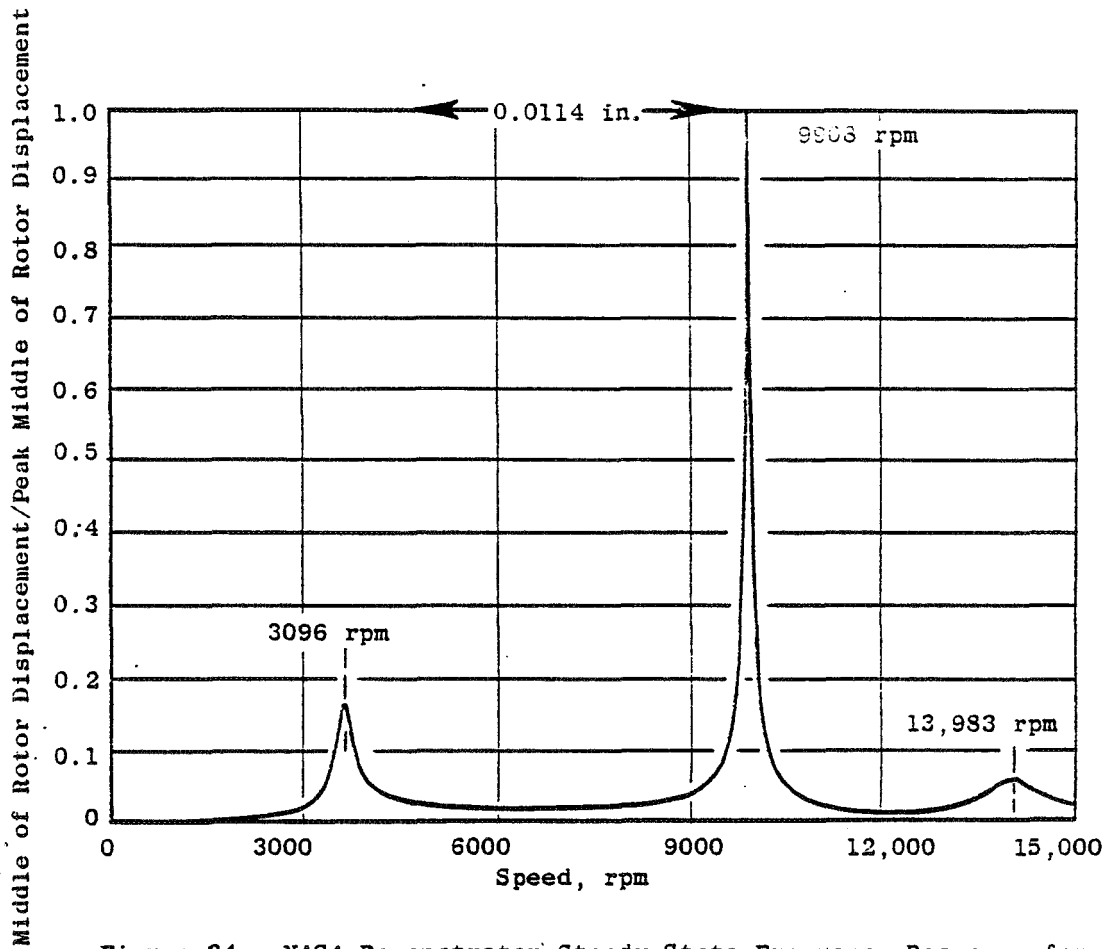


Figure 34. NASA Demonstrator Steady-State Frequency Response for 100 g-in. Fan Unbalance (No Gyro).

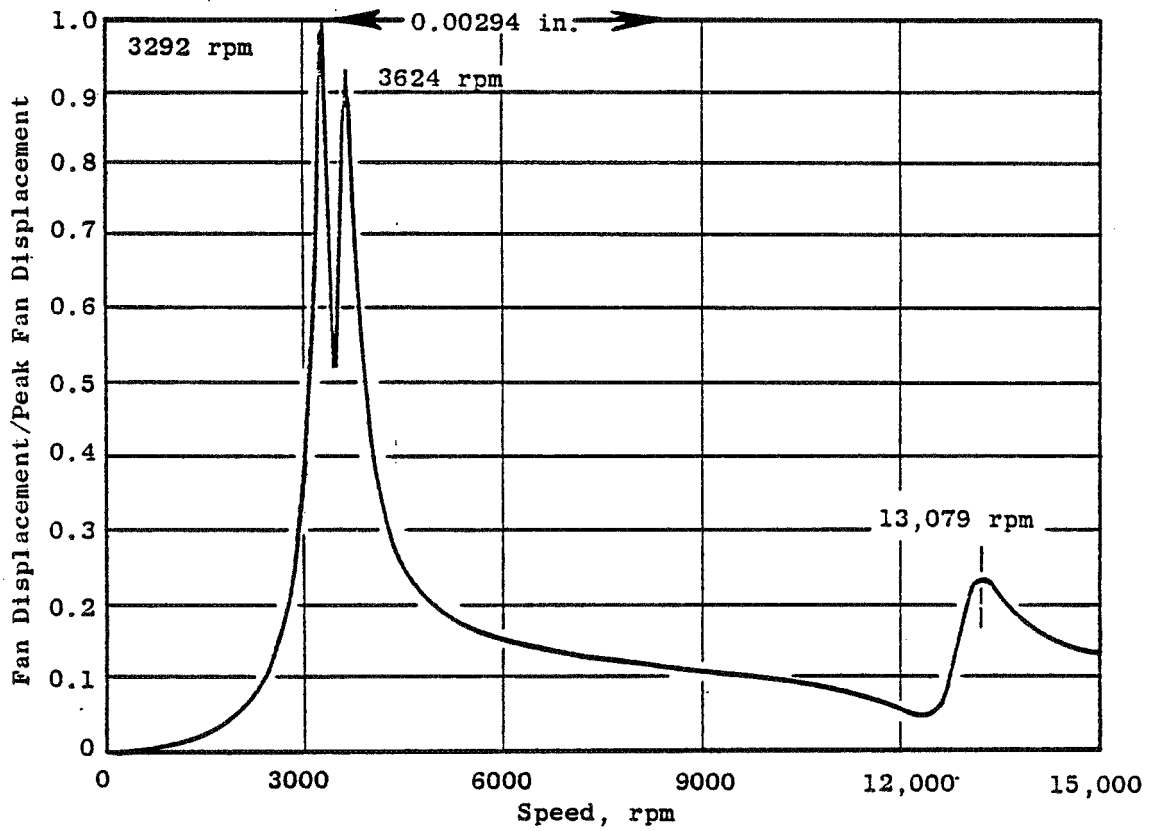


Figure 35. NASA Demonstrator Steady-State Frequency Response for 100 g-in. Fan Unbalance (Gyro at Fan and Turbine).

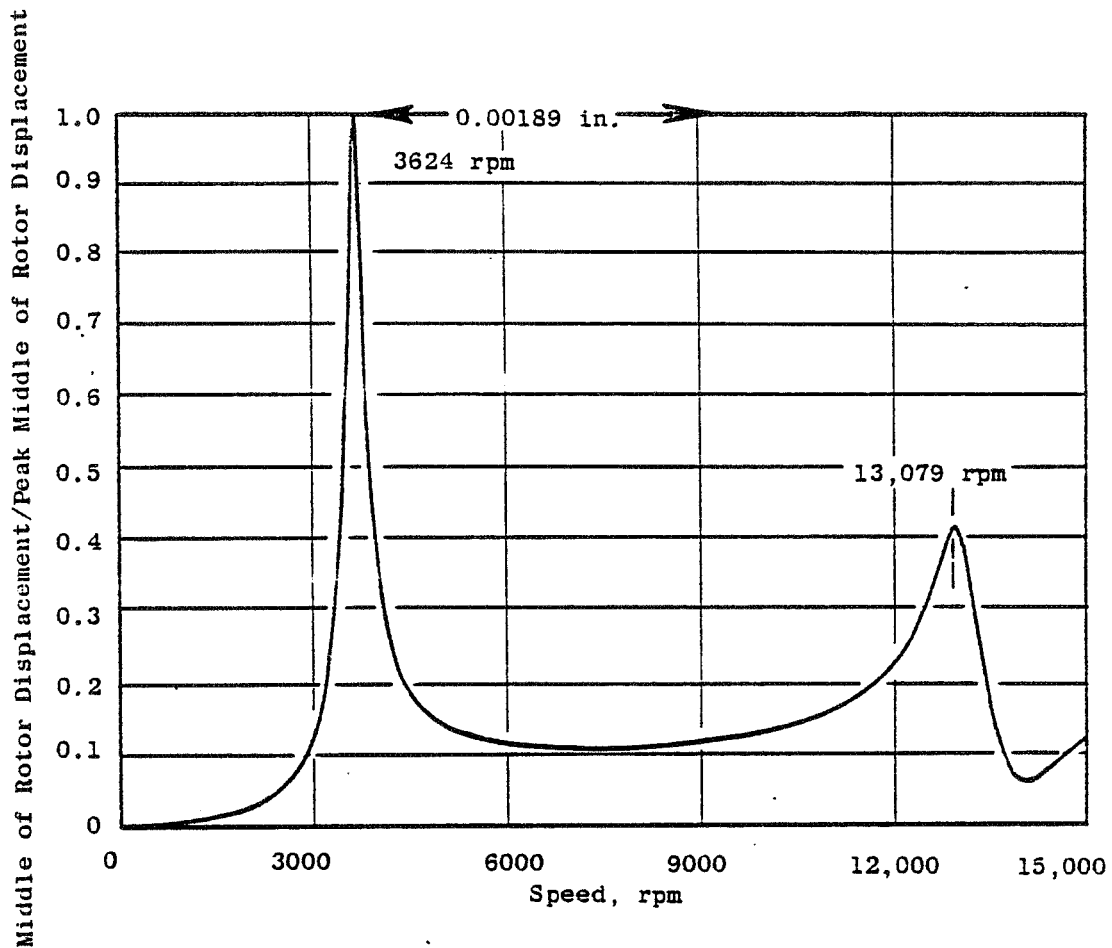


Figure 36. NASA Demonstrator Steady-State Frequency Response for 100 g-in. Fan Unbalance (Gyro at Fan and Turbine).

response for the total system with and without gyroscopic stiffening at the fan and turbine locations. Comparison of the time response, once steady-state conditions have been reached with the frequency response, shows good agreement.

Figures 37 through 42 show the results of analyses for a 2000 rpm/sec accel rate that reflects use of the TETRA restart option. The restart option allows the utilization of the results obtained from a previous analysis to continue without the introduction of pseudotransients. Each time output is printed, the TETRA program writes in a file the values for each of the generalized coordinates for the last time step, for one time step earlier, and for two time steps earlier. This information is utilized to provide the initial data needed to continue the analysis. The process can be repeated any number of times.

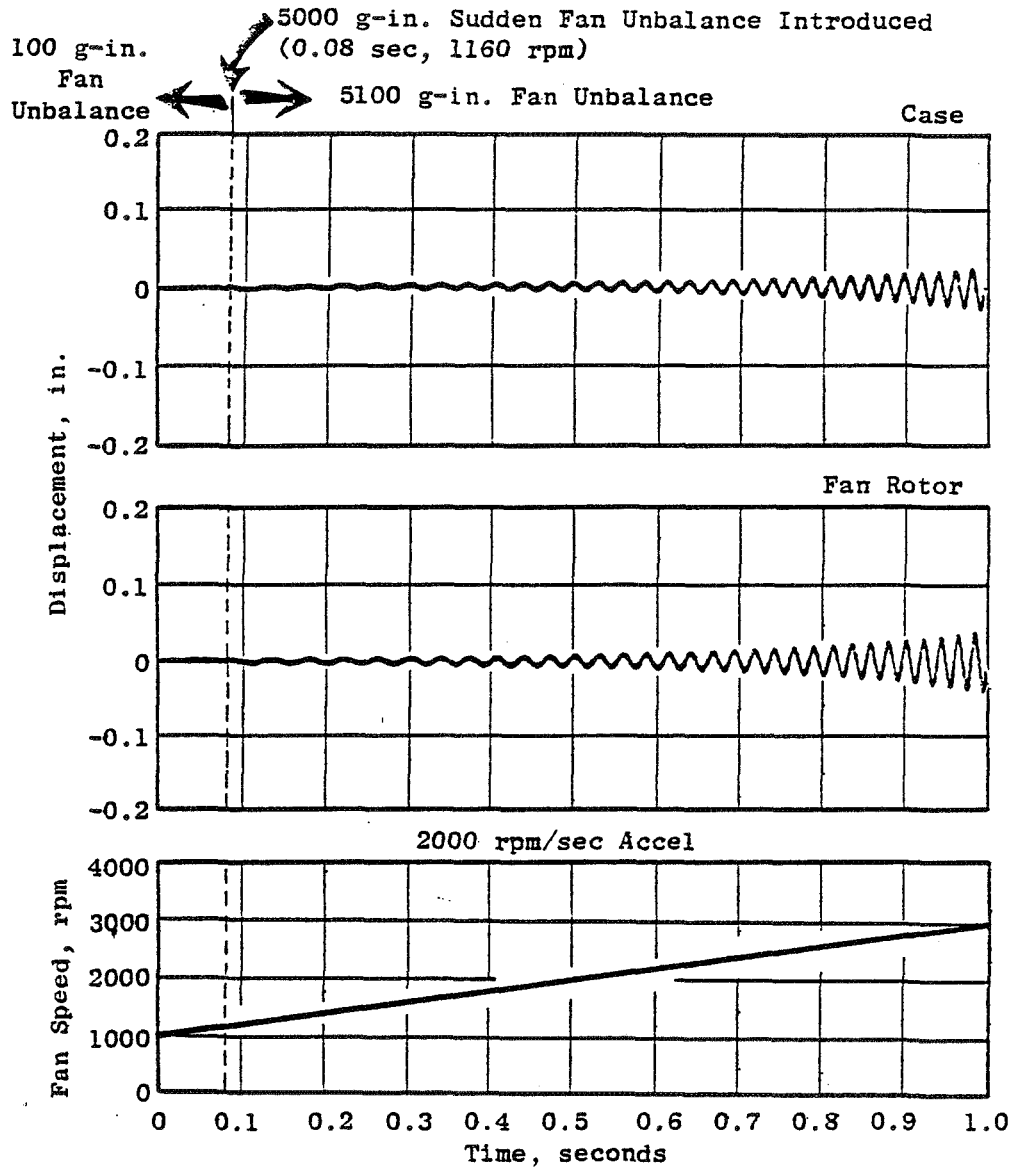


Figure 37. Response in the Vertical Direction of the Case and Fan Rotor for the NASA Demonstrator Model for 1000 to 3000 rpm Accel Segment; Radial-Displacement Dead Band Exceeds the Fan-Case Relative Displacement (No Rub).

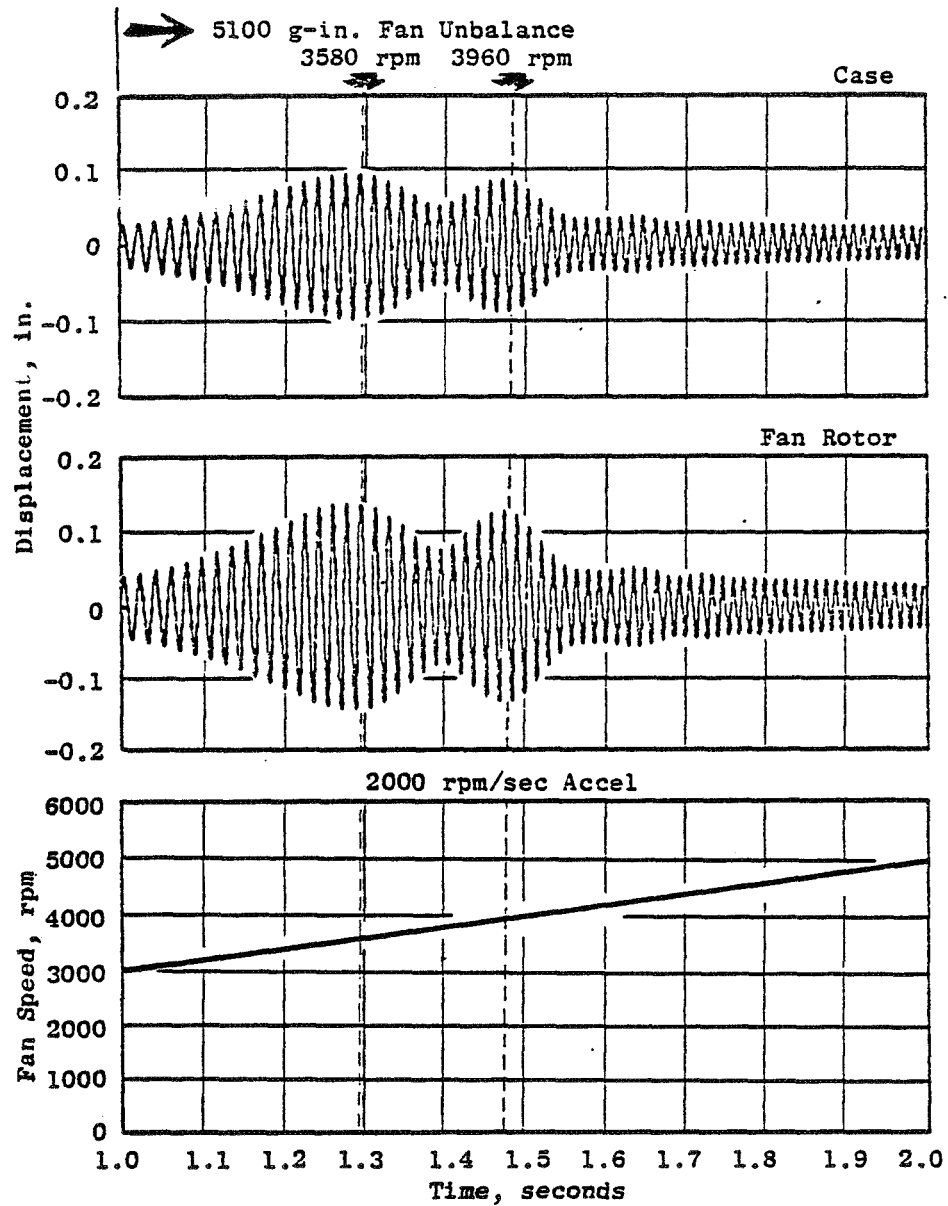


Figure 38. Response in the Vertical Direction at the Case and Fan Rotor for the NASA Demonstrator Model for 3000 to 5000 rpm Accel Segment; Radial-Displacement Dead Band Exceeds the Fan-Case Relative Displacement (No Rub).



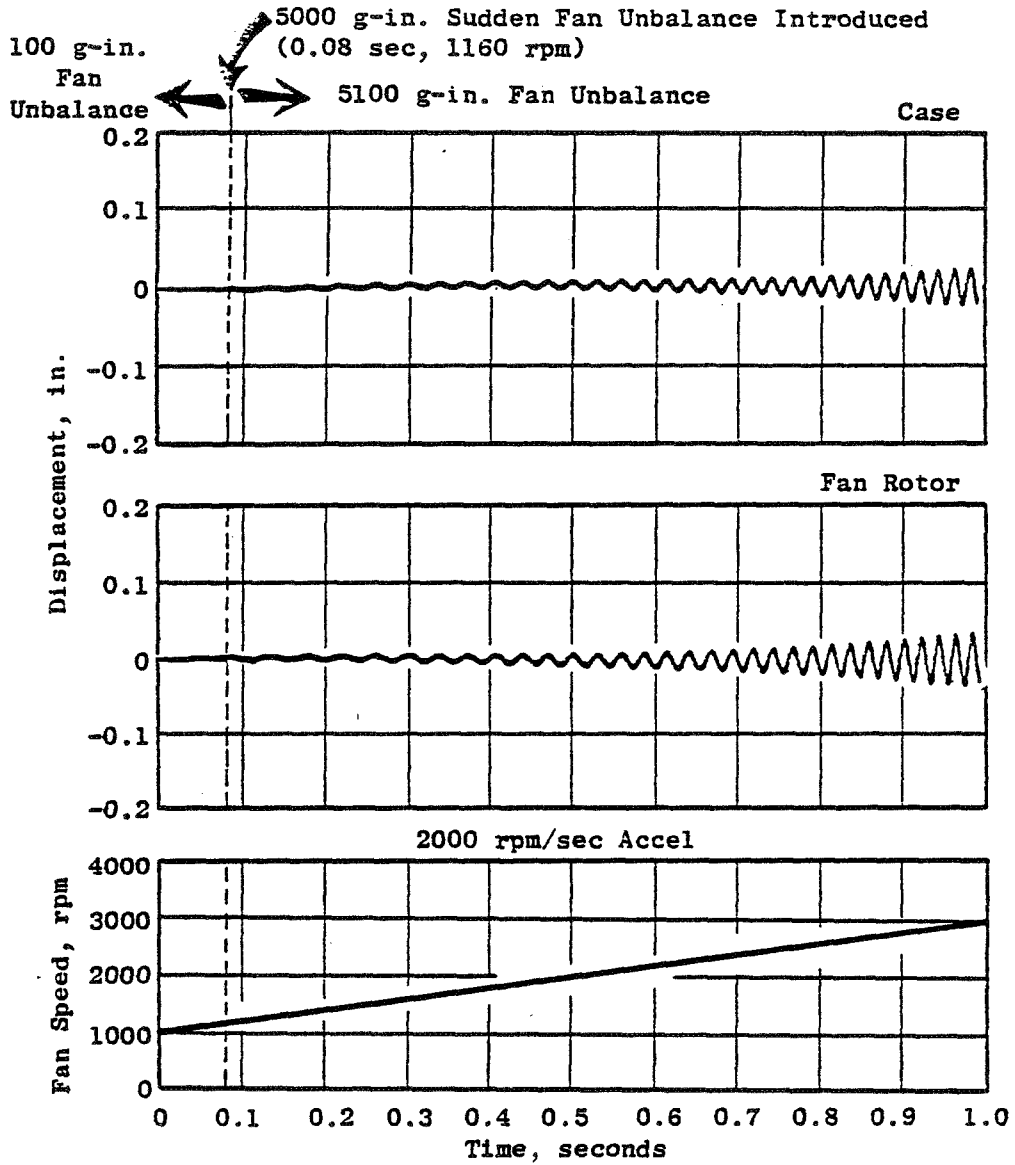


Figure 39. Response in the Vertical Direction at the Case and Fan Rotor for the NASA Demonstrator Model for 1000 to 3000 rpm Accel Segment; 10-mil Radial-Displacement Dead Band and  $1 \times 10^6$  lb/in. Rub Spring at the Fan Rotor-Case (With Rub).

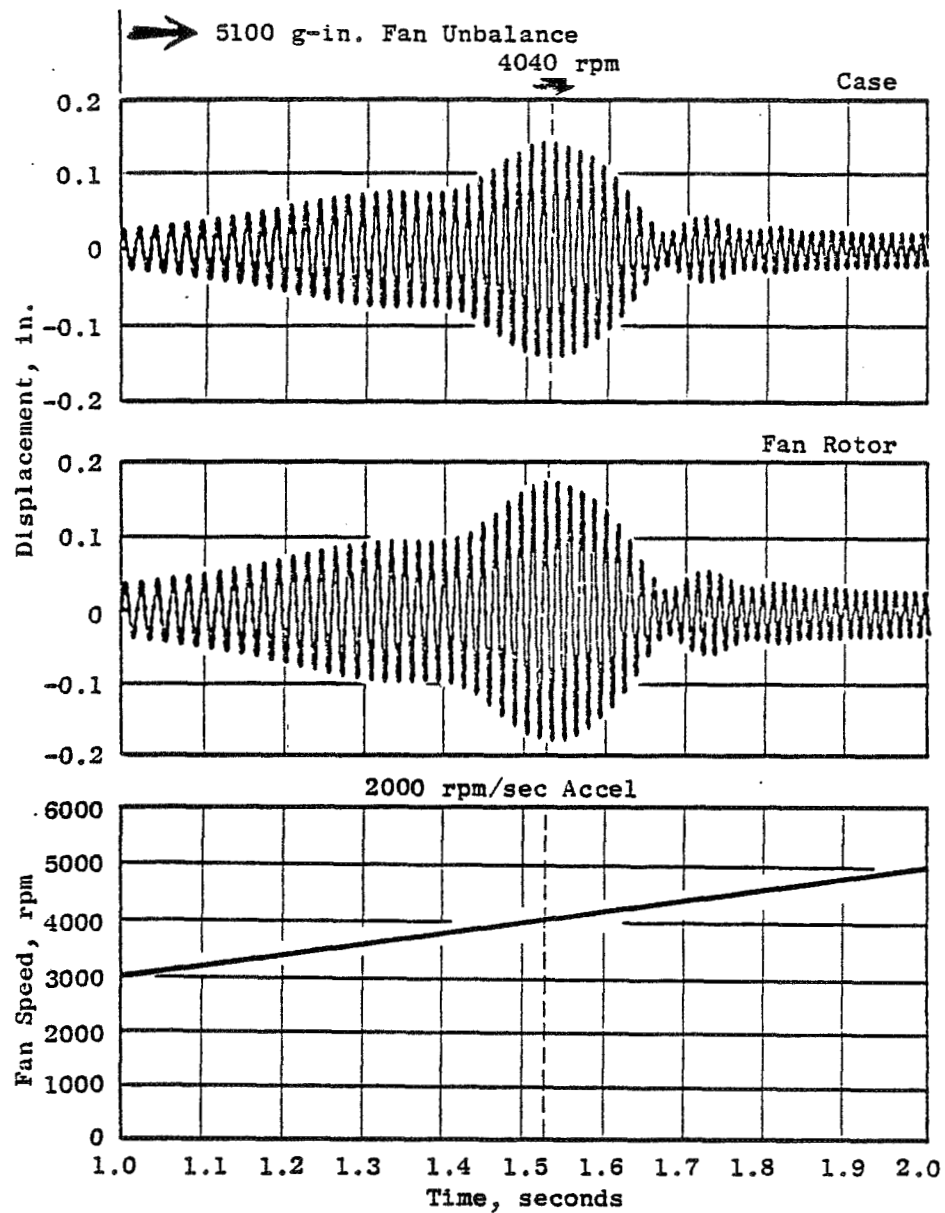


Figure 40. Response in the Vertical Direction at the Case and Fan Rotor for the NASA Demonstrator Model for 3000 to 5000 rpm Accel Segment; 10-mil Radial-Displacement Dead Band and  $1 \times 10^6$  lb/in. Rub Spring at the Fan Rotor-Case (With Rub).

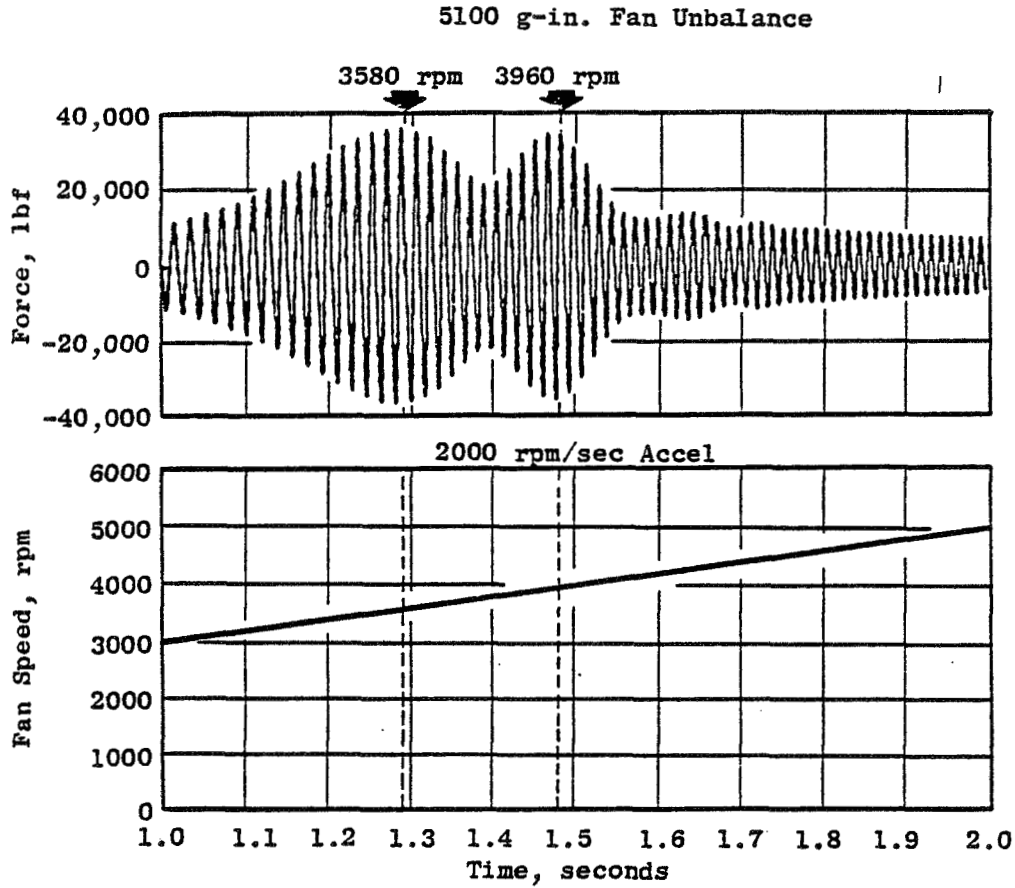


Figure 41. Force Exerted by the Forward Frame/Bearing (Spring 3) on the Rotor at Point 5 in the Vertical Direction for the NASA Demonstrator Model for 3000 to 5000 rpm Accel Segment; Radial-Displacement Dead Band Exceeds the Fan Rotor-Case Relative Displacement (No Rub).

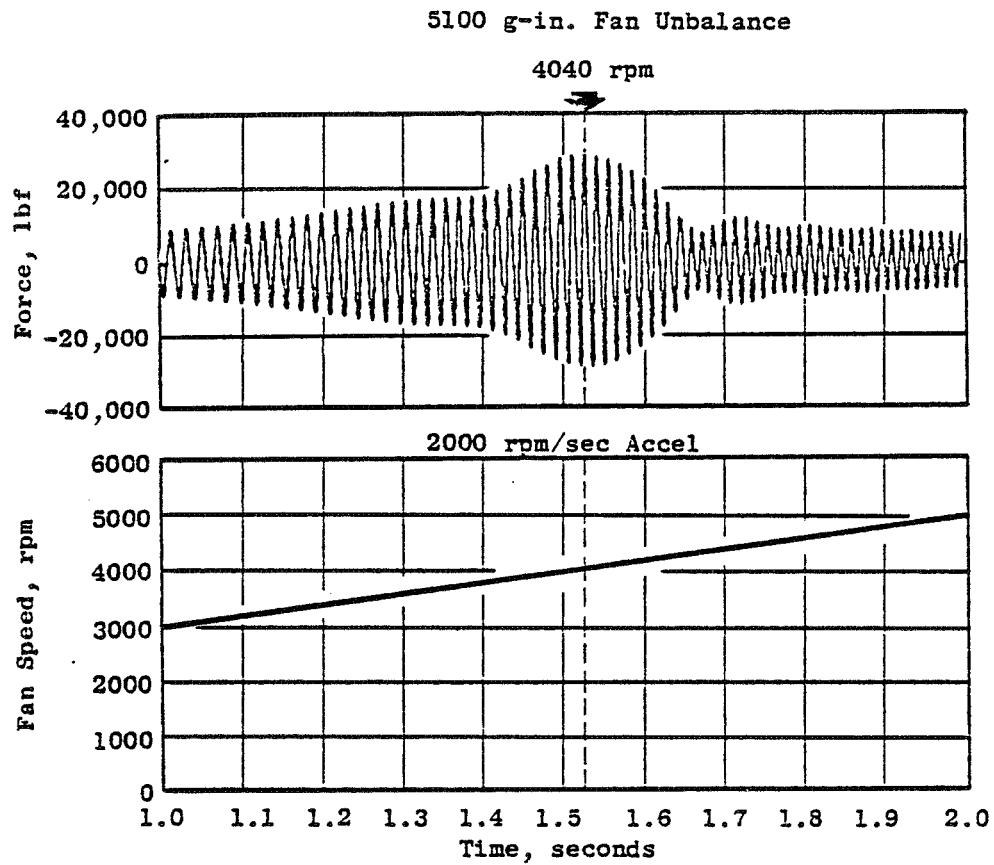


Figure 42. Force Exerted by the Forward Frame/Bearing (Spring 3) on the Rotor at Point 5 in the Vertical Direction for the NASA Demonstrator Model for 3000 to 5000 rpm Accel Segment; 10-mil Radial-Displacement Dead Band and  $1 \times 10^6$  lb/in. Rub Spring at the Fan Rotor Case (With Rub).

The computing strategy used to generate the response data shown in Figures 37 through 42 was as follows. The maximum speed for the accel was selected as 5000 rpm to encompass the two gyro-stiffened critical speeds located at 3292 rpm and 3624 rpm for steady-state operation. Modal Q-factor values of 15 were used for each of the casing subsystem modes, and the rotor subsystem modes were undamped. Physical damping for the connecting springs based on a Q-factor of 15 and a 60.4-Hz frequency, corresponding to the 3624 rpm mode, was used.

The analysis was accomplished with three restart segments for the following cases:

- Large fan-case radial clearance (200 mils)
- Small fan-case radial clearance (10 mils)

Initial constant-speed runs were made for 0.520 second of simulated time with the rotor speed set at 1000 rpm and with 100 g-in. fan unbalance to establish steady-state conditions. For the 2000 rpm/sec accel rate, the time required to accel from 1000 to 5000 rpm is

$$\frac{(5000 - 1000) \text{ rpm}}{2000 \frac{\text{rpm}}{\text{sec}}} = 2 \text{ seconds.}$$

With a integration time step of  $\Delta T = 50 \mu\text{sec}$ , the number of time steps required is equal to

$$\frac{2 \text{ seconds}}{50 \frac{\text{microseconds}}{\text{time step}}} = 40,000 \text{ time steps}$$

For both cases, two restart segments of 20,000 integration points each were used to compute the response for the 2-second accel from 1000 to 5000 rpm. For plotting purposes, the computed data were decimated so that each of the restart segments plots represents 2000 points with a time increment between points equal to 5 microseconds. This means that there are at least:

$$\frac{60}{5000} \times \frac{1}{5 \times 10^{-6}} = 24$$

plotted points per cycle at the highest rotor speed (5000 rpm). Although the plots are labeled 0 to 1.0 second for the accel from 1000 to 3000 rpm, the 0 time actually corresponds to 0.52 second. At a time 0.6 second (labeled as 0.6 - 0.52 = 0.08 second), a large unbalance increment of 5000 g-in. is added to represent sudden unbalance. It will be noted that the apparent critical speeds for the large-clearance case (i.e., no rub) occur at higher rotor speeds than the steady-state values. The 3580 rpm speed corresponds to the 3292 rpm speed, and 3960 rpm corresponds to the 3624 rpm speed. The shifting of the peak-response speeds is caused by the accel rate, and this phenomenon is discussed in Reference 9. The fan rub present for the small-clearance case causes a stiffening effect that shifts the peak response to a higher speed.

#### 4.0 APPLICATION OF TETRA TO BLADE LOSS TRANSIENT RESPONSE ANALYSIS OF TWO TEST VEHICLES AND EXPERIMENTAL VERIFICATION

##### 4.1 SUMMARY

This section discusses the results of the application of TETRA to two blade-out test vehicles and the test data obtained from these tests. Included are the descriptions of these two vehicles, the comparison of dynamic responses (predicted versus test), and an assessment of the TETRA computer program.

##### 4.2 INTRODUCTION

As Galileo and Sir Francis Bacon said centuries ago, a theory stands or falls by its ability to predict experimental results. The test of usefulness or validity of any calculation method, therefore, must be twofold: (1) prediction of the result of an experiment and (2) experimental verification by comparing predicted with measured values.

Because the TETRA program had been checked during its development with simple, degenerate cases wherein known closed-form solutions are readily available, this section will concern itself with the response of complex structures. It is part of Task II to verify the computer program developed in this task by applying it to the calculation of the transient response of a test vehicle and an engine where dynamic test data had been obtained during blade-out tests.

This section describes two experimental vehicles and presents the dynamic response calculated by TETRA under the same transient, blade-loss loading of the tests. Loads and displacements are calculated at points corresponding to the locations of instrumentation in the test vehicles.

Task III effort comprises obtaining and reducing the test data from these two vehicles and preparing them in a form to permit comparison with the predicted response.

Finally, the effectiveness of the TETRA program is assessed in Section 5.0. Refinements to improve its accuracy and to reduce its shortcomings, as well as extensions to improve its versatility and increase its scope, will be recommended.

Results from two separate blade-out tests are used to provide the experimental verification of the TETRA computer code. Both of these tests involved the loss of a single fan blade (or an equivalent unbalance) while running at high speed. One of these tests was conducted on a blade-out test vehicle and the other on a full engine. Details of these tests and their results are given in Sections 4.7 and 4.8. Analytical predictions for both of these tests were made using the TETRA computer code and are discussed in Sections 4.4 and 4.6. The TETRA model for both of these test vehicles was generated using the

VAST computer code; this is the primary tool within the General Electric Aircraft Engine Business Group for predicting engine system dynamic characteristics. This program is an extension of the Prohl-Myklestad method and addresses the branched load paths found in real engine structures. The vibratory behavior of multishaft engine systems can be analyzed, and both synchronous rotor whirl and distributed linear structural damping are considered. The program includes bending, shear deformation, and rotary and gyroscopic effects. It computes and prints out the system natural frequencies, displacements, rotations, and loads for each normal mode, together with the potential and kinetic energy distributions in the various components. In addition, VAST computes the forced frequency response at each critical speed based on modal scale factors derived from the real mode shapes, the energy distributions, and user-specified structural damping distributions.

The VAST program was specifically developed for axisymmetric structures typical of most jet engine components. It assumes planar motion with two degrees of freedom per node, i.e., lateral displacement and bending within the plane (the gyroscopic forces on the rotor are based on a circular whirling motion).

#### 4.3 BLADE-OUT TEST VEHICLE VAST ANALYSIS

The forced response of the test vehicle was predicted using the VAST program. This response will provide the basis for assessing the validity of the TETRA idealization.

A schematic diagram of the VAST model of the blade-out test vehicle is given in Figure 43. The test vehicle is made up of engine hardware (fan rotor, fan frame bearings and fan cases) and supporting slave equipment (drive system, soft mount system, and support structure). Those portions of the model representing real engine hardware were taken directly from the VAST model of the full engine. New model elements for special slave hardware were generated as necessary. In Figure 43, elements identified by circles are spans. A span is a structural element made up of small, massless, structural intervals and point masses. The structural intervals can represent beams, cones, or springs. The point masses can include weight, transverse inertia, and polar moment of inertia. The elements identified by triangles are massless springs representing bearings, frames, mounts, and supports. The VAST program computes stepping or transfer matrices for each span interval and then performs a progressive multiplication across each span to obtain equilibrium and compatibility equations that are then combined with the system boundary equations to form the dynamic equations for the entire system. The blade-out test vehicle VAST model consisted of 12 spans, 8 springs (including bearings, frames, and supports), and a total of 194 degrees of freedom. The test vehicle was analyzed in the vertical direction only. The structure was axisymmetric, as were the primary mounts. The secondary supports (spring hangers) were very soft dynamically in the vertical direction and provided no support in the horizontal direction. These spring hangers were the only major difference between the vertical and horizontal planes. Since there was no significant potential energy in these





springs in the flexible mode of interest, the critical speeds in the vertical and horizontal planes were taken to be identical. A more detailed description of the blade-out test vehicle is given in Section 4.7.

The VAST analysis of the test vehicle predicted three critical speeds in the operating range (0 to 4185 rpm). Two of these were rigid-body modes at 387 and 981 rpm, and the other was a system flexural mode at 4043 rpm. The next higher resonance was predicted to occur at approximately 6500 rpm. The mode shapes for the first three resonances are given in Appendix A.

#### 4.4 TETRA ANALYSIS OF THE BLADE-OUT TEST VEHICLE

For the TETRA analysis, the test vehicle is represented by two subsystems, the rotor and the casing, joined by two connecting elements (i.e., the Nos. 1 and 2 bearings). The mode shapes and natural frequencies of Subsystem 1, the casing structure, were calculated using the VAST program. The subsystem was modeled utilizing its physical mounting system (rounded) including the forward, middle, and aft spring hangers as well as the Barry mounts described as spring numbers 200, 100, 101, and 18, respectively. Figure 44 shows a schematic model representing the subsystem. A total of 13 resonant frequencies and modes of the casing were used in the TETRA analysis.

Subsystem 2, the rotor system, was also analyzed with the VAST program to determine the system natural frequencies and mode shapes. This subsystem was treated as a static (nonrotating) component mounted on two very soft springs (100 lb/in.); gyroscopic effects were not considered. The soft springs were used to approximate a free-free system in VAST. Figure 45 shows a schematic model representation of this subsystem. A total of four rotor modes was utilized in the TETRA analysis. The following tabulation summarizes the resonant frequencies of both the rotor and the casing subsystems:

<u>Casing Subsystem</u>		<u>Rotor Subsystem</u>	
<u>Mode</u>	<u>Frequency, rpm</u>	<u>Mode</u>	<u>Frequency, rpm</u>
	424	1	46
	976	2	146
	5,241	3	17,626
	6,535	4	78,001
	11,539		
	16,258		
	18,878		
	36,388		
	39,995		
1	41,284		
1	53,107		
1	69,016		
1	75,867		

The normalized mode shapes for both subsystems are given in Appendix B.

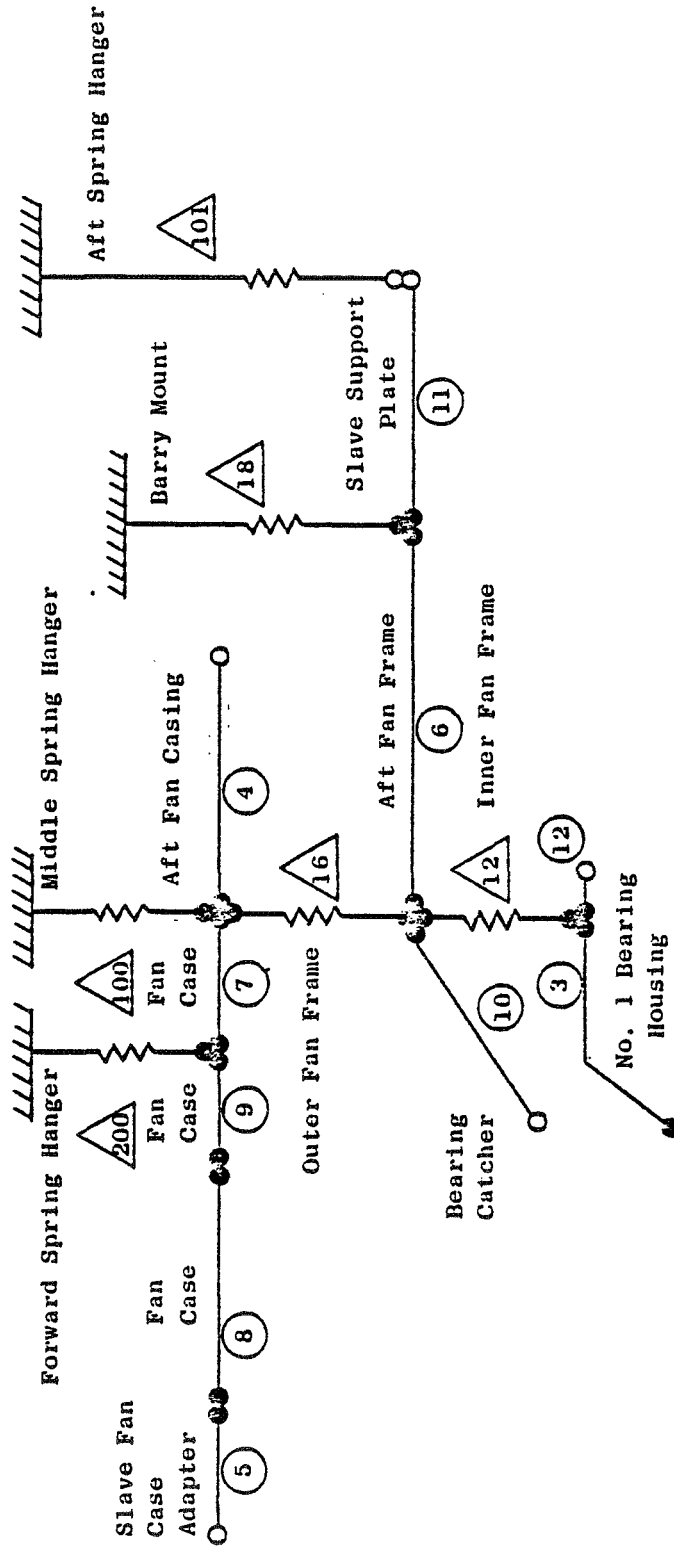


Figure 44. Blade-Out Test Vehicle Schematic Model.

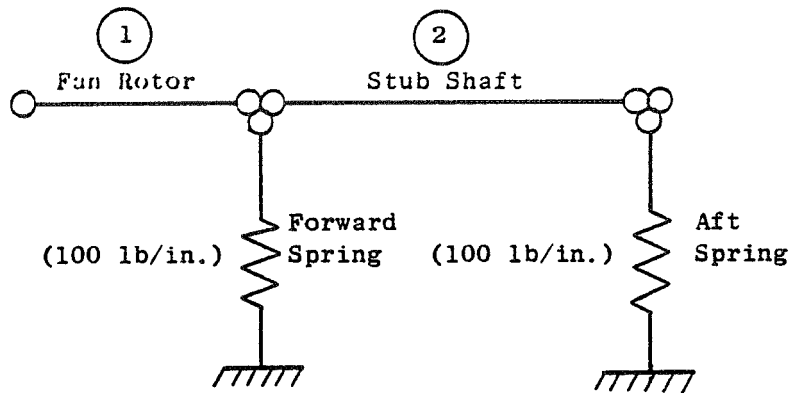


Figure 45. Blade Out Test Vehicle Rotor Subsystem.

The two subsystems were then joined in the TETRA system by use of the connecting Elements 1 and 2. A schematic model for the complete TETRA test vehicle is shown in Figure 46. This model represents the input used in TETRA for the moderate fan-unbalance (linear) analysis.

TETRA was conducted with 13 casing modes and four rotor modes. The maximum frequency used for the casing modes was 75,867 rpm. Fewer than 13 modes were initially used to formulate the problem in the TETRA program, but the results yielded poor frequency and amplitude matchup for the system resonance (4043 rpm) when compared to the VAST analysis for the steady-state forced response case. The 13-mode model gave excellent frequency agreement with VAST, but the amplitudes were slightly off. To obtain a better matchup of the No. 1 bearing load, the damping was adjusted slightly; the casing subsystem Q factor was changed from 15.0 to 12.5. This small adjustment was required to compensate for possible modal truncation errors and to control cost factors involved with analyzing the test vehicle to higher frequencies. The four rotor modes were chosen to give a maximum rotor modal frequency (78,001 rpm) approximately equal to that of the highest casing mode used (75,867 rpm). The rotor subsystem could have used less than four modes, but no additional cost factor was introduced by using four modes since the time-integration step did not have to be increased. The casing and rotor subsystem modes were entered into TETRA in both the vertical and horizontal directions (similar to VAST, assuming a symmetrical system). The connecting elements, the Nos. 1 and 2 bearings, were also defined with identical vertical and horizontal spring rates.

TETRA was initiated at Time = 0 and completed at Time = 0.32 to give ample time for the transient overshoot to be observed. Time steps of 0.00015 sec were used for the analysis. This gave 40 time intervals per cycle of vibration at the highest frequency mode used in the analysis. The test vehicle had only one mass point at which gyroscopic effects were of any importance: the fan-rotor stage. This is the only location at which gyroscopic loads were introduced in TETRA.

The time-share TETRA data file for the linear analysis of the test vehicle is given in Appendix C, together with a description of key items.

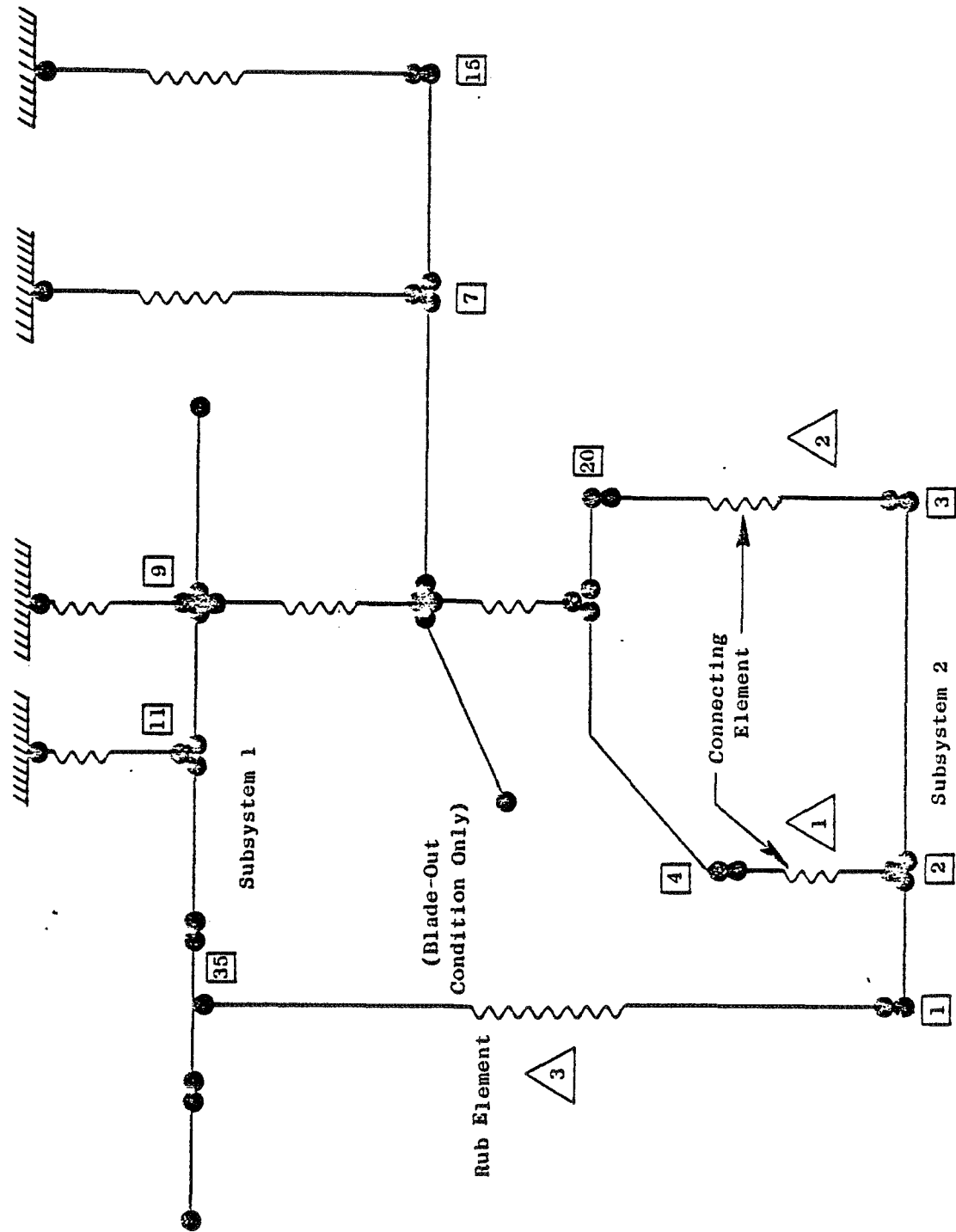


Figure 46. Blade-Out Test Vehicle TETRA Schematic.

The steady-state response as a function of speed was determined by running a succession of solutions initiated at discrete rpm's to cover the speed range of interest. Moderate unbalance levels were used to assure a linear (no rub) solution. The resulting time histories at each speed are given in Appendix D. The levels attained after the initial starting transients decayed were used to define the steady-state response as a function of speed. The No. 1 bearing load response as a function of speed is given in Figure 47. The No. 1 bearing housing displacement response as a function of rpm is given in Figure 48.

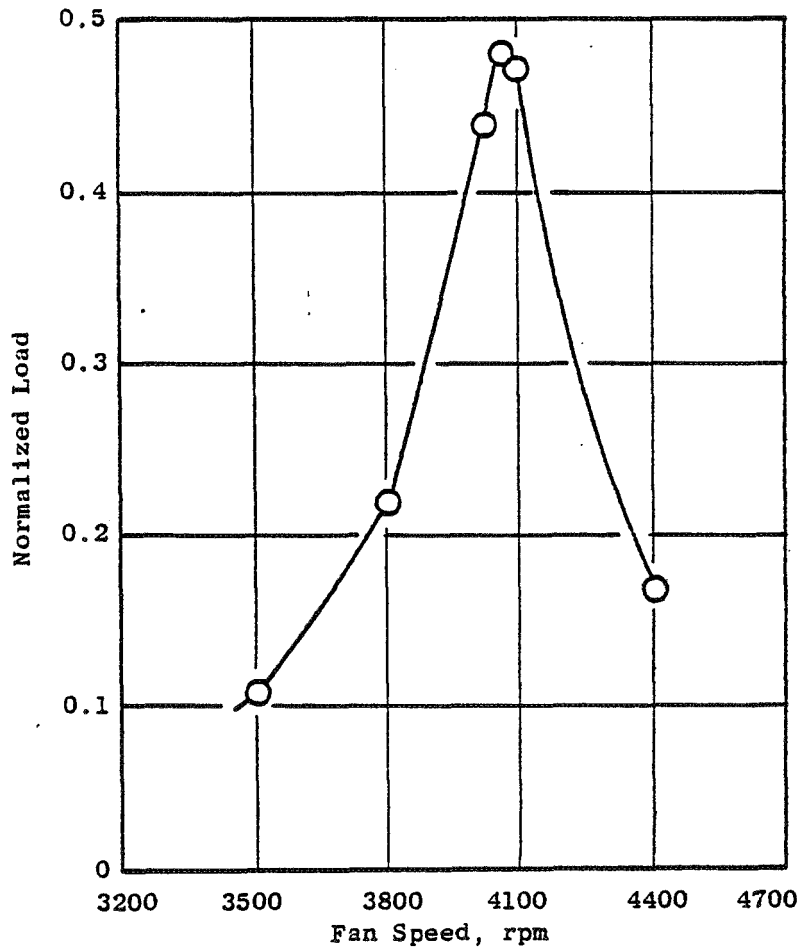


Figure 47. Test Vehicle Linear Analysis for Nominal Fan Rotor Unbalance - TETRA Results - No. 1 Bearing Load.

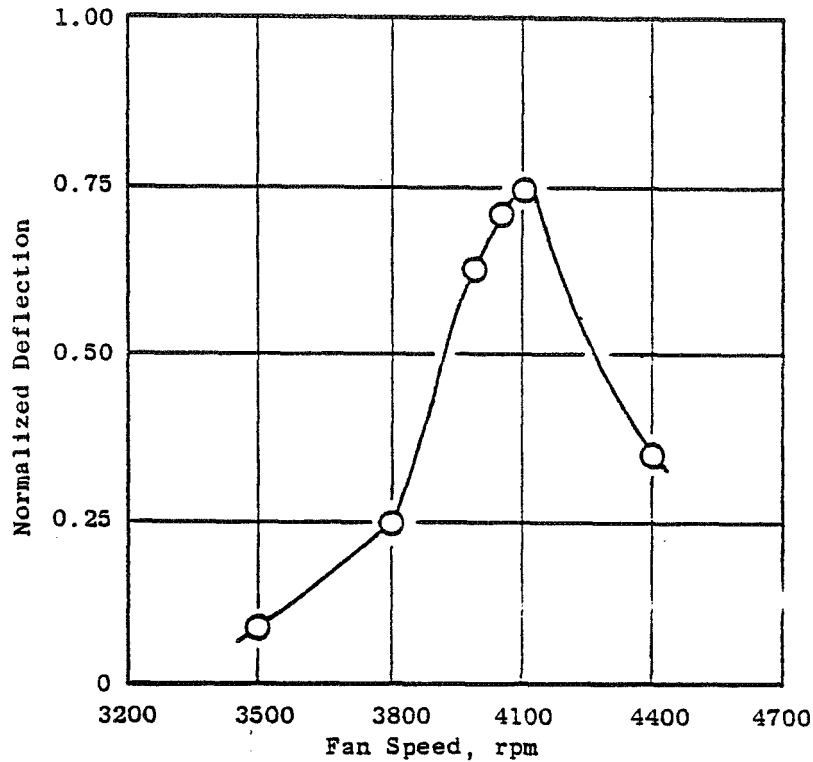


Figure 48. Test Vehicle Linear Analysis for Nominal Fan Rotor Unbalance - TETRA Results - No. 1 Bearing Housing Deflection.

The TETRA input for blade-out analysis is similar to that for the moderate fan-unbalance case. The main difference is the addition of the rub element (connecting Element 3, Figure 46) between the fan rotor and fan case to simulate the nonlinear casing constraint on the rotor. This rub element is defined in List 2 in the following manner:

```

$LIST3
ITYPE=3,
ILEM=3,
JT=1, 35,
SK=1000000,
DBAND=350.0,
CC=0,
$

```

ITYPE=3 identifies the connecting element as being a rub element, ILEM=3 being connecting element No. 3 joining points 1 (rotor) and 35 (casing). SK=1000000 is the casing ovalization stiffness (lb/in.) with a dead band (radial clearance before hard rub) of 0.350 inch.

The blade-out analysis was conducted in such a manner as to simulate the test vehicle actual speed and decel rate. The restart data file was used from

the linear analysis at 4185 rpm, the speed that the blade was released during the test. The actual decel rate was also simulated. Figures 49 and 50 show the No. 1 bearing load and deflection responses as functions of time; the speed trace is also shown.

The blade-out analysis was also conducted at a steady state of 4200 rpm, with and without the rub element, to demonstrate the difference in transient overshoot. Figure 51, with the rub element activated in the analysis, shows the overshoot clearing after 1/2 cycle. With the rub element eliminated from the input data file (Figure 52), a steady buildup in response occurs and reaches a steady-state response after 10 cycles. It is interesting to note that the rub tends to significantly reduce the amplitude of the response.

#### 4.5 BLADE-OUT ENGINE VAST ANALYSIS

As with the test vehicle, a similar VAST analysis was conducted for the complete turbofan engine to evaluate the TETRA idealization.

The blade-out test was conducted on a turbofan engine mounted in a simulated typical aircraft installation (i.e., inlet, cowling, reverser, and pylon). The engine was a two-spool machine with a high pressure rotor system and a low pressure rotor system. For further discussion of the blade-out engine test see Section 4.8. The blade-out test engine was analyzed using the VAST computer code to predict the system critical speeds and also the subsystem modal data for input into TETRA. The VAST schematic diagram is shown in Figure 53. The VAST model consisted of 26 spans, 15 springs, and a total of 732 degrees of freedom. Five resonances were predicted to be in or near the operating range of the engine (the blade was released at 3366 rpm). They were rigid-body modes at 318 and 737 rpm, a pylon-bending mode at 1506 rpm, and system modes at 2923 and 3761 rpm.

#### 4.6 TETRA ANALYSIS OF THE BLADE-OUT ENGINE

For TETRA, the engine is represented to be two subsystems, the rotor and casing, joined by four connecting elements: the Nos. 1, 2, 6, and 7 bearings. Subsystem 1, the casing subsystem, includes the engine casing, high pressure rotor, and aircraft pylon components. The subsystem was analyzed with the VAST program to predict the natural frequencies and mode shapes of the structure. The VAST model was supported on its own pylon mounts for the analysis. Figure 54 shows a schematic diagram representing this subsystem. A total of 26 resonant frequencies and modes of the casing subsystem were utilized in TETRA; the highest frequency was 24,268 rpm.

Subsystem 2, the low pressure rotor system, was also analyzed with the VAST program to determine the system natural frequencies and mode shapes. This subsystem was treated as a static (nonrotating) component mounted on two very soft springs (100 lb/in.) without gyroscopic effects. The soft springs were used to approximate a free-free system in VAST. A schematic model of this subsystem is shown on Figure 55. Six modes, including two rigid-body and

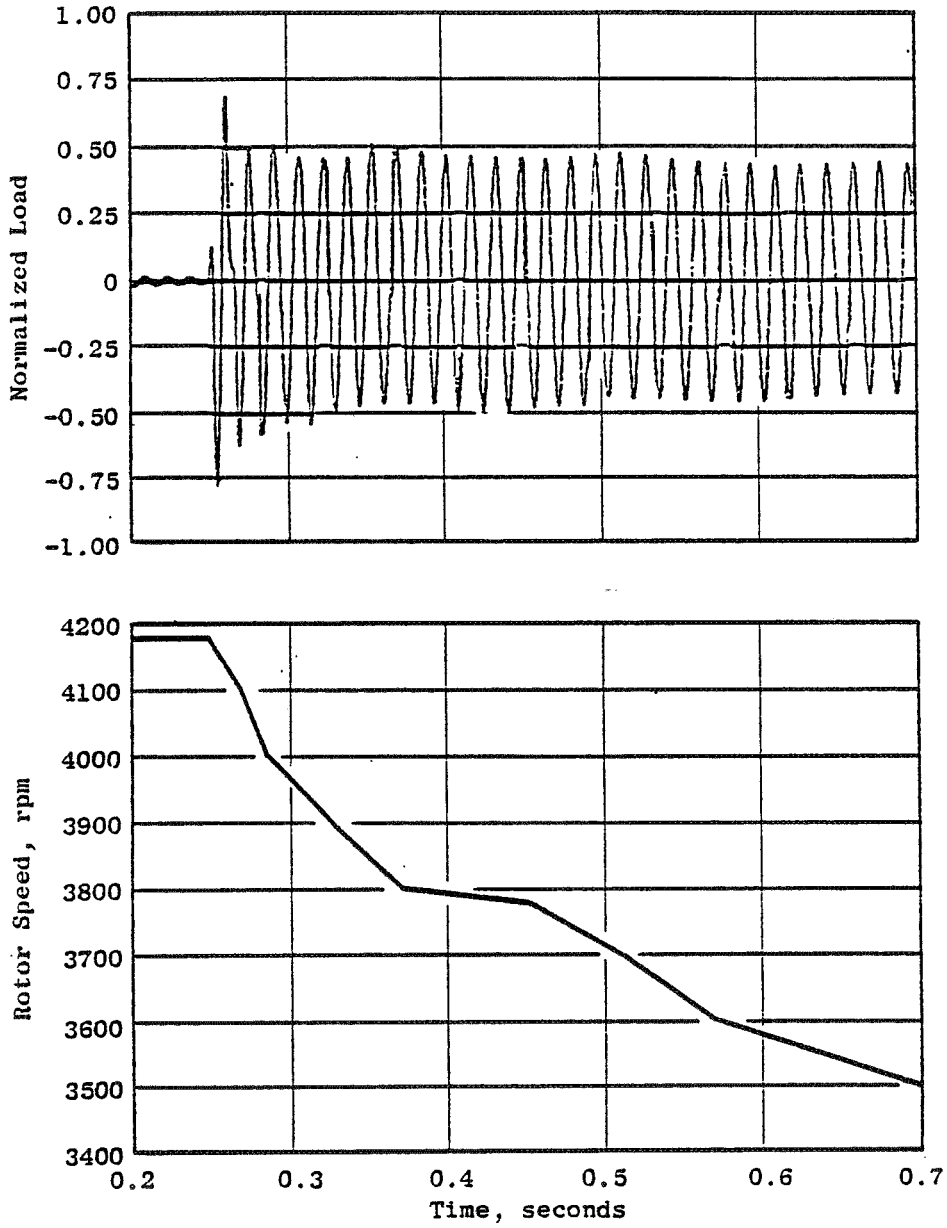


Figure 49. Test Vehicle Blade-Out - TETRA Analysis - No. 1 Bearing Load.



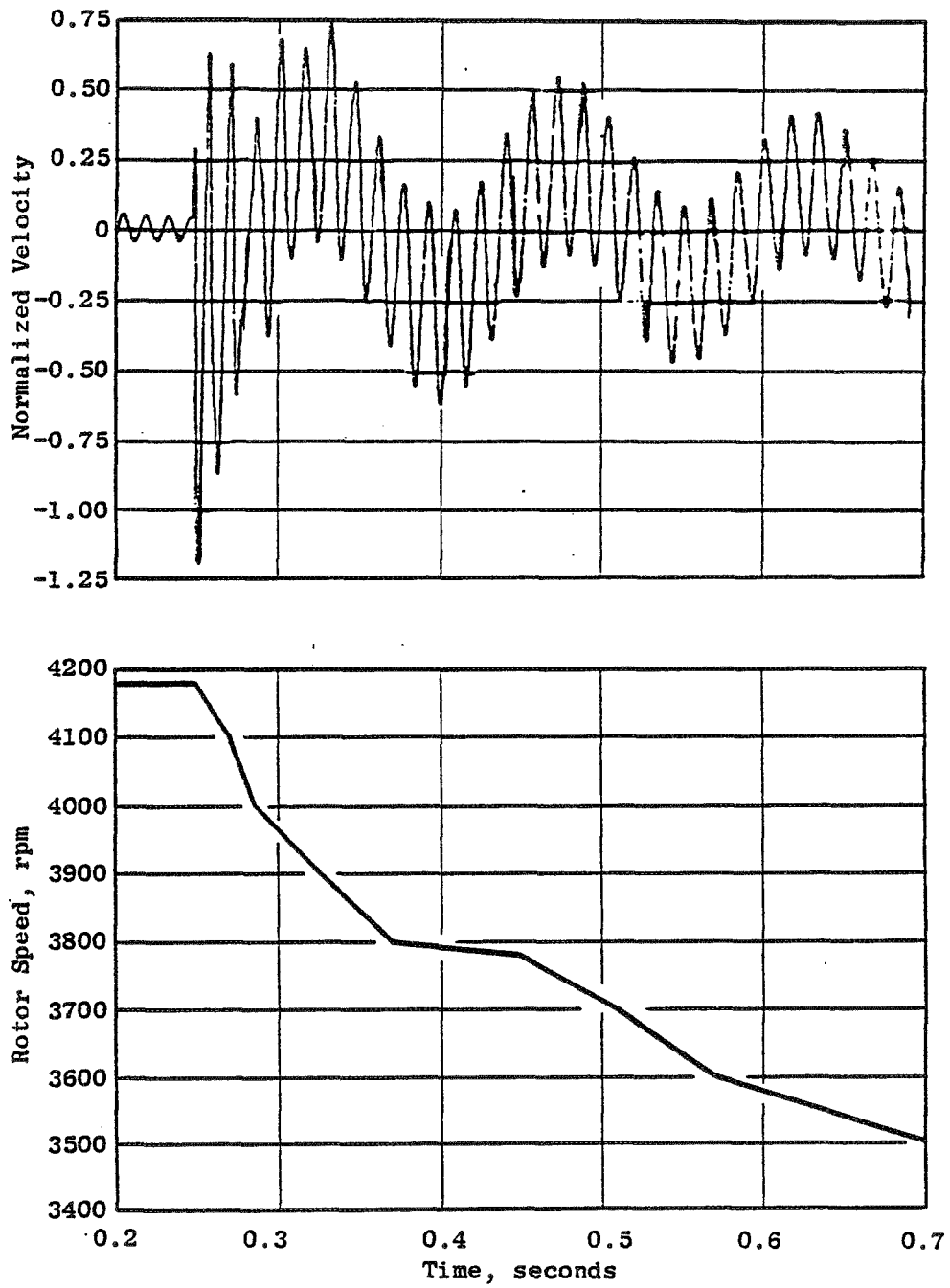


Figure 50. Test Vehicle Blade-Out - TETRA Analysis - No. 1 Bearing Velocity.

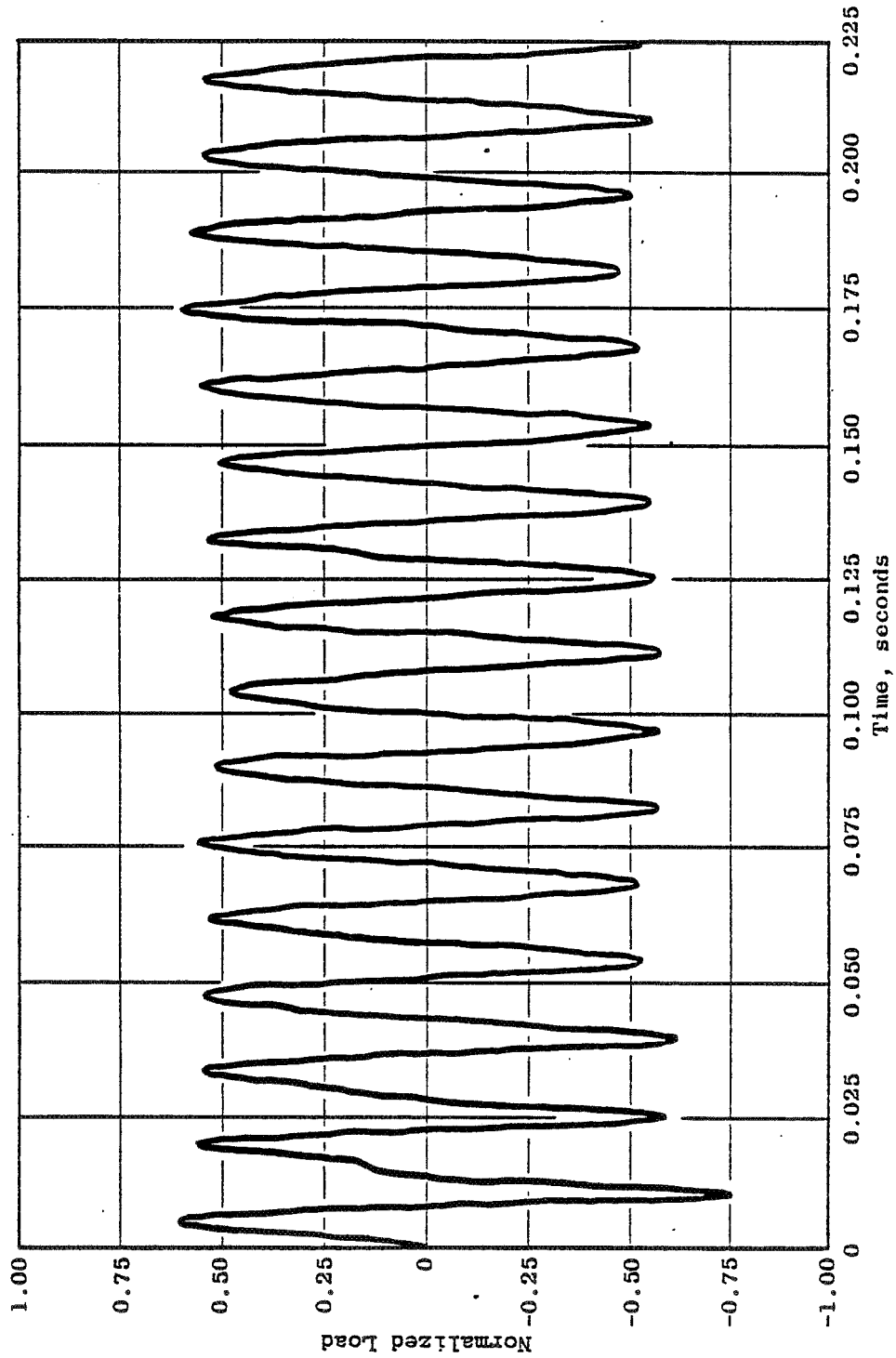


Figure 51. TETRA Test Vehicle Blade-Out Analysis - Rub Element Included - No. 1 Bearing Loads at 4200 rpm.

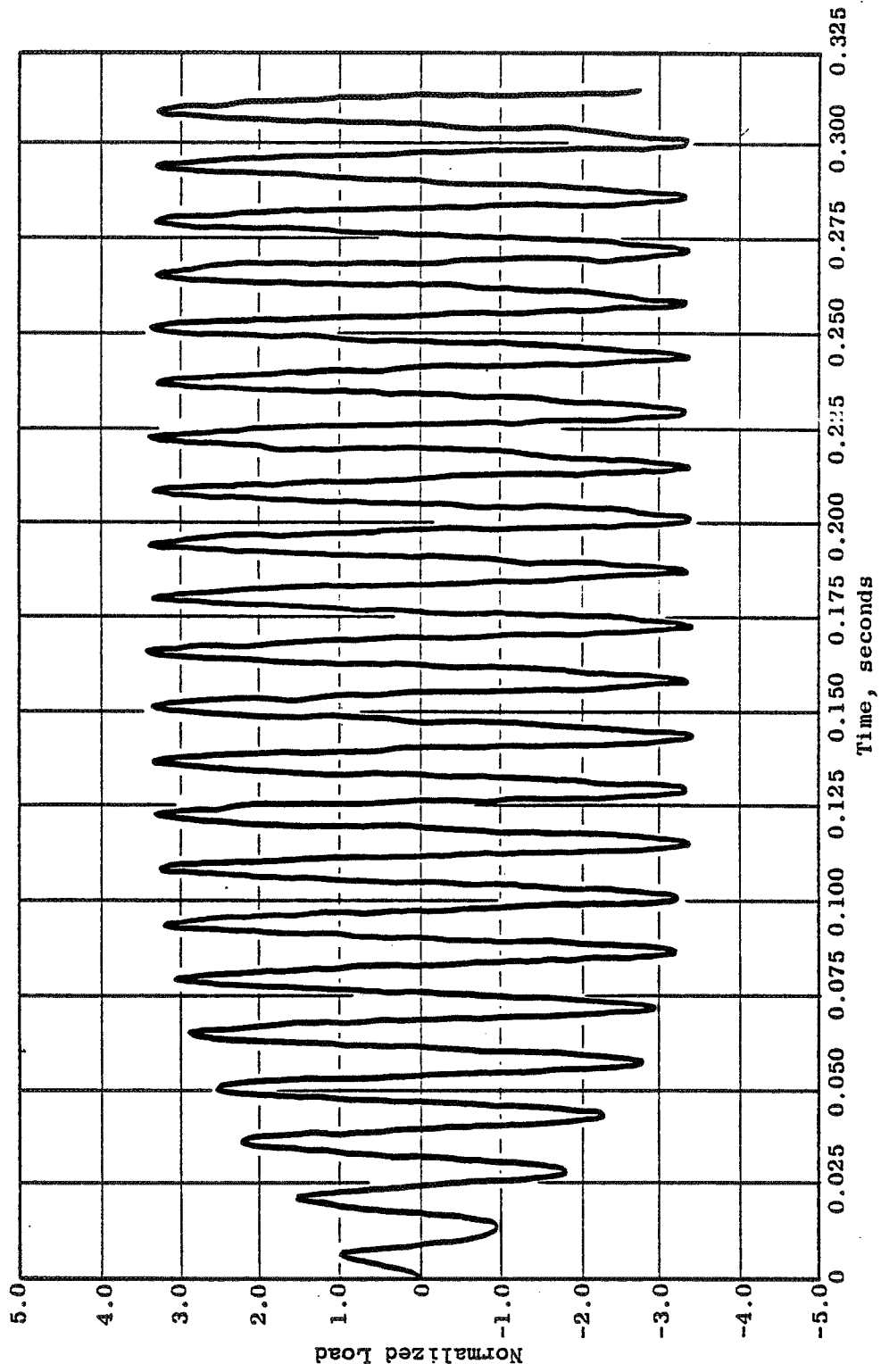


Figure 52. TETRA Test Vehicle Blade-Out Analysis - Rub Element Excluded - No. 1 Bearing Loads at 4200 rpm.

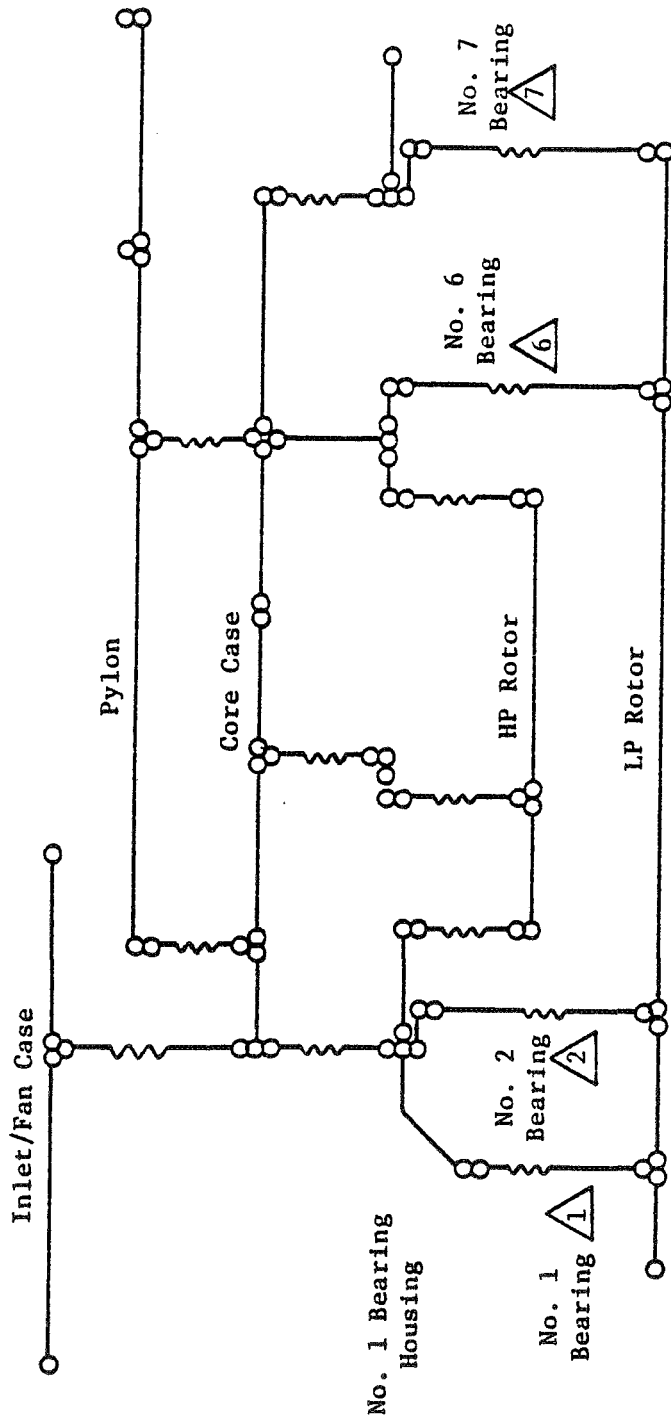


Figure 53. Engine VAST Schematic.

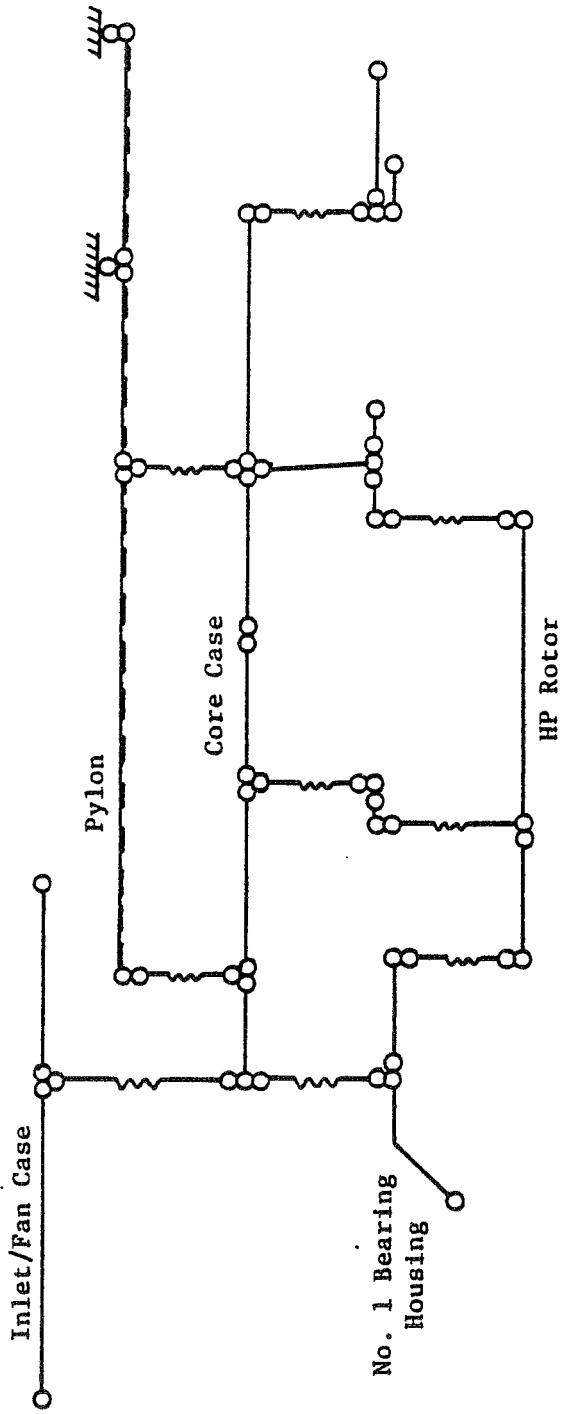


Figure 54. Engine Casing VAST Schematic.

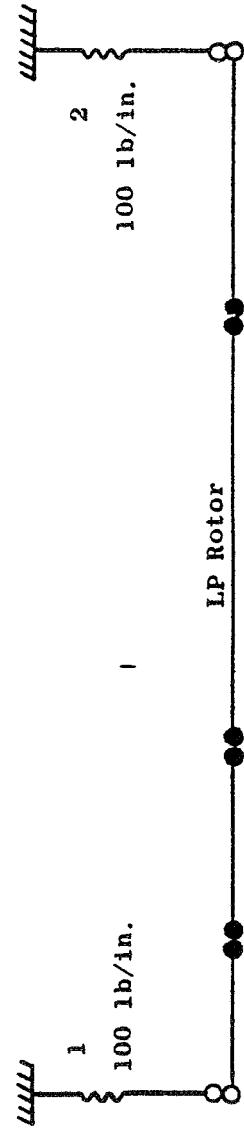


Figure 55. Engine Rotor VAST Schematic.

the first four bending modes, were used in TETRA with the highest frequency being 11,081 rpm. The modal frequencies used in the TETRA analysis for the Subsystems 1 and 2 are summarized below:

Engine Subsystem Modal Frequencies

<u>Subsystem 1</u>		<u>Subsystem 2</u>	
<u>Mode</u>	<u>Frequency, rpm</u>	<u>Mode</u>	<u>Frequency, rpm</u>
1	353	1	55
2	731	2	73
3	1,703	3	972
4	2,978	4	2,421
5	5,110	5	5,627
6	5,370	6	11,081
7	5,655		
8	6,485		
9	6,815		
10	7,076		
11	7,852		
12	8,982		
13	9,644		
14	10,379		
15	11,632		
16	12,665		
17	13,354		
18	15,130		
19	15,469		
20	18,172		
21	18,845		
22	19,480		
23	21,616		
24	22,085		
25	23,181		
26	24,268		

The normalized mode shapes for the engine casing and rotor subsystem are given in Appendix E.

The two subsystems were then joined in TETRA by connecting Elements 1 through 4. The schematic model for the complete TETRA engine is shown in Figure 56. This model was used in TETRA for the moderate fan-unbalance analysis.

As previously noted, TETRA was conducted with 26 casing modes and 6 rotor modes. The maximum frequency used in the casing subsystem was 24,268 rpm. Attempts using fewer casing modes in TETRA resulted in poor frequency and amplitude agreement at the peak response predicted by VAST at 3761 rpm for linear forced vibration response. The six rotor modes utilized, with a maximum frequency of 11,081 rpm, were deemed sufficient to define the subsystem. The current model of 26 casing modes and six rotor modes yields excellent frequency agreement with the VAST predictions. But, like the test vehicle, the

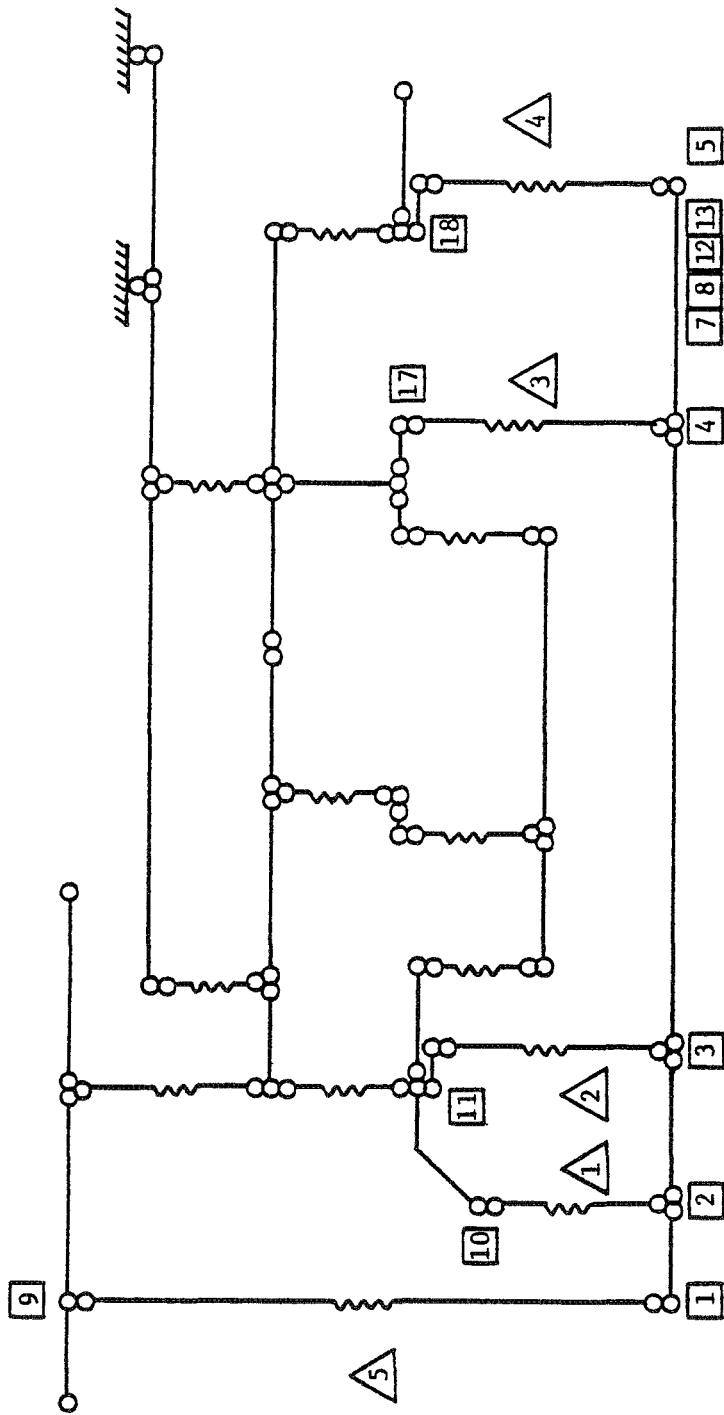


Figure 56. Turbopan Engine TETRA Schematic.

amplitude on the No. 1 bearing loads with  $Q = 15.0$  gave higher amplitude for TETRA compared to the VAST analysis. Similar to the case with the test vehicle, a  $Q$  of 12.5 in TETRA would give excellent amplitude agreement on the No. 1 bearing loads between the two analyses. Again, as was the case on the test vehicle, the change in the  $Q$  value is justified to account for possible modal truncation effects and the cost factors involved with analyzing the engine to higher frequency.

The casing and rotor subsystem modes were entered into TETRA both in the vertical and the horizontal directions. Likewise, the connecting elements were defined with identical vertical and horizontal spring rates.

TETRA was initiated at Time = 0 and terminated at Time = 0.36 to give ample time for the transient overshoot to be observed. The time step was defined as 50  $\mu$ sec. This is a conservative time step and is generated by giving 40 time intervals per cycle of vibration at the highest subsystem frequency mode considered for the analysis. Gyroscopic effects were introduced at five locations: Joints 1, 7, 8, 12, and 13.

The TETRA data file for the linear analysis of the engine is given in Appendix F. List 1 calls in the casing and rotor subsystems from previously created (by VAST) data files. List 2 defines the four connecting elements which tie the two subsystems together. And finally, List 3 is the TETRA command section of the data file.

The steady-state response as a function of speed was determined by running a succession of solutions initiated at discrete rpm's to cover the speed range of interest. Moderate unbalance levels were used to assure a linear (no rub) solution. The resulting time histories at each speed are given in Appendix G. The levels attained after the initial starting transients decayed were used to define the steady-state response as a function of speed. The No. 1 bearing load response as a function of speed is given in Figure 57. The No. 1 bearing housing displacement response as a function of rpm is given in Figure 58.

The TETRA input for the fan blade-out analysis on the engine is similar to the moderate fan unbalance case with one exception: the addition of the rub element. This rub element is defined in the following List 2:

```
200 $
201 $LIST2
202 ITYPE=3
203 ILEM=5,
204 JT=1,9,
205 SK=1000000,
206 DBAND=350,0,
207 CC=0,
208 $
```

The engine blade-out analysis was conducted in such a manner to simulate the actual sequence of the engine test. The restart data file was used from



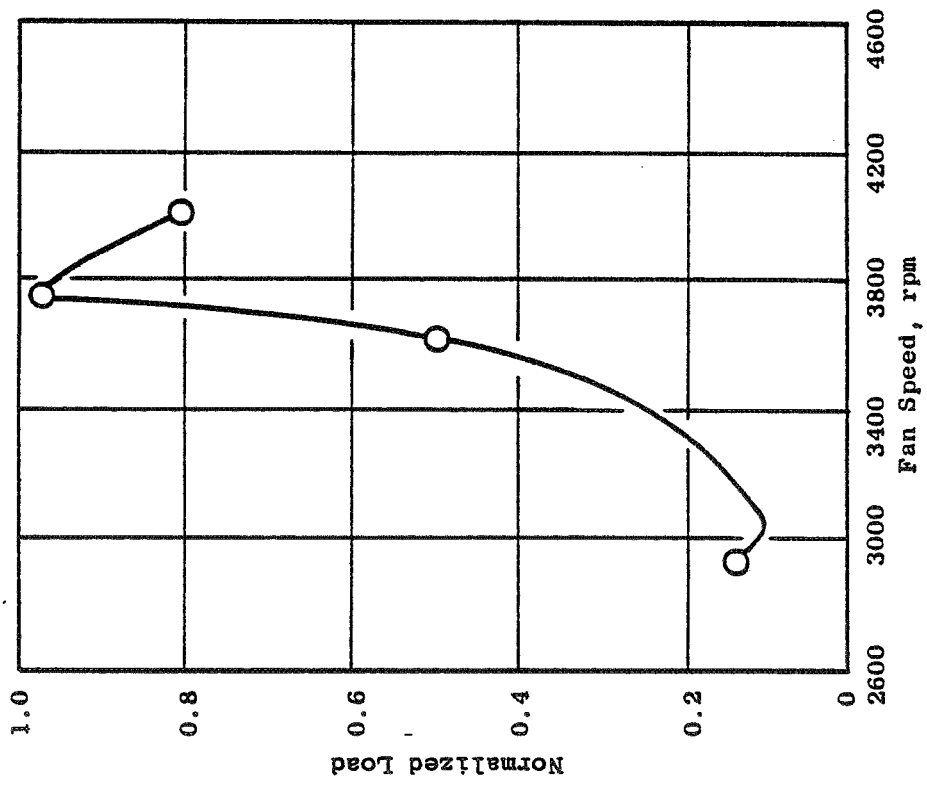


Figure 57. Engine Linear Analysis for Nominal Fan Unbalance - TETRA Results - No. 1 Bearing Load.

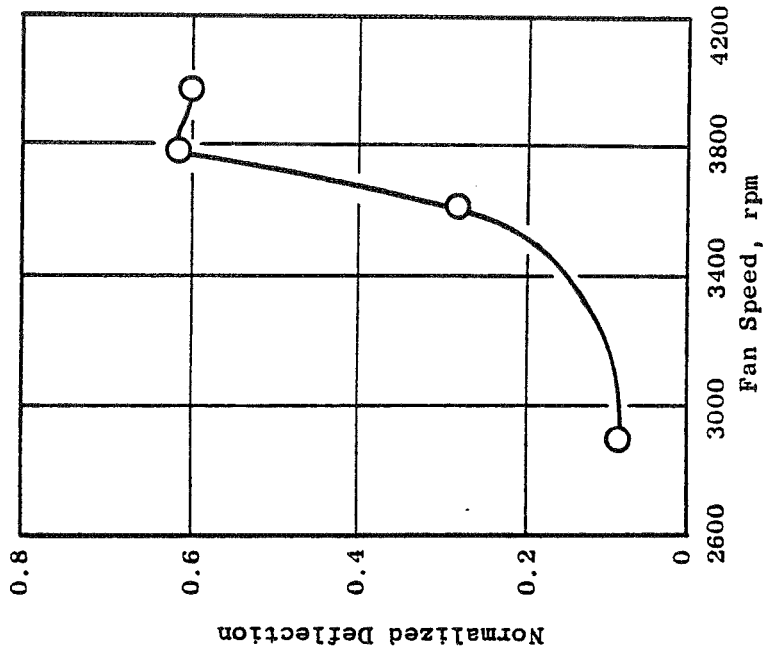


Figure 58. Engine Linear Analysis for Nominal Fan Unbalance - TETRA Results - No. 1 Bearing Deflection.

the linear analysis at 3366 rpm, the speed at which the fan blade was actually released. The engine test decel rate was also utilized. Figures 59 and 60 show the No. 1 bearing load and deflection response as a function of time with the decel rate included.

Figure 59 shows that there was no significant transient load response overshoot predicted by TETRA for the blade-out engine test. Figure 60 shows that TETRA did predict a transient velocity (or displacement) response overshoot. The magnitude of the predicted transient overshoot was approximately 45%. The duration of the transient overshoot was very brief and was essentially over in one cycle.

#### 4.7 BLADE-OUT VEHICLE TEST DESCRIPTION AND RESULTS

The blade-out test vehicle consisted of a fan module from a turbofan engine mounted on soft supports and driven by an electric motor through flexible couplings. The fan module consisted of the fan rotor and shaft, the fan frame, the fan casing, and the No. 1 and No. 2 bearing supports and bearings. The fan module was mounted on a heavy facility support plate mounted from soft elastomeric shock mounts and spring hangers. The spring hangers were very soft dynamically and were used primarily for vehicle alignment. Except for the spring hangers, the vehicle was totally axisymmetric. The front of the fan case was attached with a rubber boot to a larger belljar. The entire vehicle and belljar were filled with helium in order to reduce the horsepower required to reach the desired rotor speed.

The instrumentation used during the blade-out vehicle rig test consisted of four No. 1 bearing strain gages and No. 1 bearing vertical and horizontal accelerometers. Figure 61 shows the installation of the instrumentation. The strain gages were mounted on the bearing outer race in the hoop direction so as to read dynamic load due to the rotating force vector. The four gages were 90° apart. All of the data were recorded on magnetic tape for future data analysis. The test was conducted in two steps. The first step was a mechanical checkout of the vehicle up to maximum speed, 4185 rpm, including trim balancing the fan rotor, and the second step was the actual bladeout test. Figure 62 shows the No. 1 bearing load during the mechanical checkout, and Figure 63 shows the No. 1 bearing displacement response during the same run. The results show that the rotor passes through a response peak at approximately 4000 rpm. The VAST analysis predicts this peak to be at 4043 rpm. The comparison of test and VAST predicted bearing load given in Figure 64 shows generally reasonable agreement, particularly near the resonance.

The blade-release mechanism for the fan blade-out test was an explosive charge installed in a hole drilled through the root of a single blade just above the dovetail. The explosive charge was detonated while running at a stabilized speed of 4185 rpm. As soon as the blade was released, the electric motor was deenergized, and the rotor coasted down. Figure 65 shows the rpm of the rotor as a function of time during the coastdown. All significant unbalance (released blade plus secondary damage) occurred within 1/4 of a revolution. Figure 66 shows the raw signals from two of the No. 1 bearing strain

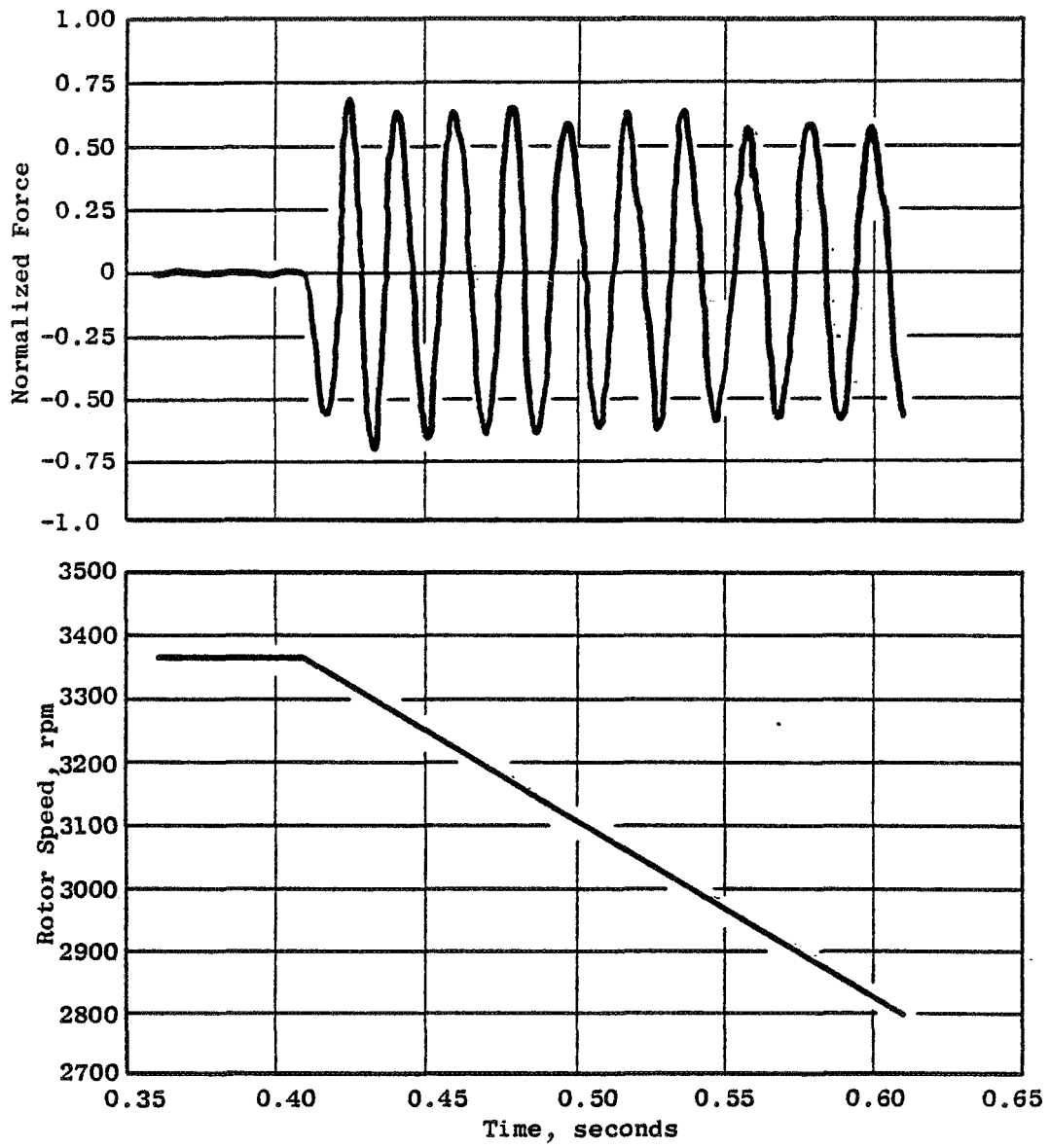


Figure 59. TETRA Engine Blade-Out Analysis - No. 1 Bearing Load.

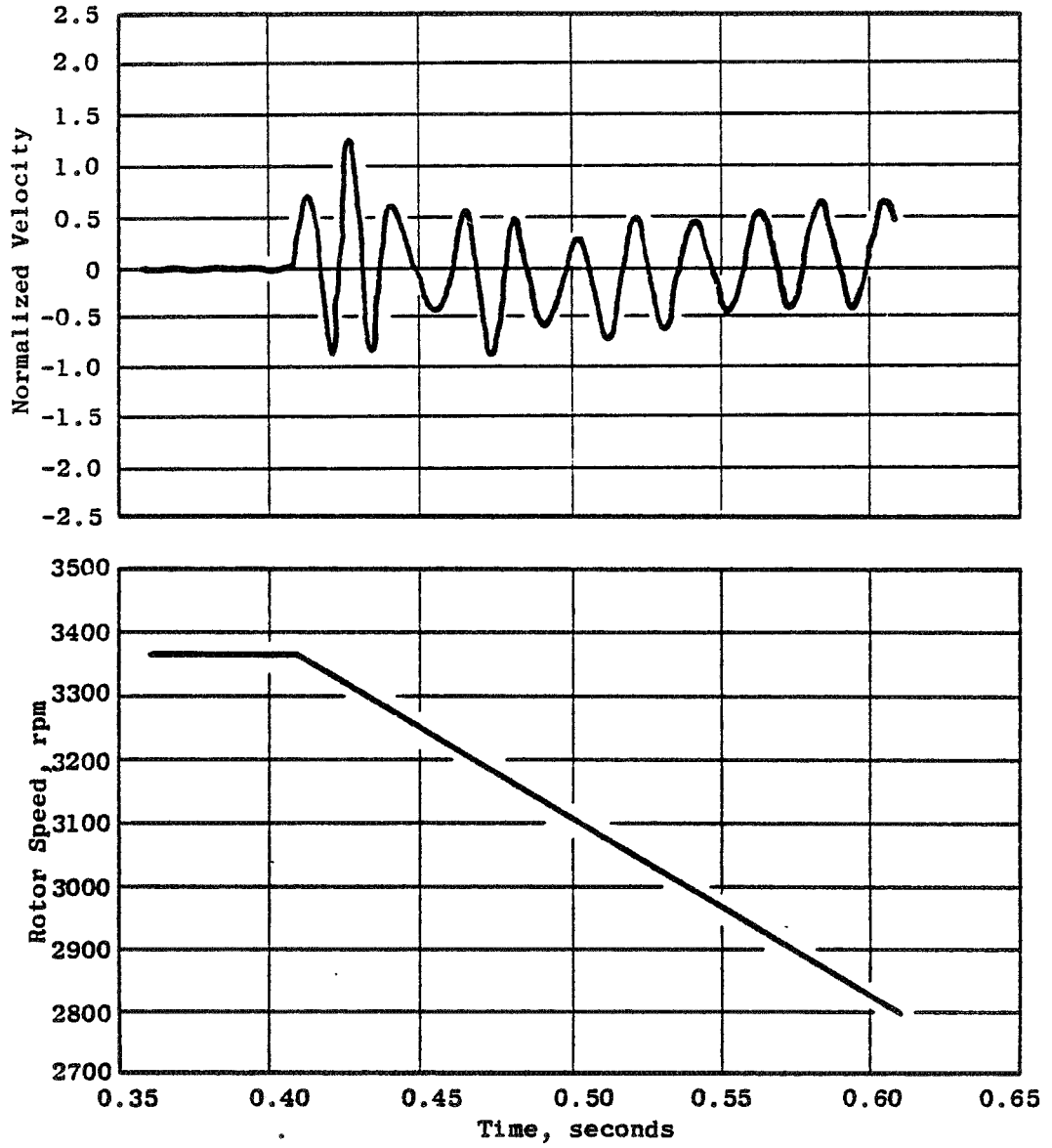


Figure 60. TETRA Engine Blade-Out Analysis - No. 1 Bearing Velocity.

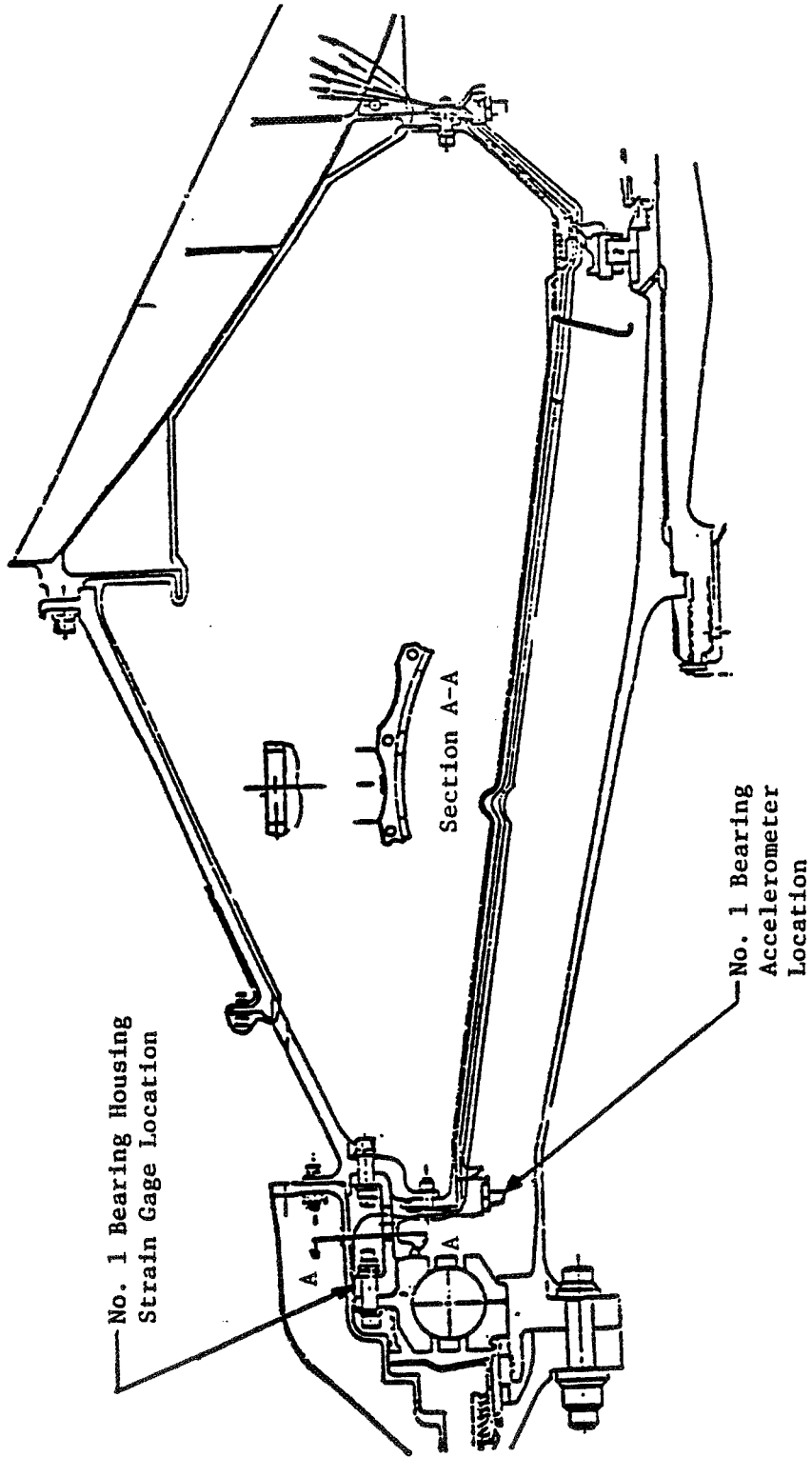


Figure 61. Blade-Out Test Vehicle Instrumentation.

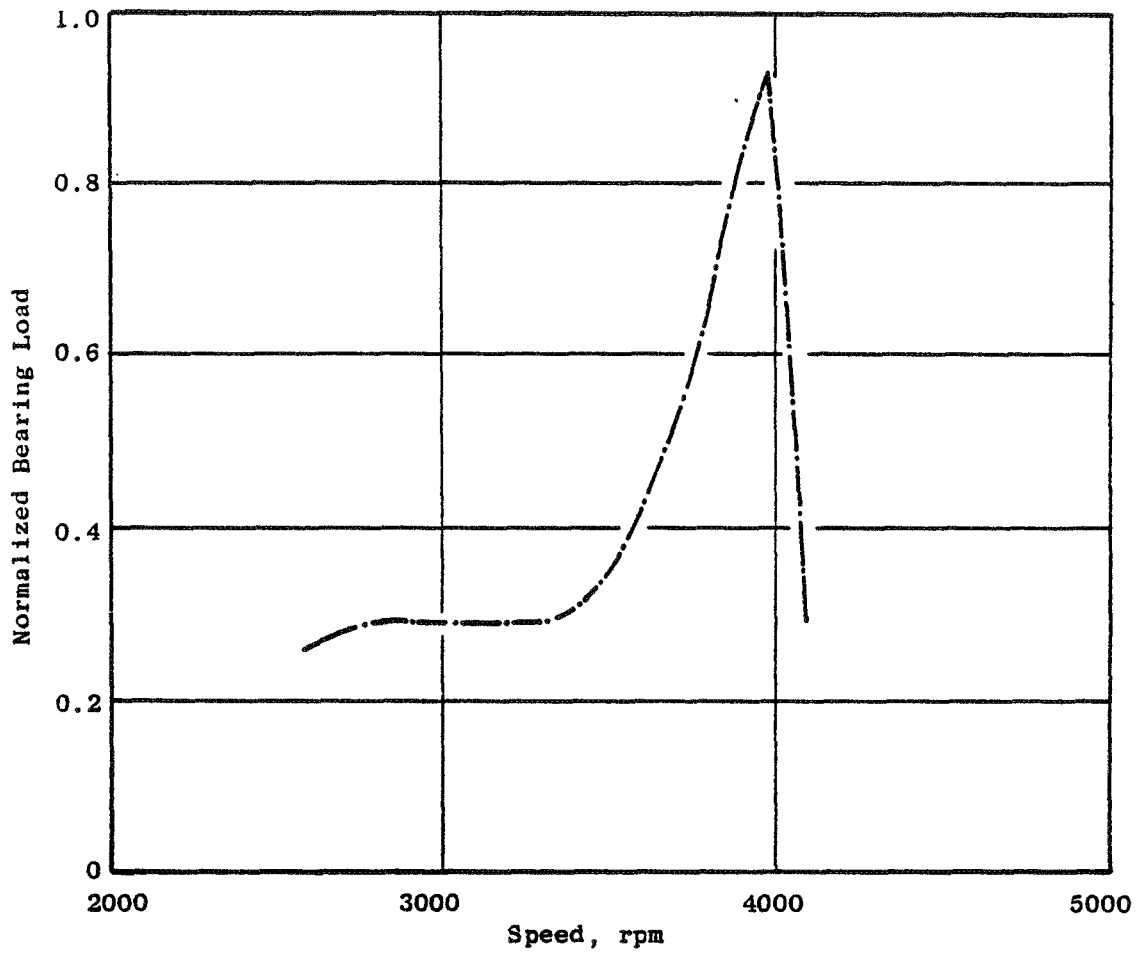


Figure 62. Blade-Out Test Vehicle - No. 1 Bearing Load.

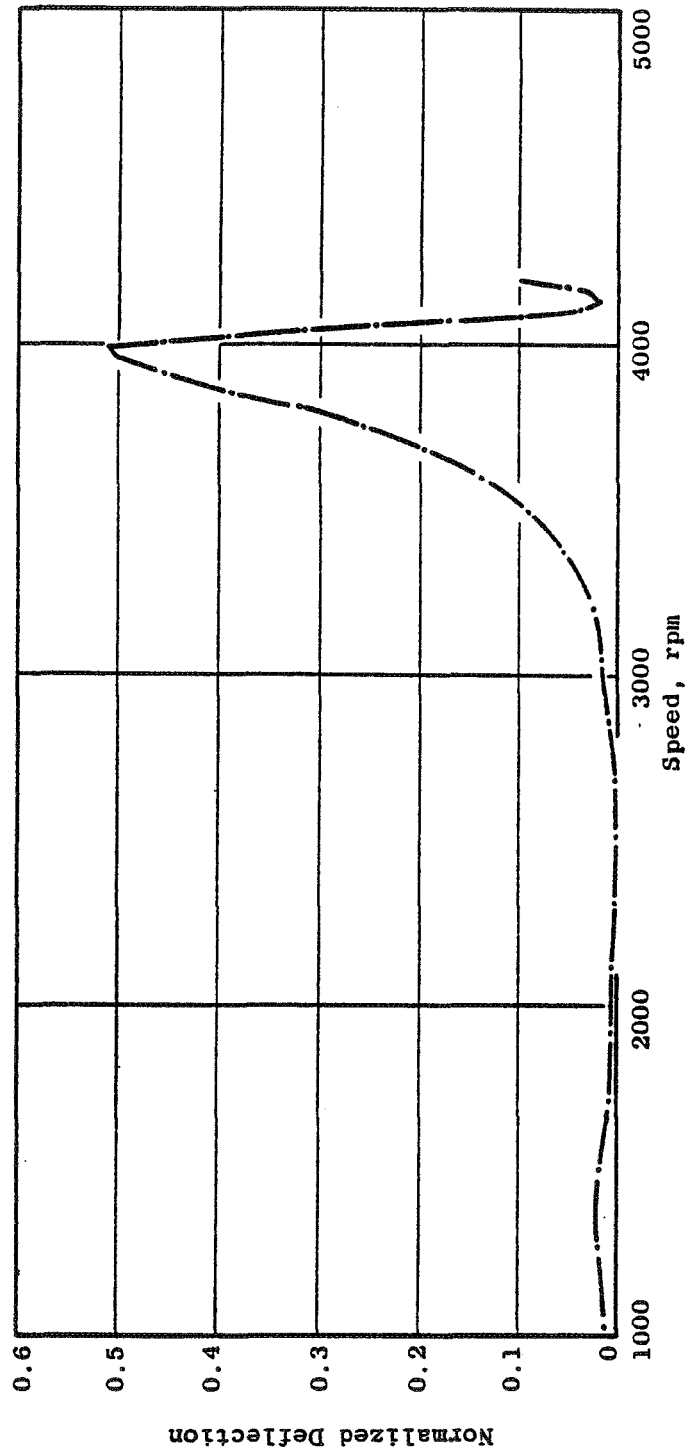


Figure 63. Blade-Out Test Vehicle - No.1 Bearing Deflections.

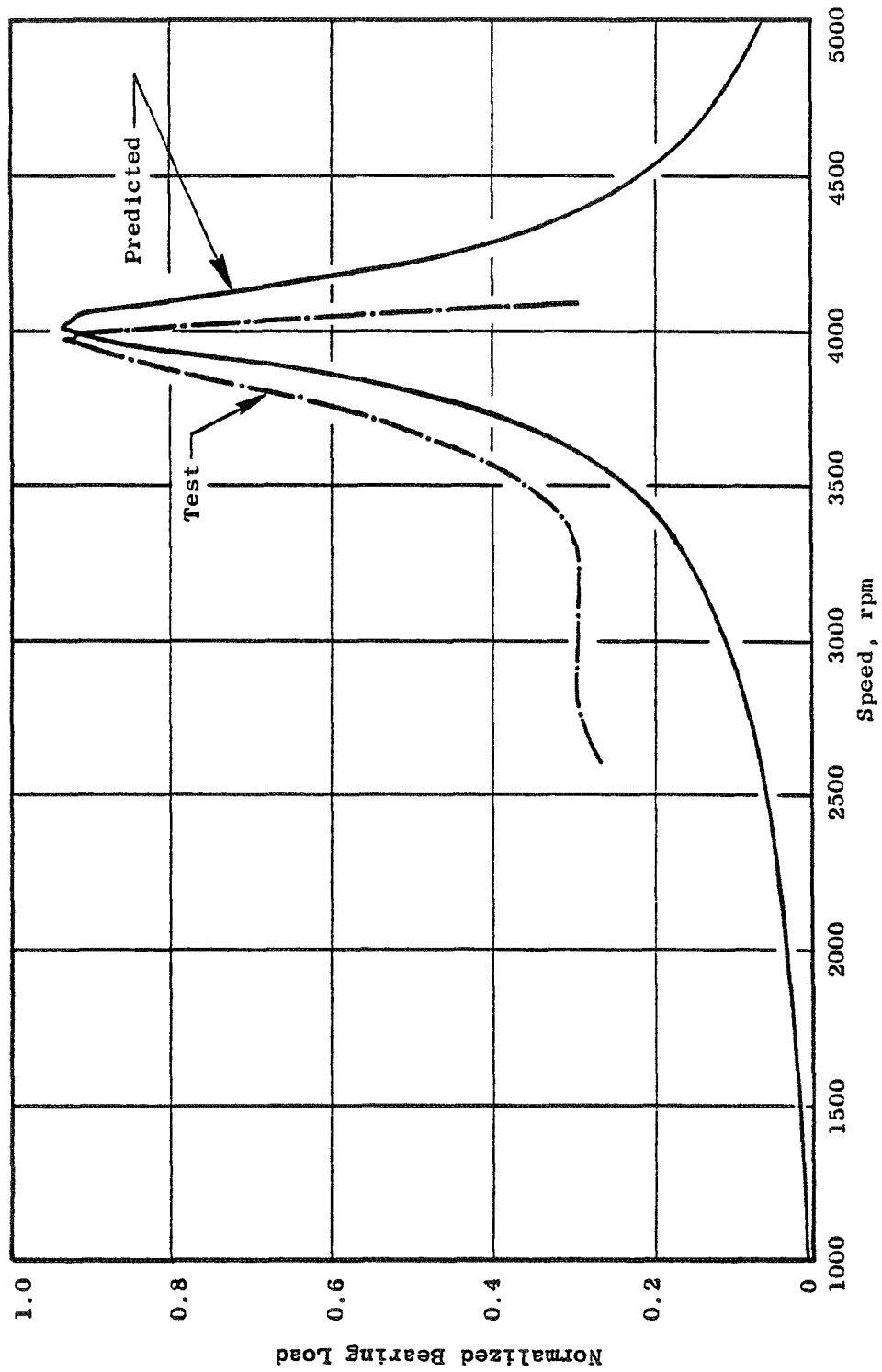


Figure 64. Blade-Out Test Vehicle - Test Versus Predicted No. 1 Bearing Load Linear Pressure for Nominal Unbalance.



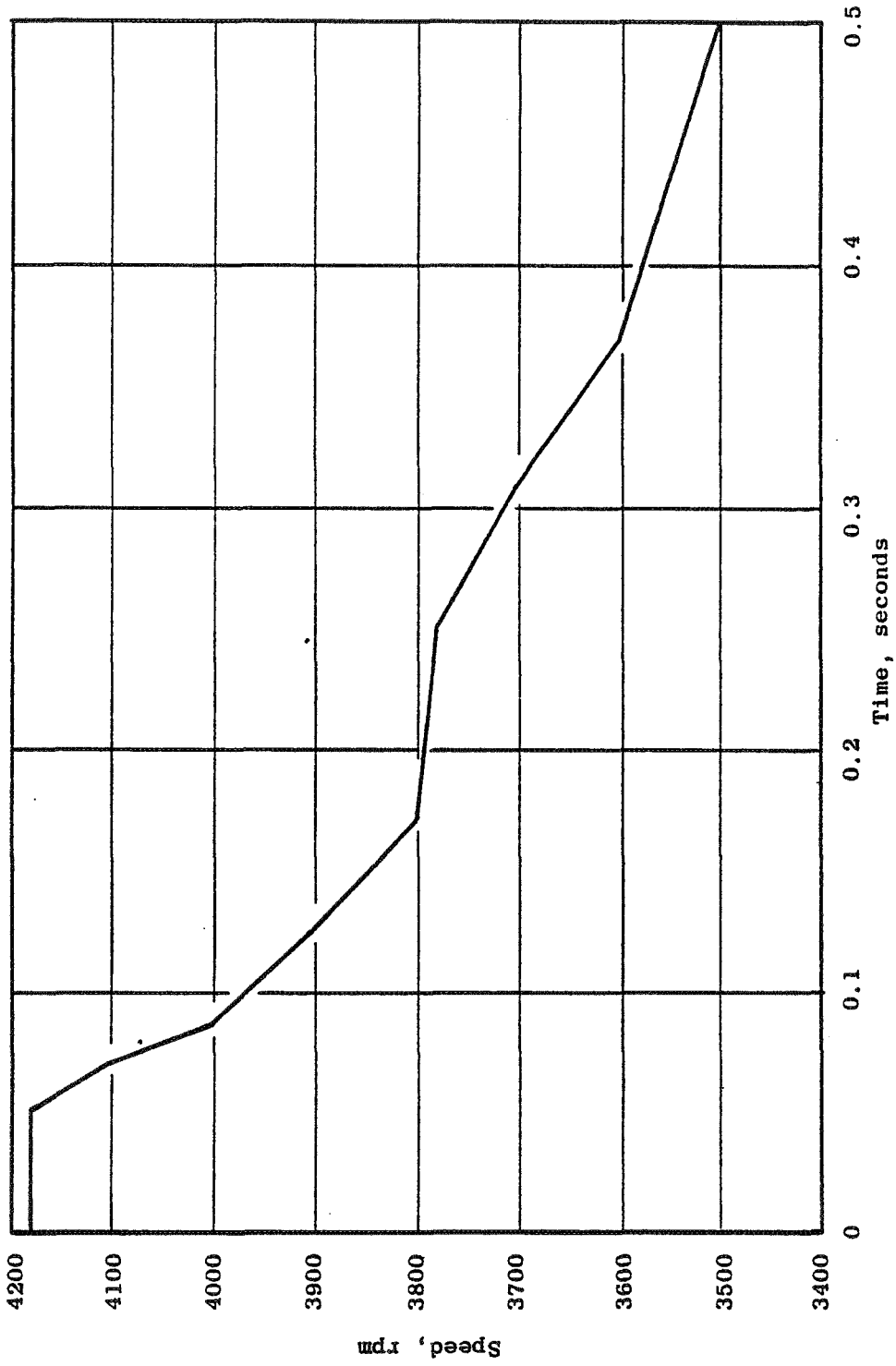


Figure 65. Blade-Out Test Vehicle Decel Time History.

Blade Release

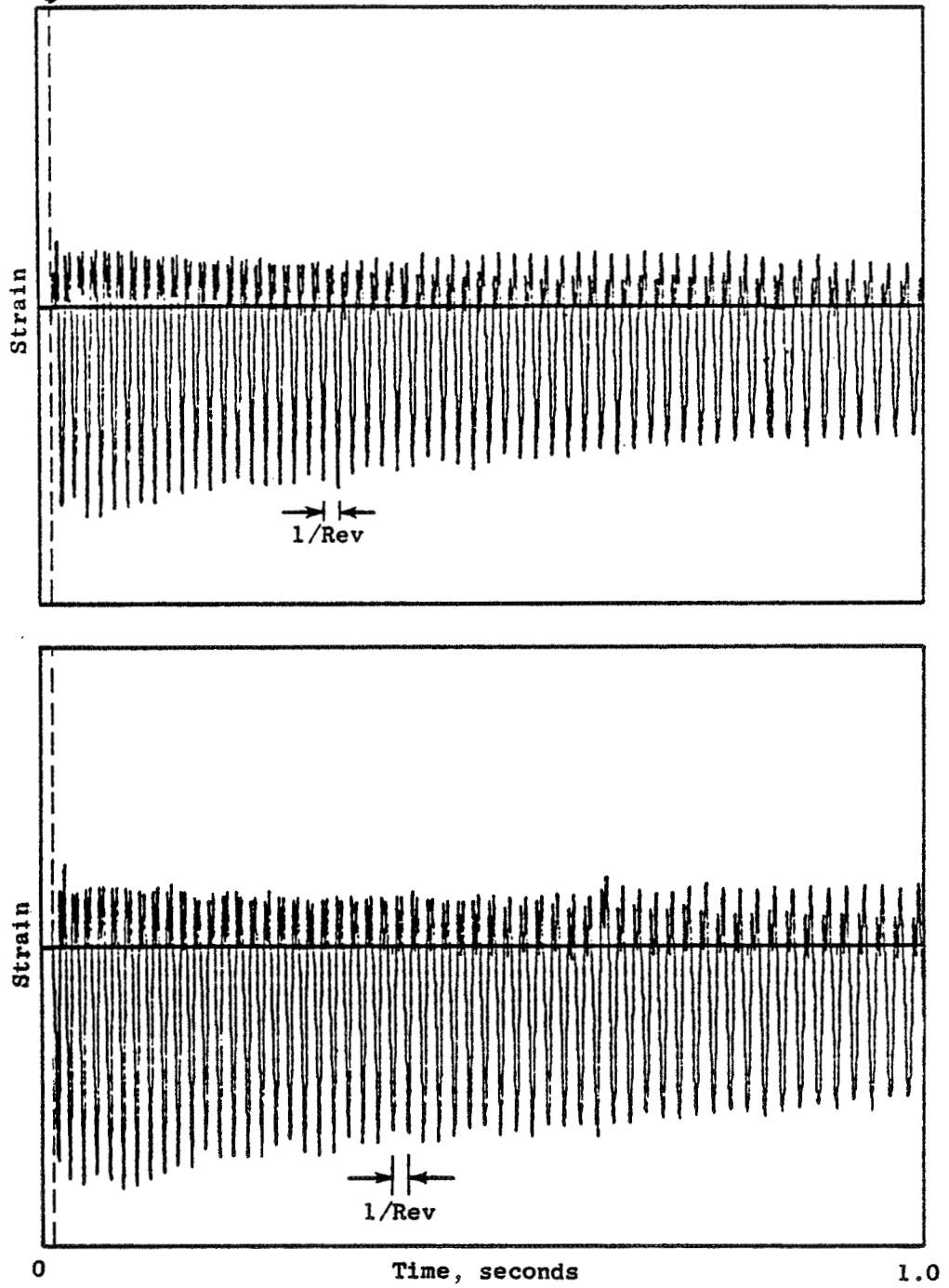


Figure 66. Blade-Out Test Vehicle - No. 1 Bearing Housing  
153° and 330° Strain Gages.

gages 180° apart. Since the gages are measuring hoop strain, they only measure an appreciable strain when the load vector is in the direction of the gage. When the load vector rotates 180°, there is little compressive strain on the gage; therefore, the raw strain signal is asymmetric. In order to obtain the true bearing load signal, the high-speed digitizing capability of the fast Fourier transform analyzer was used to digitize the data from the two gages at 153° and 333°, change the strain to load by applying the nonlinear calibration curve, reconstituting the full load versus time signal by changing the sign of the 333° strain gage signal, and then combining the two tension portions of the two signals. The resulting true load versus time response signature is given in Figure 67. Figure 68 shows the same data with an expanded time scale and the first six cycles of response data. As can be seen from the data, there was very little, if any, transient overshoot following the blade release. Figure 69 shows the No. 1 bearing response (velocity) following the blade release. Figure 70 shows the same response with an expanded time scale.

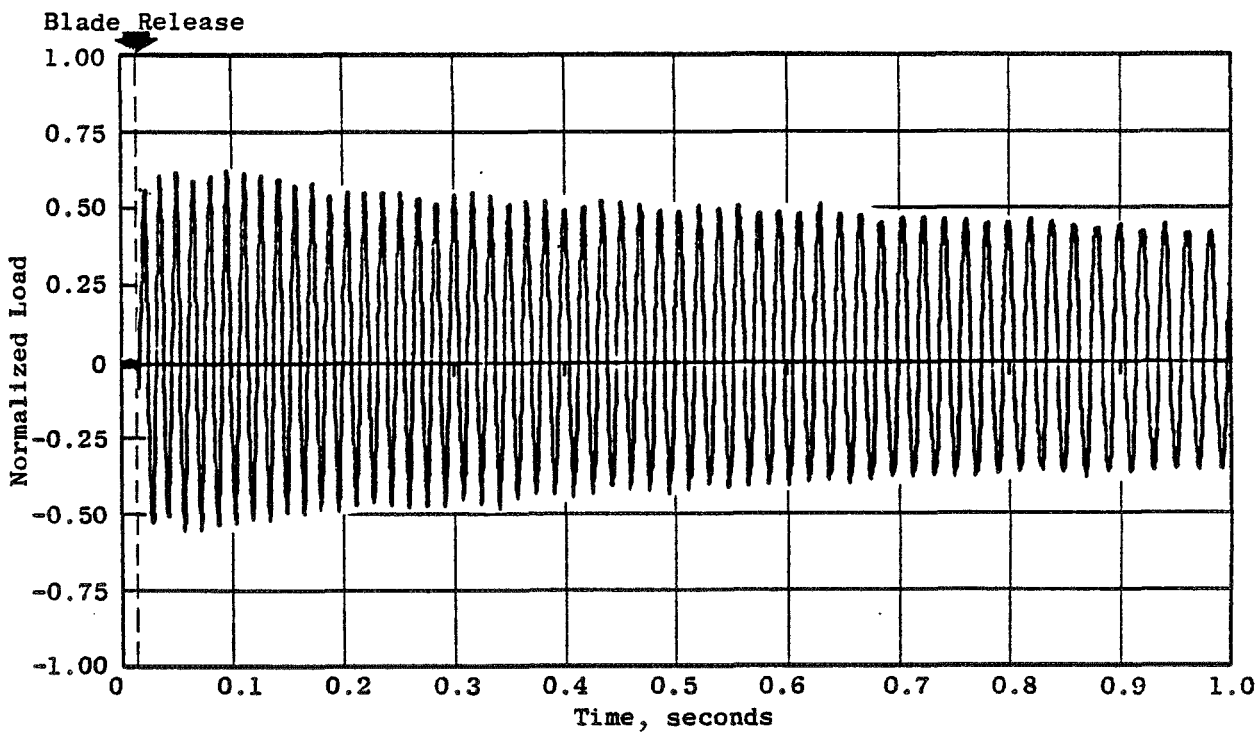


Figure 67. Blade-Out Test Vehicle - Reconstituted No. 1 Bearing Housing Load Generated from 153° and 330° Strain Gages.

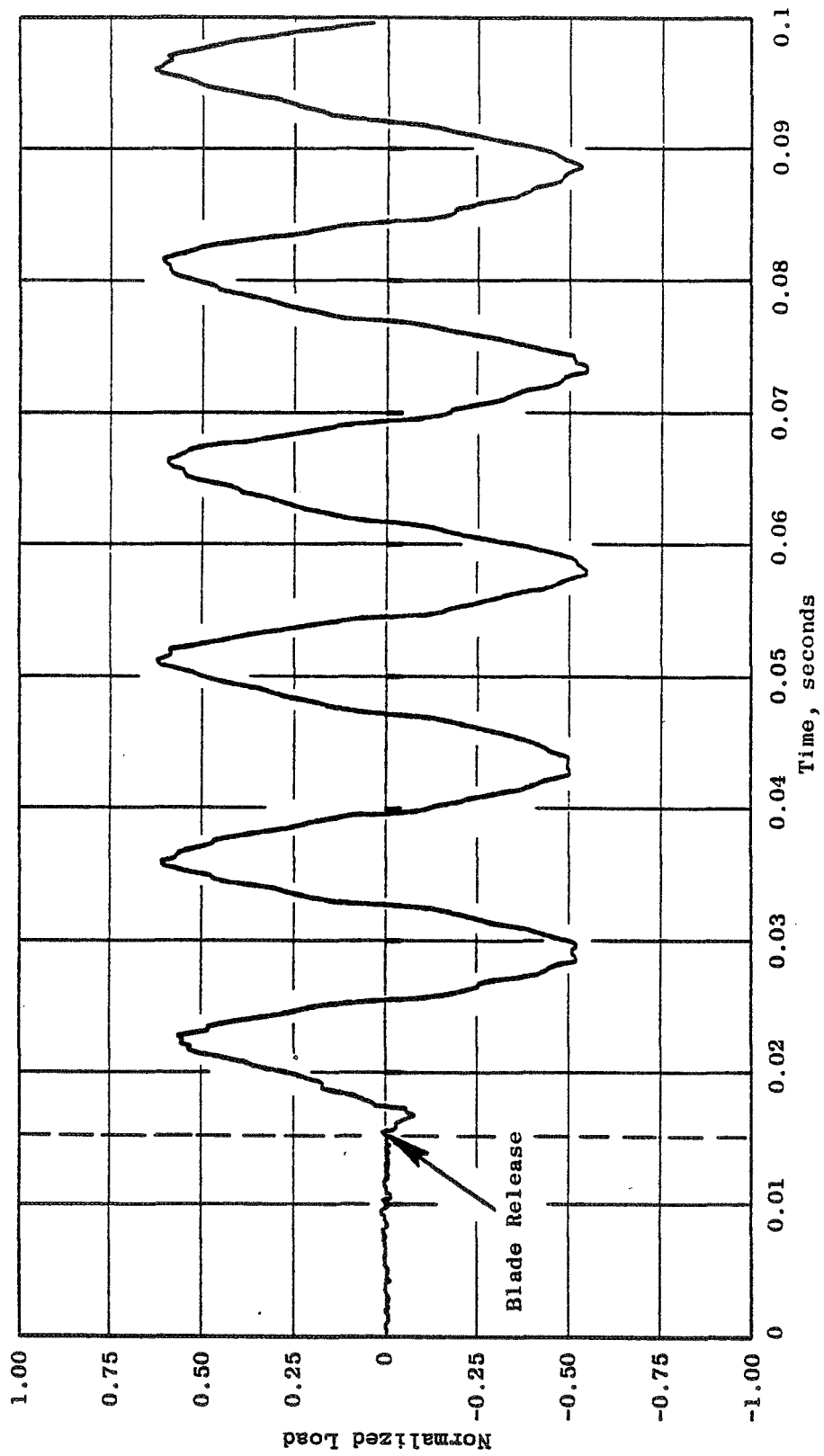


Figure 68. Blade-Out Test Vehicle - Reconstituted No. 1 Bearing Housing Load Generated from 153° and 333° Strain Gages (Expanded).

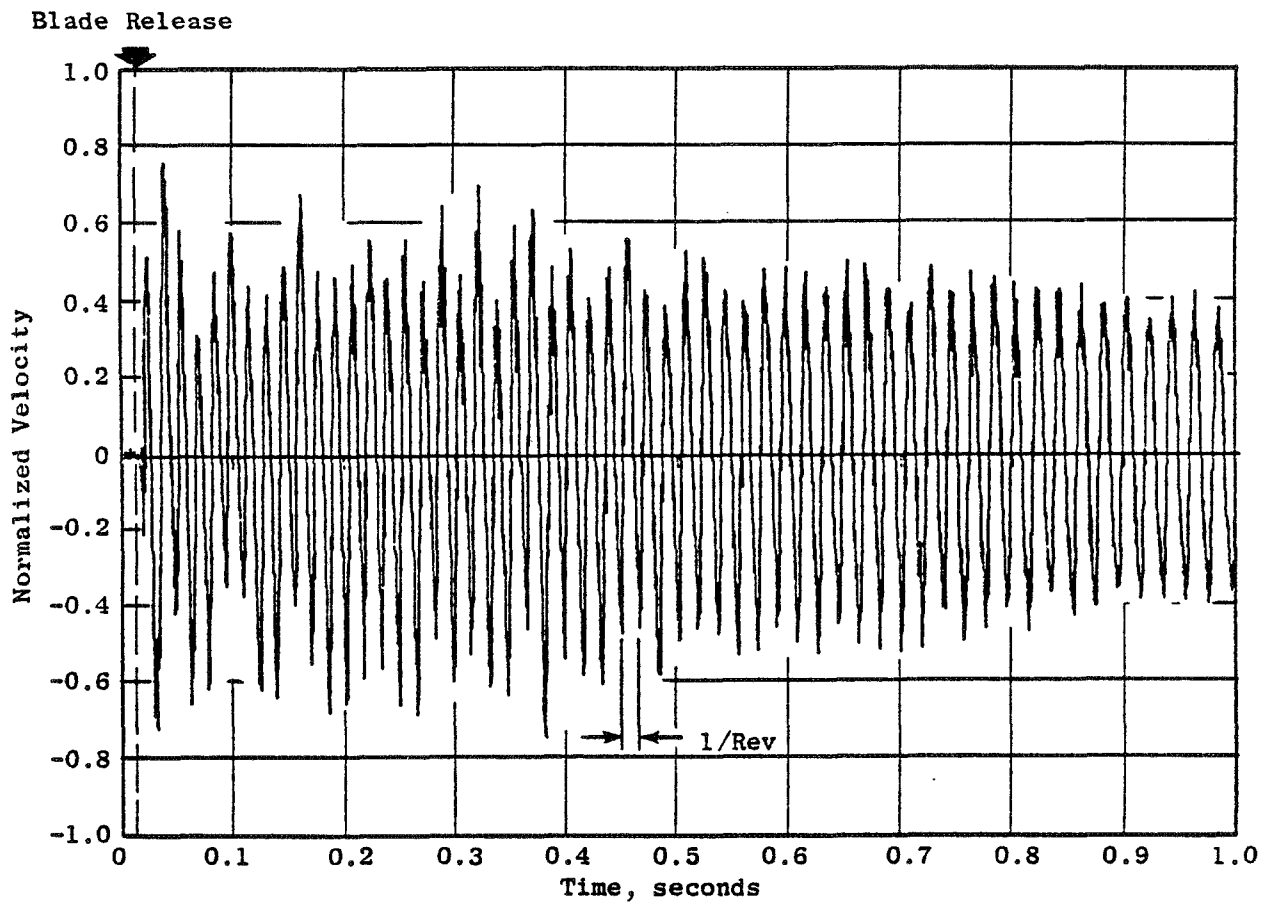


Figure 69. Blade-Out Test Vehicle - No. 1 Bearing Response.

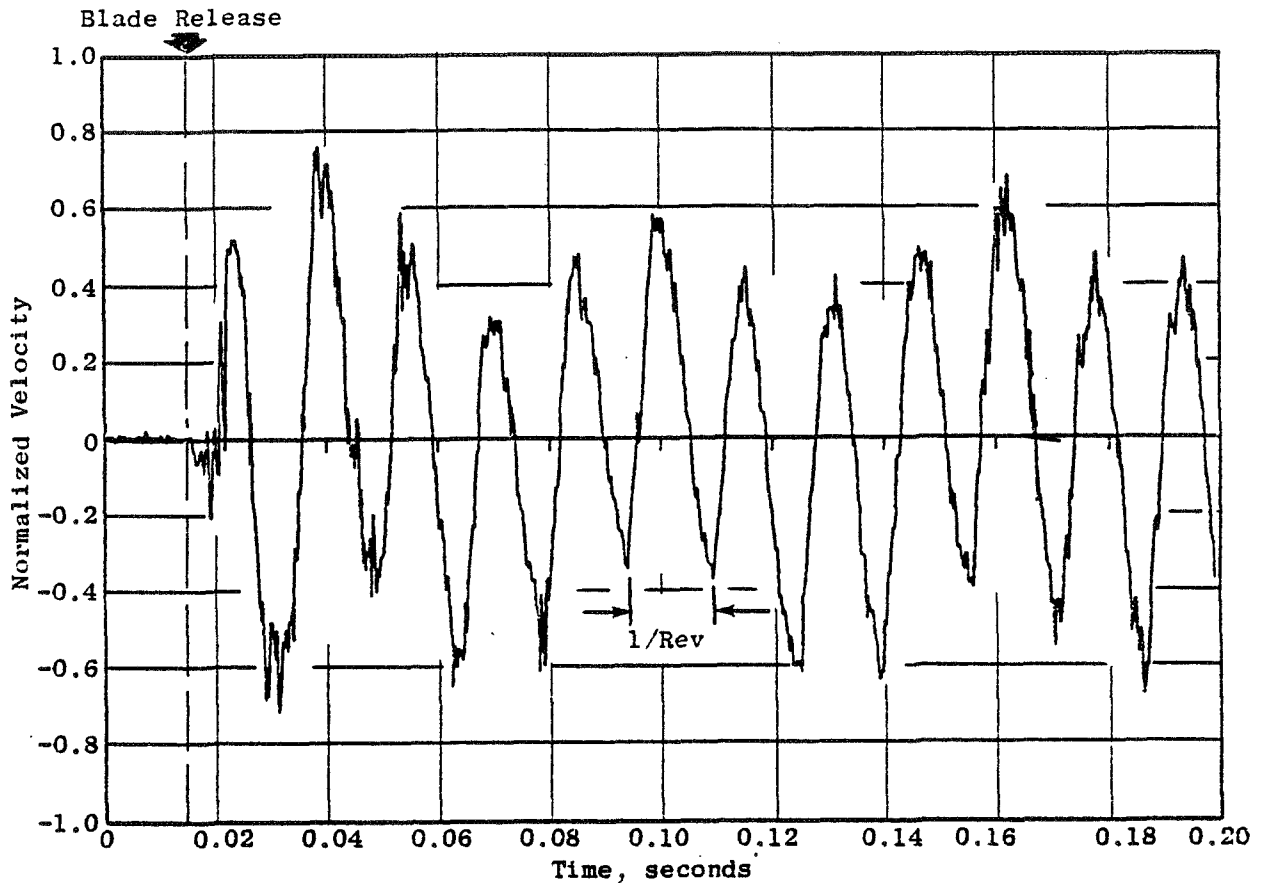


Figure 70. Blade-Out Test Vehicle - No. 1 Bearing Response (Expanded).

#### 4.8 BLADE-OUT ENGINE TEST DESCRIPTION AND RESULTS

The blade-out engine test was conducted on an operating turbofan engine. The test was conducted at the General Electric off-site Peebles Test Operation. The engine was mounted in an aircraft pylon and included the inlet, cowl, and thrust reverser. The intent of the test was to release portions of two fan blades, separated circumferentially by  $39^\circ$ , so that the vector sum of the unbalance was equal to the loss of a single blade. The blade-release mechanisms were two explosive carriers bolted to the blades at approximately mid-span. The two explosive charges were wired to the same detonator circuit so that the blades were released simultaneously. High-speed motion pictures verified that the two blades were released simultaneously.

The primary instrumentation for the blade-out engine test was the accelerometers and strain gages on the No. 1 bearing housing. This instrumentation was similar to that used during the blade-out rig test (Figure 61). All of the vibration and strain signals were recorded on magnetic tape for posttest analysis.

The blades were released at an engine speed of 3366 rpm. Figure 71 shows engine rpm as a function of time following the blade release. Figures 72 and 73 show the raw strain gage signals following the blade release. These signals were reconstituted in the same manner as the rig test bearing strain to give the true bearing load signature (Figure 74). As with the vehicle test, transient overshoot after the blade release is small, although a little larger on the engine. The No. 1 bearing velocity-response signature is given in Figures 75 and 76. The displacement response shows a possible small transient overshoot followed by a gradual decrease in response as rpm drops.

#### 4.9 COMPARISON OF TETRA RESULTS FOR THE BLADE-OUT VEHICLE WITH LINEAR ANALYSIS AND TEST

The blade-out test vehicle was analyzed using TETRA for two different conditions, i.e., linear with moderate unbalance and nonlinear with high unbalance (loss of a fan blade). The linear analysis results will be compared with the VAST linear predictions, and the nonlinear results will be compared to the blade-out test results.

The linear VAST analysis conducted on the test vehicle was summarized in Section 4.3. From this analysis, plots of the No. 1 bearing loads and deflections as a function of speed were generated for a nominal fan unbalance. The TETRA results for this same unbalance were summarized in Section 4.4. This analysis considered six different steady-state speed conditions compared with the VAST results. As noted in Section 4.4, the Q factor for the TETRA results was adjusted slightly from 15.0 (the VAST Q) to 12.5 in order to yield similar No. 1 bearing loads.

The results of this comparison of No. 1 bearing normalized loads and deflections are shown in Figures 77 and 78, respectively. The No. 1 bearing loads, although slightly modified to account for modal truncation, show excellent agreement for both frequency and amplitude of the response. The No. 1 bearing deflections show good frequency agreement and a 25% lower response for TETRA. Both of these comparisons are made for points on the casing subsystem. Figure 79 shows a comparison for the rotor deflections at the fan-stage centerline. Again, the frequency response between the two analyses are similar; the TETRA amplitude is slightly lower than the VAST predictions (7%).

Figure 80 is a comparison of the No. 1 bearing transient load signature, following the blade release, for both the predicted response (i.e., TETRA results) and the experimental data. The TETRA analysis predicts a transient overshoot followed by a near-constant-amplitude response. The test data do not show a No. 1 bearing transient load overshoot but instead show a gradual increase in response over several cycles and then a slow decrease as speed falls off (Figure 49) for the speed decay time).

Figure 81 compares the No. 1 bearing normalized deflection transient response signatures following blade release. The TETRA predicted synchronous 1/rev deflections are approximately the same on the measured response during

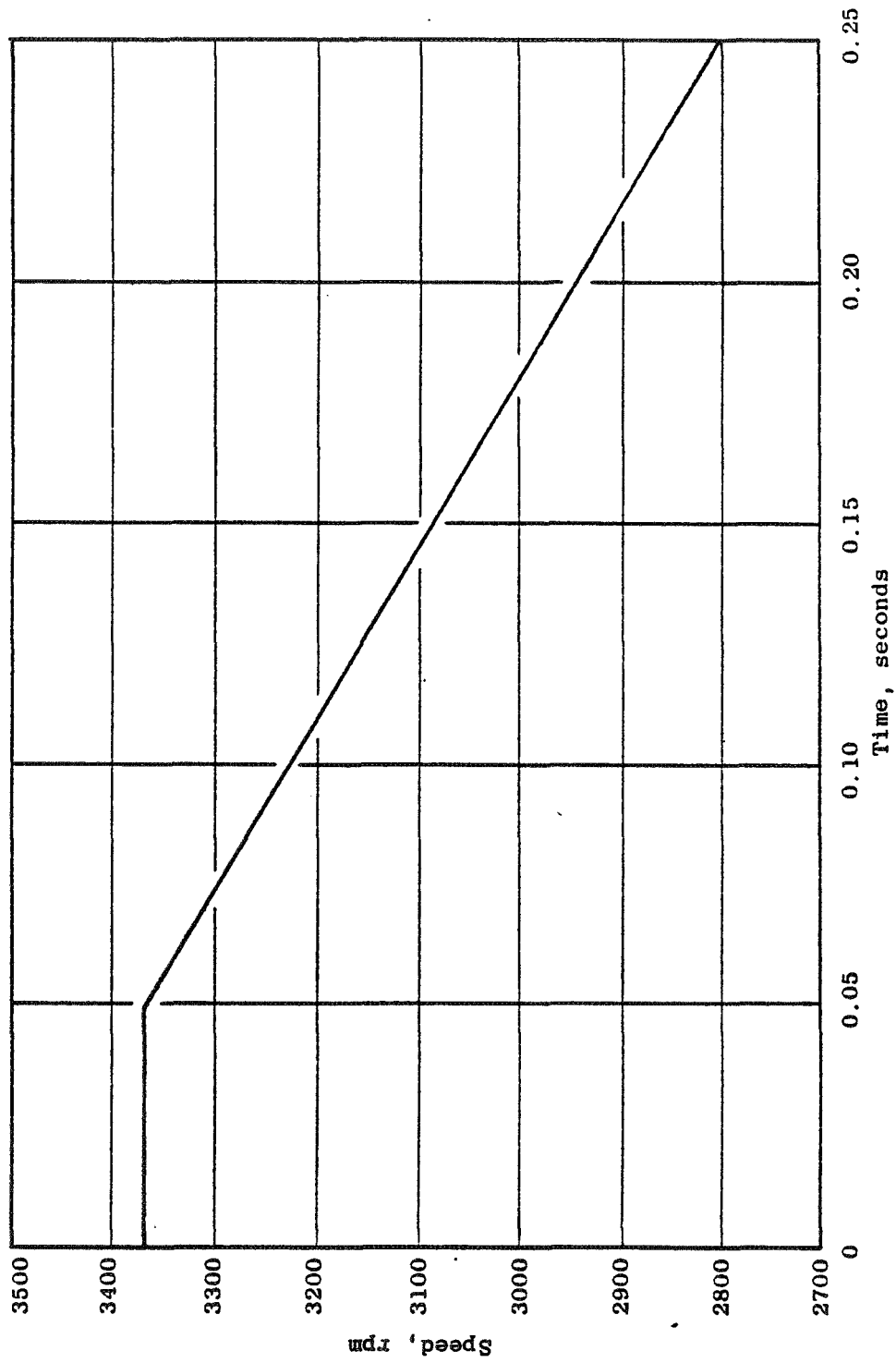


Figure 71. Blade-Out Engine Test Decel Time History.



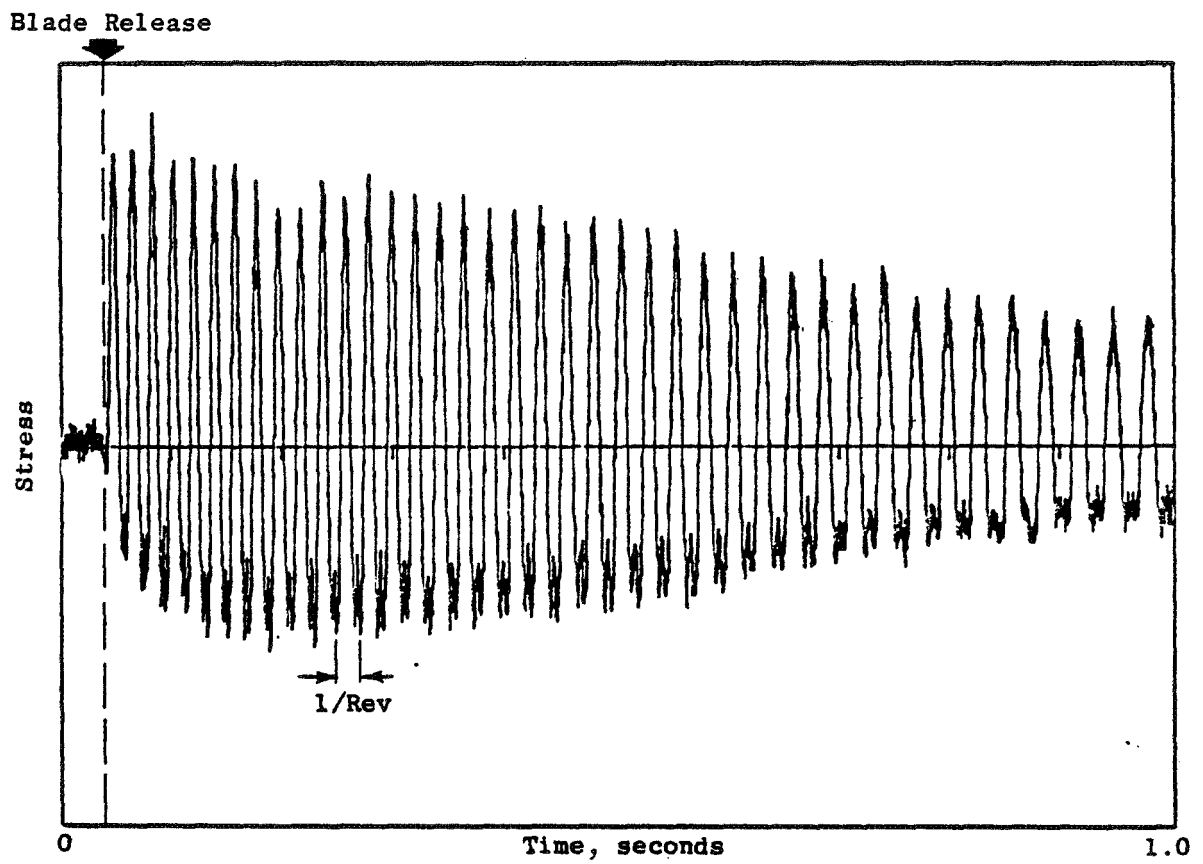


Figure 72. Blade-Out Engine Test - No. 1 Bearing Housing Stress at 153°.

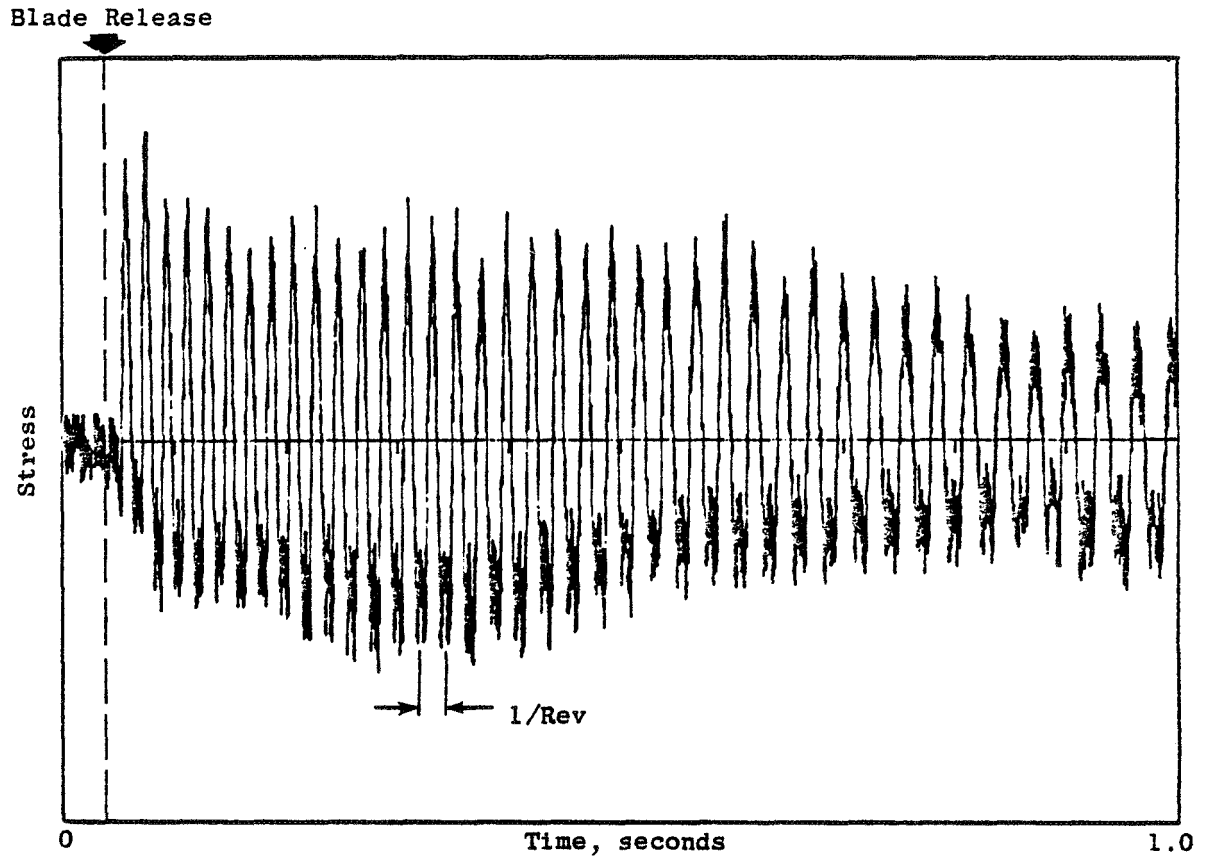


Figure 73. Blade-Out Engine Test - No. 1 Bearing Housing Stress at 333°.

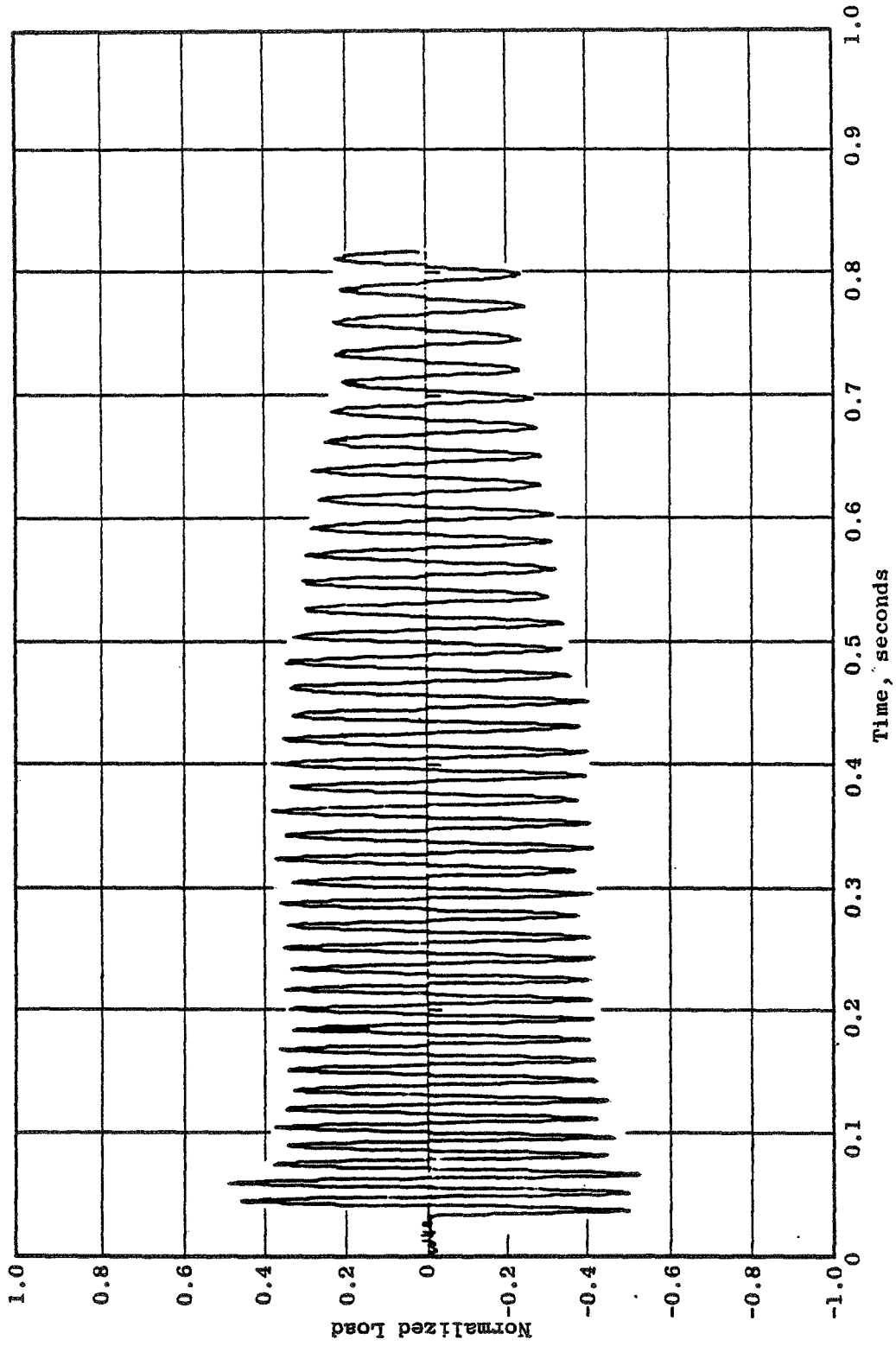


Figure 74. Blade-Out Engine Test - Reconstituted No. 1 Bearing Load.

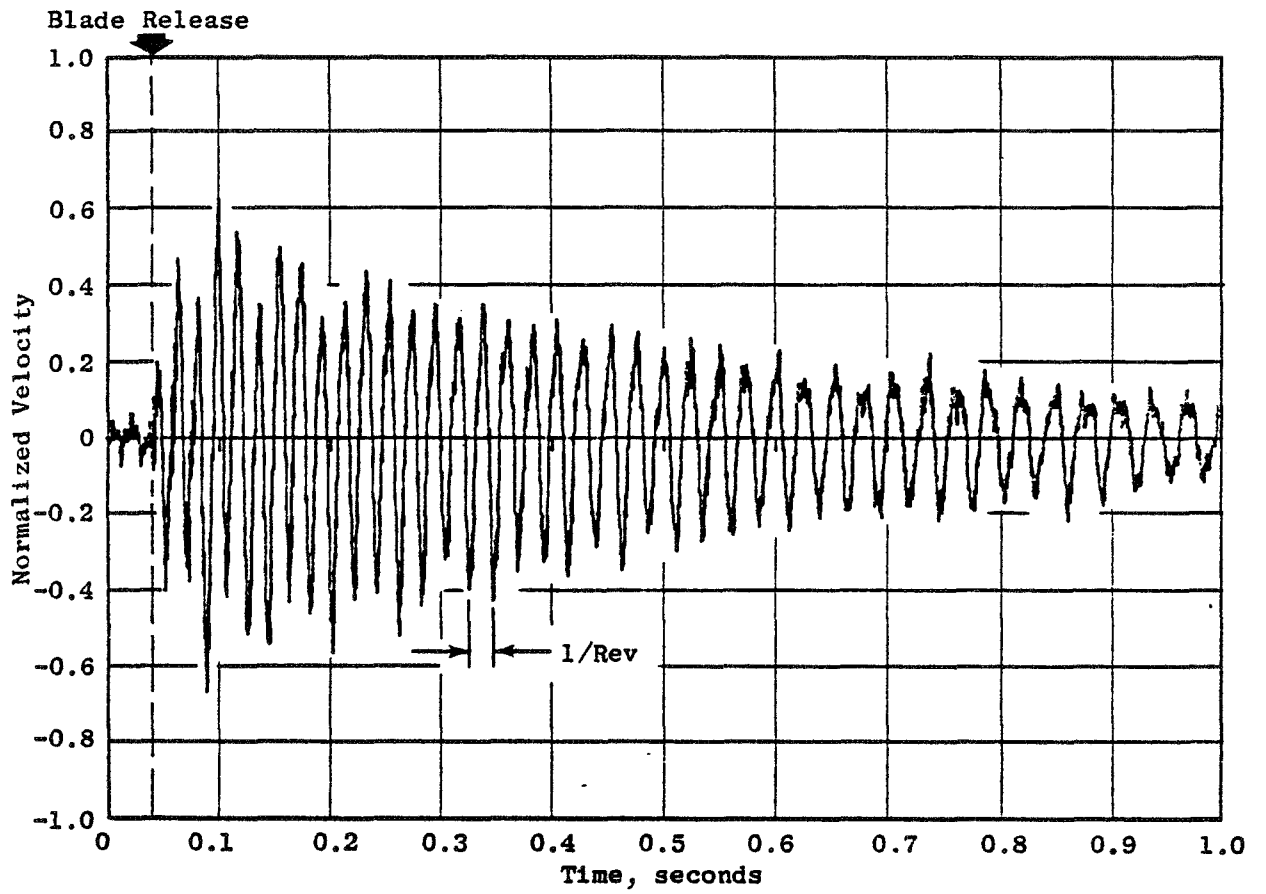


Figure 75. Blade-Out Engine Test - No. 1 Bearing Response.

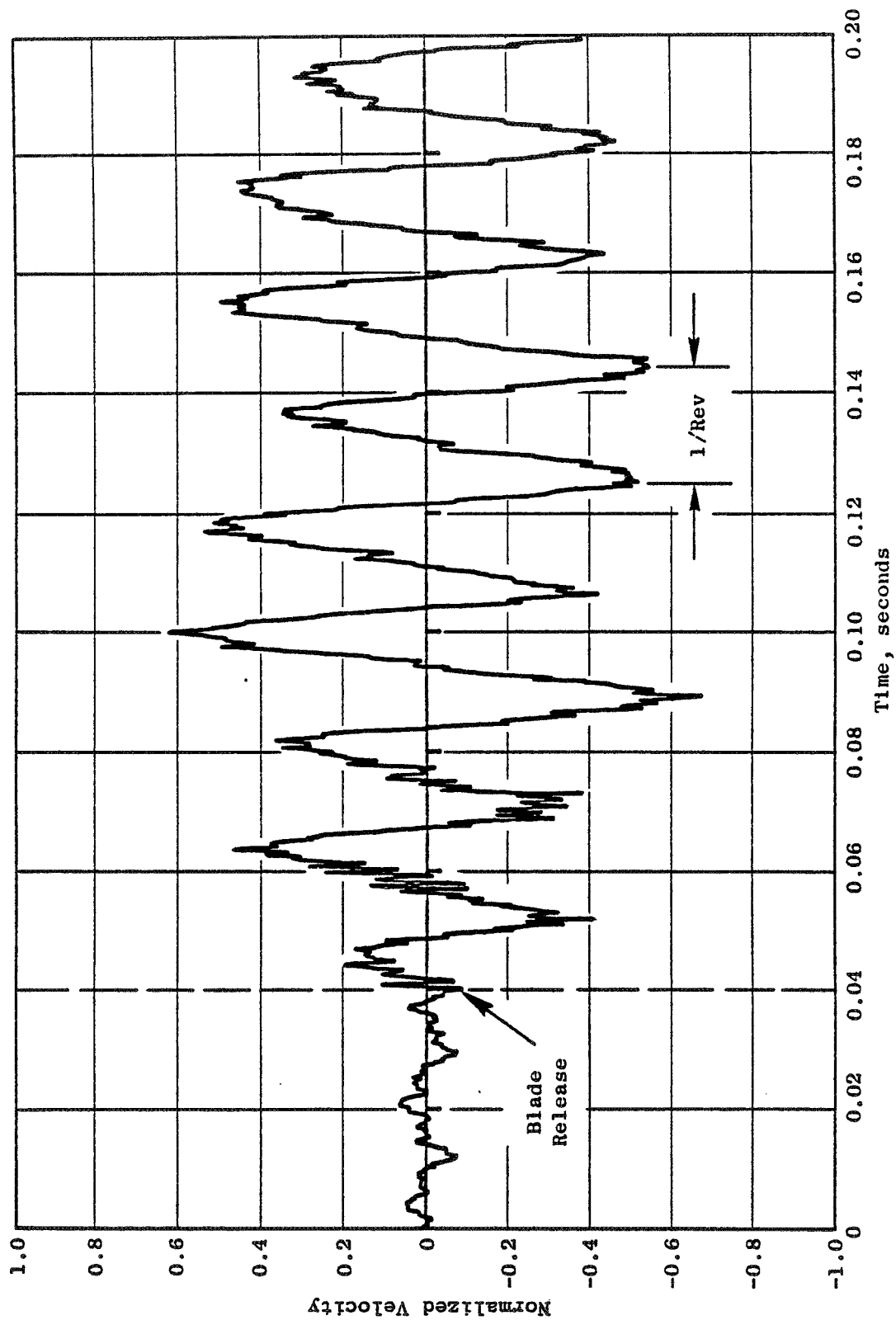


Figure 76. Blade-Out Engine Test - No. 1 Bearing Response (Expanded).

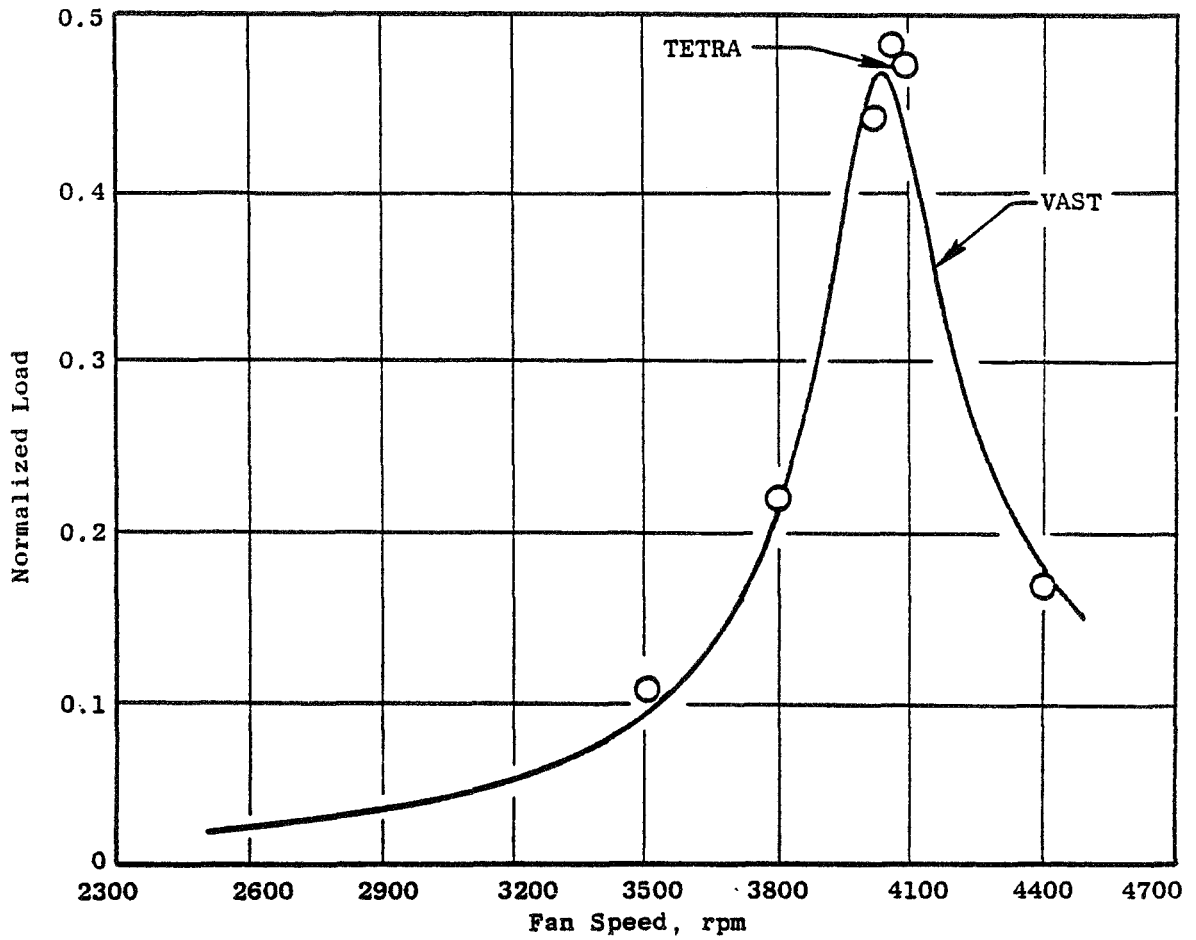


Figure 77. Test Vehicle Linear Analysis for Nominal Fan Rotor Unbalance - TETRA Versus VAST - No. 1 Bearing Load.

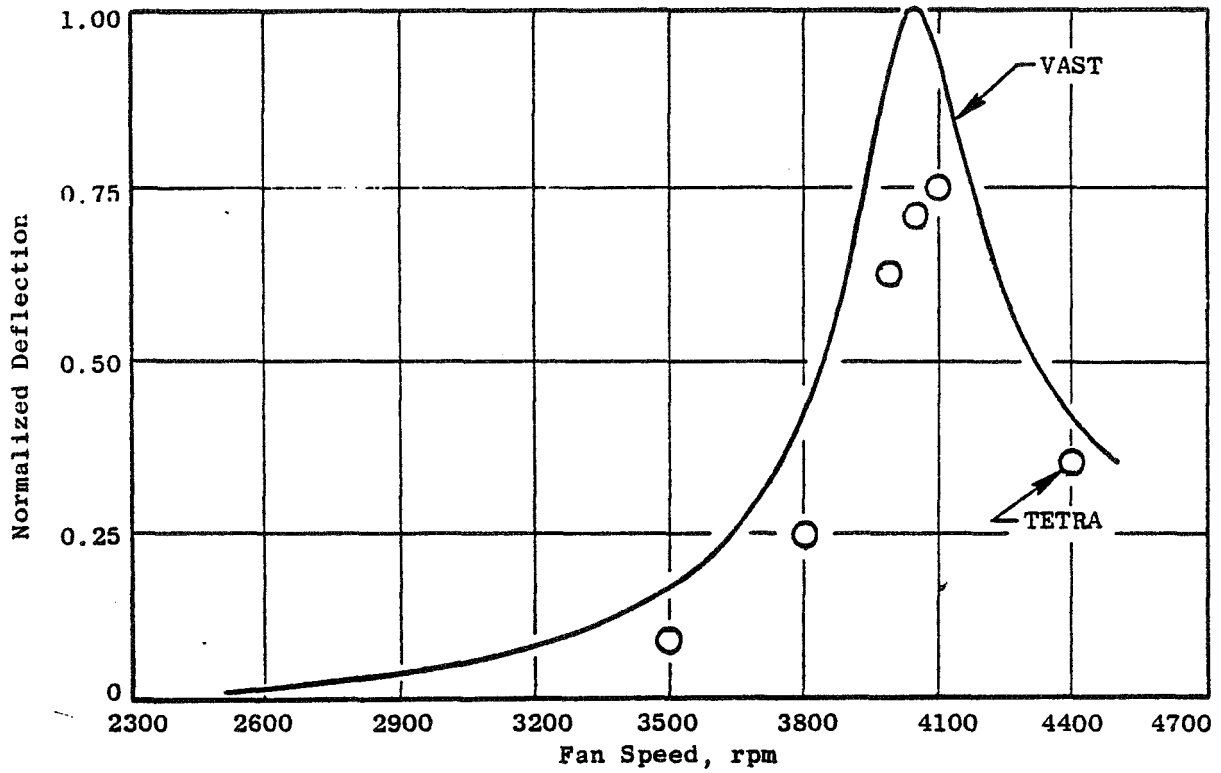


Figure 78. Test Vehicle Linear Analysis for Nominal Fan Rotor Unbalance - TETRA Versus VAST - No. 1 Bearing Housing Deflection.

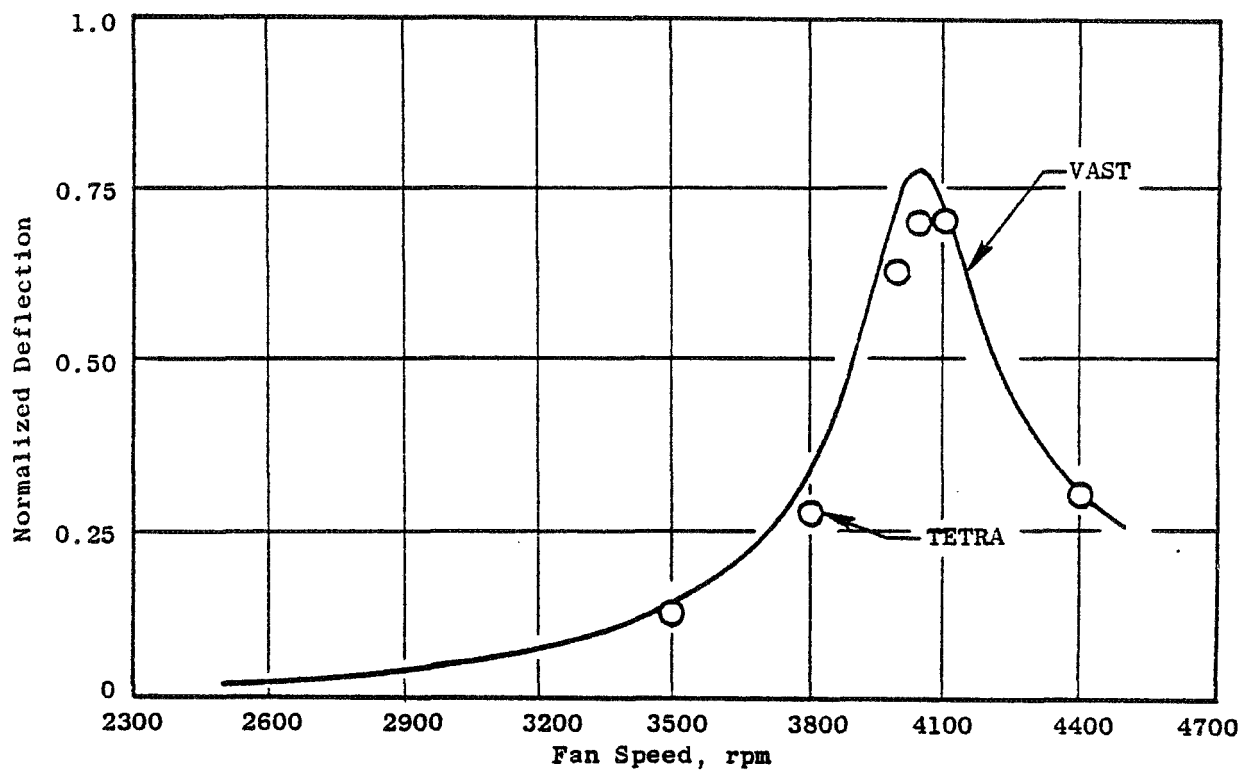


Figure 79. Test Vehicle Linear Analysis for Nominal Fan Rotor Unbalance - TETRA Versus VAST - Fan Stage Centerline Deflection.



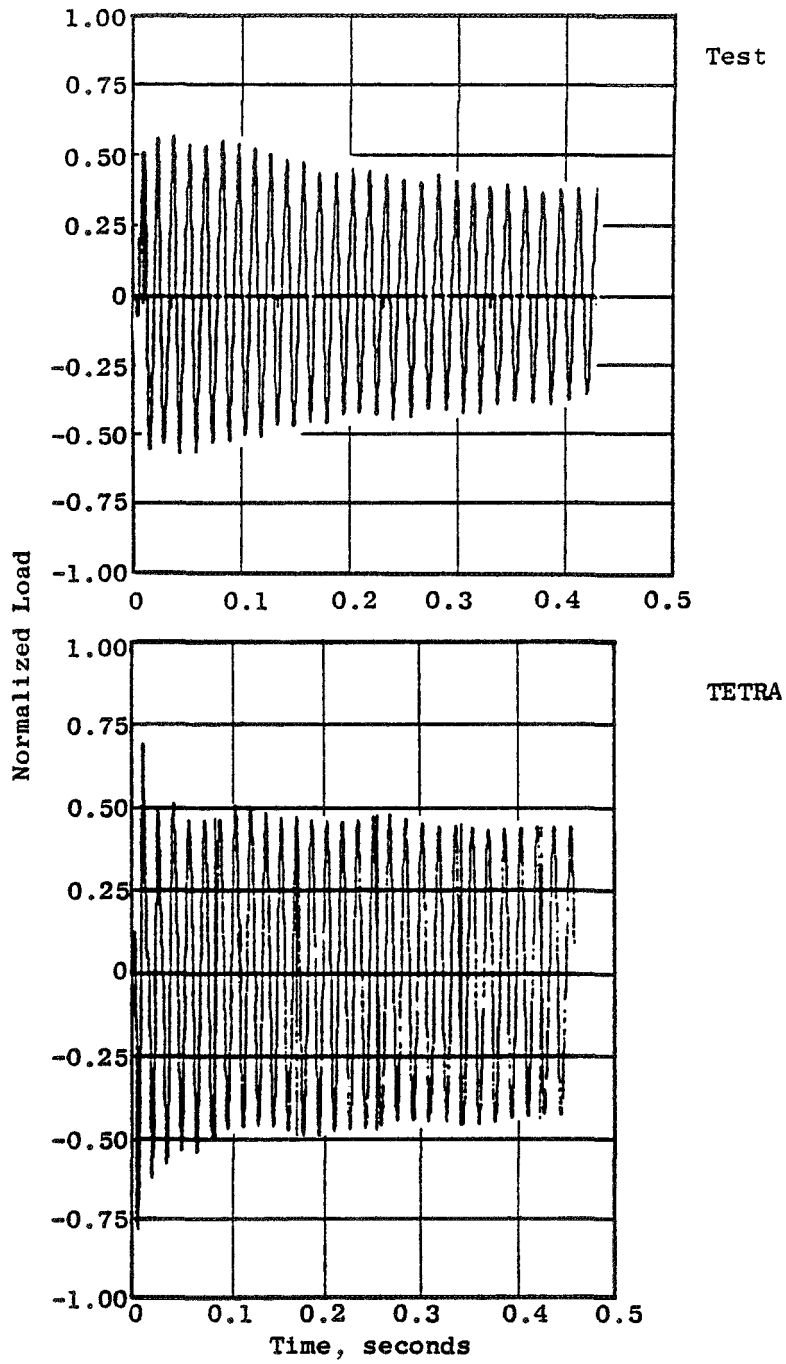


Figure 80. Blade-Out Test Vehicle - TETRA Versus Test for Blade-Out Condition - No. 1 Bearing Load.

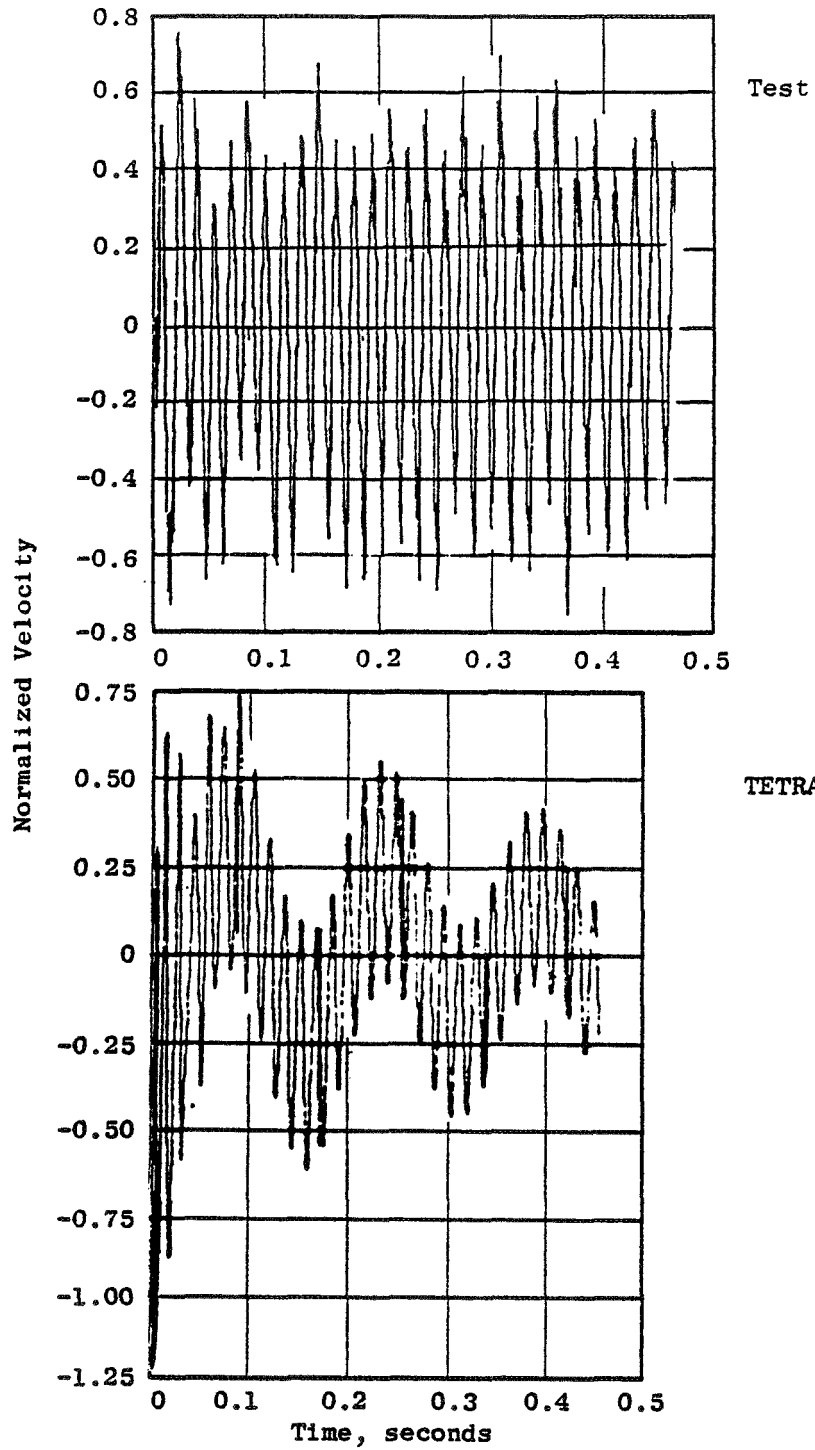


Figure 81. Blade-Out Test Vehicle - TETRA Versus Test for Blade-Out Condition - No. 1 Bearing Response.

the first cycle following the blade release. The test data show that the response remained approximately constant during the first 30 cycles of vibration; however, as the rotor speed decreased the TETRA predicted response shows a drastic reduction in amplitude, down to less than 25% of the initial response in a few cycles of vibration. Note that the low-frequency content predicted by TETRA does not show up in the test data since the accelerometer charge amplifiers filter out signals below 15 Hz. Figures 82 and 83 compare the measured and predicted No. 1 bearing loads and deflections, respectively, as a function of rpm. They show the same story as the time histories: generally reasonable correlation between TETRA and the analysis for the loads and very poor agreement between TETRA predicted displacement response and the measured response.

It should be noted that the bearing-housing strain gages were calibrated in a static-load calibration fixture that accounted for the bearing load distribution on the housing. On the other hand, the accelerometer senses response at a discrete point and includes out-of-round shell response. It is impossible to calibrate the accelerometer to eliminate this effect. TETRA and VAST analyses assume that plan sections remain round and plane; therefore, it is reasonable to consider that the difference between the measured and predicted performance is due to the method of measurement and not errors in the prediction technique.

#### 4.10 COMPARISON OF TETRA RESULTS FOR BLADE-OUT ENGINE WITH LINEAR ANALYSIS AND TEST COMPARISON

Comparison of TETRA linear analysis of the engine with the linear VAST predictions shows essentially the same results as the comparison for the blade-out test vehicle. Figure 84 compares the normalized bearing load for the steady-state solutions versus rpm, and Figure 85 compares the normalized deflections. The TETRA and VAST analyses both were conducted using a system quality factor Q of 15. If the TETRA Q had been adjusted to 12.5, like the test vehicle data presented in Section 4.9, then the loads would have agreed very well, and the TETRA predicted deflections would have been slightly less than the VAST predictions.

Figure 86 compares the normalized bearing load transient response following blade release for the TETRA predictions and the blade-out engine test. The signatures look very similar; the maximum load occurs within the first few cycles, and the load drops off slowly thereafter as the rpm decreases (see Figure 71 for the decel rate). Even though the signatures look similar, with only a small amount of transient overshoot, the TETRA predicted loads are approximately 2-1/2 times as high as the measured data.

Figure 87 compares the TETRA predicted normalized velocity response with the test data. The test data show a more gradual buildup to the peak value, requiring approximately three cycles of vibration, while the TETRA predicted response is approximately twice the maximum measured values; however, once the initial predicted transient overshoot is dissipated, the response levels are very similar. Figure 88 compares the normalized loads as a function of rpm

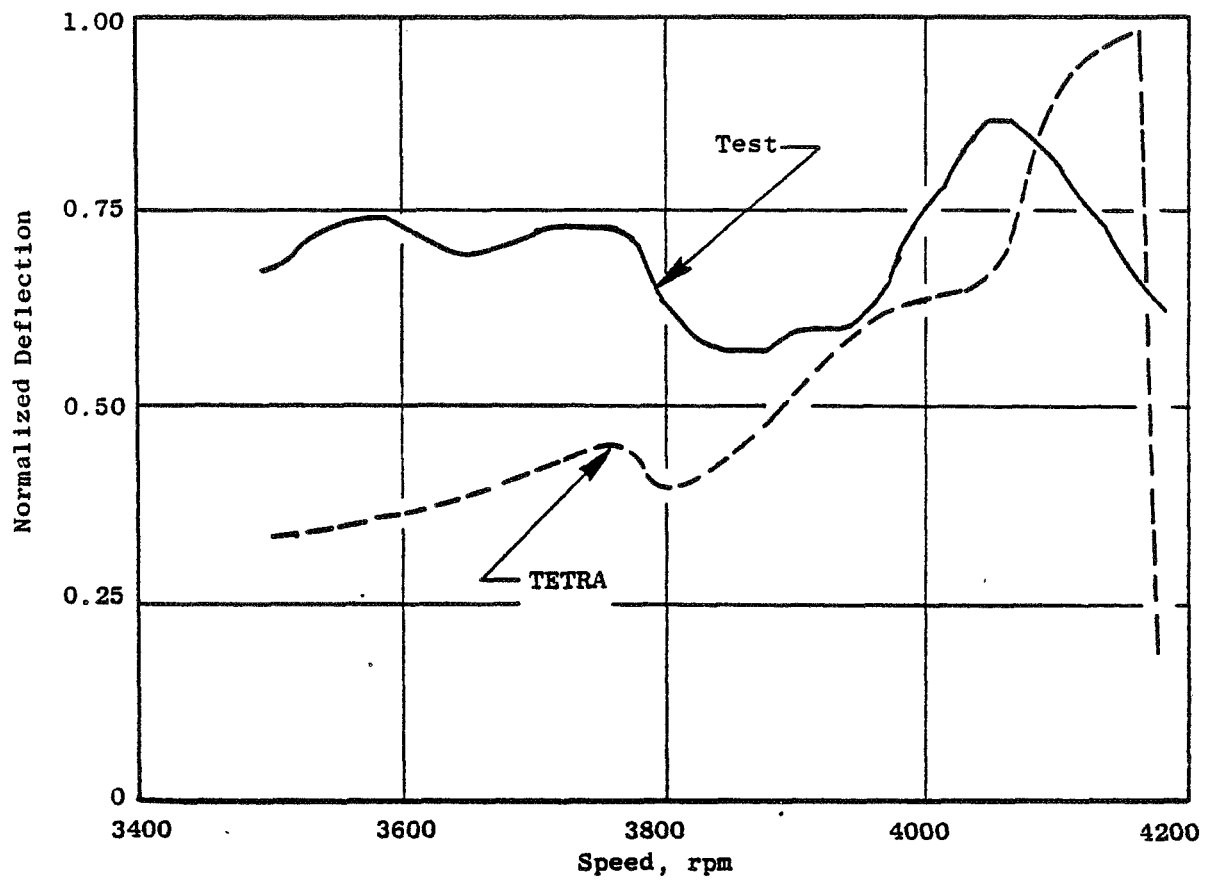


Figure 82. Blade-Out Test Vehicle - TETRA Versus Test for Blade-Out Condition - No. 1 Bearing Deflection.

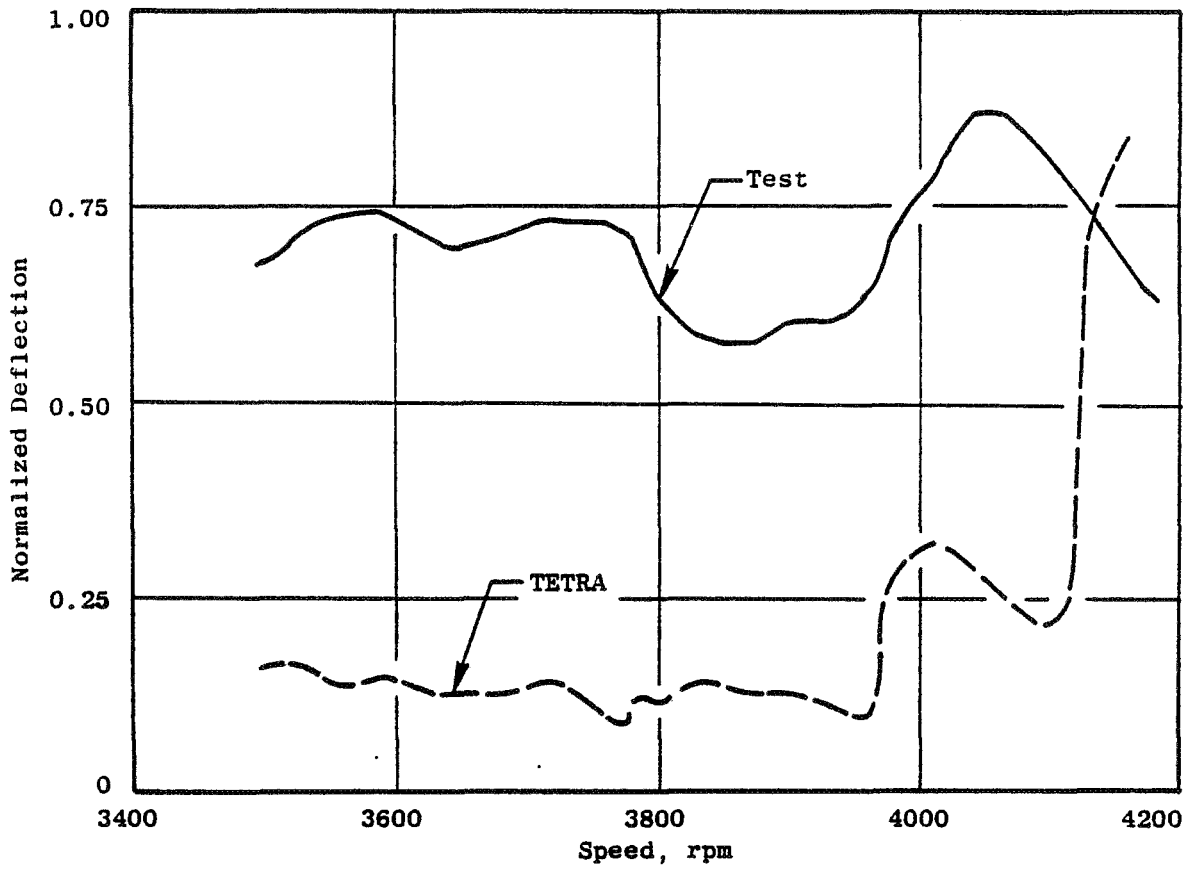


Figure 83. Blade-Out Test Vehicle - TETRA Versus Test for Blade-Out Condition - No. 1 Bearing Deflection.

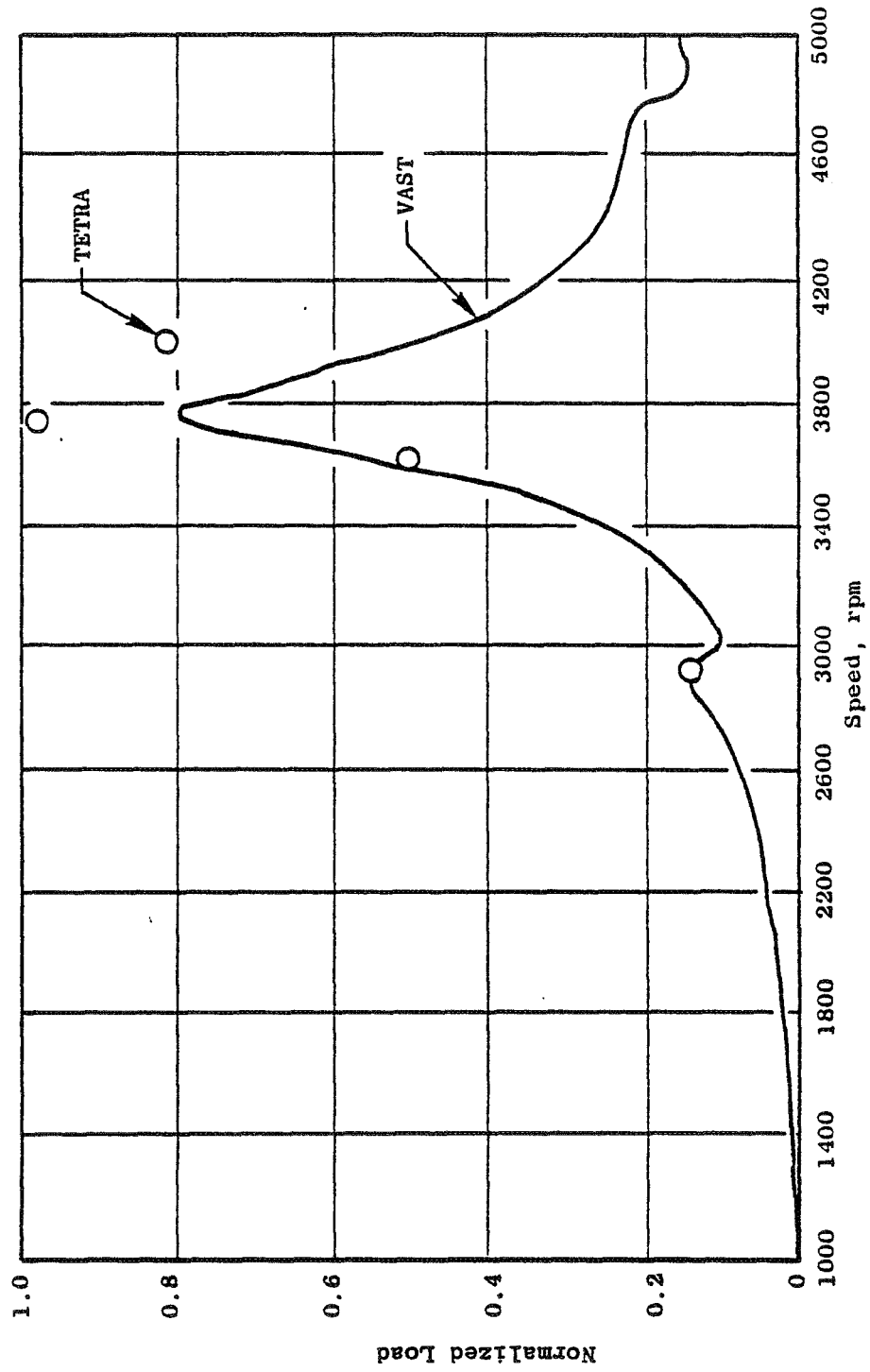


Figure 84. Engine Linear Analysis for Nominal Fan Unbalance - TETRA Versus VAST - No. 1 Bearing Load.

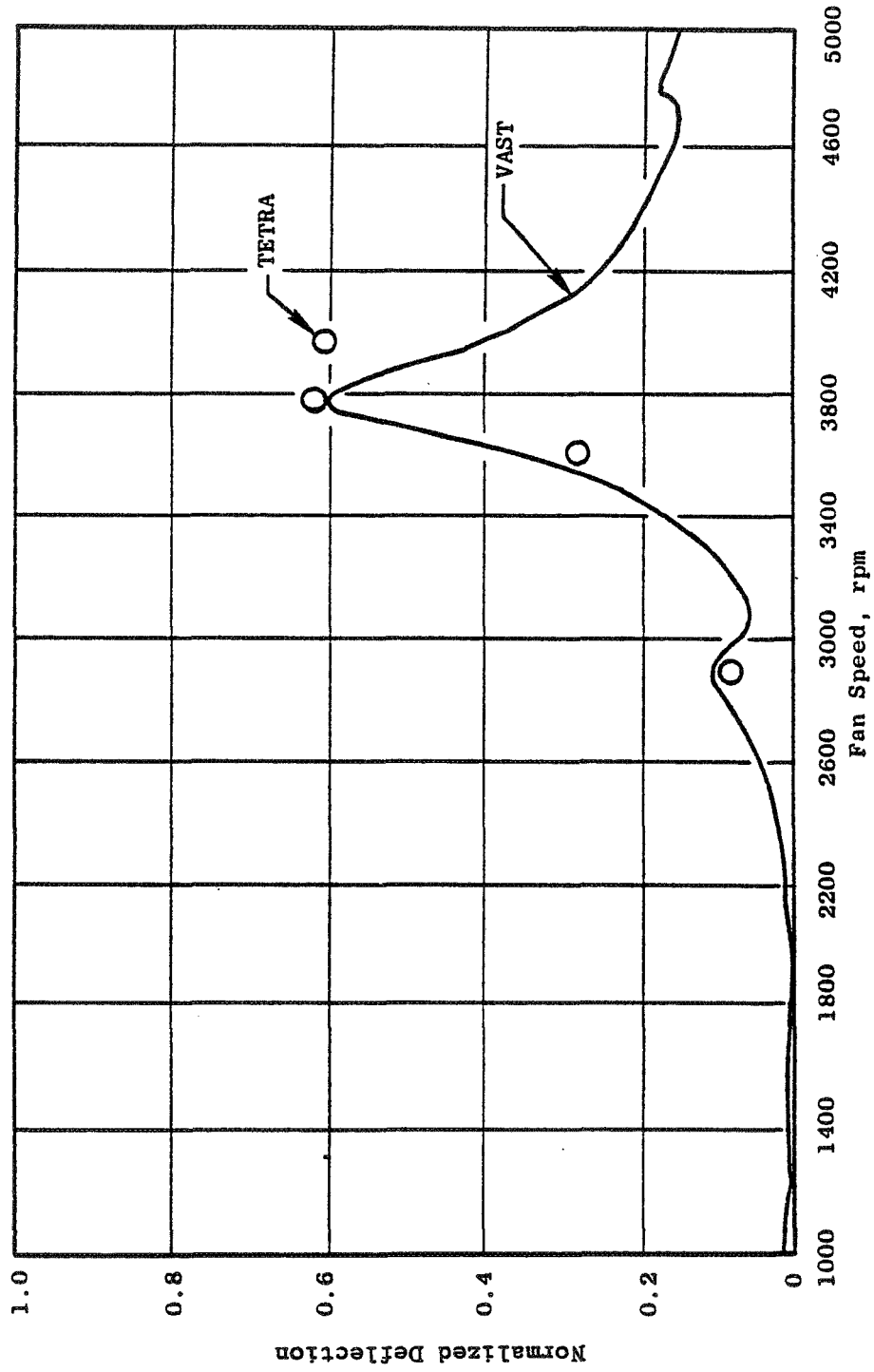


Figure 85. Engine Linear Analysis for Nominal Fan Unbalance - TETRA Versus VAST - No. 1 Bearing Deflection.

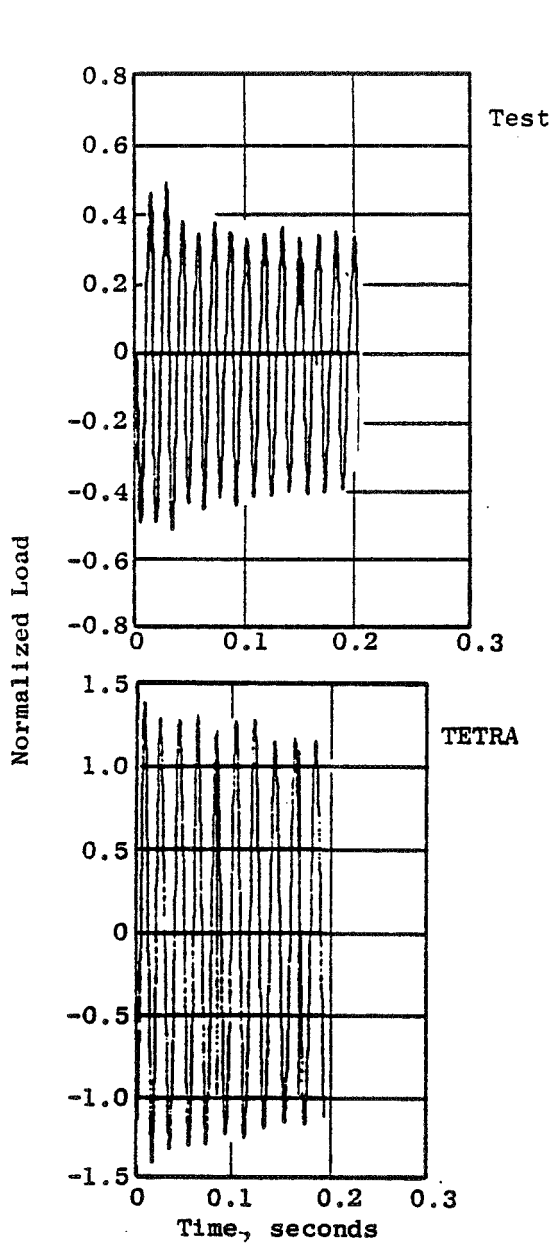


Figure 86. Blade-Out Engine - TETRA Versus Test for Blade-Out Condition - No. 1 Bearing Load.

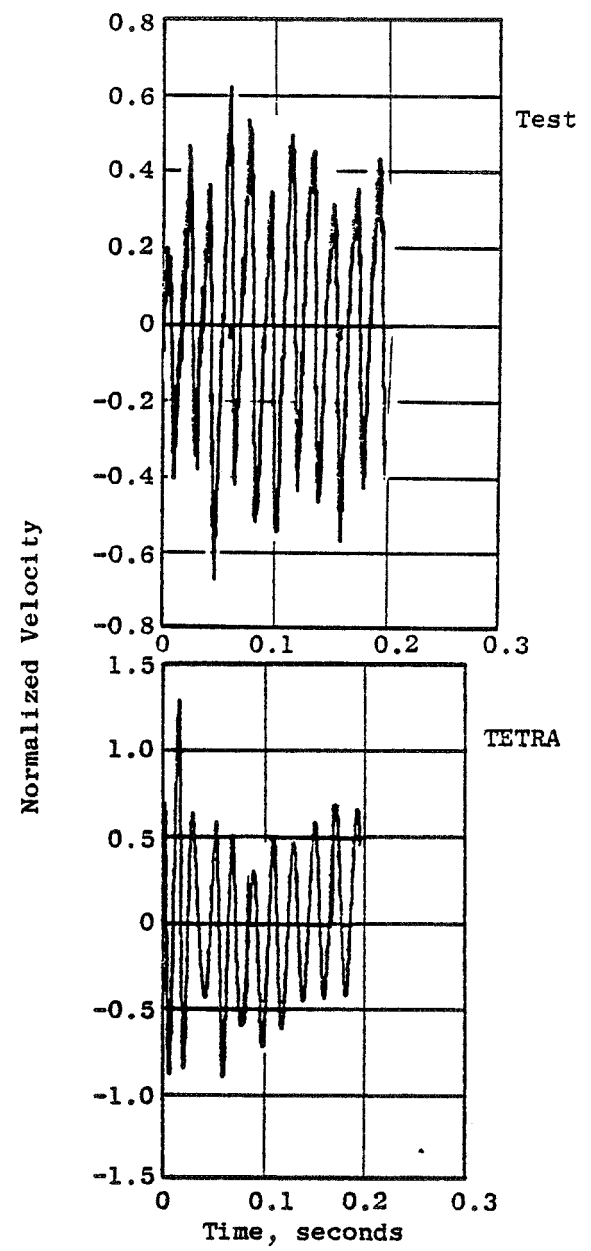


Figure 87. Blade-Out Engine - TETRA Versus Test for Blade-Out Condition - No. 1 Bearing Response.



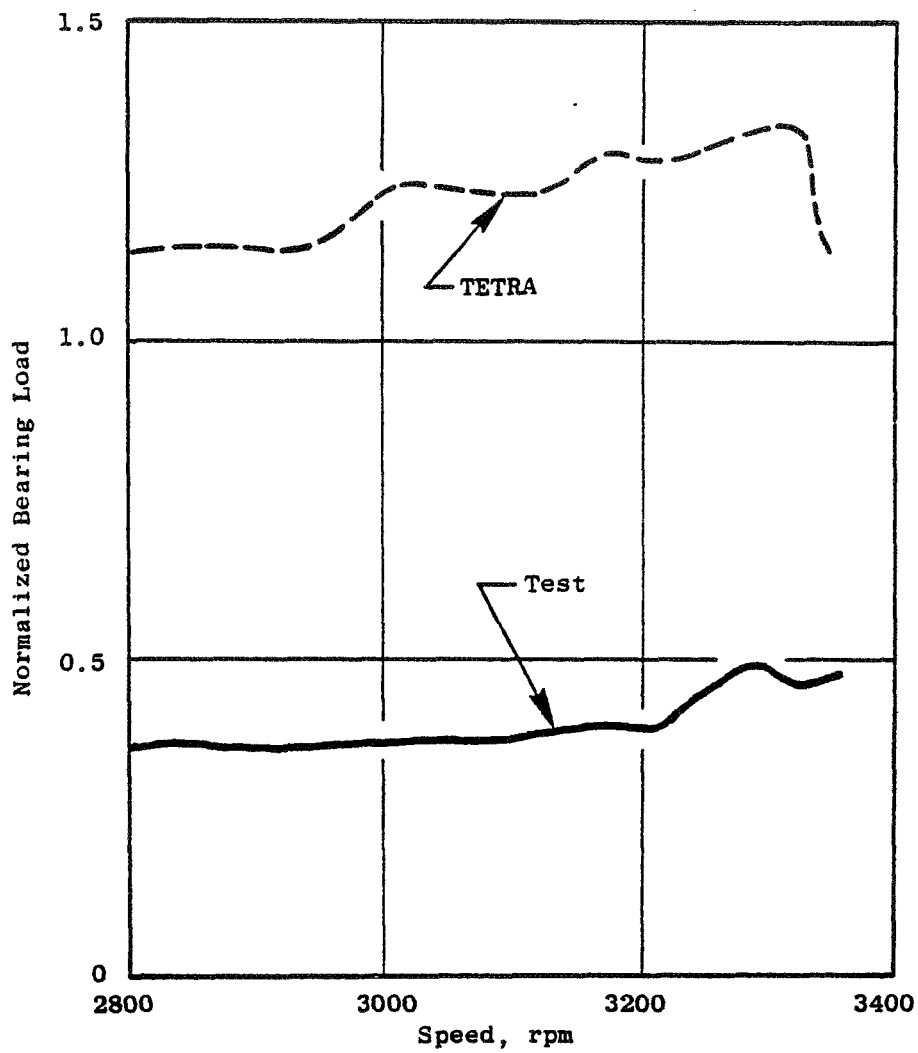


Figure 88. Blade-Out Engine Test Normalized Load Versus rpm.

during the decel following the blade release. Figure 89 shows similar curves for the normalized deflections. Figures 88 and 89 both show that the response, a function of rpm, is very similar between TETRA predictions and measured data except for the differences in magnitude and transient overshoot previously noted.

#### 4.11 DISCUSSION OF TETRA VERIFICATION RESULTS

The TETRA linear analyses agreed reasonably well with the VAST linear analyses, especially in terms of response frequencies, for both the test vehicle and the engine. Both analyses were dependent on the number of modes used to define the subsystems; the engine analysis were the more critical due to the increased complexity of the model. The discrepancies in the TETRA results are in the direction that might be expected due to modal truncation; i.e., frequency and loads are slightly too high, and deflections are slightly too low. Table IX is a comparison of the complexity of the vehicle and engine models.

The comparison of the nonlinear results showed a much larger disparity between the test vehicle and the engine. The vehicle showed reasonable agreement on the bearing loads, but the predicted deflections were much lower than test. For the engine, predicted loads were more than twice the measured loads, but the deflections showed reasonable agreement following the initial transient overshoot. For both the vehicle and the engine, TETRA predicted more transient overshoot than was observed during the blade-out tests.

It was apparent from preliminary analyses and the correlation studies that the number of modes used to represent the subsystems is a key to the accuracy of the TETRA response. No proven guideline is currently available to define what a reasonable number of modes should be; however, Table IX may give some insight. Table IX shows that, even though the number of casing modes used in the engine analysis was twice that used in the vehicle analysis, the ratio of the highest casing frequency to the maximum operating frequency was only one-third of that for the vehicle. Likewise, the ratio of the number of degrees of freedom to the number of modes used was twice as high for the engine although it is not clear that the number of subsystem degrees of freedom is a relevant parameter. It was apparent from the data that the test vehicle analysis more closely represented both the linear VAST analysis and the test results; this would imply that improvements in the engine predictions could have been obtained by using similar ratios of maximum subsystem frequency to operating speed and/or number of degrees of freedom to the number of modes used. Incorporating these criteria into the engine analysis would have increased the computational cost to perhaps prohibitive values: approximately \$3500 for 0.5 seconds of data; with the current analyses, each cost approximately \$600. This may not be a prohibitive value for a design analysis, if there is confidence in the results and it would not require repetition to evaluate the effect of other combinations of modes on the results. A possible

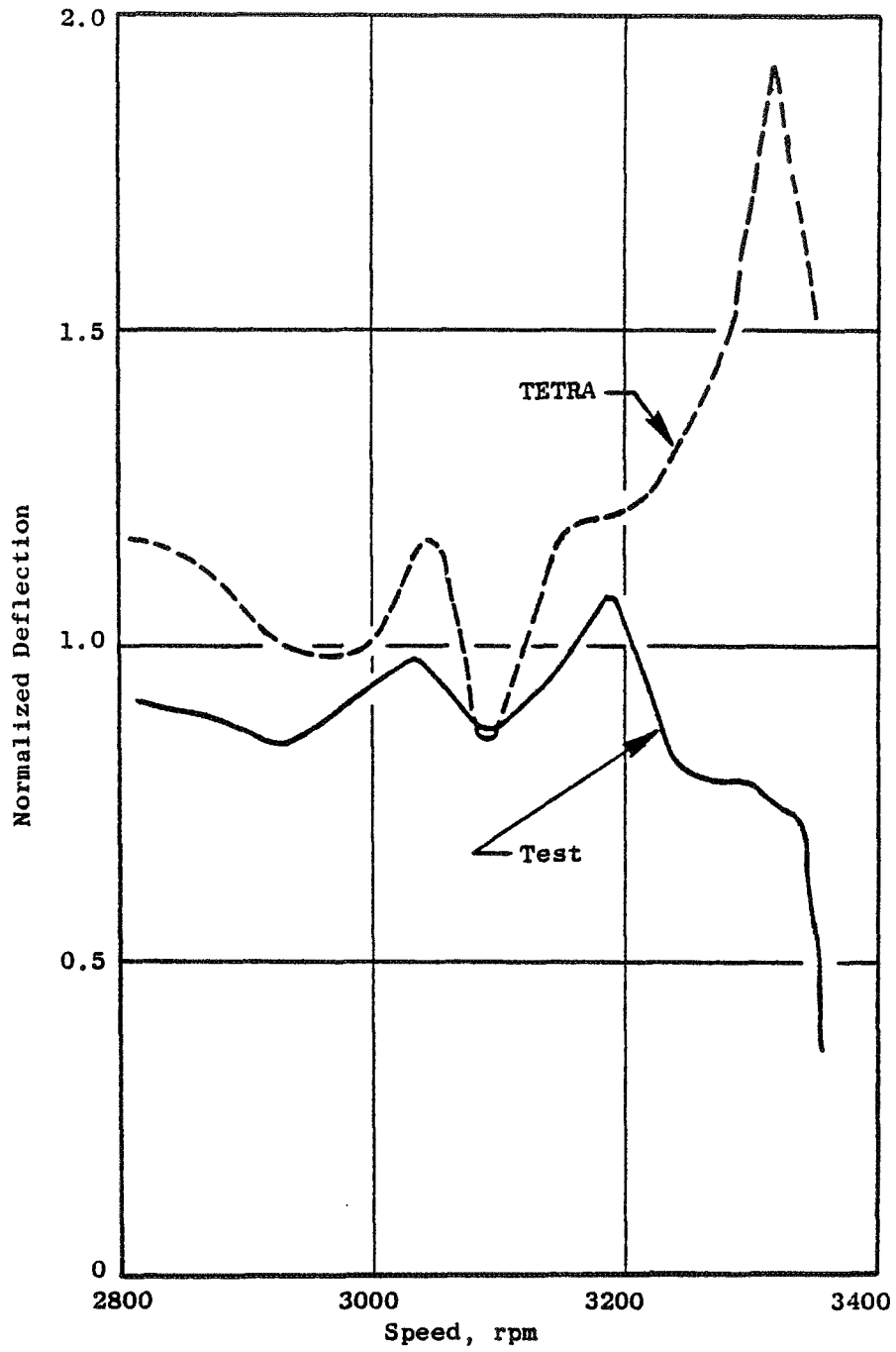


Figure 89. Blade-Out Engine Test Normalized Deflection.

Table IX. TETRA Model Complexity.

Parameter	Vehicle	Engine
Max. Operating Speed	4,185 rpm	3,366 rpm
Max. Casing Frequency	75,867 rpm	24,268 rpm
Max. Rotor Mode	78,001 rpm	11,081 rpm
Ratio $\frac{\text{Max. Casing Freq.}}{\text{Max. Oper. Speed}}$	18.1	7.2
Ratio $\frac{\text{Max Rotor Freq.}}{\text{Max. Oper. Speed}}$	18.6	3.3
No. DOF, Casing Subsystem	170	590
No. DOF, Rotor Subsystem	38	190
No. of Subsystems	2	2
Ratio $\frac{\text{Casing DOF}}{\text{No. Modes}}$	13.1	22.7
Ratio $\frac{\text{Rotor DOF}}{\text{No. Modes}}$	9.5	31.7
No. of Connecting Elements	2	4
Cost to Run 0.5 second	\$600	\$630

way of increasing the accuracy would be to break the engine down into more and simpler subsystems such as the low pressure rotor, the high pressure rotor, the high pressure casing, the low pressure casing, and the pylon. Each of these systems would require fewer modes to get a high ratio of subsystem frequency to operating frequency and also to achieve a low ratio of degrees of freedom to number of modes used. The integration time step would have to be small to account for the higher frequency, and the analysis would be more complicated with more subsystems and more connecting elements, so the true effect on cost is unknown.

Other factors which may have had an effect on the comparison of predicted response and test results are:

- System damping at high amplitudes
- Tip clearance and casing ovalization stiffness

- Accuracy of measured loads and deflections
- System complexity.

It has been observed in other studies that the Q factor has a small effect on the nonlinear response. The tip clearance and ovalization stiffness were determined by measurement and finite-element analysis of the casing structure. In the past, small variations of these parameters have been seen to have a minor effect on the results. As was mentioned in Section 4.9, there are some inherent inaccuracies in the deflection measurements which could account for some of the differences between the predicted and measured response of the blade-out test vehicle.

From these comparisons between TETRA calculated responses and the test results from both test vehicle and engine blade-out tests, the following observations are made:

- TETRA shows reasonable agreement with both linear analysis and nonlinear test results when a sufficient number of modes are included.
- TETRA tends to predict more transient overshoot than was observed during both blade-out tests but significantly lower overshoot than predicted by linear analysis (no rub).
- Transient overshoot is insignificant in the test data.
- Modal truncation can have a significant effect on the accuracy of TETRA computed response.
- Other real-world factors, difficult to quantify, affect the response of real engines. Some of the more important ones are plastic deformation and the effect of high impulsive loading on structure damping and stiffness.

## 5.0 CONCLUSIONS AND RECOMMENDATIONS

A comparison of analytical predictions with test data for the two configurations tested was given in Sections 4.9 and 4.10. The essence of these comparisons and other observations is:

- Loads were more accurately measured in test than were displacements and, therefore, are taken as the prime reference for comparison.
- Analysis and test agree well if a sufficient number of subelement modes are used.
- The test vehicle analytical results agree very well with test, but the engine results compare poorly. The latter used subelement modes up to a maximum frequency of roughly one-third that used for the test vehicle.
- Discrepancies between analysis and test depend strongly on the maximum frequency of the subelement modes relative to the maximum operating frequency.
- Test results show relatively little transient overshoot in loads; the analysis shows about 30%.

To attempt a rough quantification of results, a comparison is given below between predicted loads and test results both for the transient overshoot and the steady-state values. Some license was taken in developing this table since the determination of transient and steady-state values is subjective, especially since no steady-state condition was truly obtained. While it is readily conceded that other parameters (such as the number of subelements, etc.) may have as important an influence, the table of comparisons is made only on the basis of the ratio of the maximum subelement modal frequency to the maximum rotational frequency of the test.

<u>Configuration</u>	<u>Max Modal Freq.</u> <u>Rotational Freq.</u>	<u>No. of</u> <u>Modes</u>	<u>% Difference</u> <u>Steady-State</u> <u>Load</u>	<u>Test-Analysis</u> <u>Test</u> <u>= Transient</u> <u>Load, %</u> <u>x 100</u>
Test Vehicle	18	13	8%	-33%
Engine	7	26	144%	131%

The test vehicle results show very good correlation, especially for steady-state response, but the engine shows poor. Also, the analysis tends to predict greater overshoot than actually occurs. An implication is that even better results from the test vehicle might be obtained, especially for the transient response. It is not clear that the only factor producing the difference noted between analysis and test is related solely to the maximum subelement modal frequency. As mentioned previously, how the system is modeled may be equally important. For instance, the engine was modeled as two subelements, one representing the LP rotor and the other representing a combination of basically soft and stiff elements such as the pylon, casings, frames, and HP rotor. Perhaps better results are possible if the pylon, casing, and HP rotor are each represented as a subelement.

Also, it may be possible to obtain better results if a different subelement modal representation is used. In the approach used in TETRA, free-free modes are used to define the subelement (except for elements tied to ground, for which grounded boundary conditions are used). It seems reasonable to believe that faster convergence and fewer modes would be required if the subelement modes were taken to be pinned-pinned at the connection points, or tied to ground through springs having the support structure spring rates. These modes could be closer in frequency and shape to the dominant modes of the combined system and, therefore, could require fewer modes to obtain good results. Another complicating factor is the influence of fan tip rub which produces a secondary load path and essentially a "stiffer" system. Hence, a greater number of modes would be required for this condition than one would expect to use to obtain good results for the linear case.

It is evident from the results of these discussions that criteria and guidance are needed if the analyst is to proceed with assurance that he will predict accurate loads and stresses in a cost-effective manner. These guidelines and criteria are not at hand and must be developed as part of this approach. The question of minimizing truncation errors for complex systems involving nonlinear stiffening elements is difficult. Furthermore, the most effective modeling approach must be identified.

Based on these discussions, the following list of areas requiring further study was compiled:

1. Truncation Errors - Need to develop criteria for determining the number of subelement modes required to produce acceptable results, including the effect of nonlinear elements.
2. Modeling Guideline - Need to develop criteria for guiding the analyst in the selection of the best subelement breakdown. Criteria should include a balance between increasing number of subelements, diminishing time increments, and improved accuracy consistent with cost.

3. Component Modes - The current analysis uses free-free subelement modes at discrete points, usually at bearings or frames. The use of subelement normal modes pinned-pinned at these points, or sprung by elements having stiffnesses equal to the connecting element stiffness, may produce better results and require fewer modes. These approaches should be explored.
4. Transient Overshoot - The criteria and modeling techniques studies discussed above, must also address the problem of predicting overshoot or lack thereof. This may also include criteria defining the required time increments.
5. Cost - The cost of running complex, real-engine systems using the large number of modes indicated by the results and the large number of time increments required to obtain good results can be prohibitive. We need to study methods for reducing computer time and cost.
6. Instrumentation - Accurate measurements of displacements and loads under high-amplitude and duration testing is difficult, especially when local shell deformations occur. A further study of this area is needed.
7. Experience - More experience in the use of this approach is required on a variety of complex problems to explore its full capabilities.

The work and methods developed under this contract provide a useful tool that was demonstrated to give good prediction of blade-out test results. This study also showed that the use of this tool is not straightforward, and the analyst must be provided with criteria and guidelines to assure good results. Developing these guides is the next logical step for making this method a useful design tool.





APPENDIX A

BLADE-OUT VEHICLE SYSTEM NORMAL MODE SHAPES

The mode shapes for the first three resonances predicted by analysis of the blade-out test vehicle are given in Figures 90, 91, and 92. The first two are rigid-body modes, and the other is a system flexural mode.

*Preceding page blank*

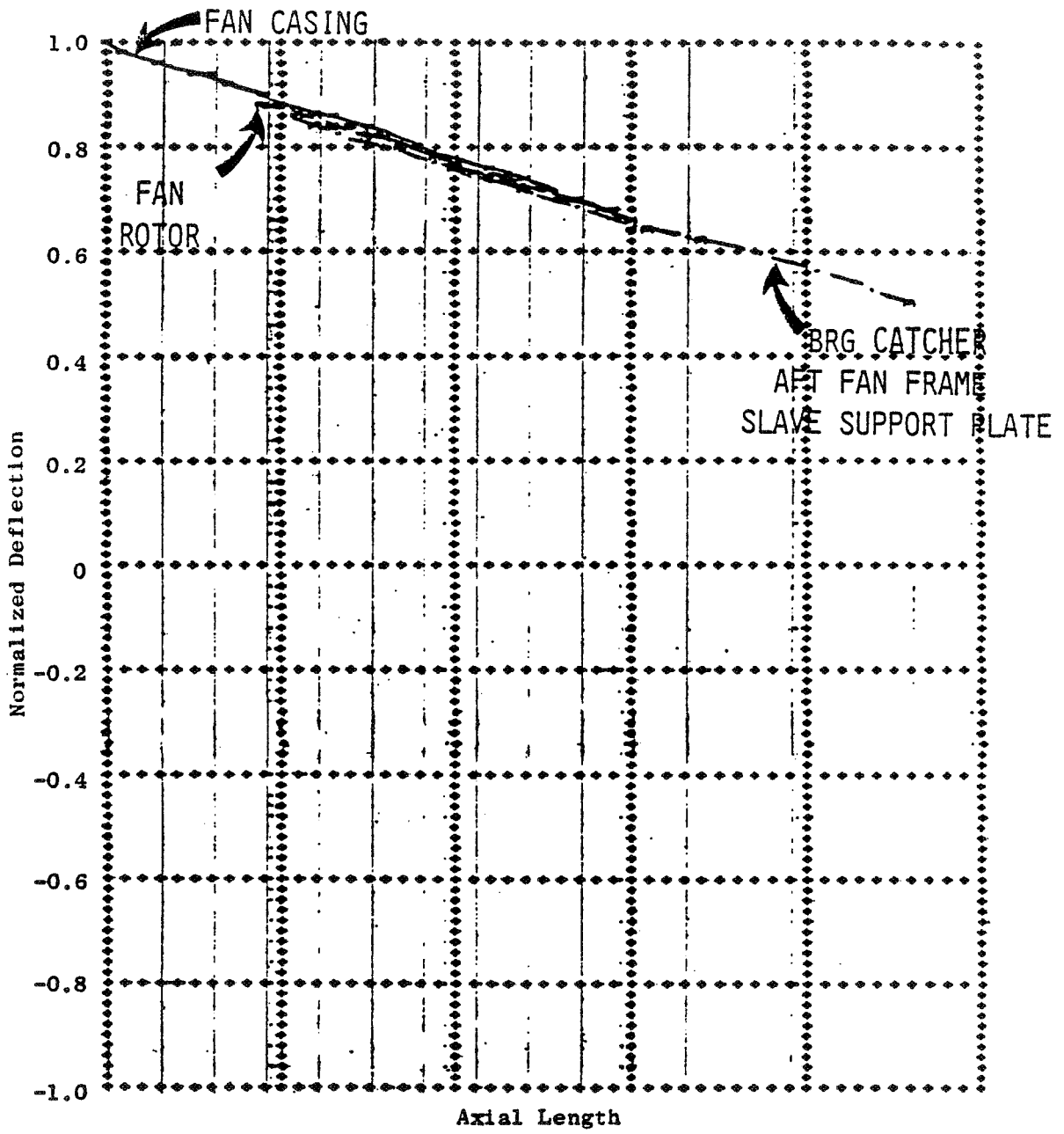


Figure 90. Blade-Out Test Vehicle Predicted Mode Shape at 387 rpm.

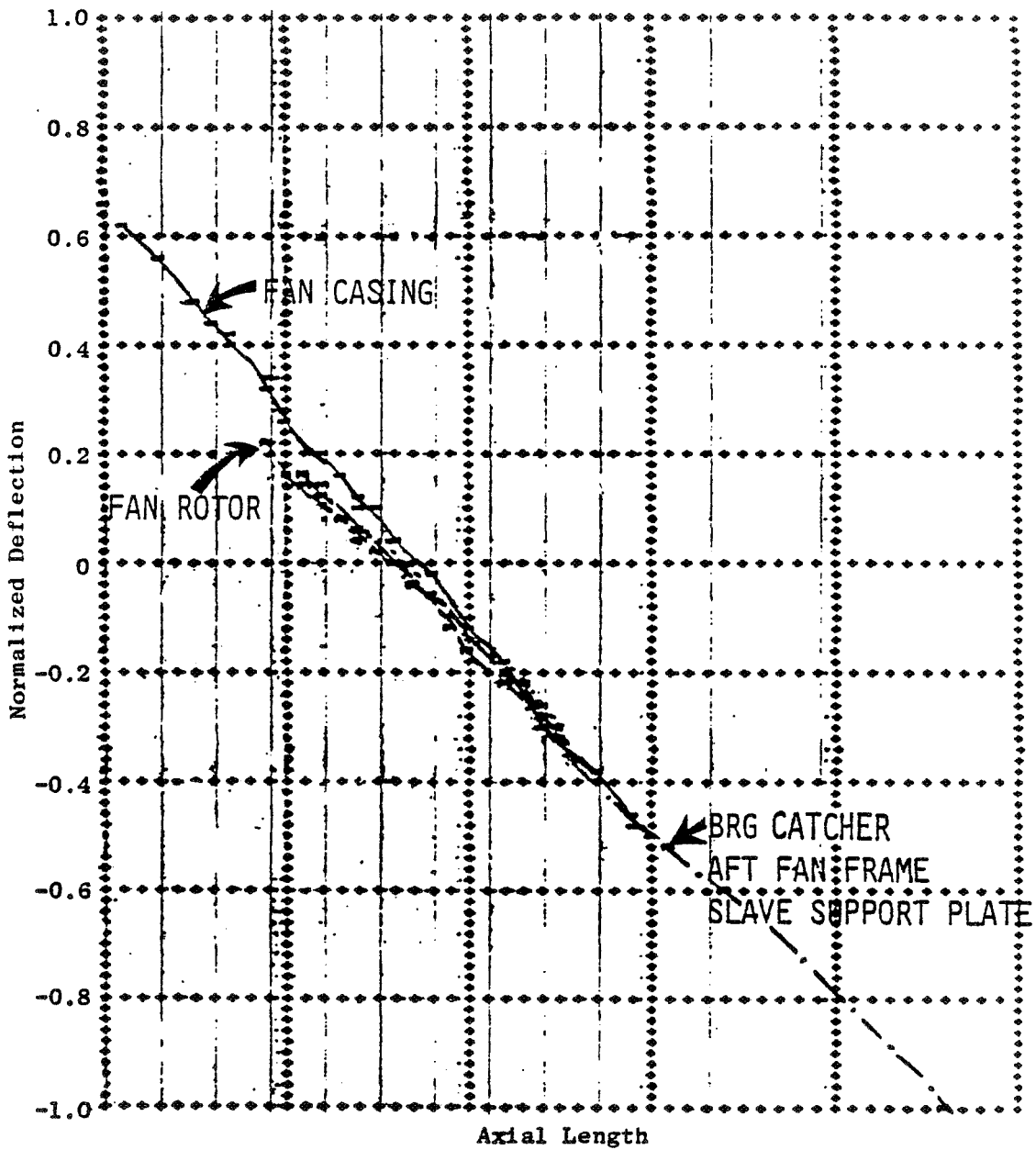


Figure 91. Blade-Out Test Vehicle Predicted Mode Shape at 981 rpm.

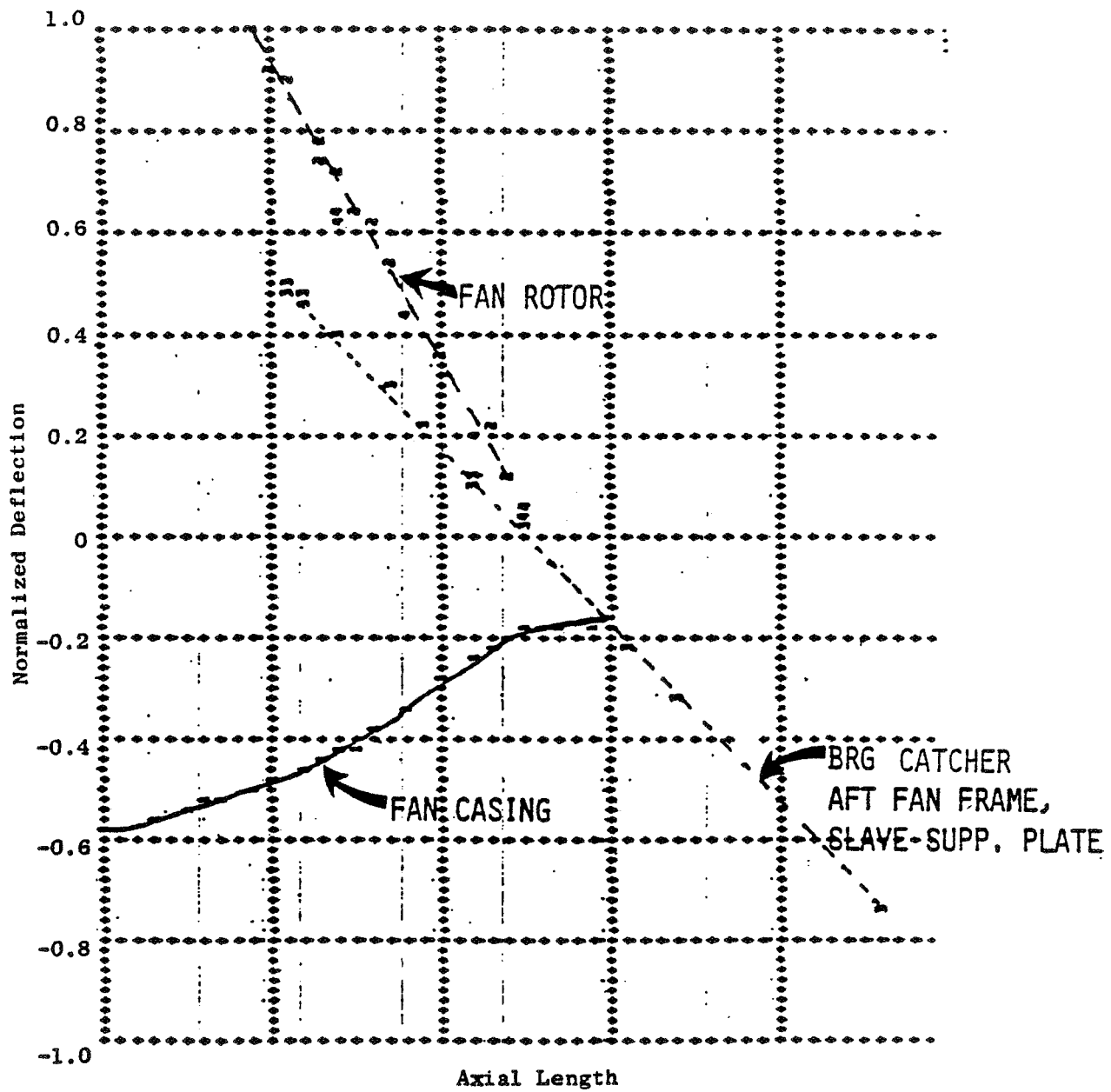


Figure 92. Blade-Out Test Vehicle Predicted Mode Shape at 4043 rpm.

APPENDIX B

BLADE-OUT TEST VEHICLE SUBSYSTEM NORMAL MODE SHAPES

Figures 93 through 105 show the natural frequencies and normalized mode shapes predicted for the casing subsystem. Figures 106 through 109 present the frequencies and normalized shapes for the rotor subsystems.

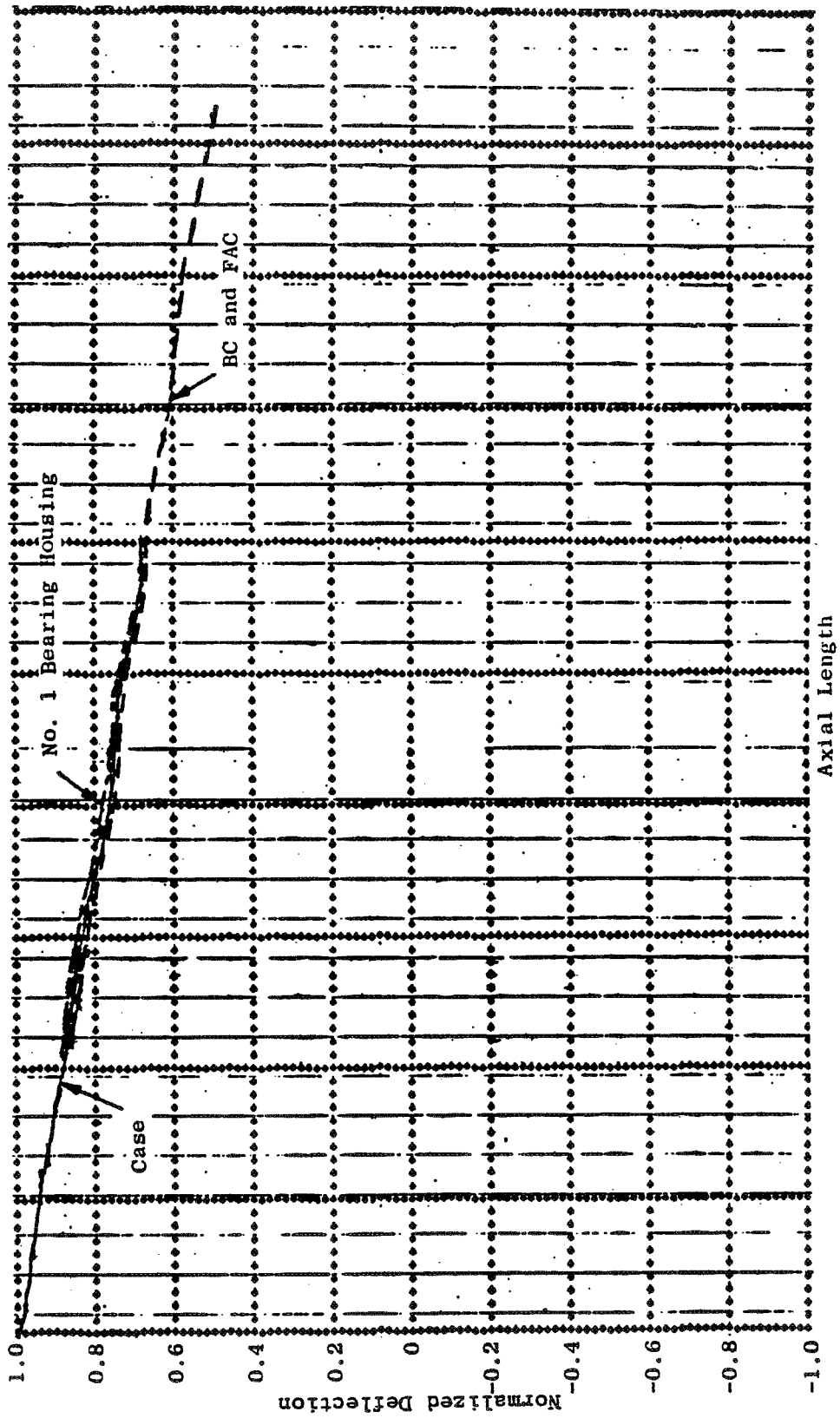


Figure 93. Blade-Out Test Vehicle, Subsystem 1 (Casing), 424 rpm.

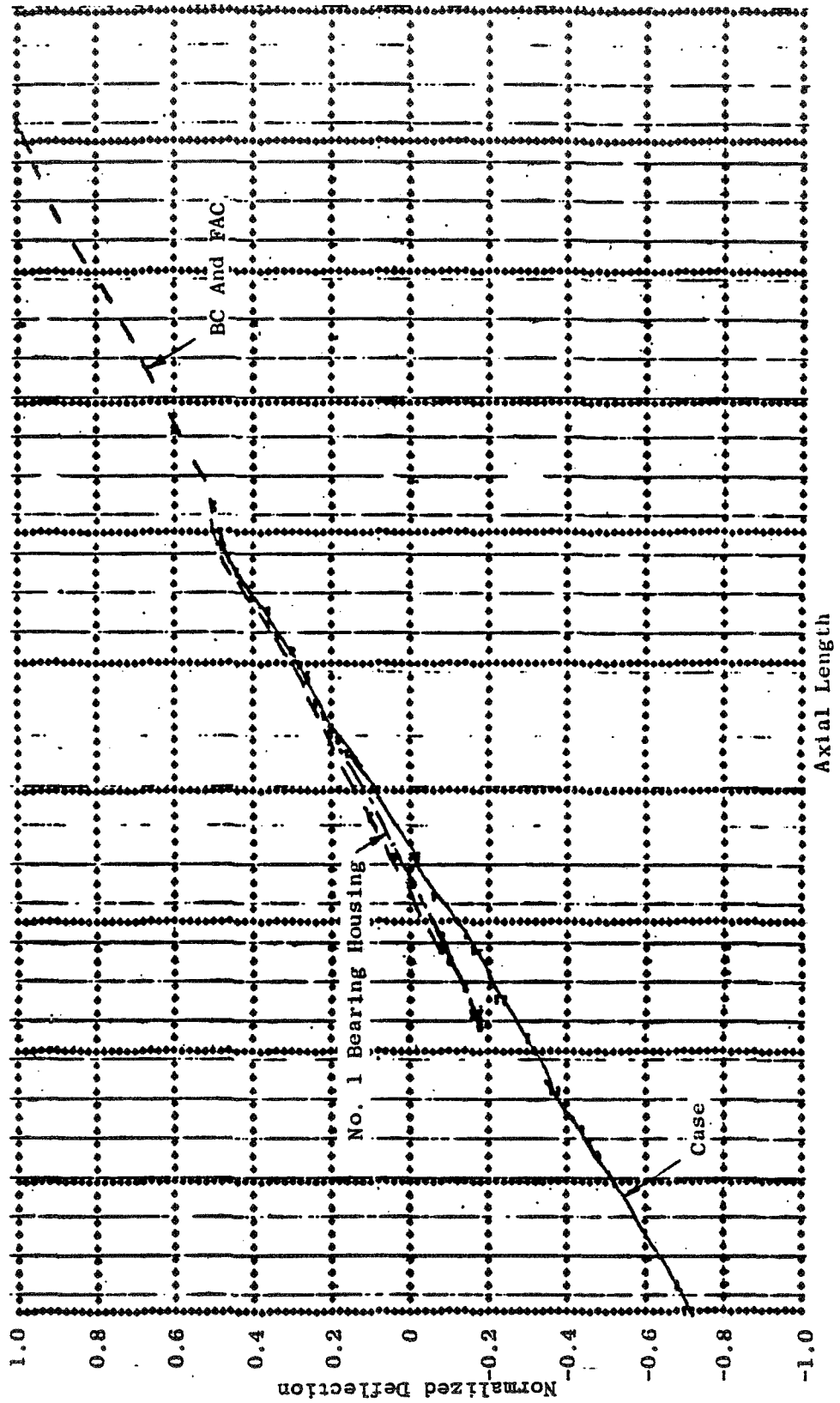


Figure 94. Blade-Out Test Vehicle, Subsystem 1 (Casing), 976 rpm.



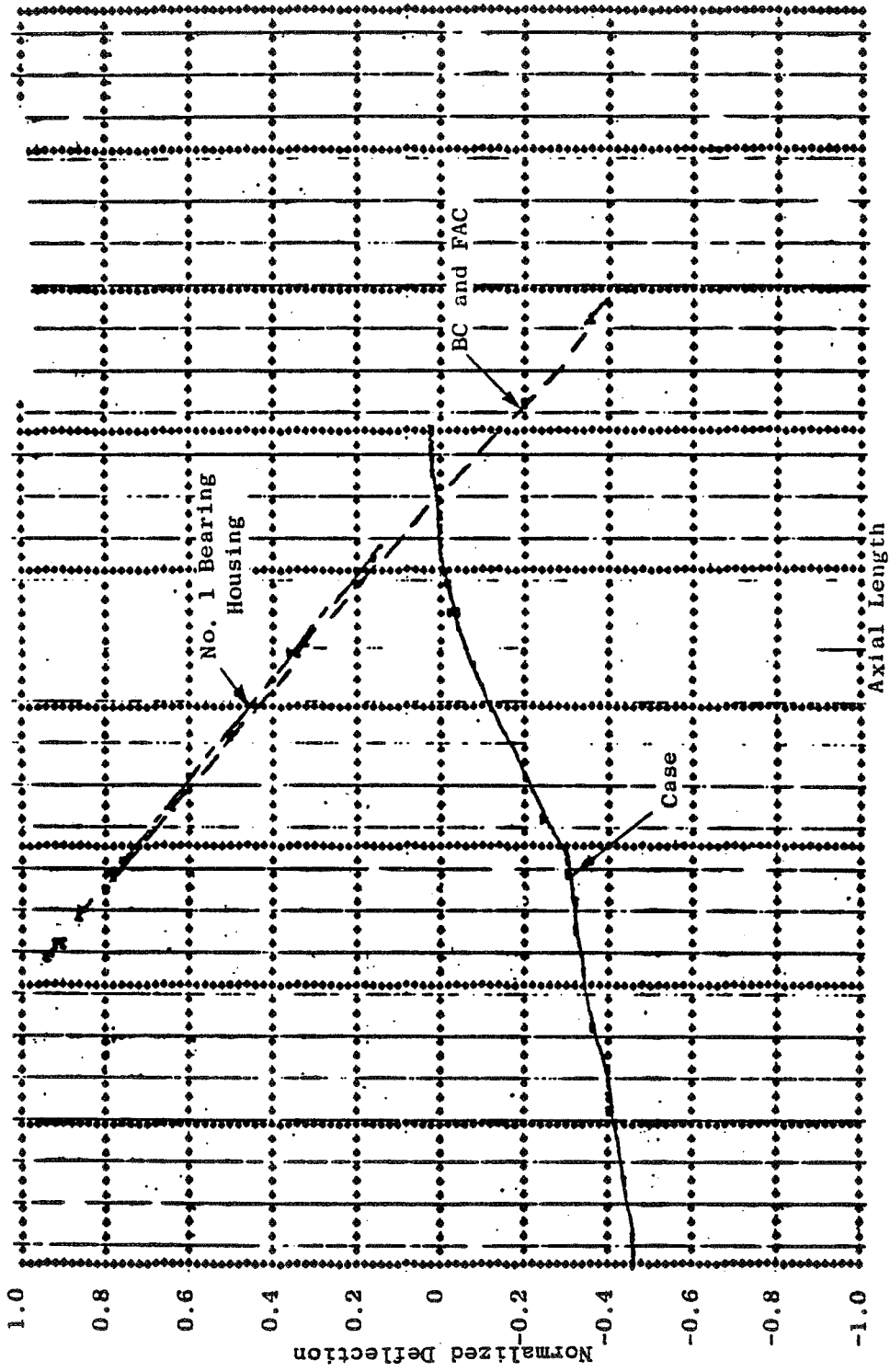


Figure 95. Blade-Out Test Vehicle, Subsystem 1 (Casing), 5241 rpm.

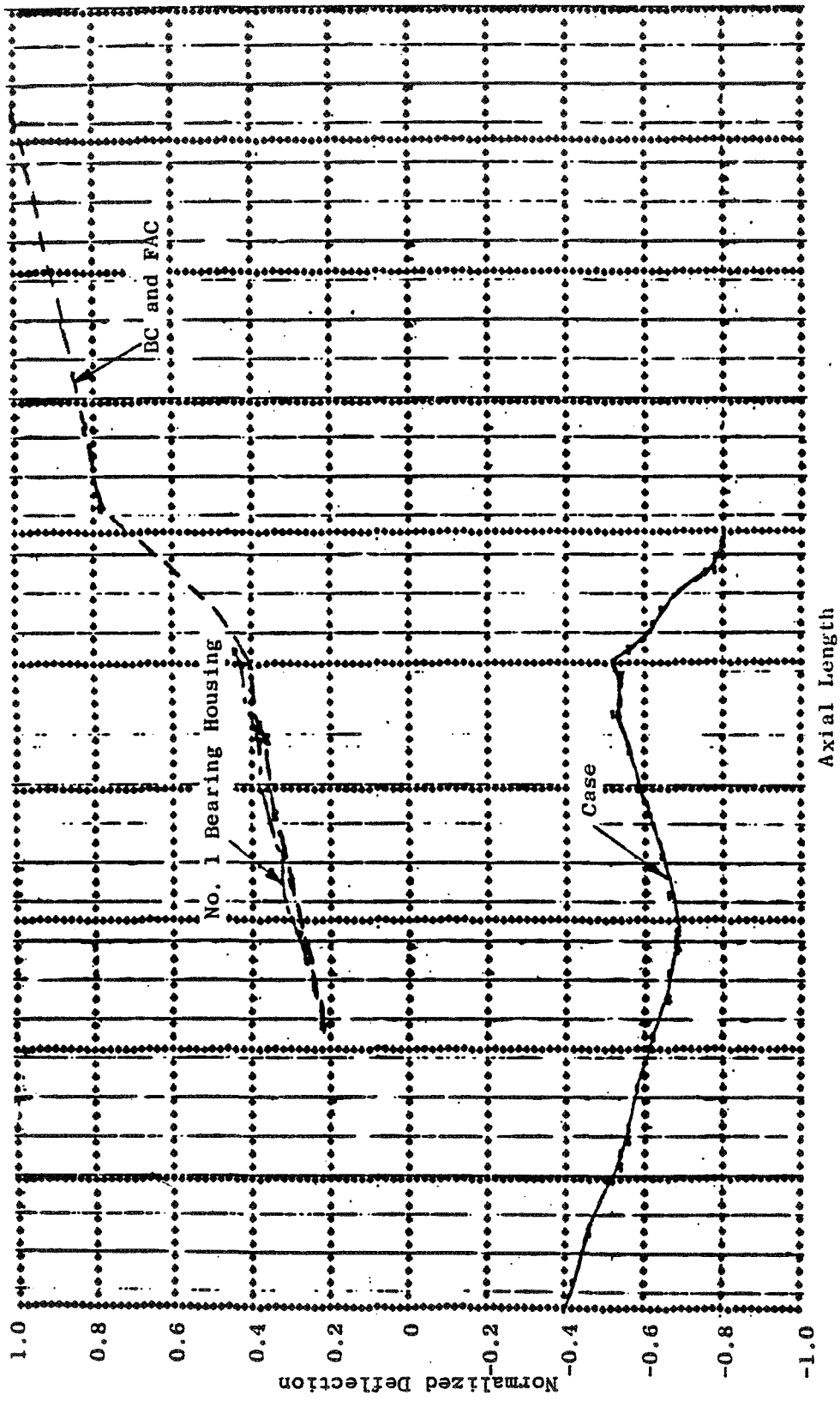


Figure 96. Blade-Out Test Vehicle, Subsystem 1 (Casing), 6535 rpm.

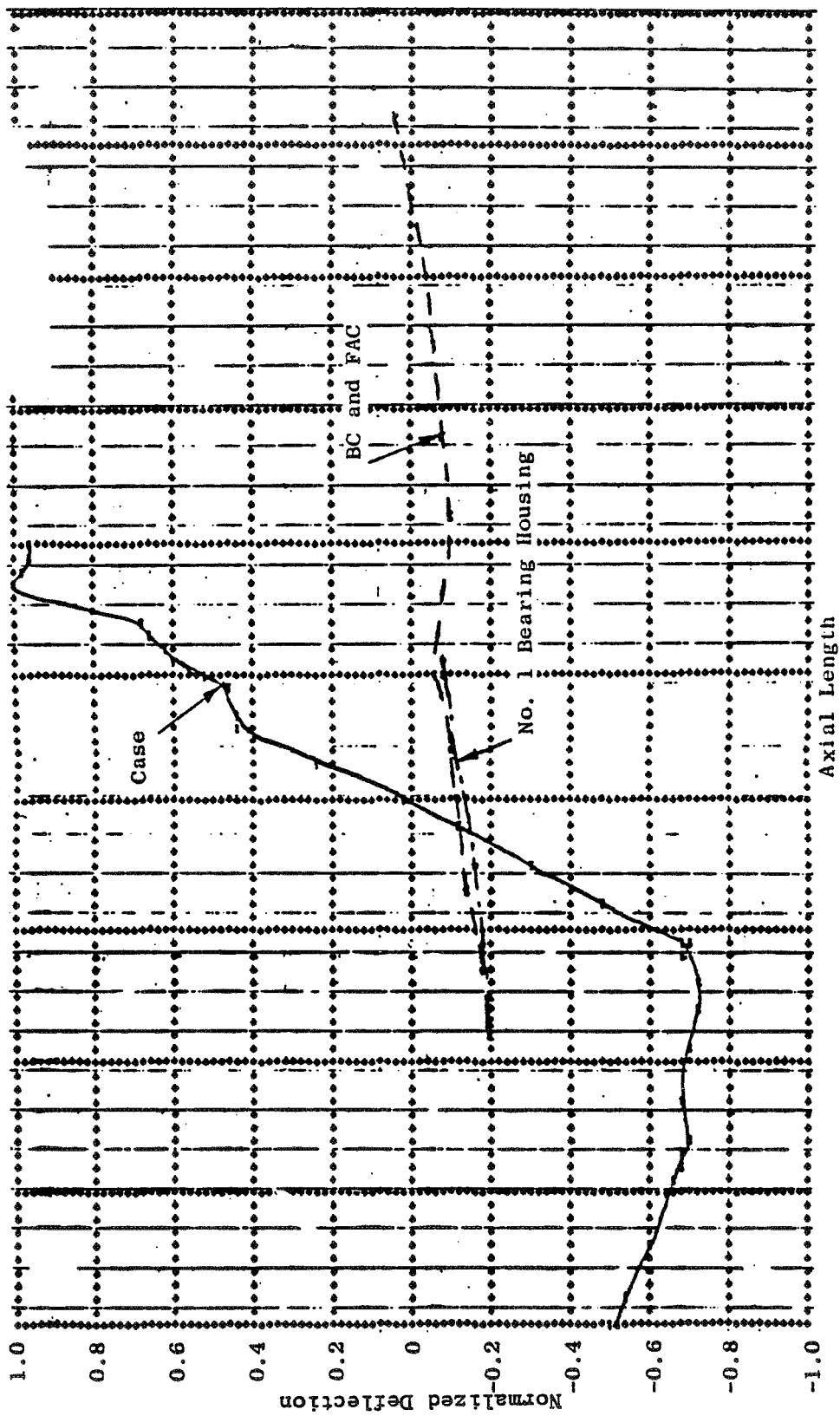


Figure 97. Blade-Out Test Vehicle, Subsystem 1 (Casing), 11,539 rpm.

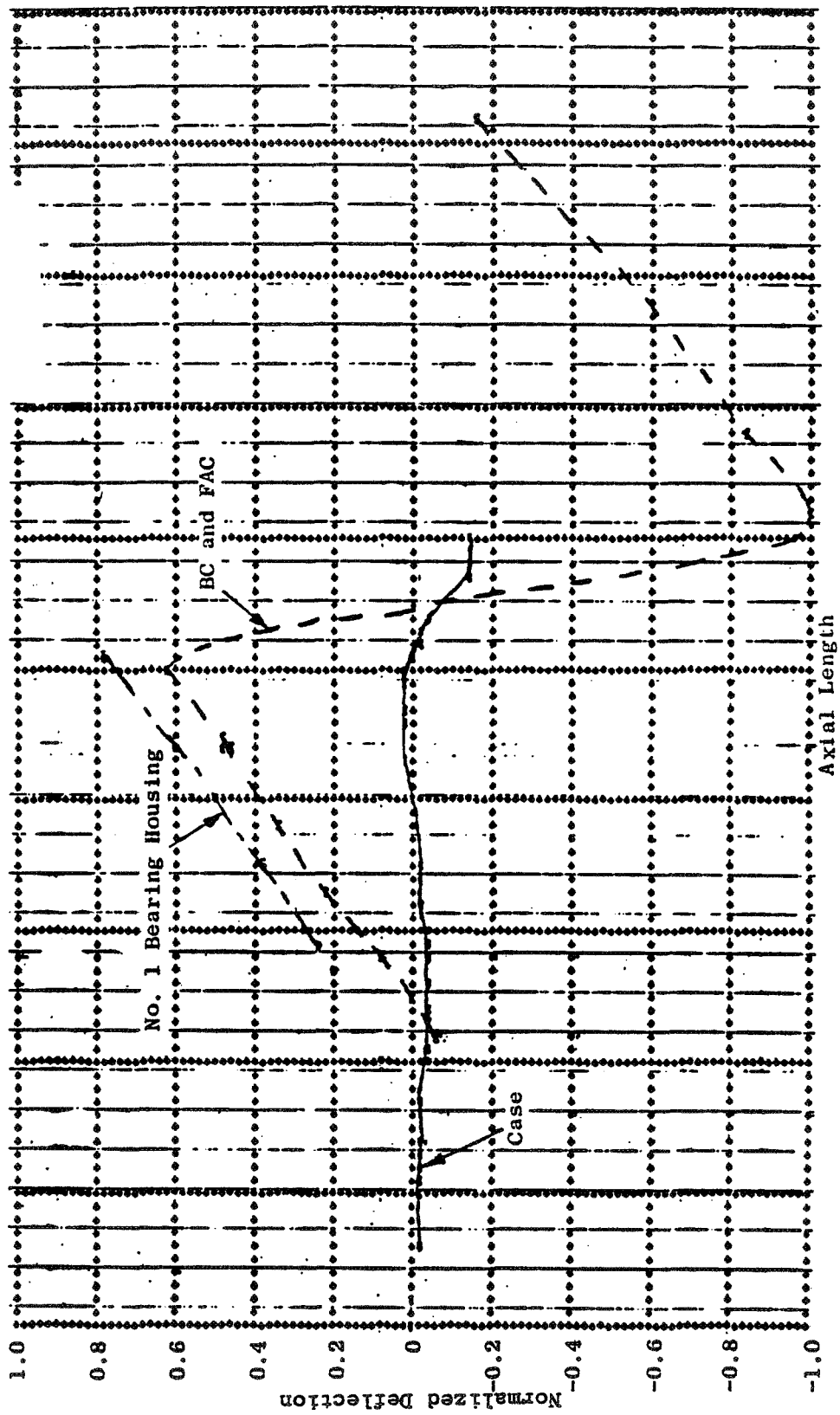


Figure 98. Blade-Out Test Vehicle, Subsystem 1 (Casing), 16,258 rpm.

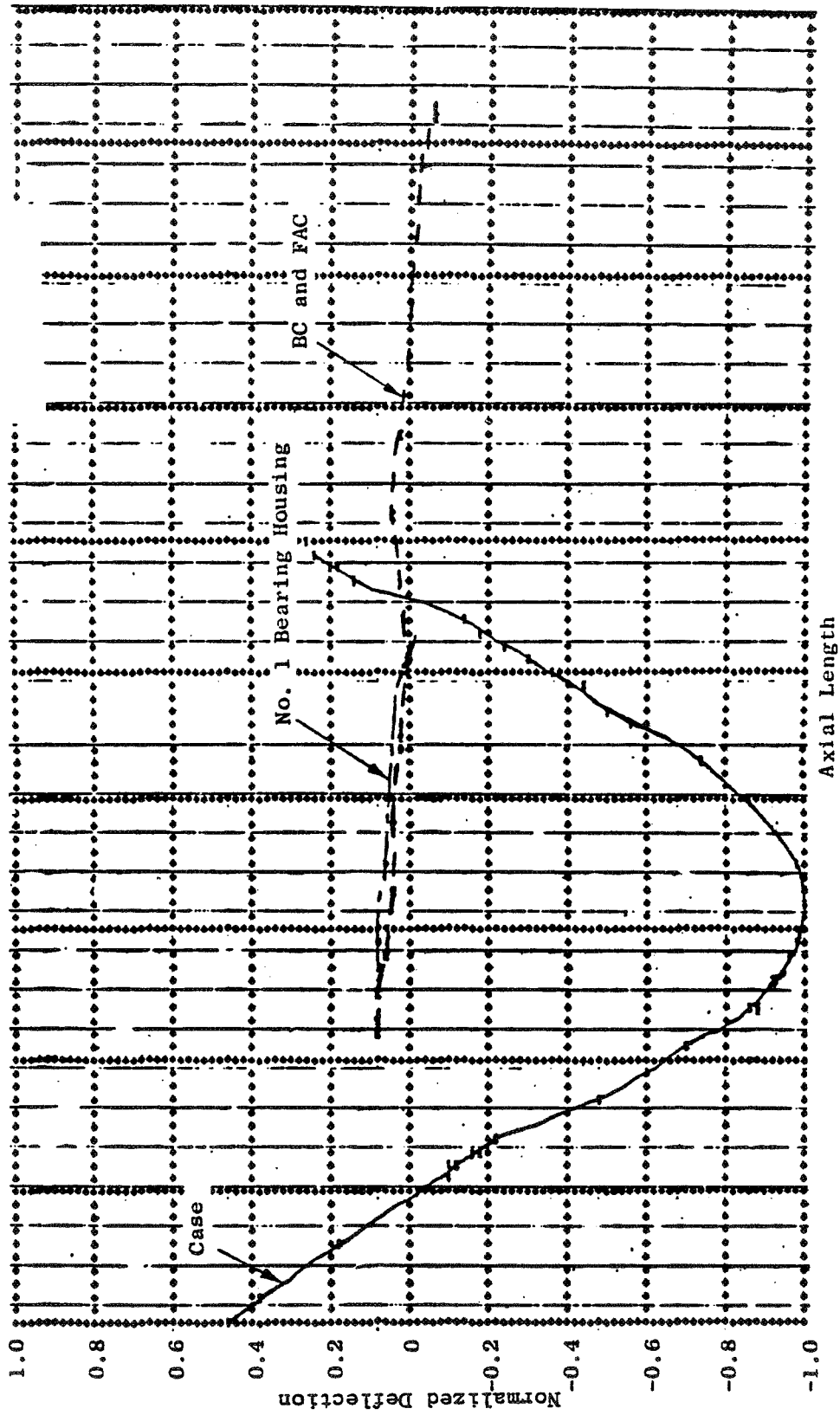


Figure 99. Blade-Out Test Vehicle, Subsystem 1 (Casing), 18,878 rpm.

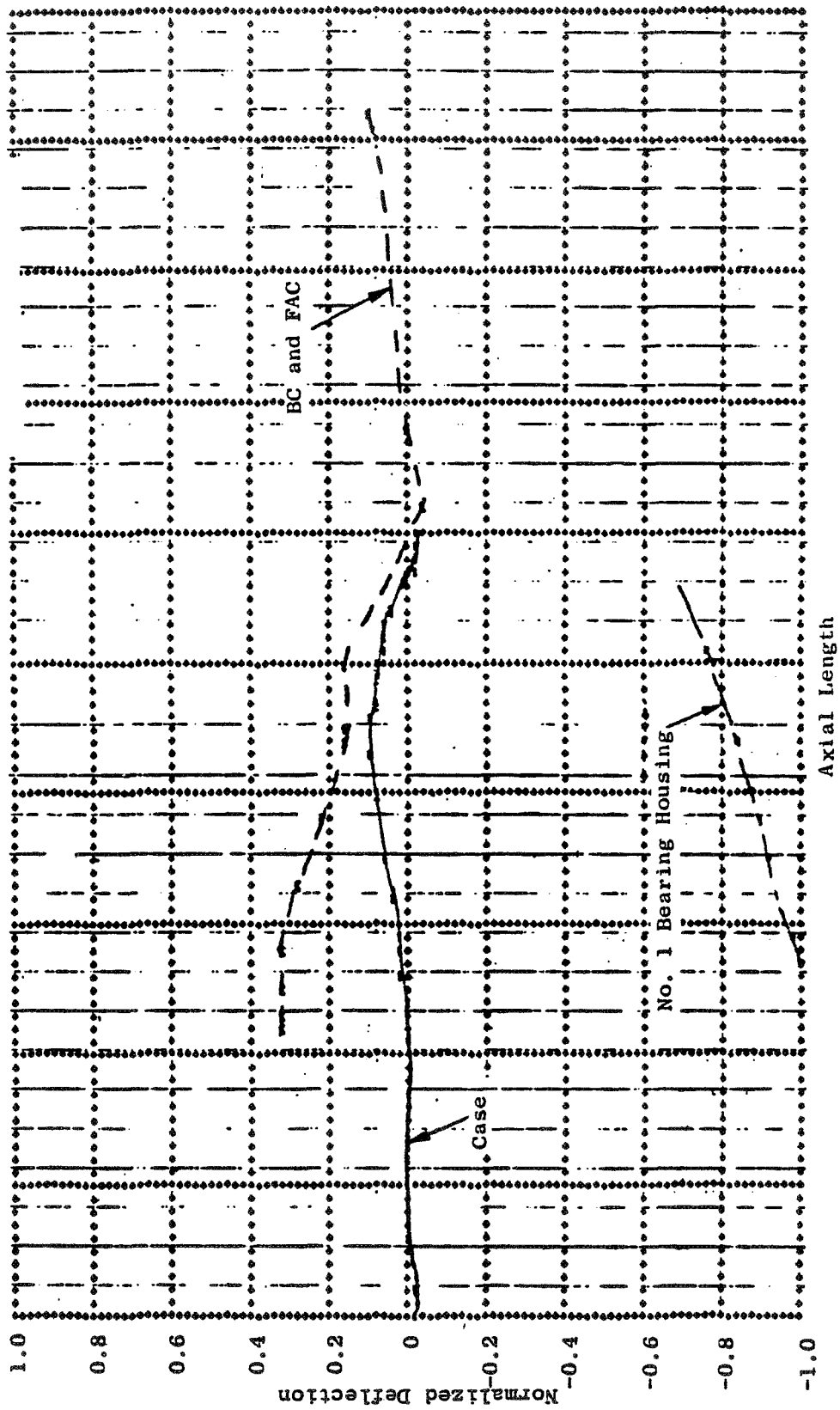


Figure 100. Blade-Out Test Vehicle, Subsystem 1 (Casing), 36, 388 rpm.

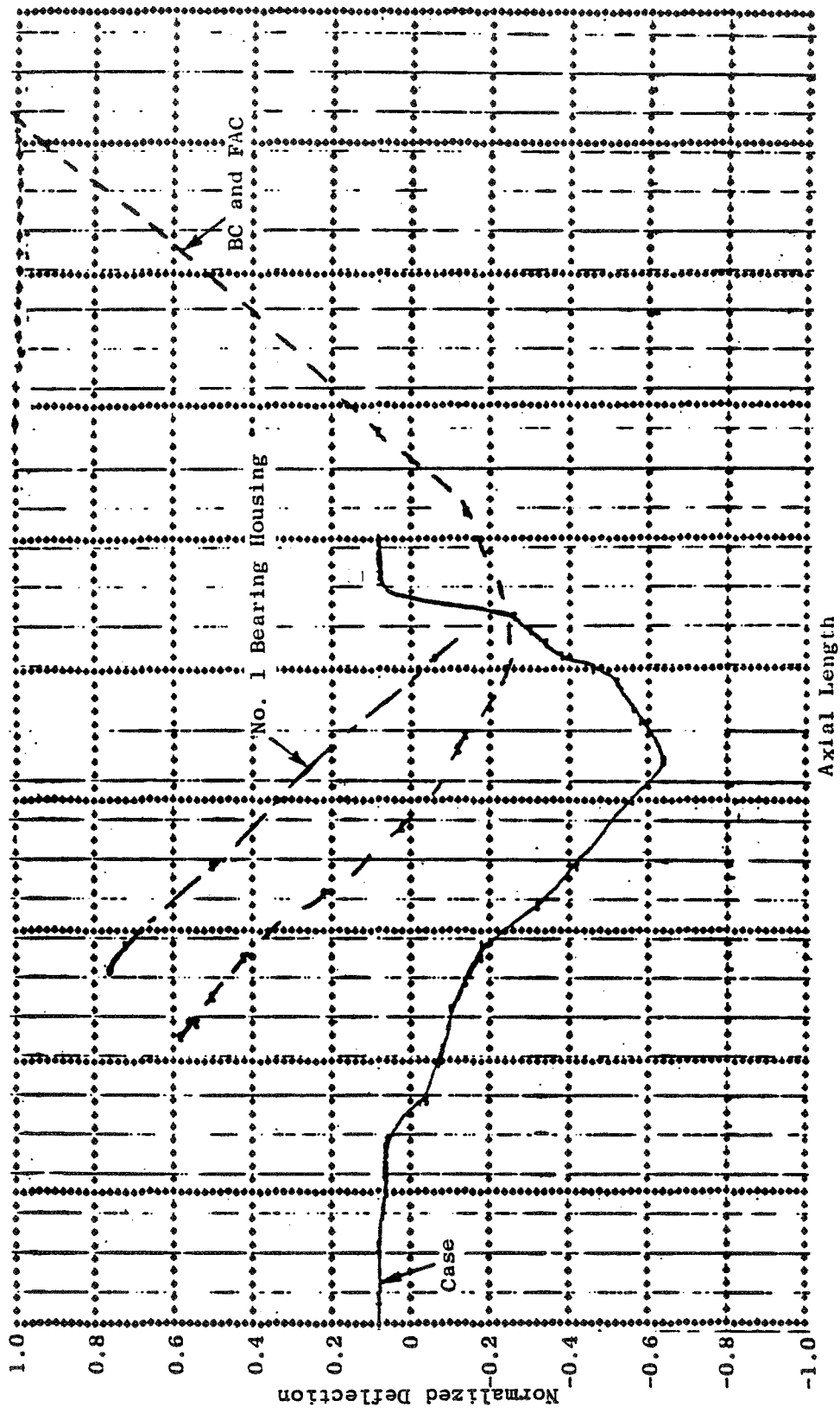


Figure 101. Blade-Out Test Vehicle, Subsystem 1 (Casing), 39,995 rpm.

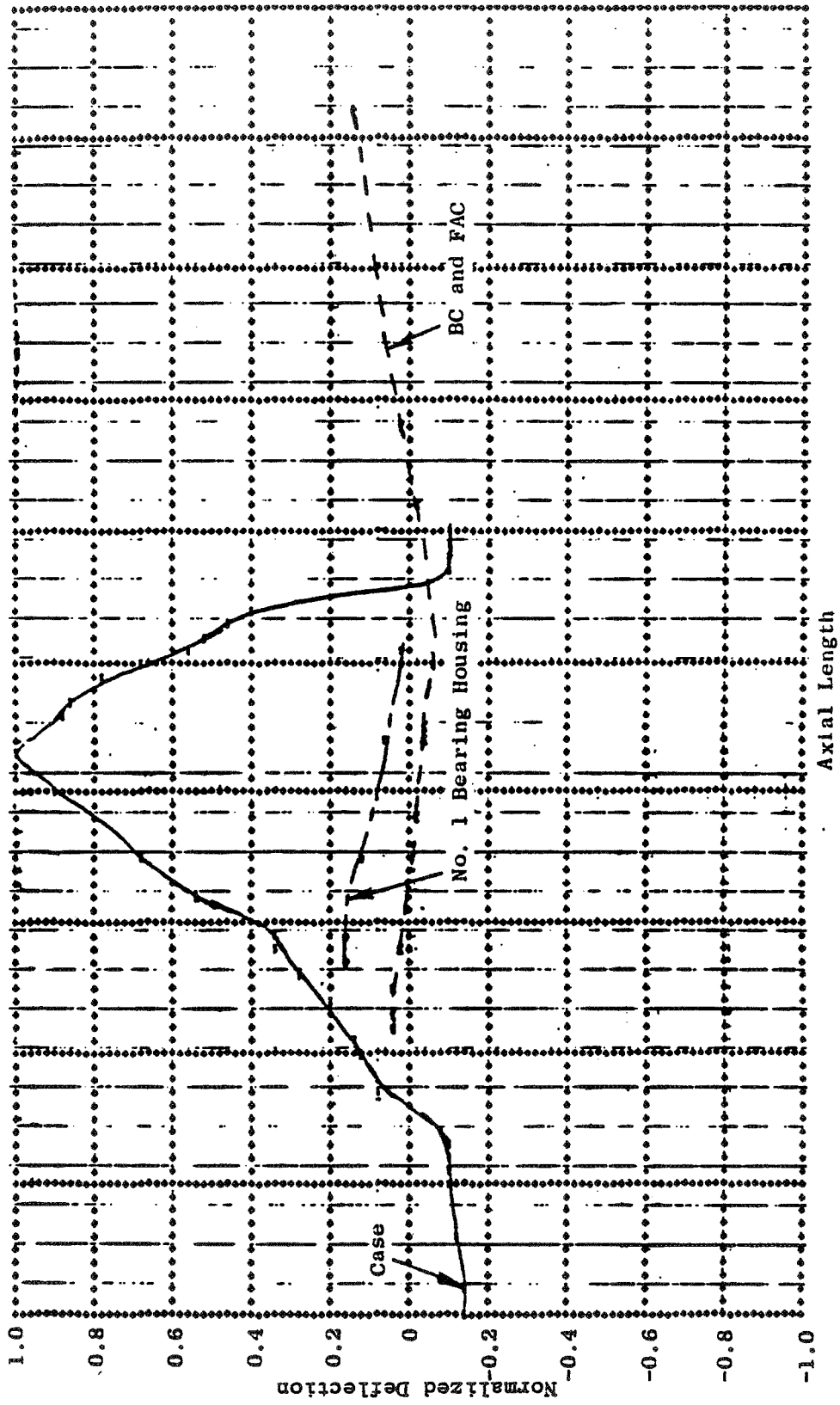


Figure 102. Blade-Out Test Vehicle, Subsystem 1 (Casing), 41,284 rpm.

ORIGINAL PAGE IS  
OF POOR QUALITY



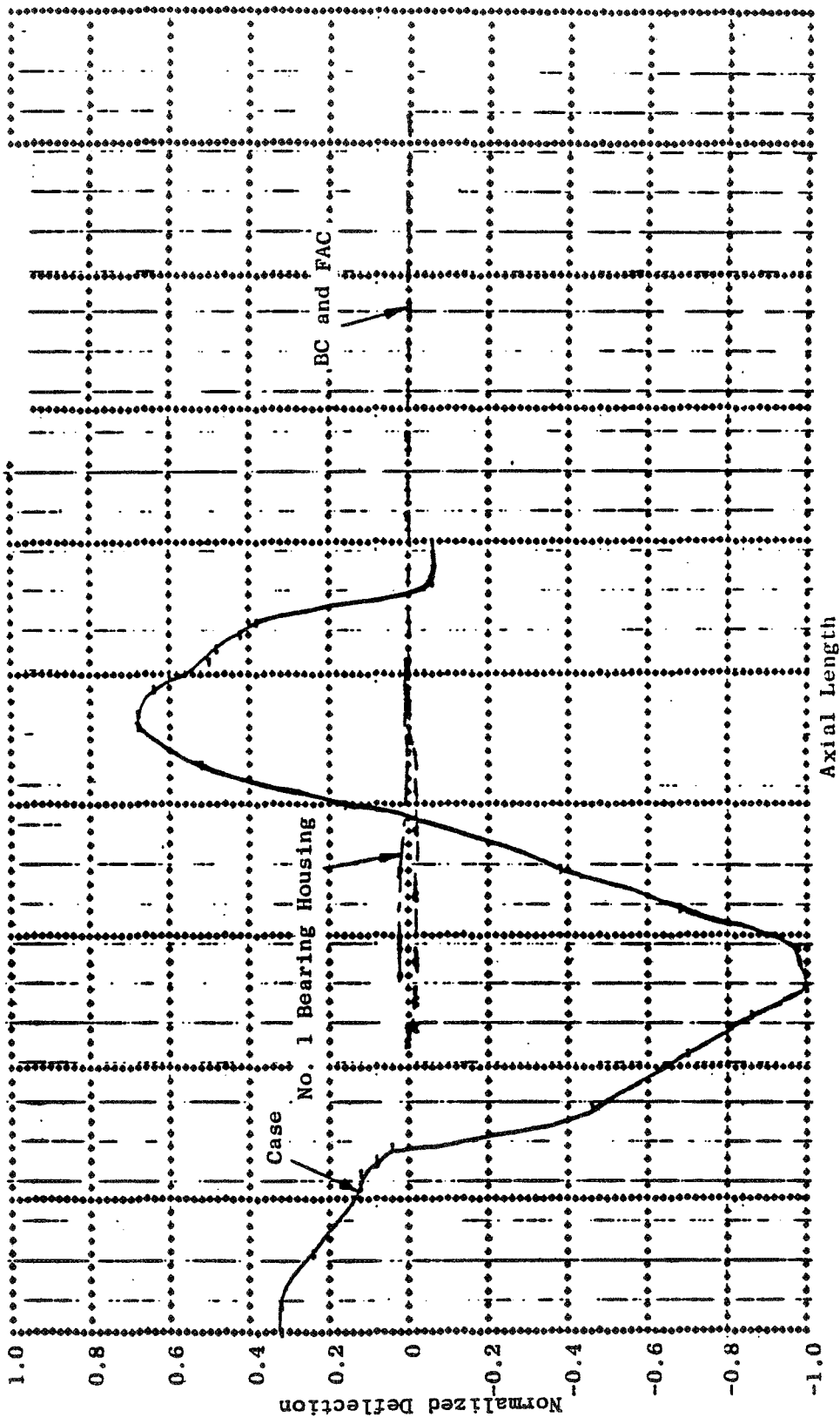


Figure 103. Blade-Out Test Vehicle, Subsystem 1 (Casing), 53,107 rpm.

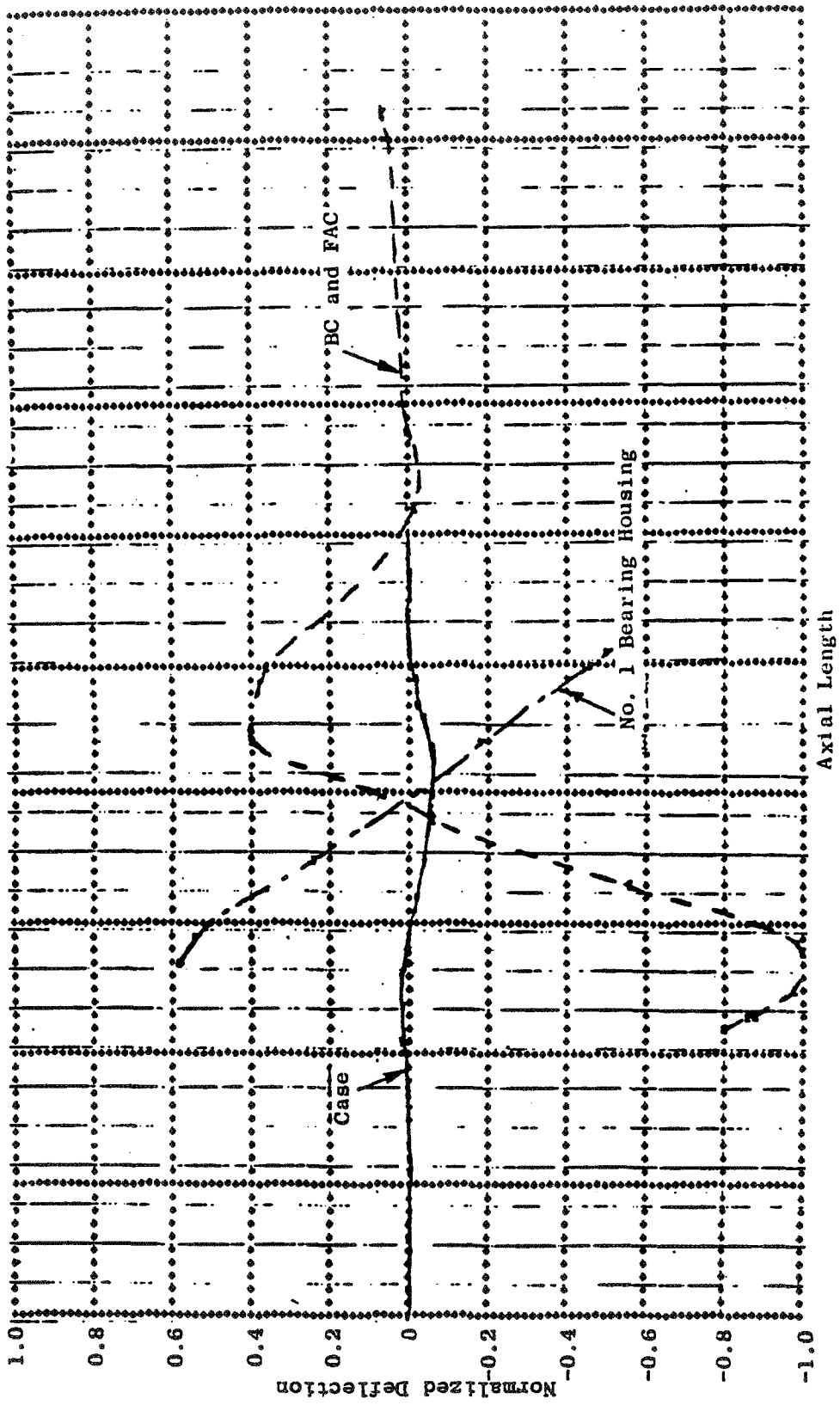


Figure 104. Blade-Out Test Vehicle, Subsystem 1 (Casing), 69,016 rpm.

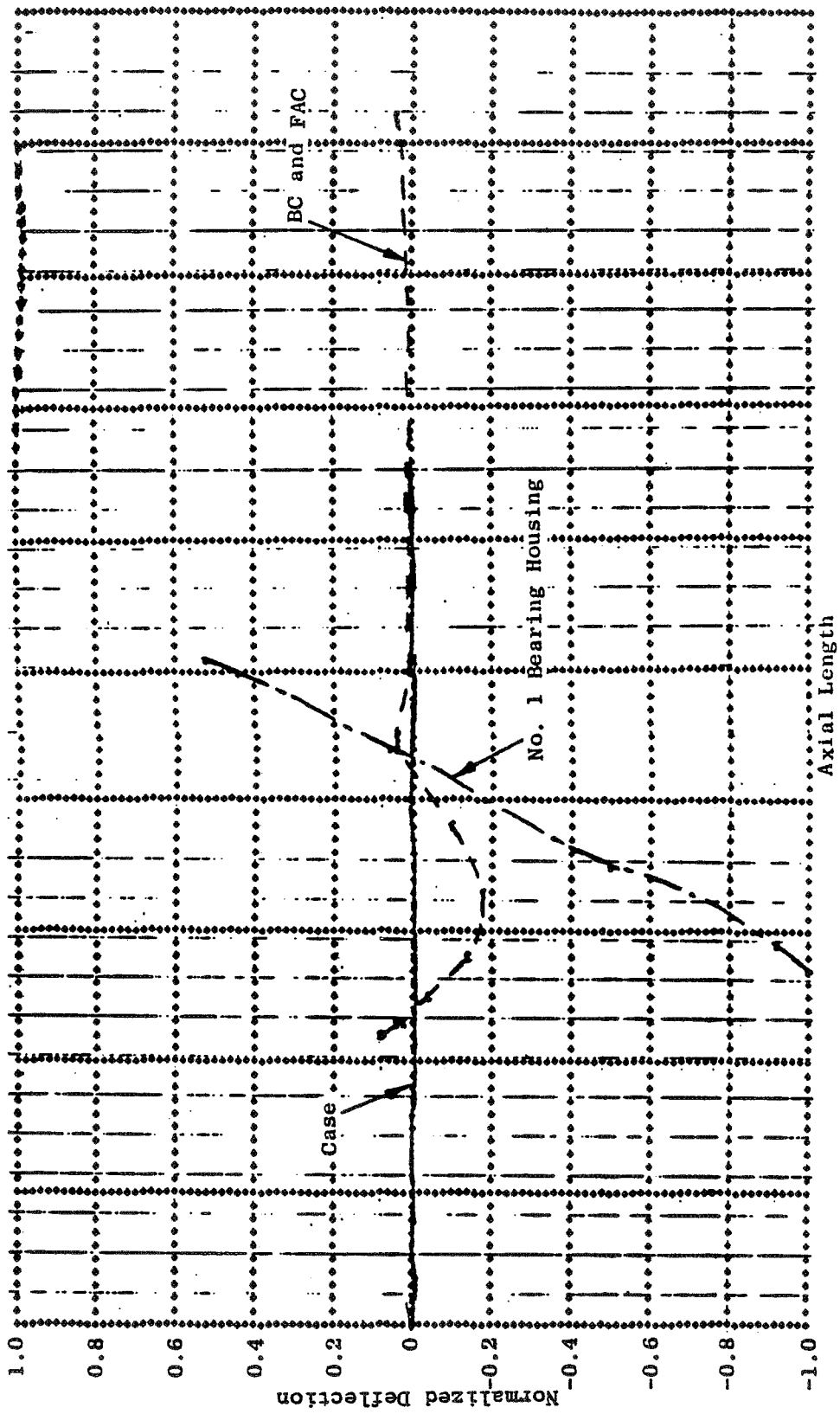


Figure 105. Blade-Out Test Vehicle, Subsystem 1 (Casing), 75,867 rpm.

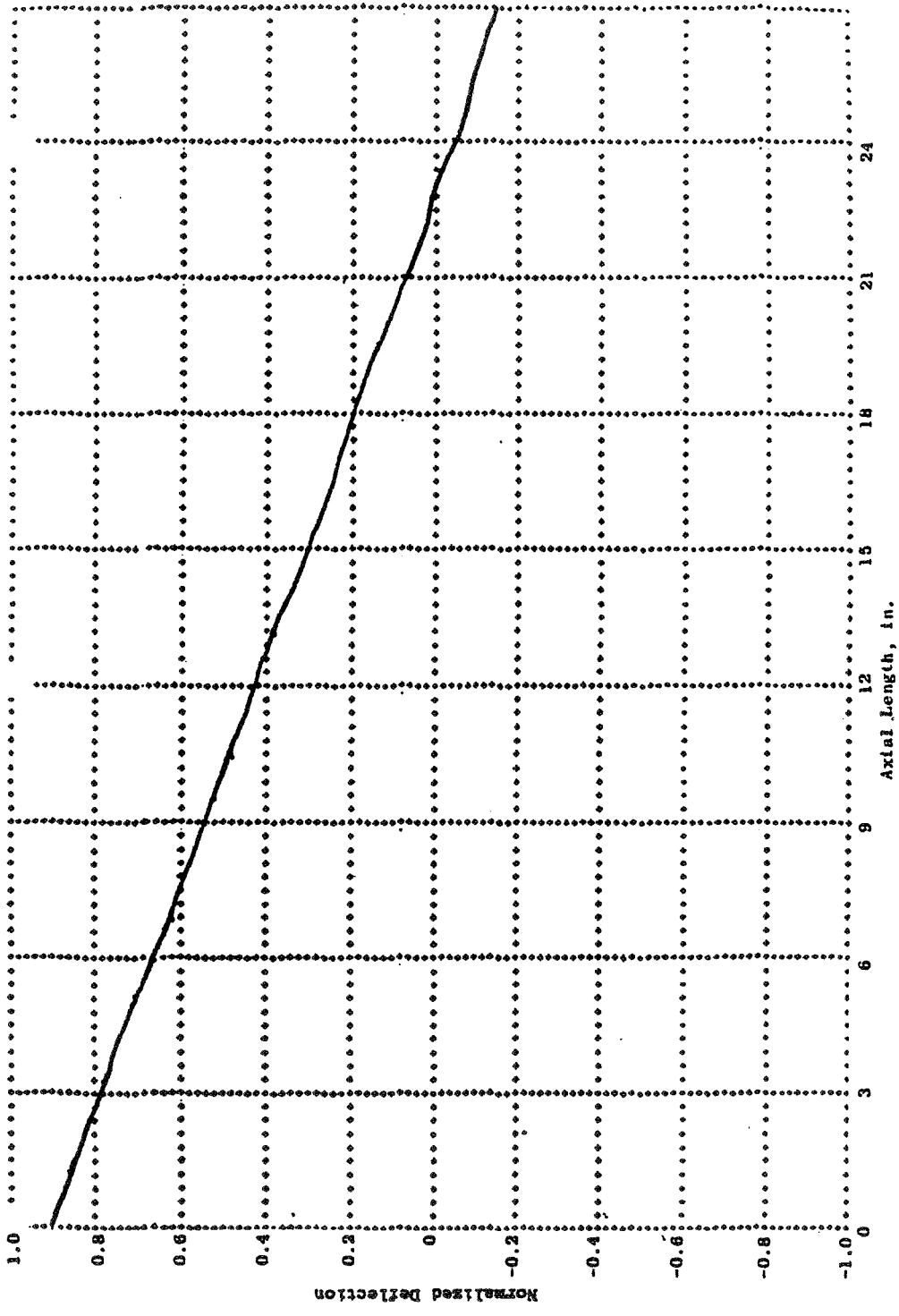


Figure 106. Blade-Out Test Vehicle, Subsystem 2 (Rotor), 46 rpm.

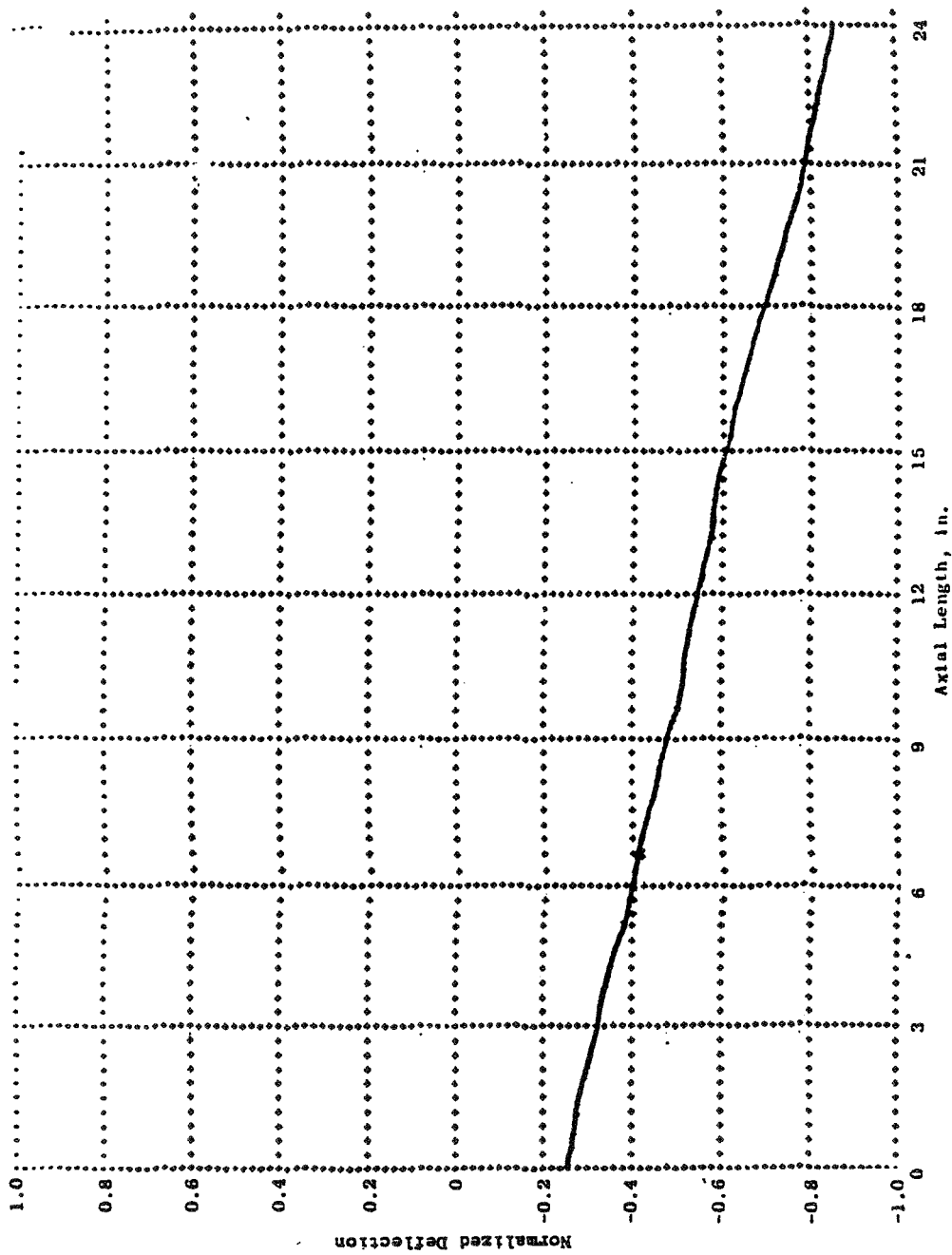


Figure 107. Blade-Out Test Vehicle, Subsystem 2 (Rotor), 146 rpm.

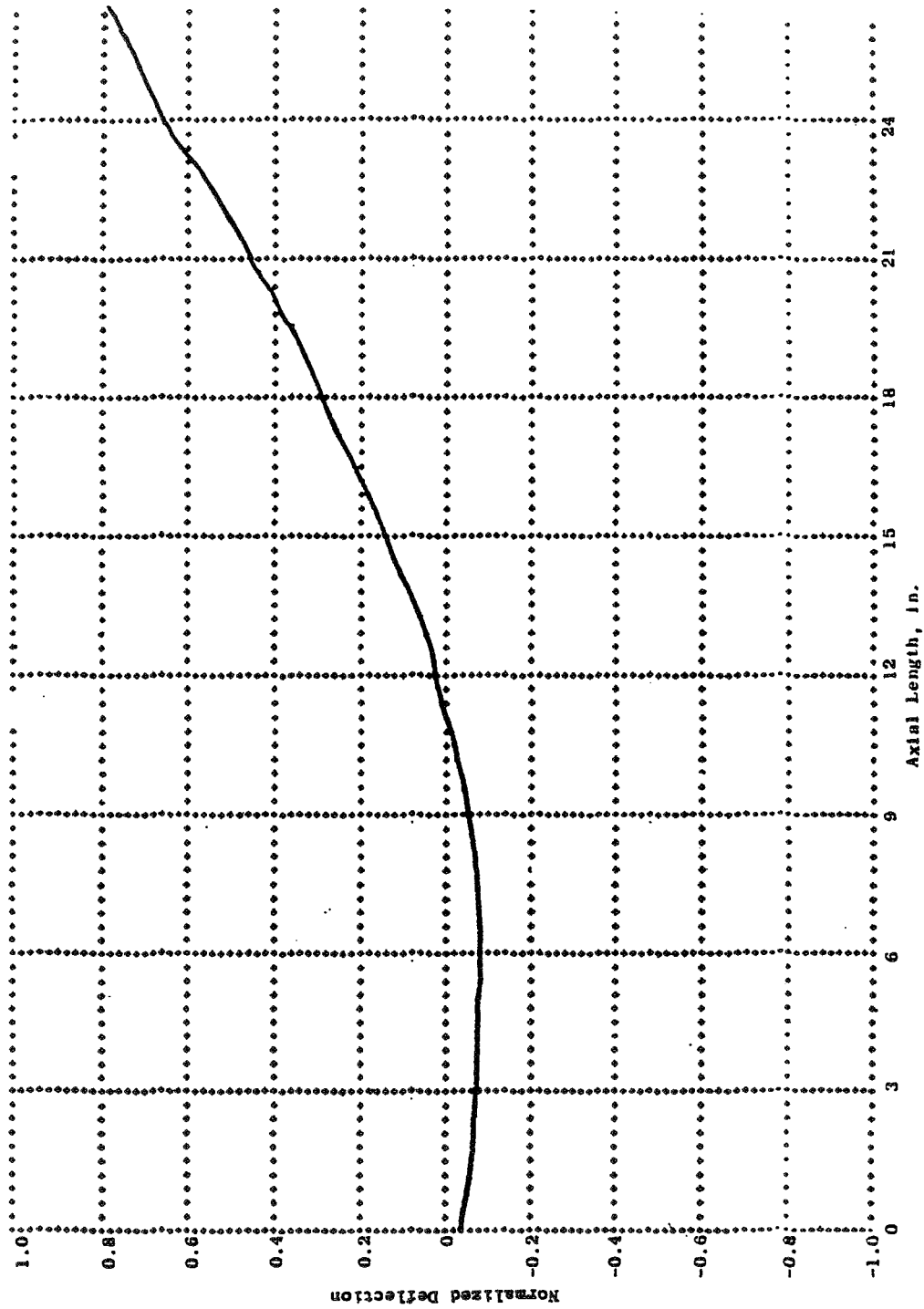


Figure 108. Blade-Out Test Vehicle, Subsystem 2 (Rotor), 17,626 rpm.

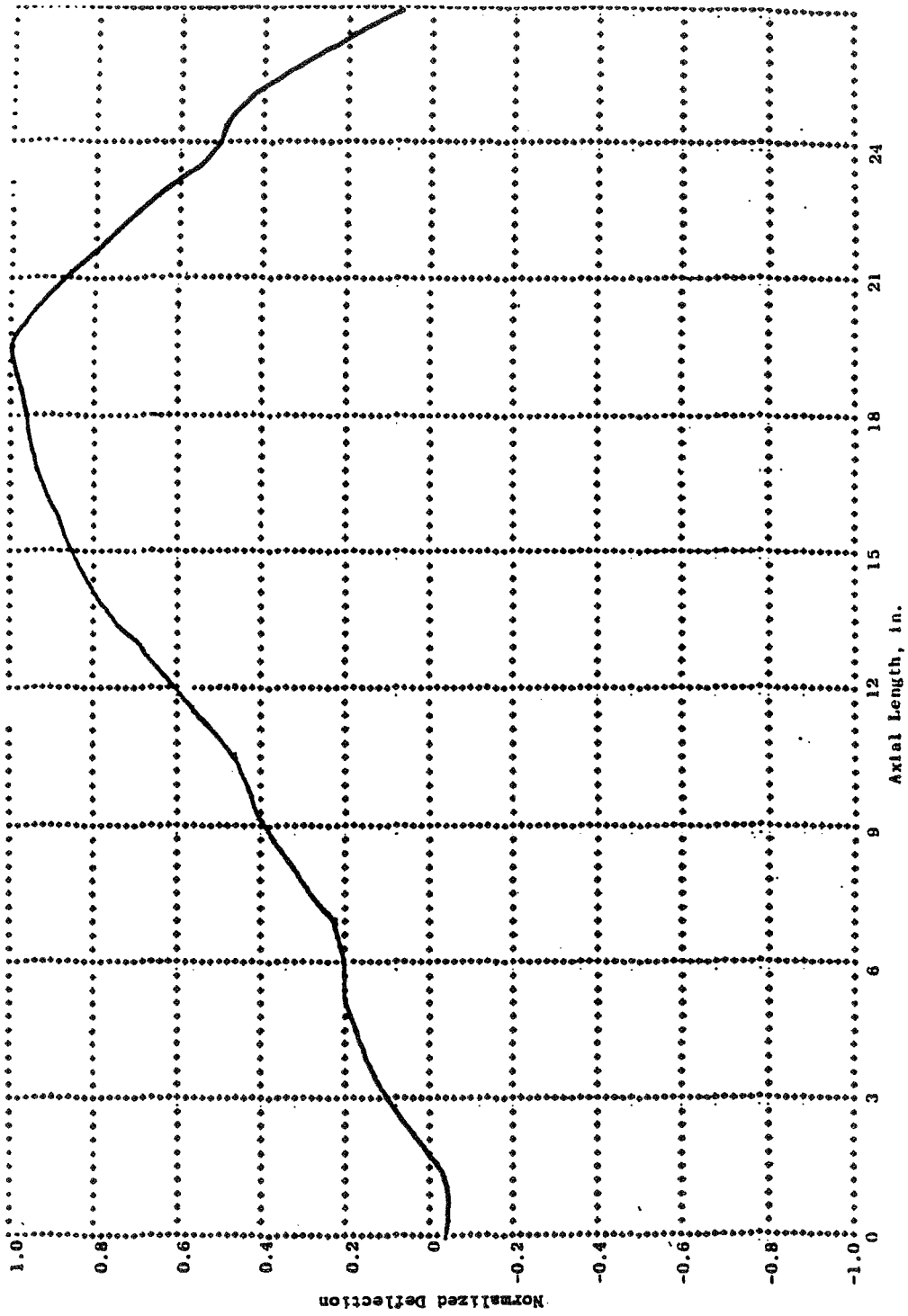


Figure 109. Blade-Out Test Vehicle, Subsystem 2 (Rotor), 78,001 rpm.

APPENDIX C

TETRA DATA FILE FOR THE BLADE-OUT VEHICLE LINEAR ANALYSIS

Figure 110 is a listing of the time-share TETRA data file for the linear analysis of the test vehicle.

LIST1 (Lines 100-760) - Lines 200 and 201 are control statements, for the casing subsystem, that call in the model data in the vertical and horizontal directions respectively. The model files were previously created by the VAST computer code. For Figure 110, the same model data is used in either direction. The number 15.0 is the Q of the casing subsystems. Lines 220 and 224 are the calling statements for the rotor subsystem data files.

LIST2 (Lines 770-1000) - These lines define the connecting elements utilized to join the casing and rotor subsystems.

Lists 1 and 2 define the boundary conditions of the test vehicle. List 3 is the command section of the data file. The key items on this list are the following:

Line No.	
1090	Definition of the beginning speed (4100).
1120	Magnitude of the unbalance (gram-inches) time at initiation of unbalance = 0.00004 seconds with the unbalance located at Joint 1.
1130	Definition of joints where gyroscopic effects need to be considered.
1150-1330	Definition of joints and directions requested for the plotting output file.



```

100 $LIST1
110 NAME=60HBACH-CALLARDO DATE 8-80 CHARGE 19510
120 ADDRES=60H 500 BSMT MAIL DROP K71 EXT 4279
130 IDENT1=60HWHIRLIGIG TEST VEHICLE TETRA SETUP STAND HOUSING
140 IDENT2=60HCHECK CASE VERT & HORZ MODEL -GROUNED CASING
200 SS(1,1)=7,0,0,0,15,0,15,
210 8,0,0,0,15,0,15,
220 1,0,0,0,0,10,
225 2,0,0,0,0,10
760 $
770 $LIST2
780 ITYPE=5,
790 ILEM=1,
800 JT=4,2,
805 YS=1.103E6,
810 ZS=1.103E6,
850 IDAMP=1,
860 GELEM=15,
870 GFREQ=67.3,
880 $
890 $LIST2
900 ITYPE=5,
910 ILEM=2,
920 JT=20,3,
925 YS=3.4E6,
930 ZS=3.4E6,
970 IDAMP=1,
980 GELEM=15,
990 GFREQ=67.3,
1000 $
1010 $LIST3
1020 ISTART=0,
1030 DELTA=0.000015,
1040 TFINAL=0.32,
1050 IPRMUL=500,
1060 IPLMUL=10,
1070 IROTI=1,
1080 BEGTIM=0,
1090 BEGRPM=4100,
1100 TRHIS(1,1)=
1110 .32,0,
1120 UNBAL(1,1)=.00004,1, 10,
1130 GYRO(1,1)=
1140 1,3.20E5,
1150 NPD(1,1)=
1160 1,1,
1170 35,1,
1180 2,1,
1190 4,1,-
1200 3,1,
1200 NEPD(1,1)=
1290 1,4,1,
1295 1,4,3,
1310 2,20,1,
1315 2,20,3,
1330 $

```

Figure 110. Listing of TETRA Input Data File.

## APPENDIX D

### BLADE-OUT VEHICLE TETRA RESULTS FOR MODERATE UNBALANCE

Steady-state response as a function of speed was determined by running a succession of solutions initiated at discrete rpm's to cover the speed range of interest. Moderate unbalance levels were used to assure a linear (no rub) solution. The resulting time histories at each speed are given in this Appendix. The levels attained after the initial starting transients decayed were used to define the steady-state response as a function of speed.

The individual TETRA time histories with moderate unbalance are given in Figures 111 through 122. These plots show No. 1 bearing loads and deflections (vertical direction) at each steady-state speed point as a function of time. In each case, the unbalance was initiated at Time = 0.0004 second.

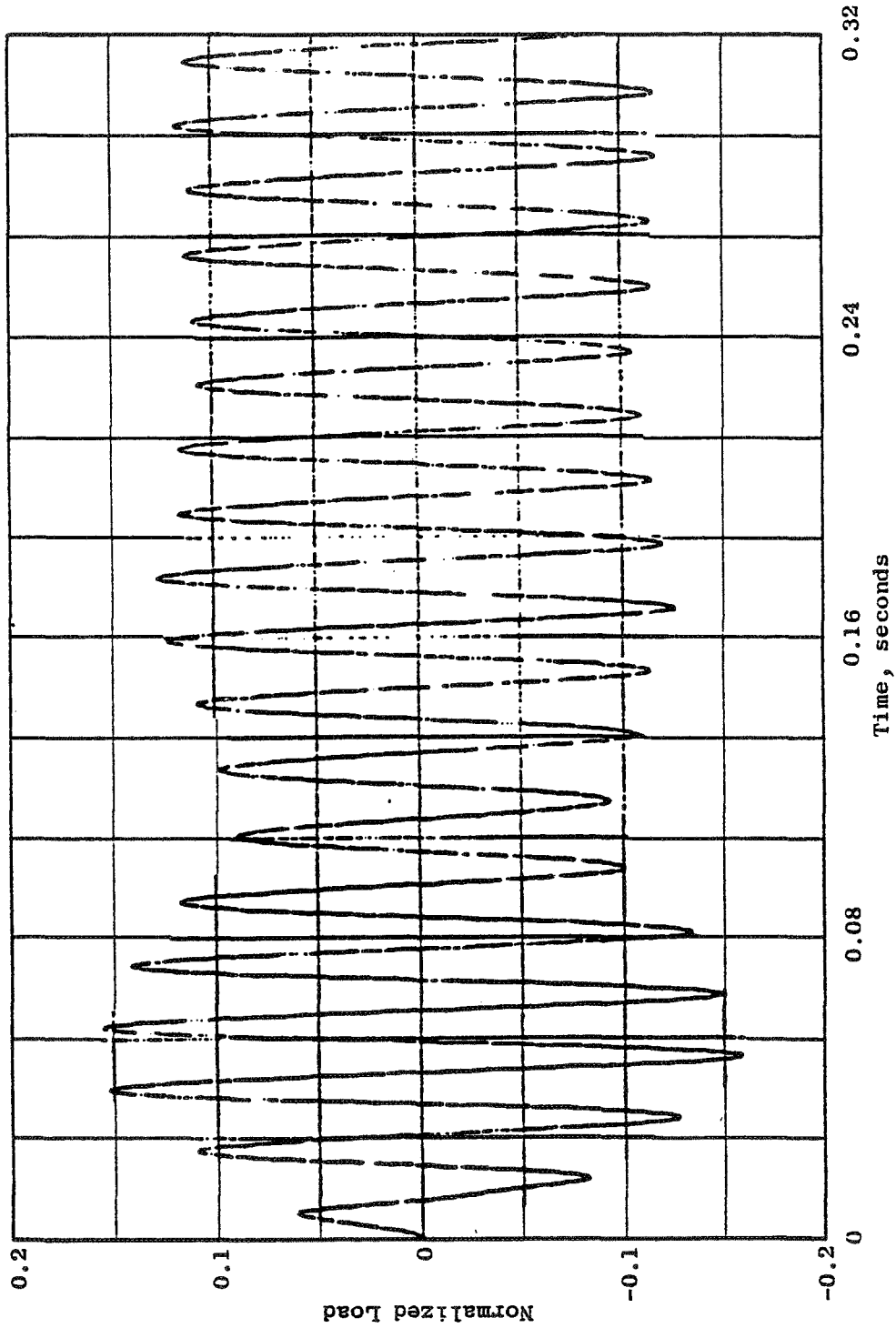


Figure 111. No. 1 Bearing Load at 3500 rpm.

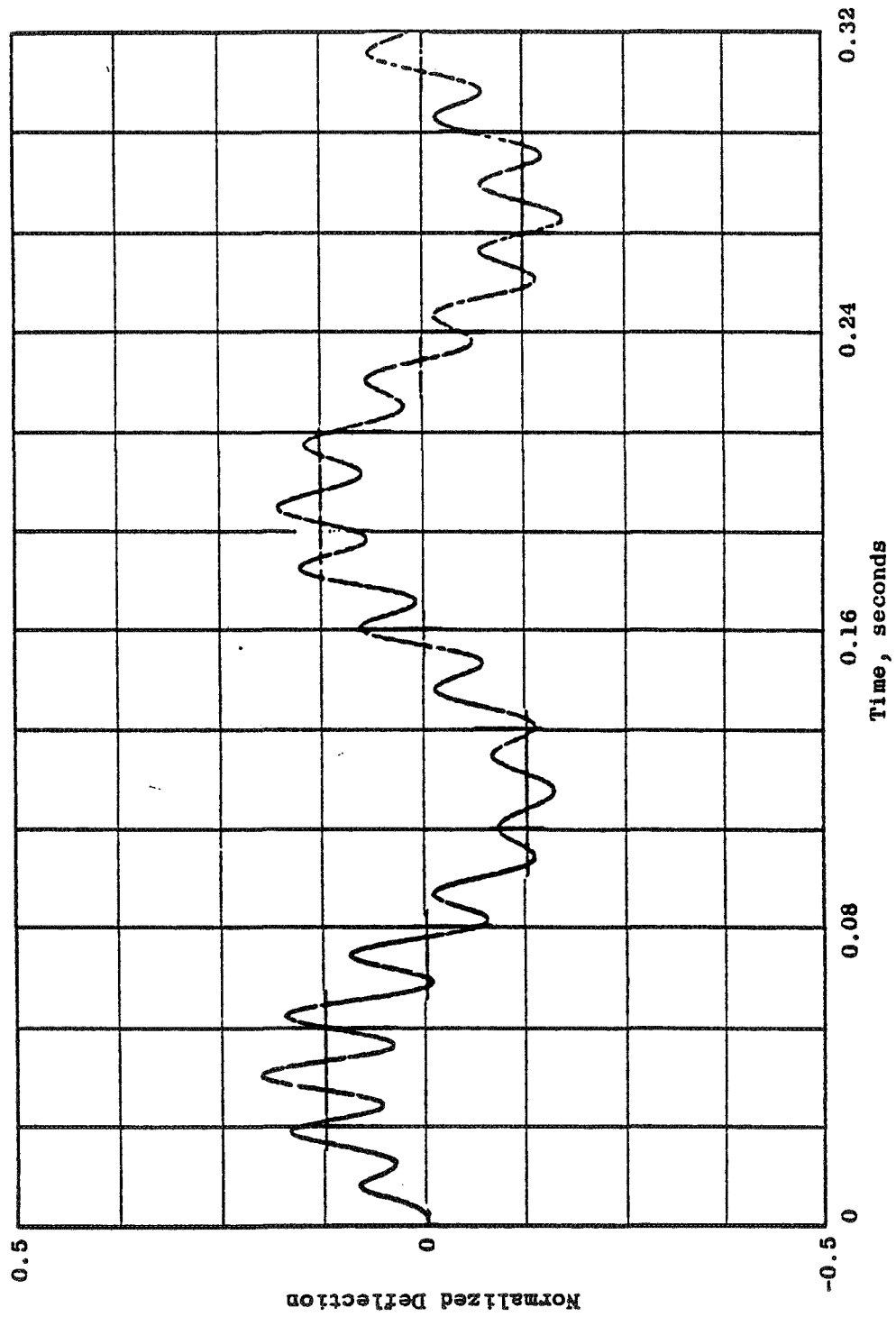


Figure 112. No. 1 Bearing Deflection at 3500 rpm.

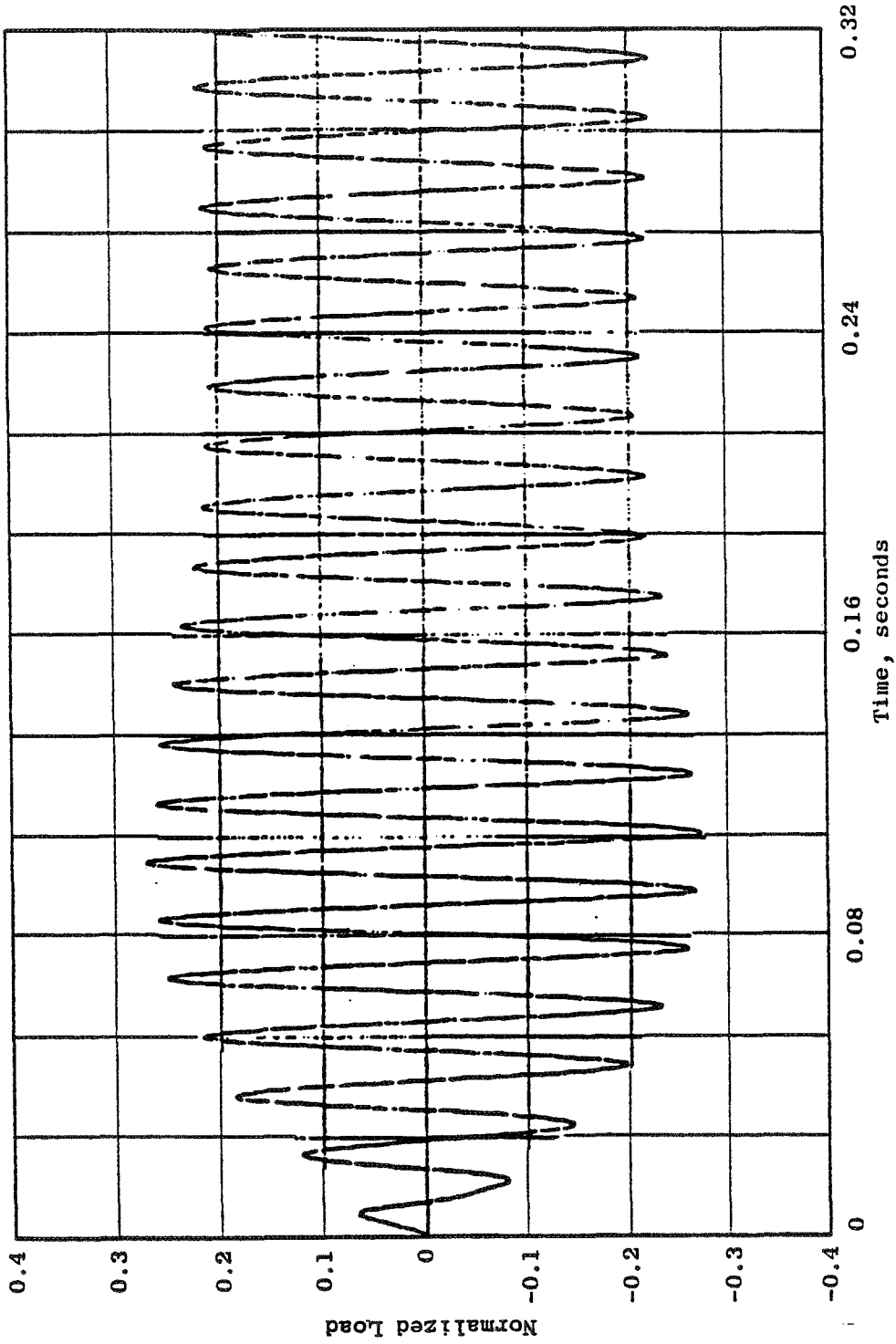


Figure 113. No. 1 Bearing Load at 3800 rpm.

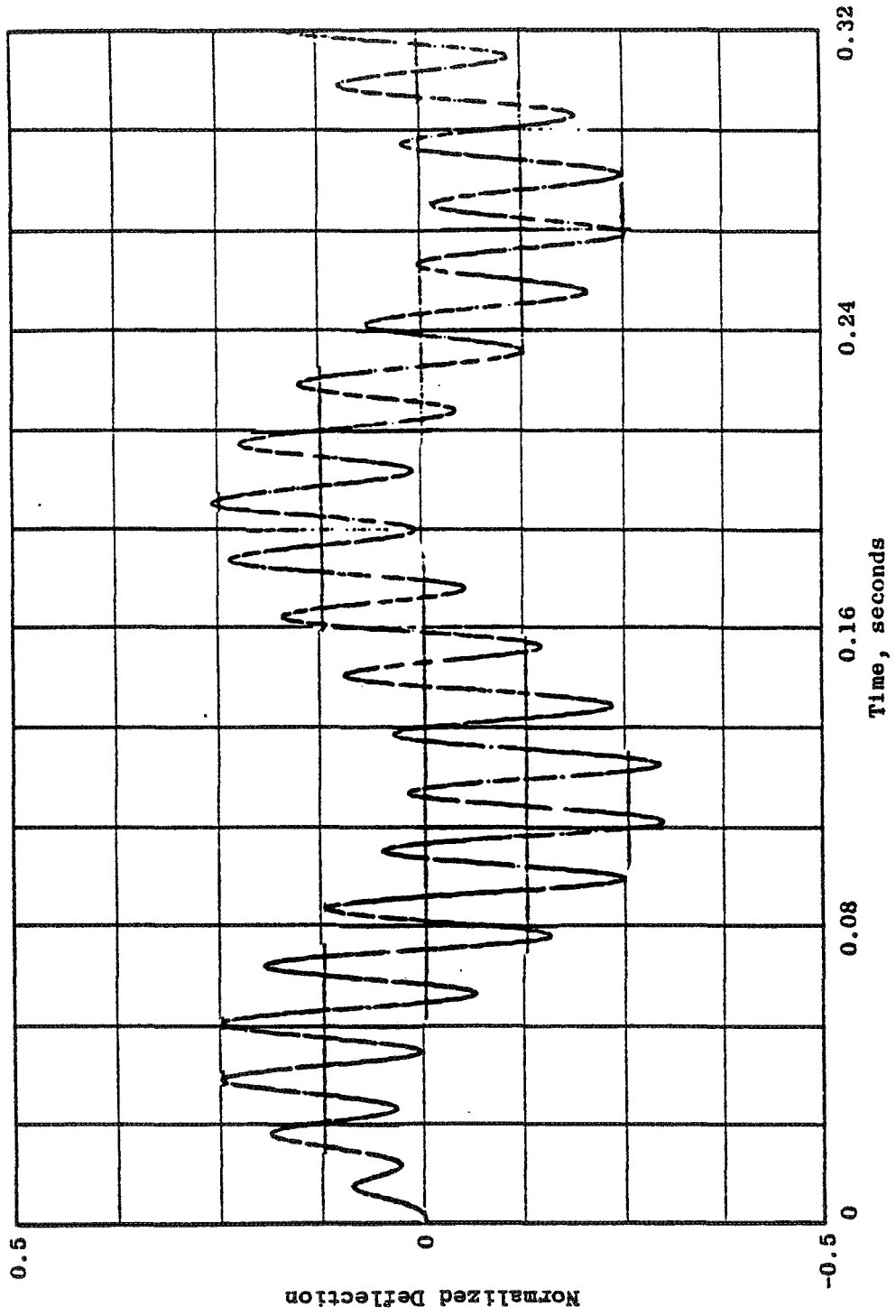


Figure 114. No. 1 Bearing Deflection at 3800 rpm.

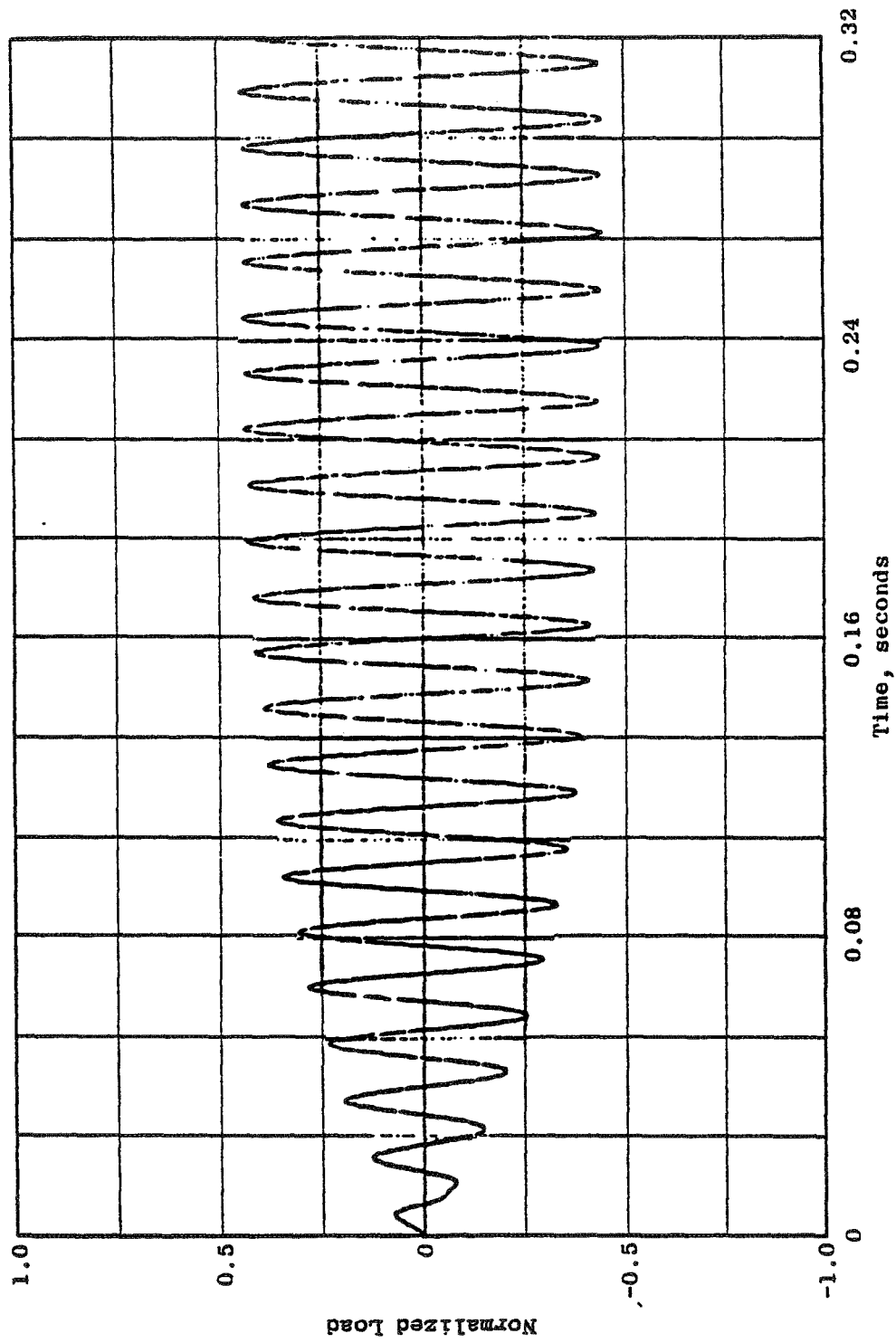


Figure 115. No. 1 Bearing Load at 4000 rpm.

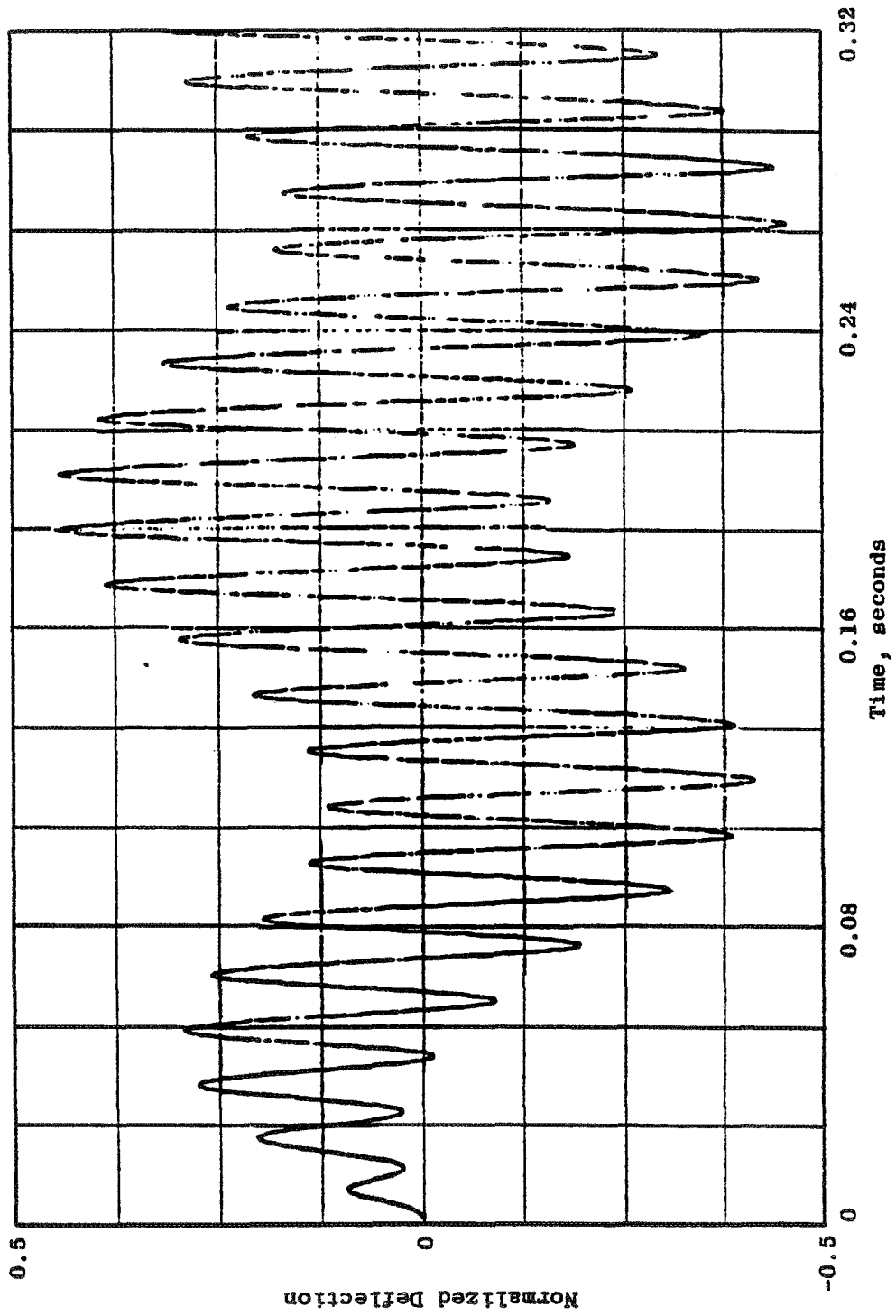


Figure 116. No 1 Bearing Deflection at 4000 rpm.



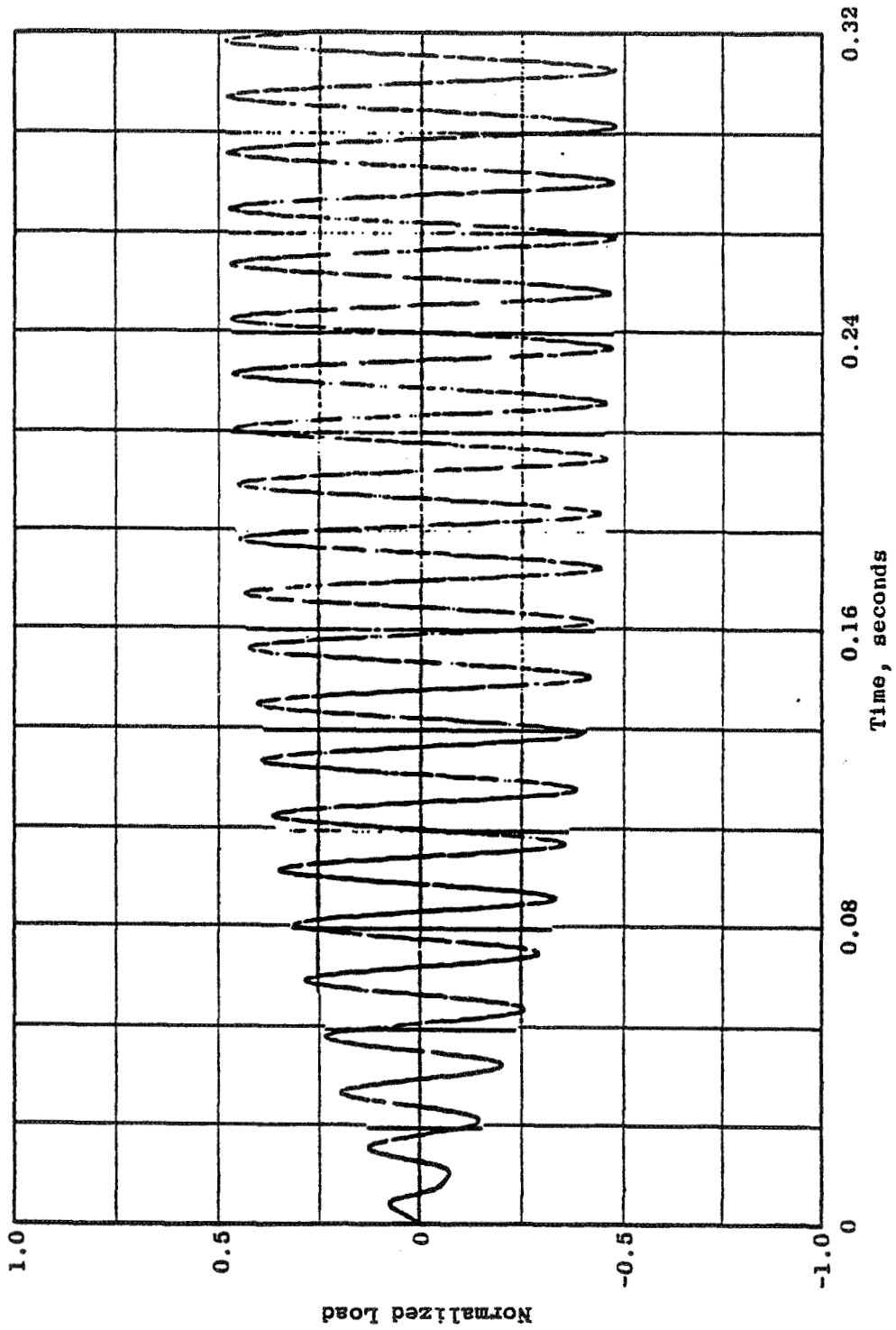


Figure 117. No. 1 Bearing Load at 4050 rpm.

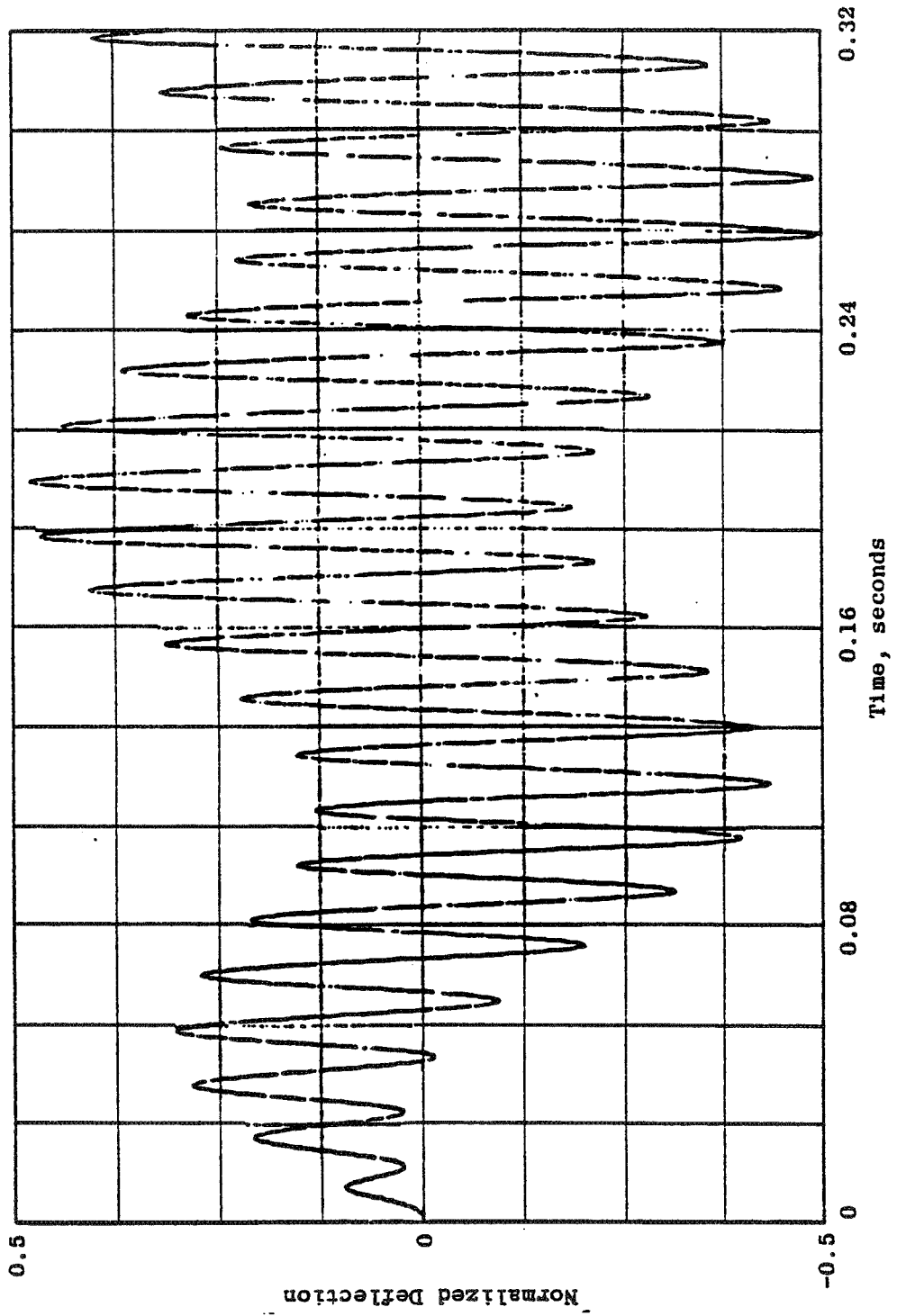


Figure 118. No. 1 Bearing Deflection at 4050 rpm.

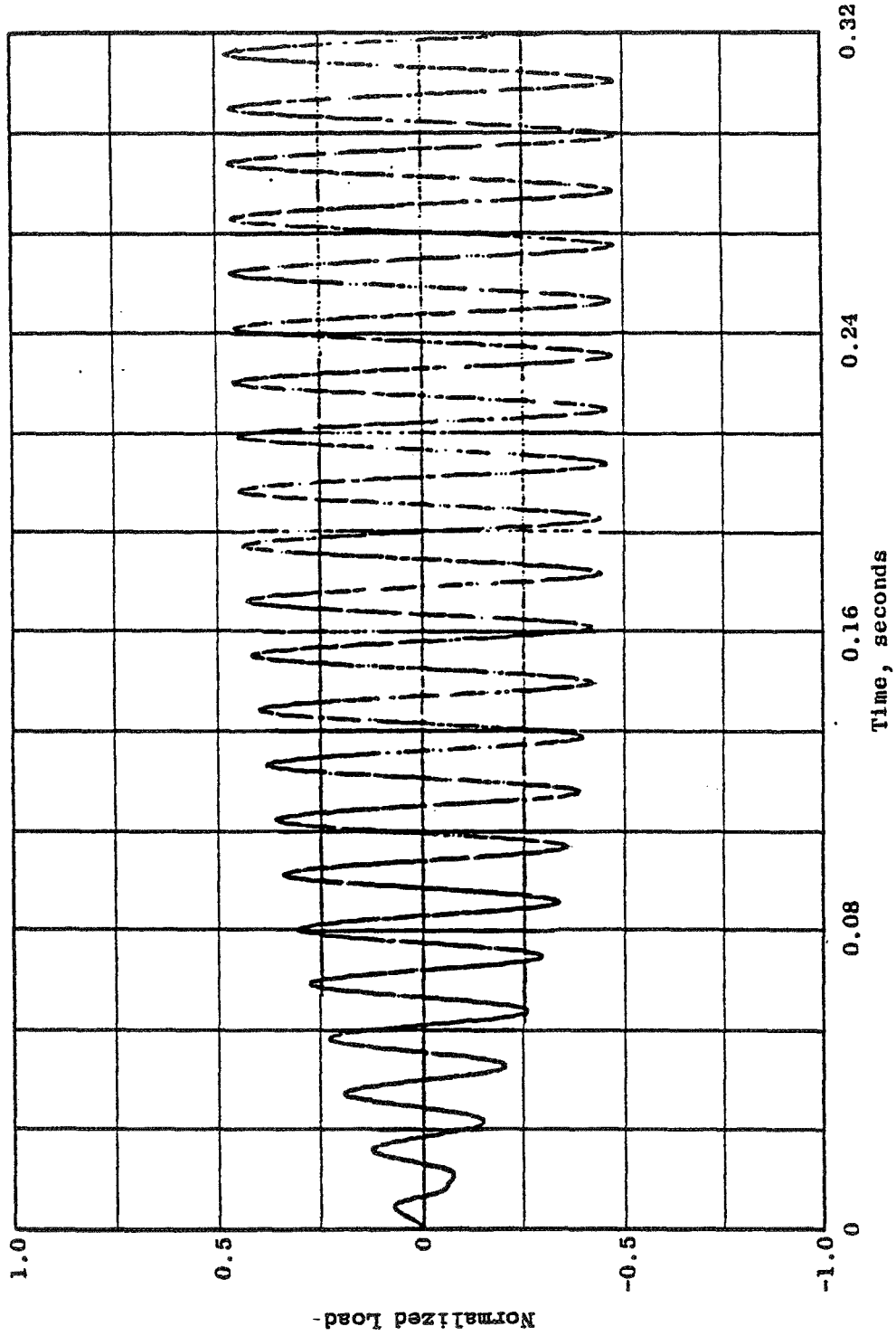


Figure 119. No. 1 Bearing Load at 4100 rpm.

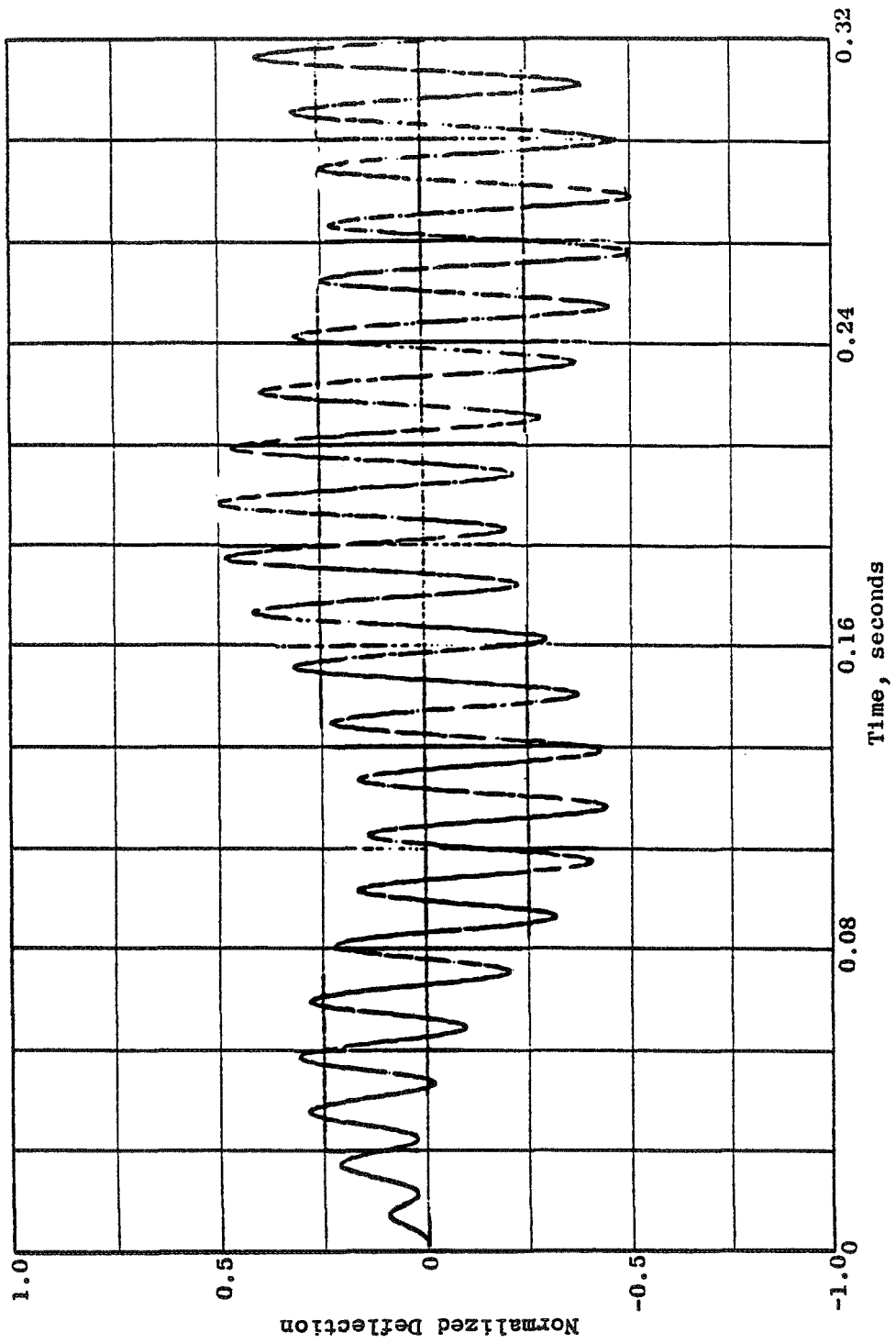


Figure 120. No. 1 Bearing Deflection at 4100 rpm.

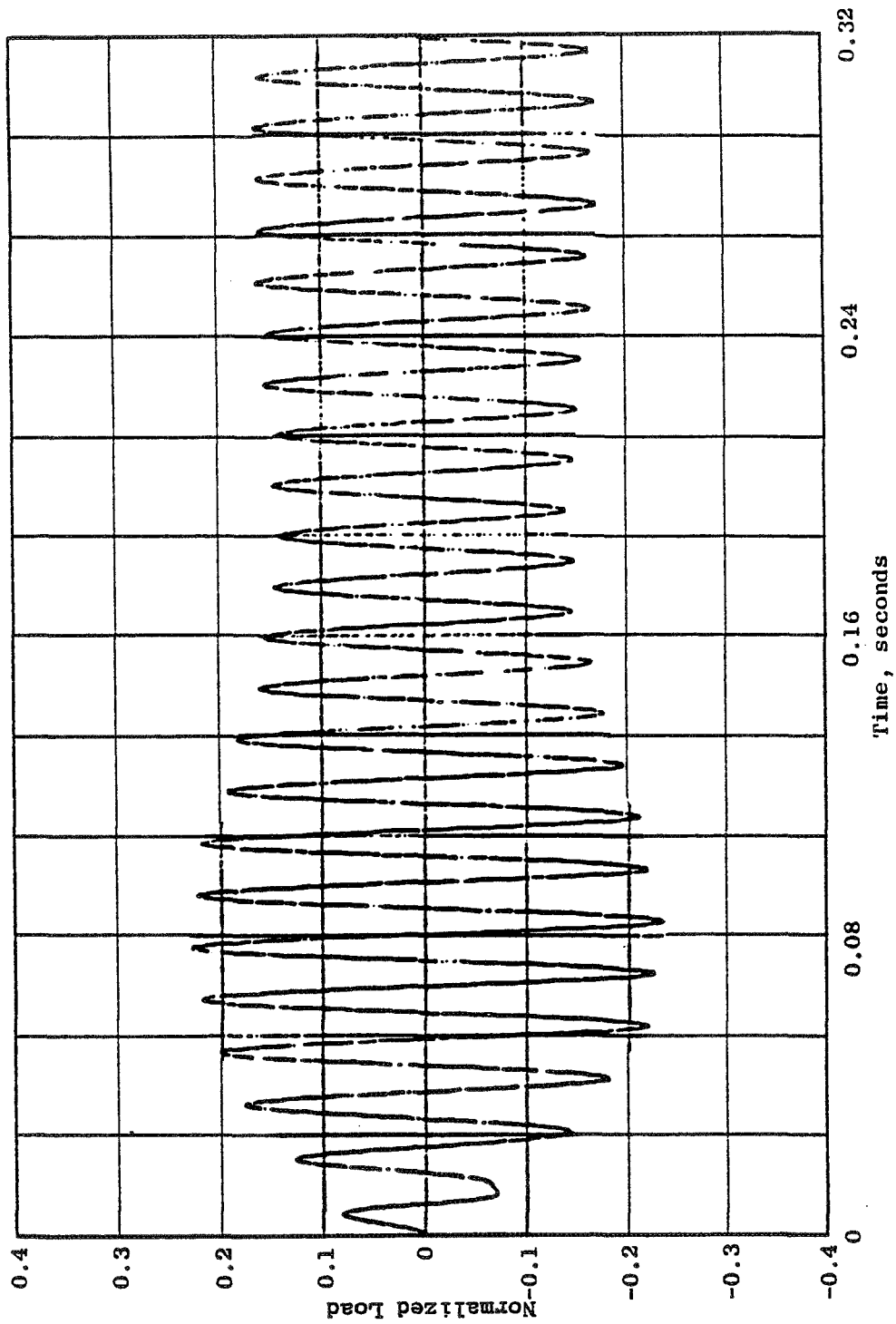


Figure 121. No. 1 Bearing Load at 4400 rpm.

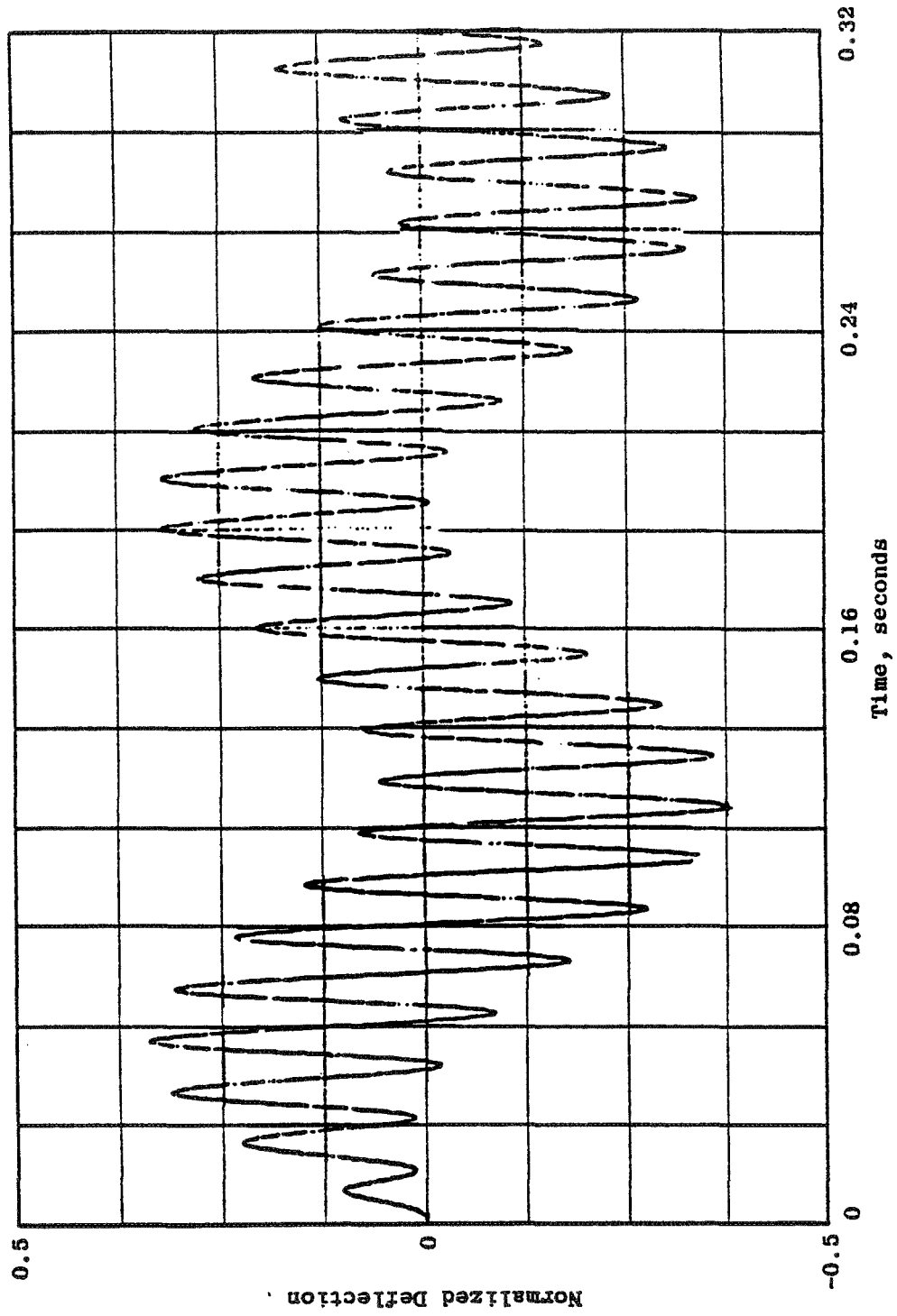


Figure 122. No. 1 Bearing Deflection 4400 rpm.

APPENDIX E

BLADE-OUT ENGINE NORMALIZED SUBSYSTEM MODE SHAPES

The normalied mode shapes for the casing subsystem are presented in Figures 123 through 148. Normalized mode shapes for the rotor subsystem follow in Figures 149 through 154.

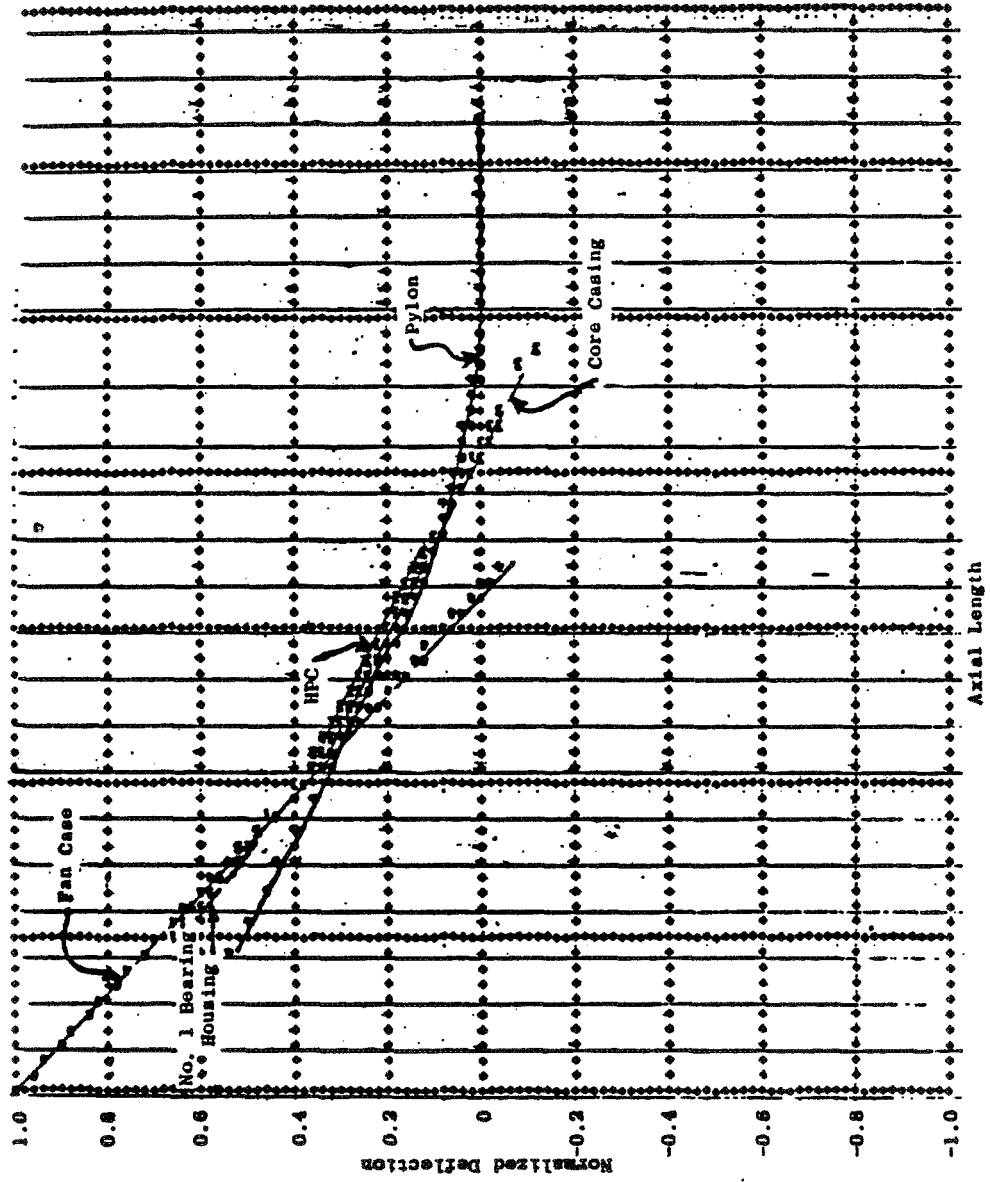


Figure 123. Subsystem 1 (Casing) Normalized Mode Shapes at 353 rpm.



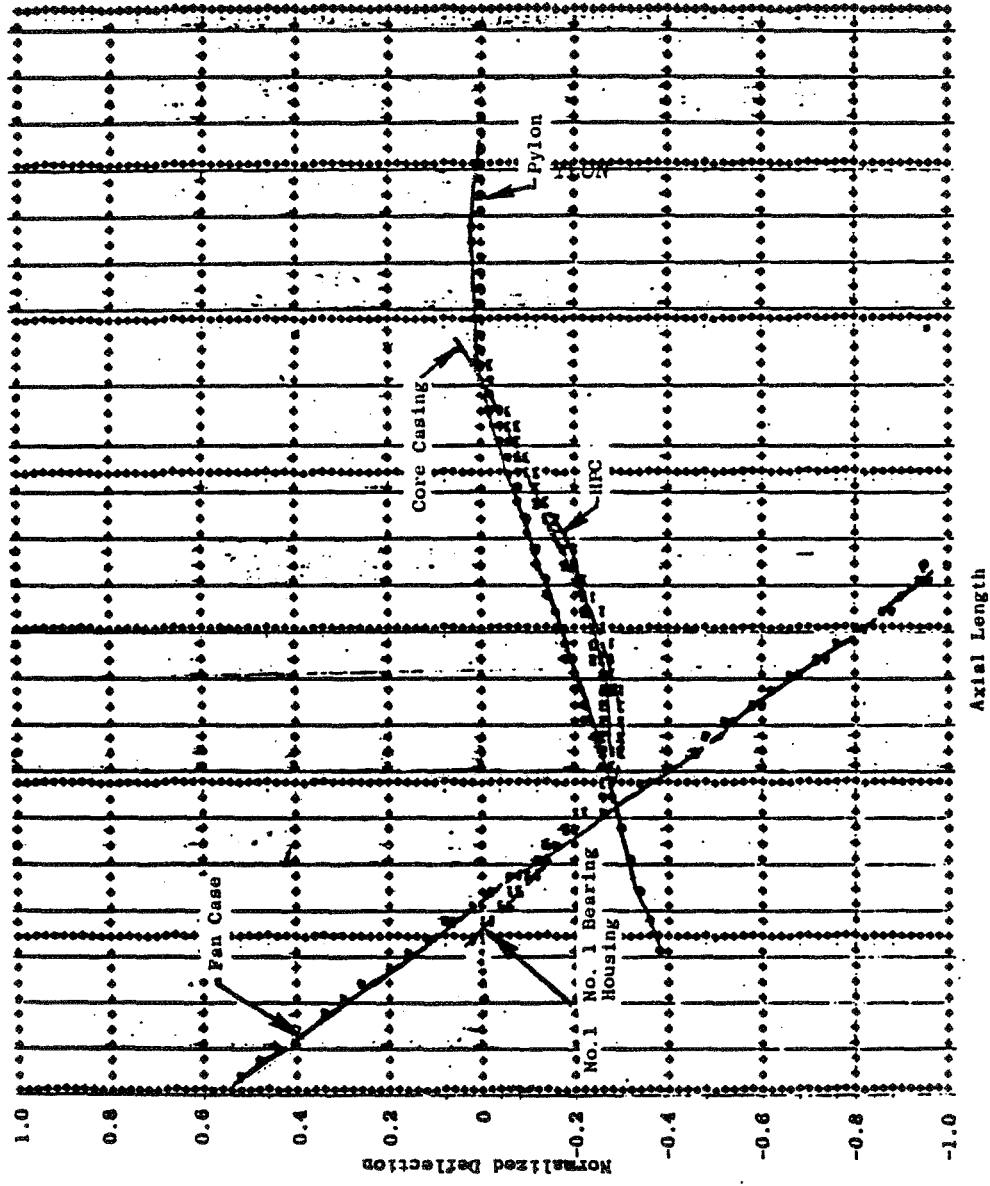


Figure 124. Subsystem 1 (Casing) Normalized Mode Shapes at 731 rpm.

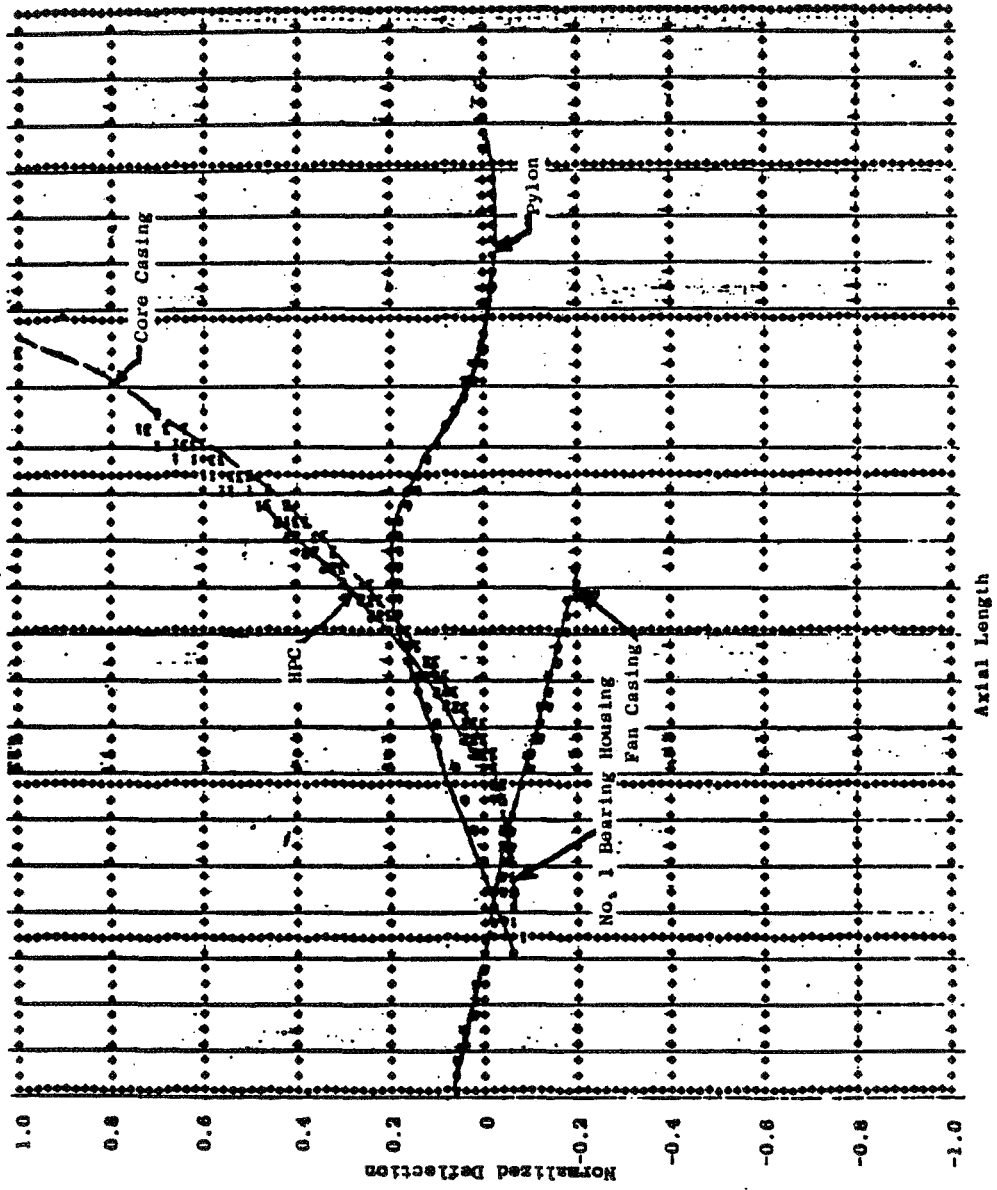


Figure 125. Subsystem 1 (Casing) Normalized Mode Shapes at 1703 rpm.

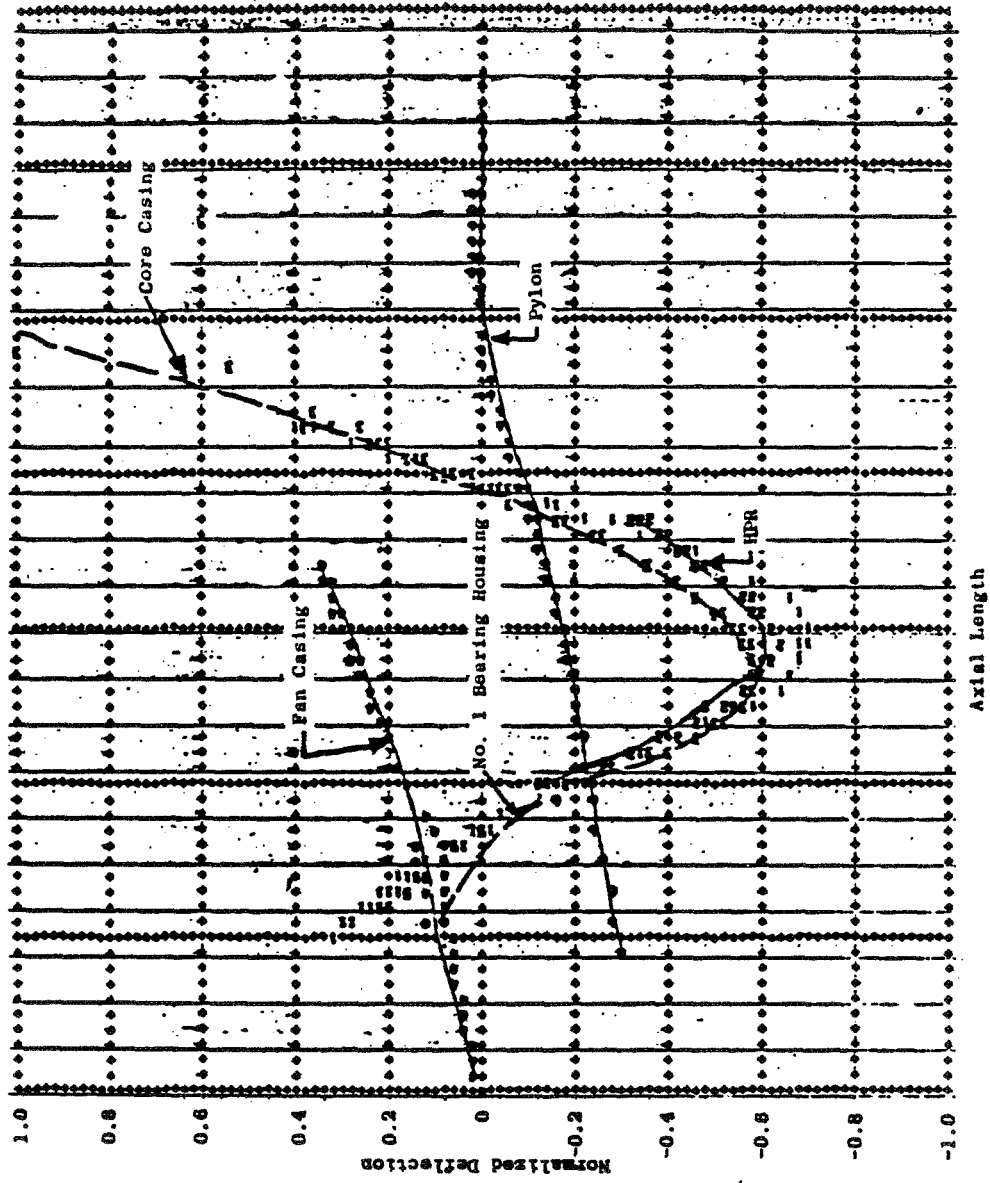


Figure 126. Subsystem 1 (Casing) Normalized Mode Shapes at 2978 rpm.

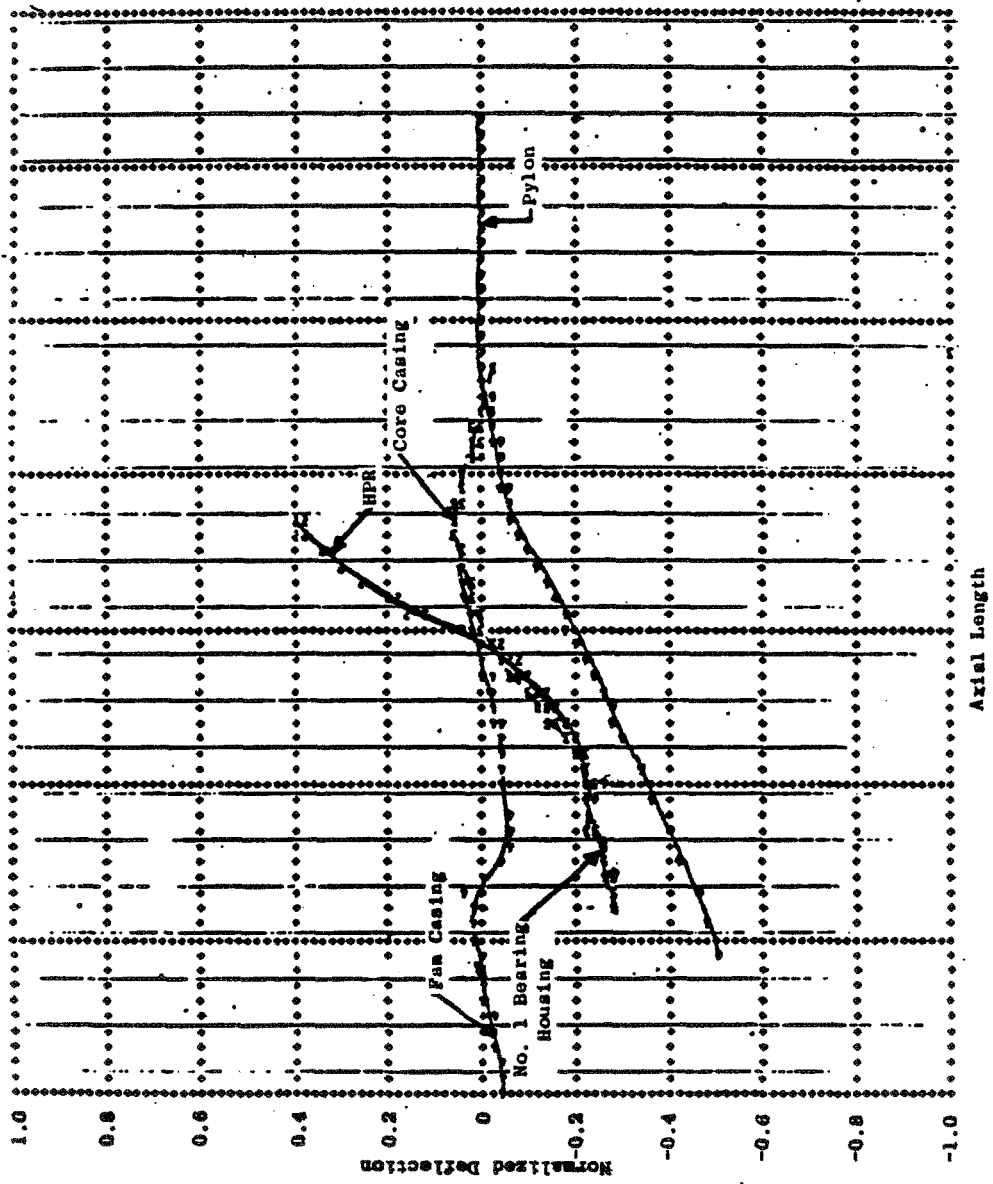


Figure 127. Subsystem 1 (Casing) Normalized Mode Shapes at 5110 rpm.

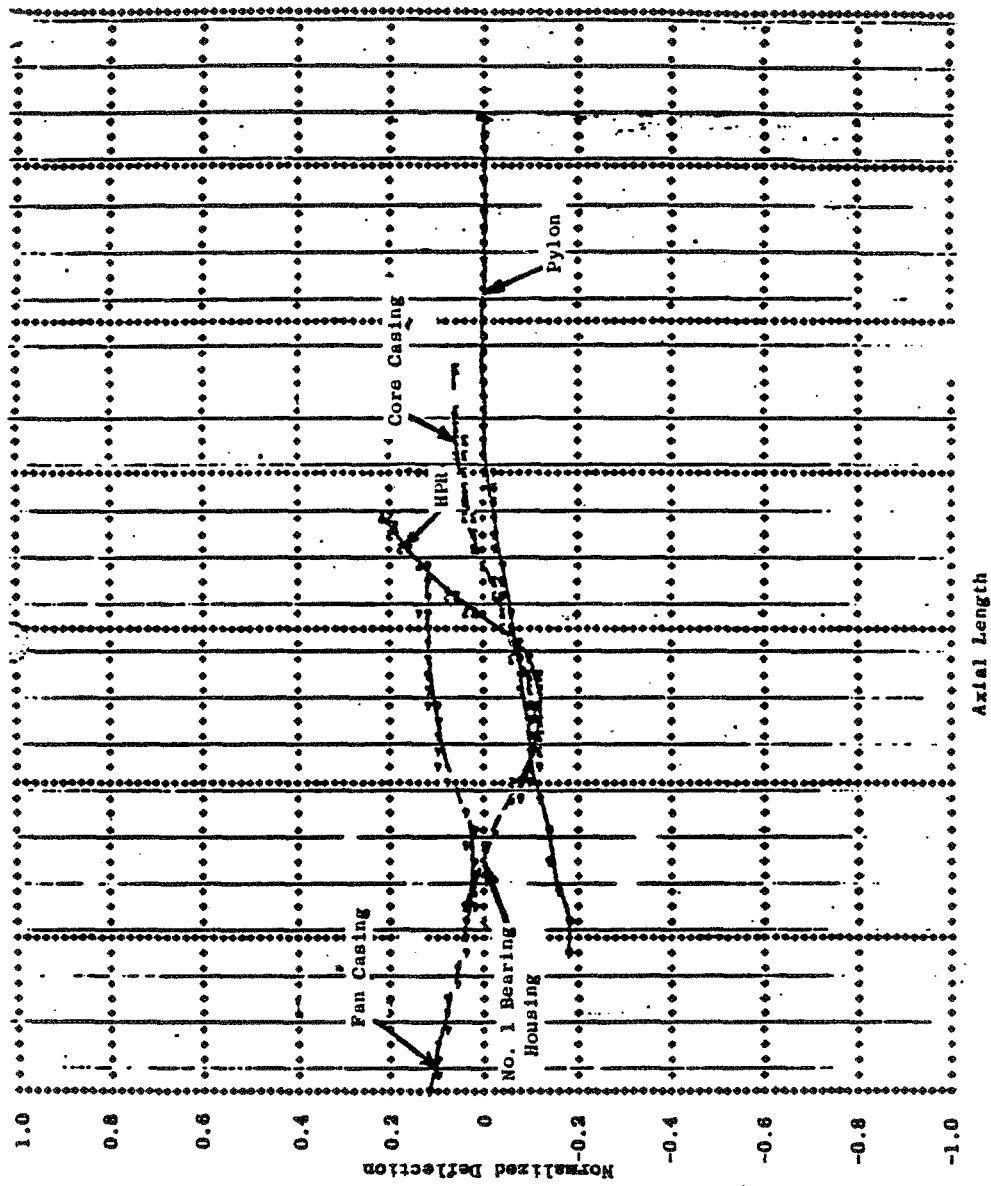


Figure 128. Subsystem 1 (Casing) Normalized Mode Shapes at 5370 rpm.

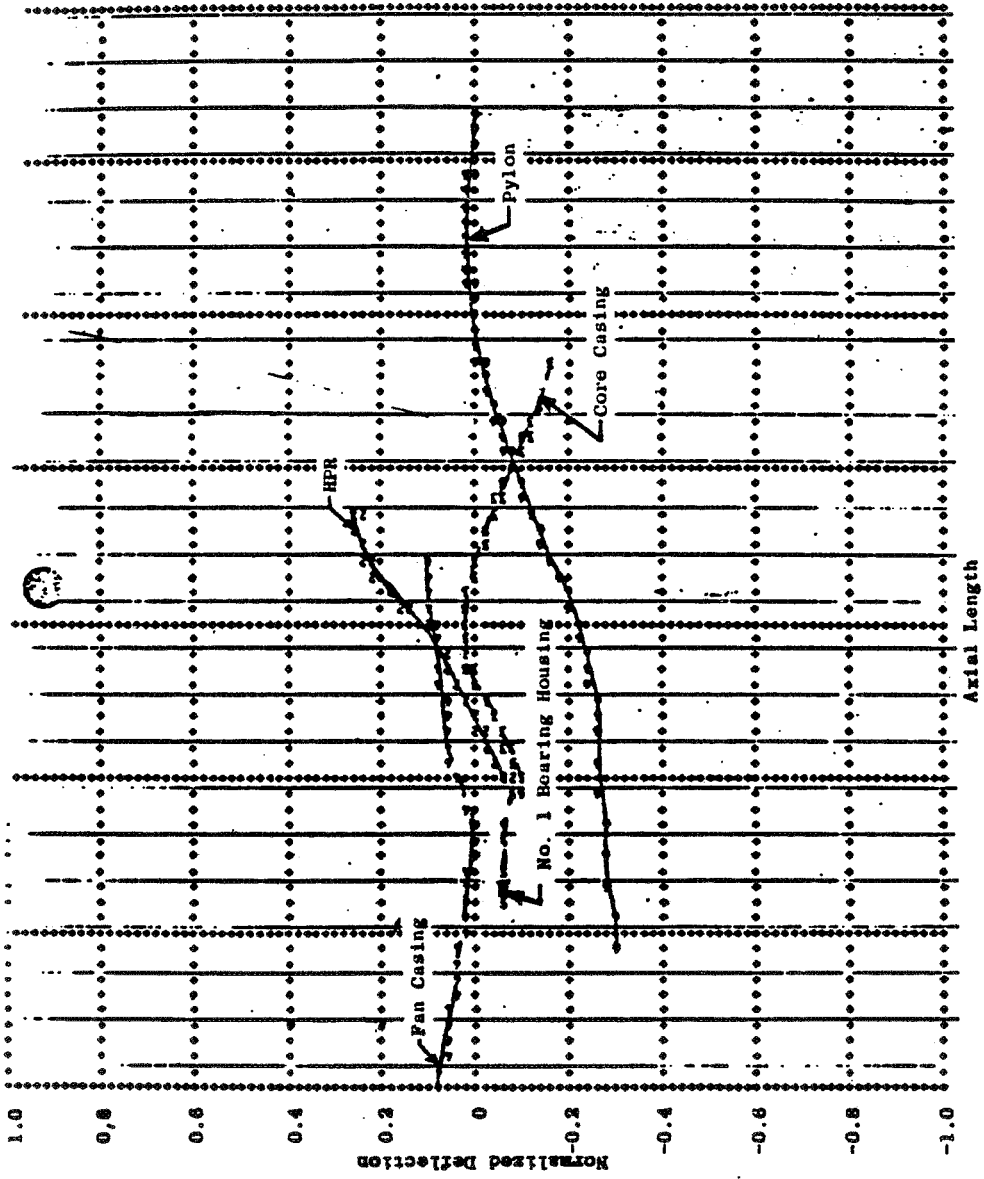


Figure 129. Subsystem 1 (Casing) Normalized Mode Shapes at 5655 rpm.

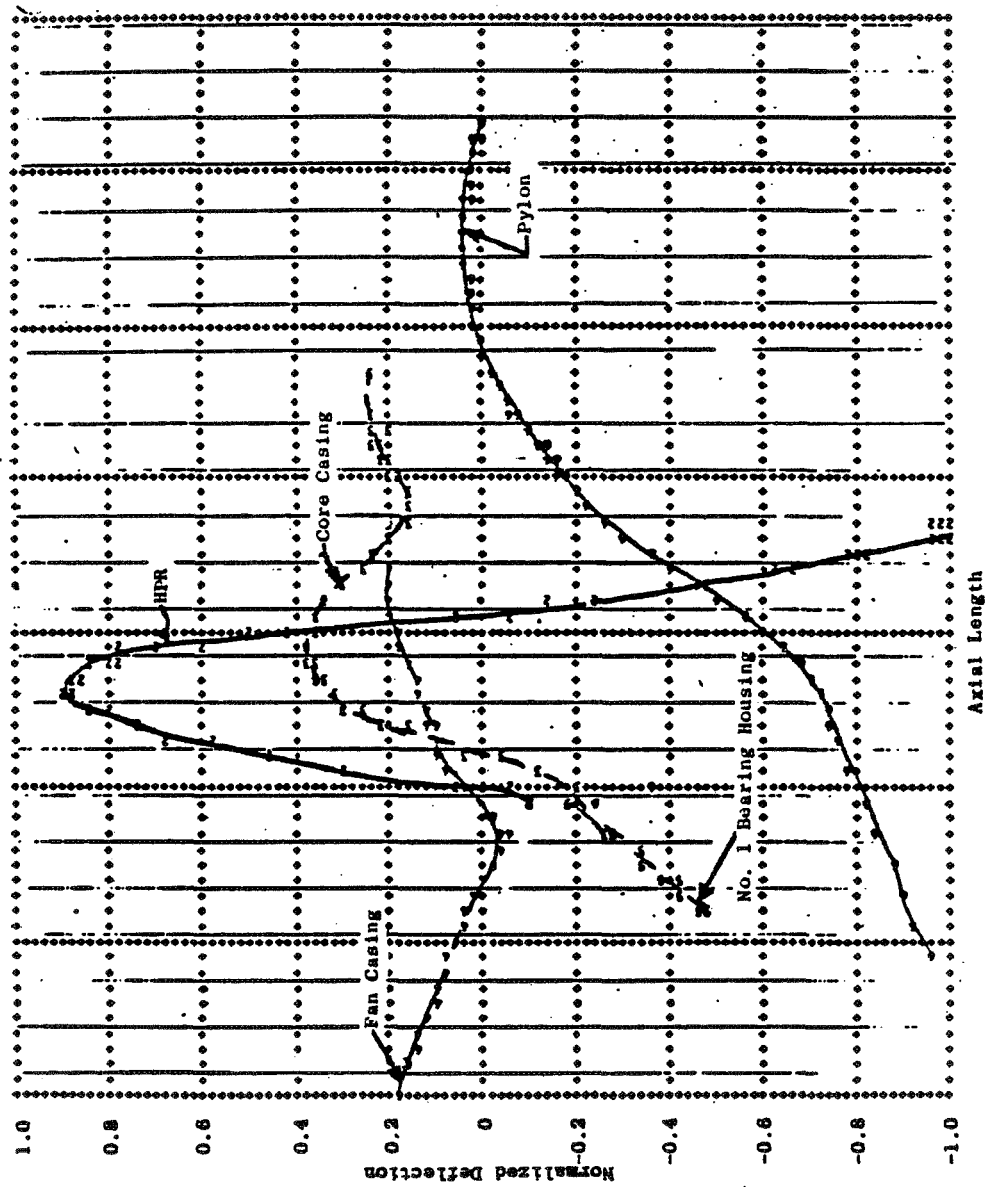


Figure 130. Subsystem 1 (Casing) Normalized Mode Shapes at 6485 rpm.

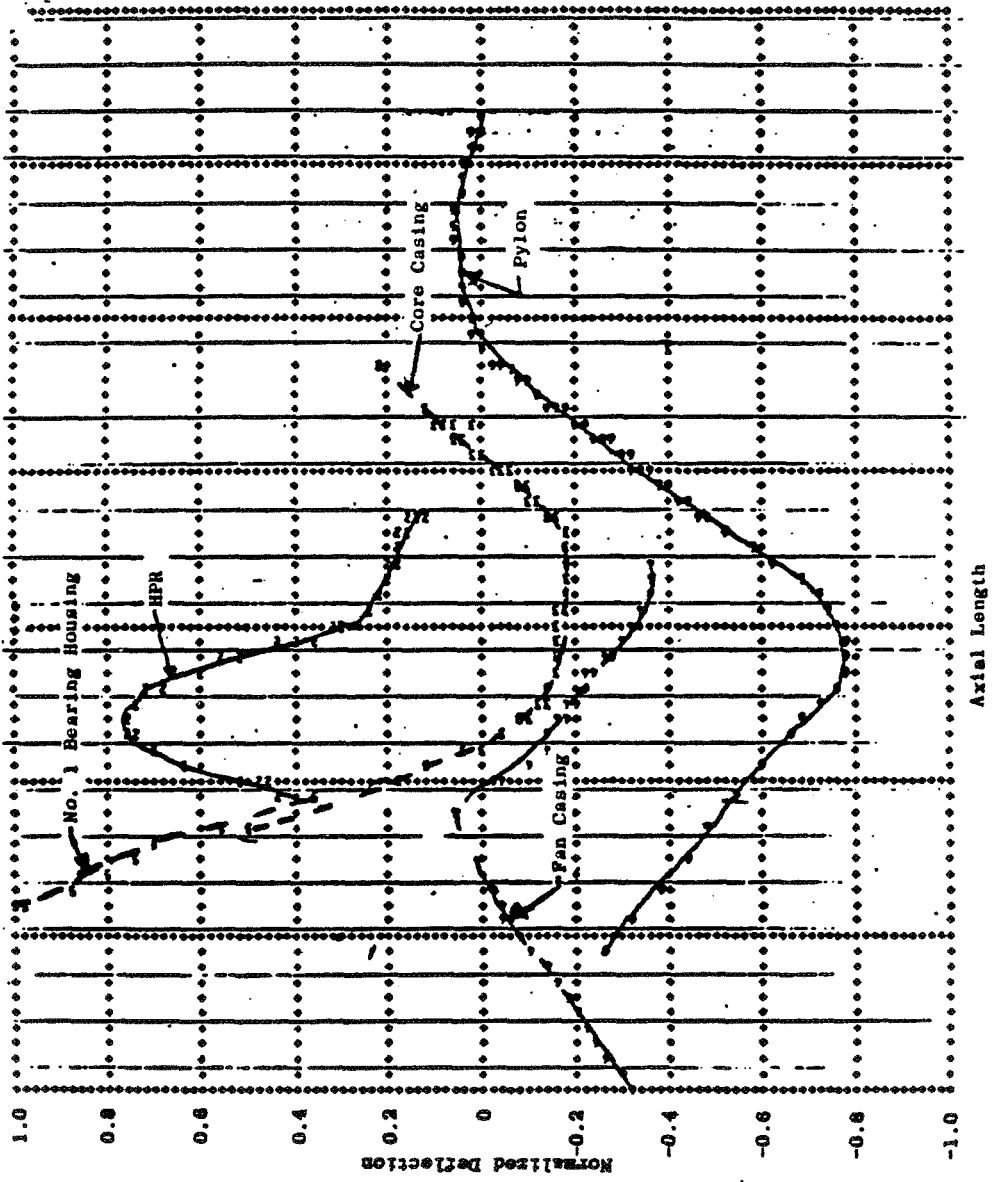


Figure 131. Subsystem 1 (Casing) Normalized Mode Shapes at 6815 rpm.



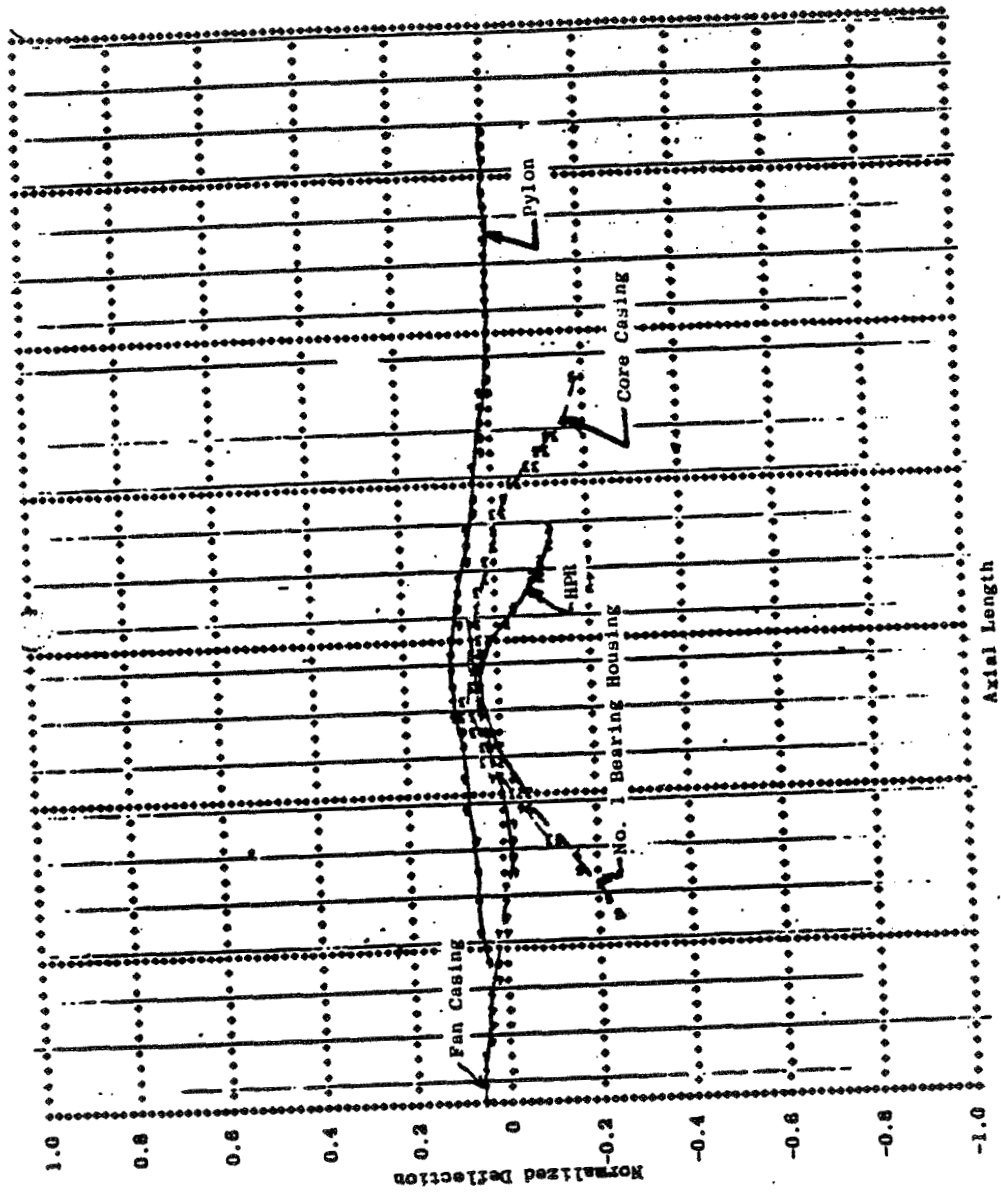


Figure 132. Subsystem 1 (Casing) Normalized Mode Shapes at 7076 rpm.

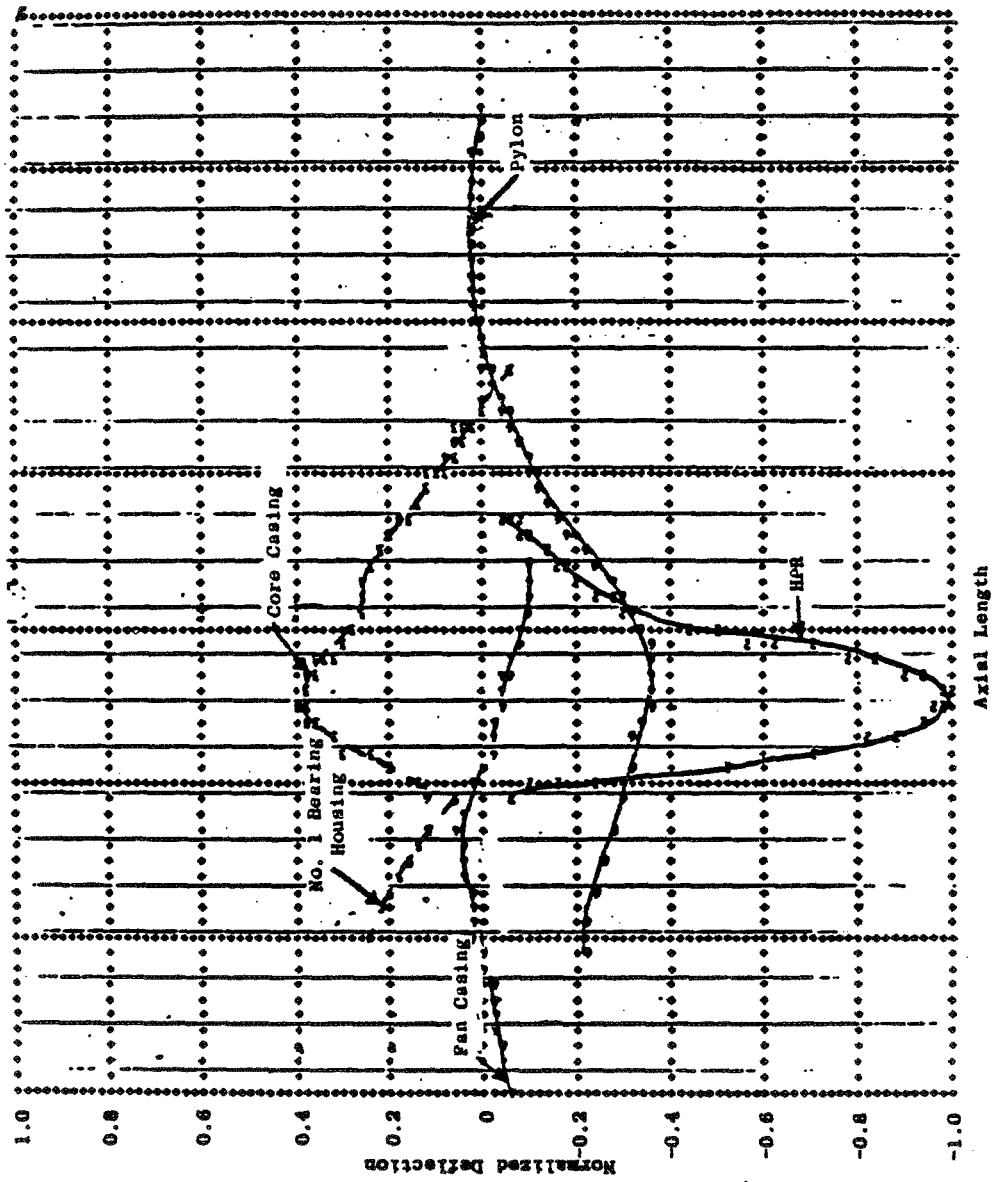


Figure 133. Subsystem 1 (Casing) Normalized Mode Shapes at 7852 rpm.

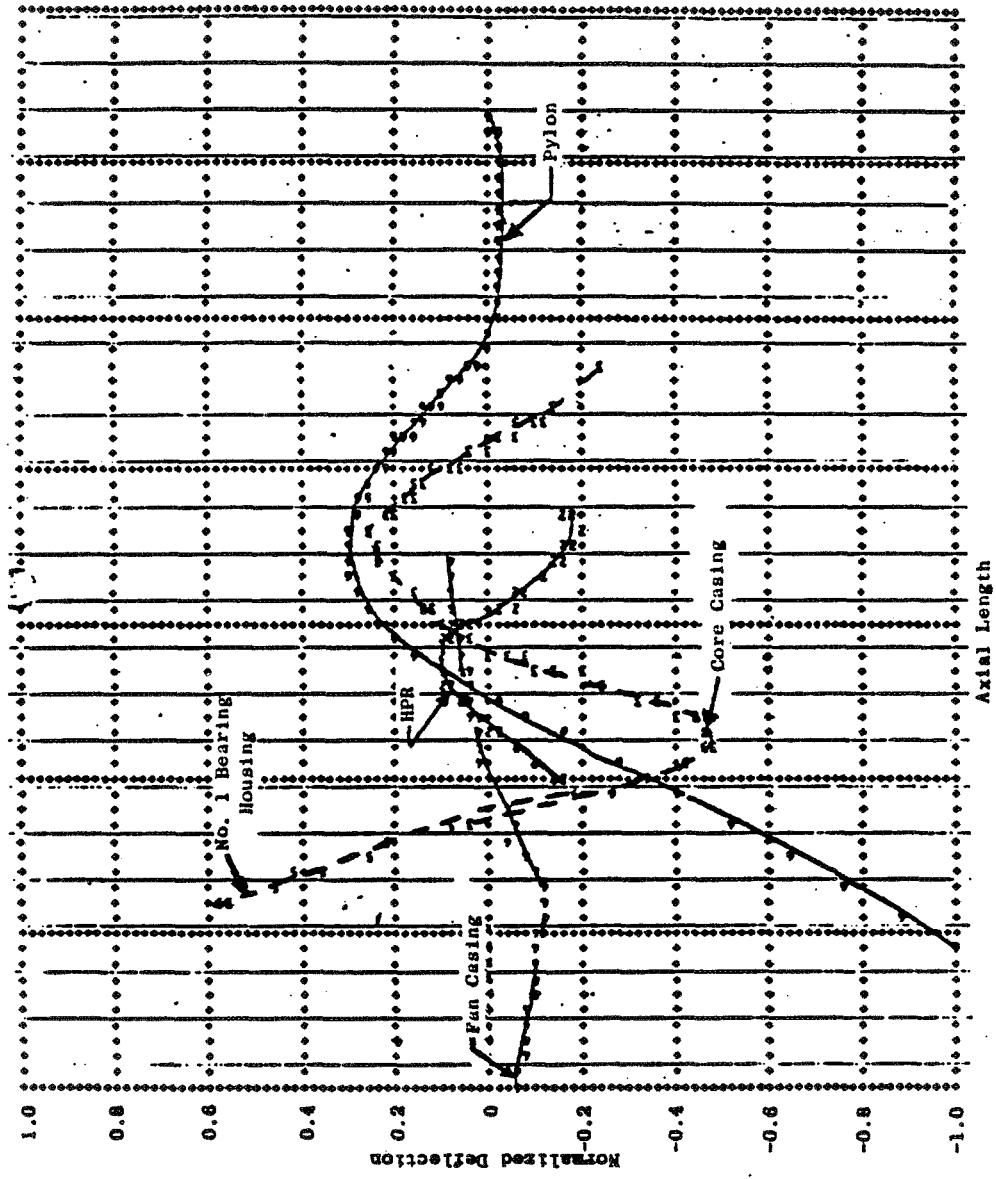


Figure 134. Subsystem 1 (Casing) Normalized Mode Shapes at 8982 rpm.

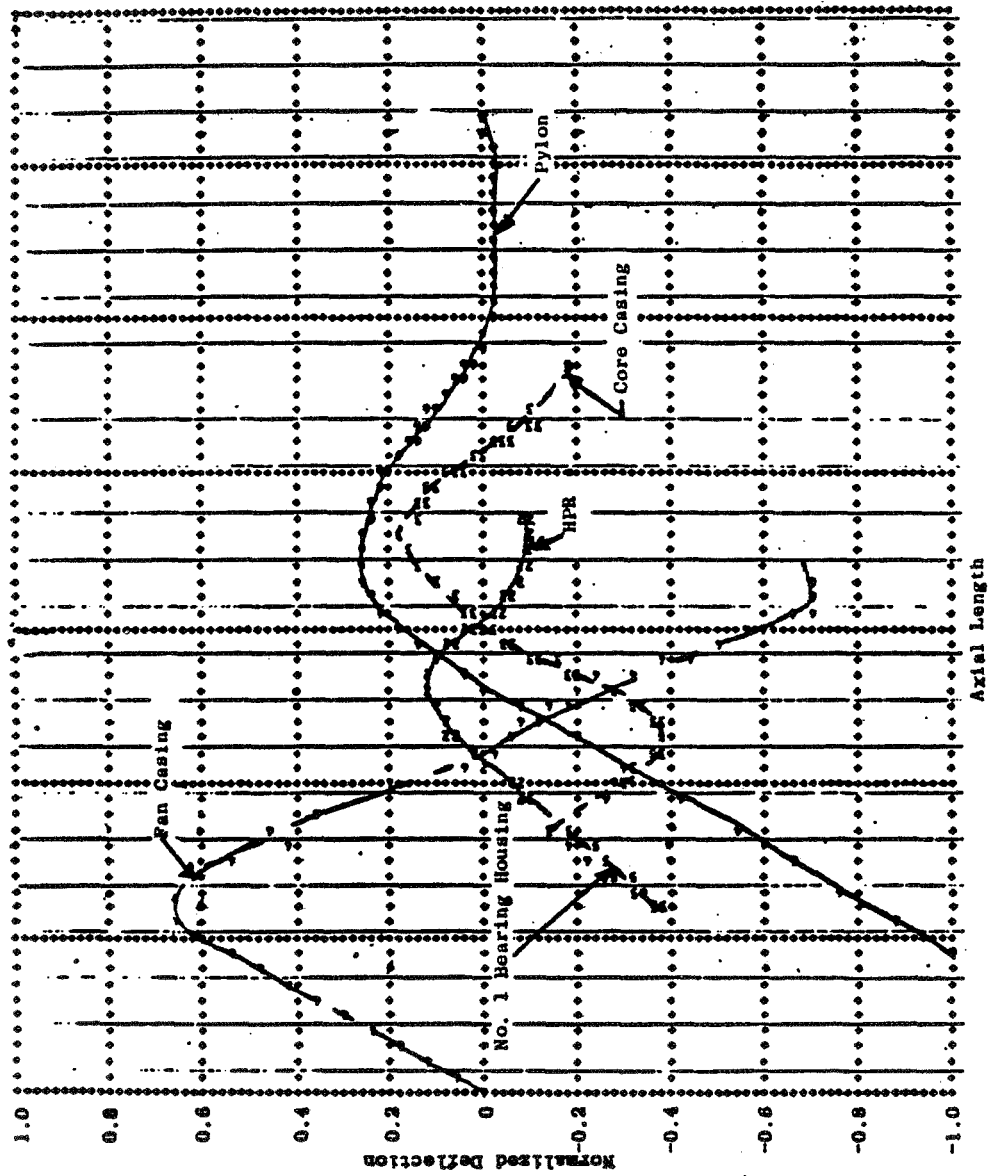


Figure 135. Subsystem 1 (Casing) Normalized Mode Shapes at 9644 rpm.

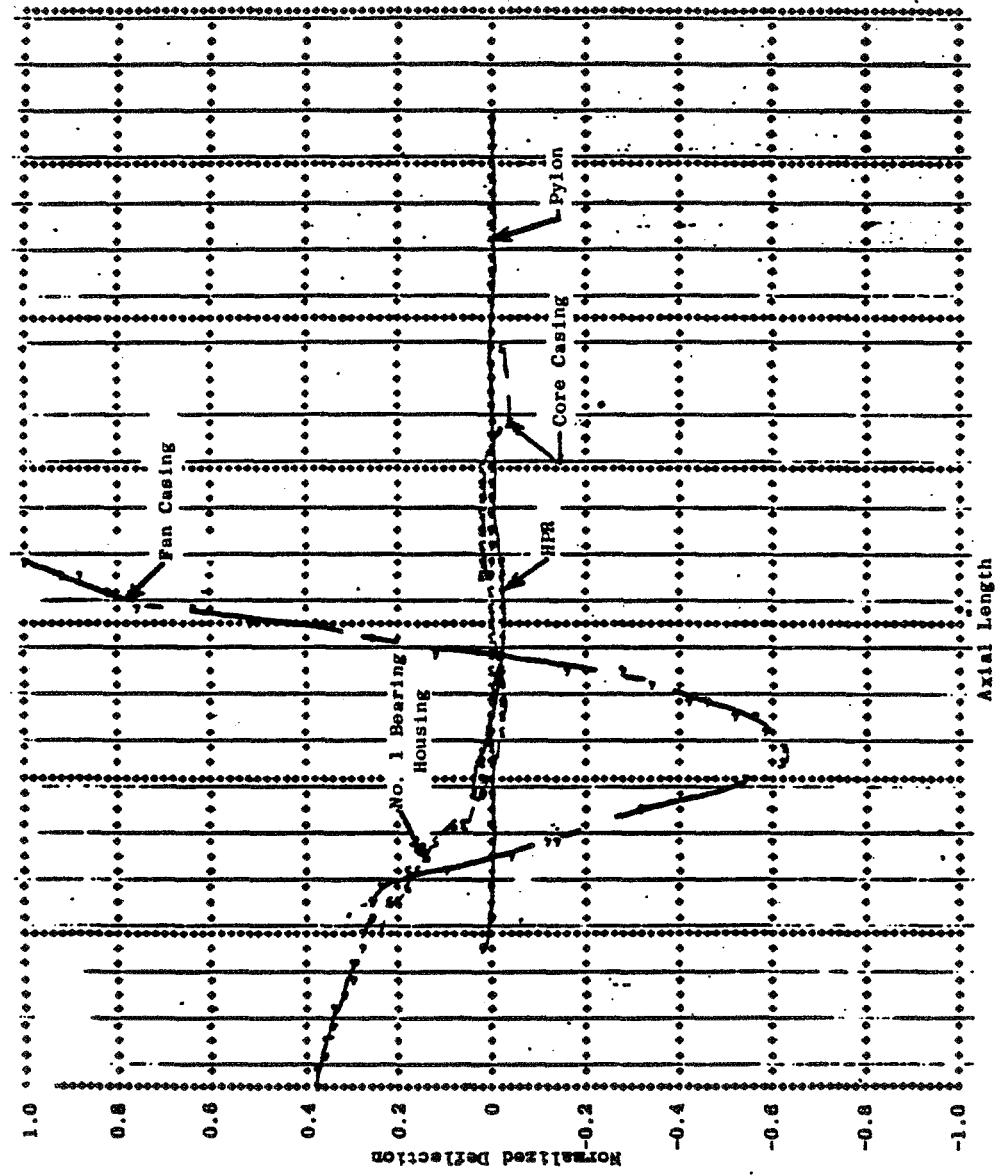


Figure 136. Subsystem 1 (Casing) Normalized Mode Shapes at 10,379 rpm.

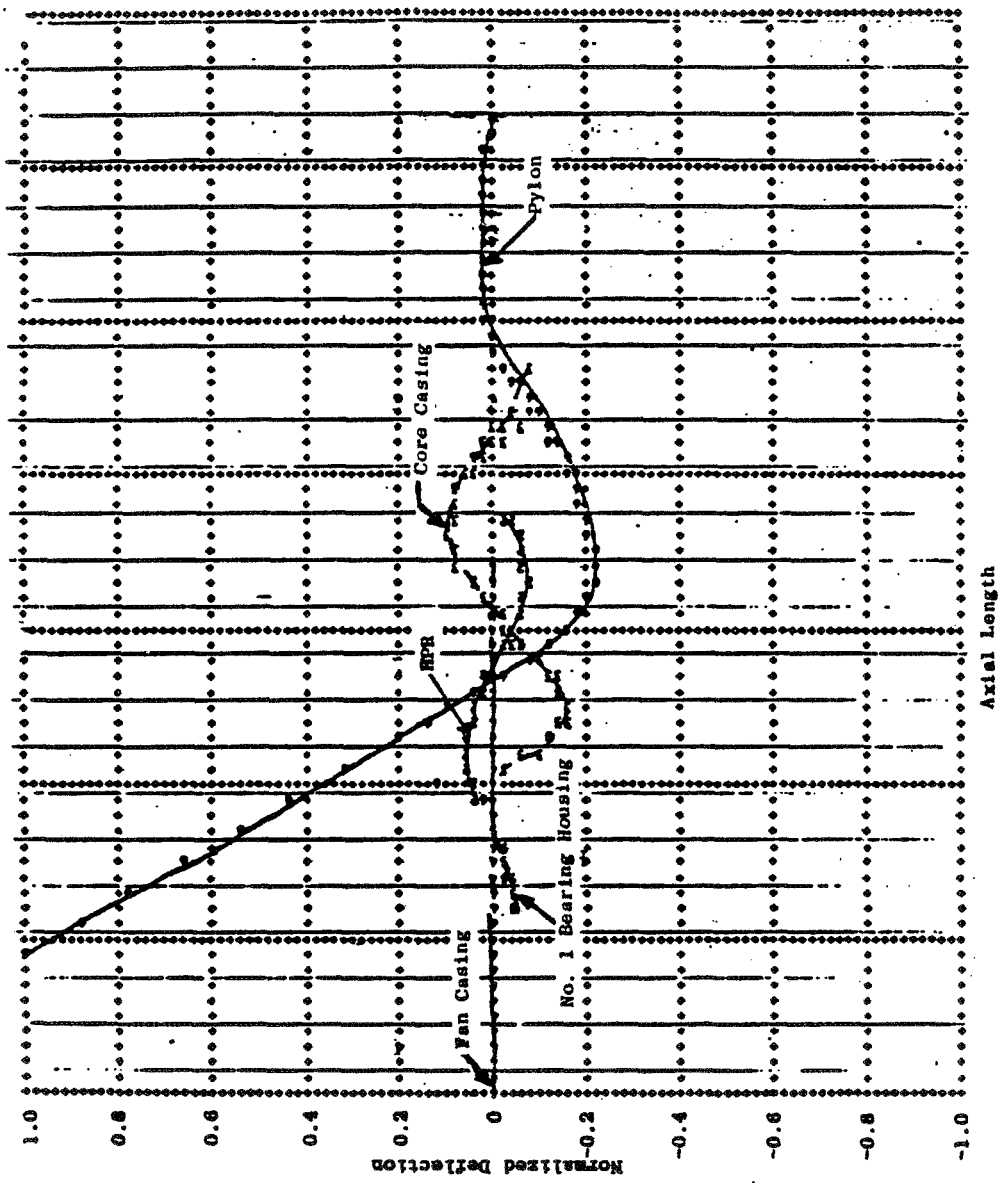


Figure 137. Subsystem 1 (Casing) Normalized Mode Shapes at 11,632 rpm.

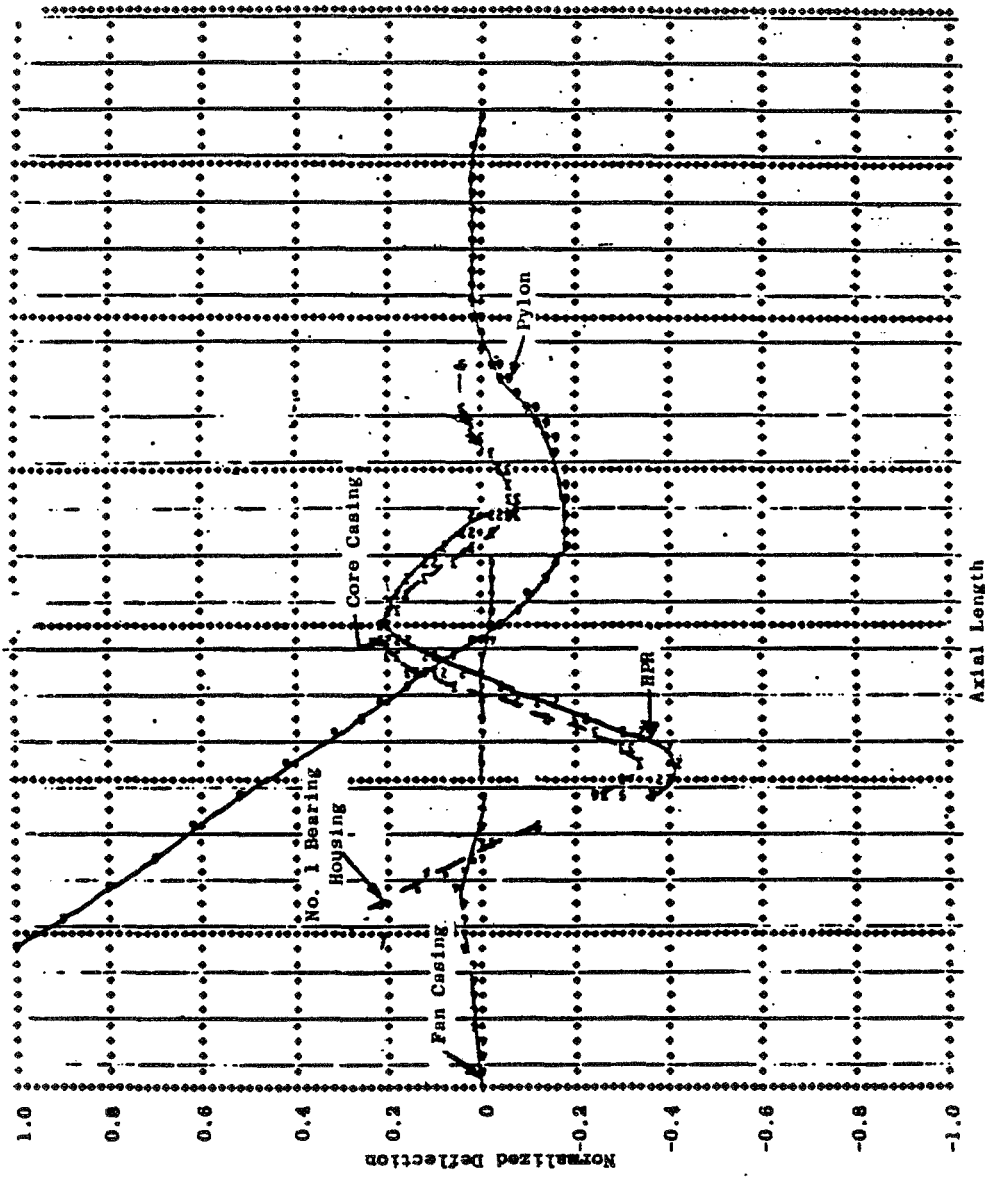


Figure 138. Subsystem 1 (Casing) Normalized Mode Shapes at 12,665 rpm.

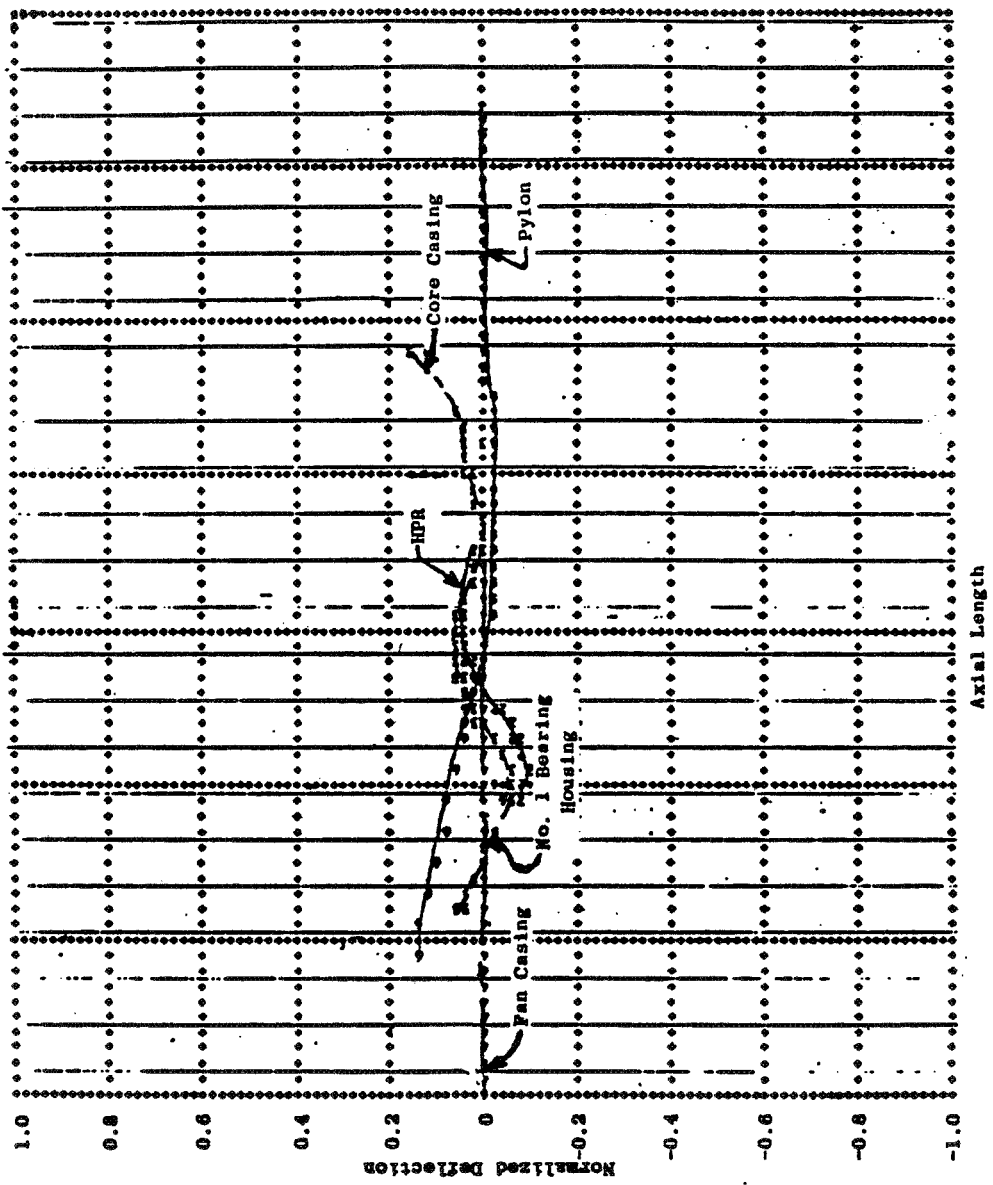


Figure 139. Subsystem 1 (Casing) Normalized Mode Shapes at 13,354 rpm.



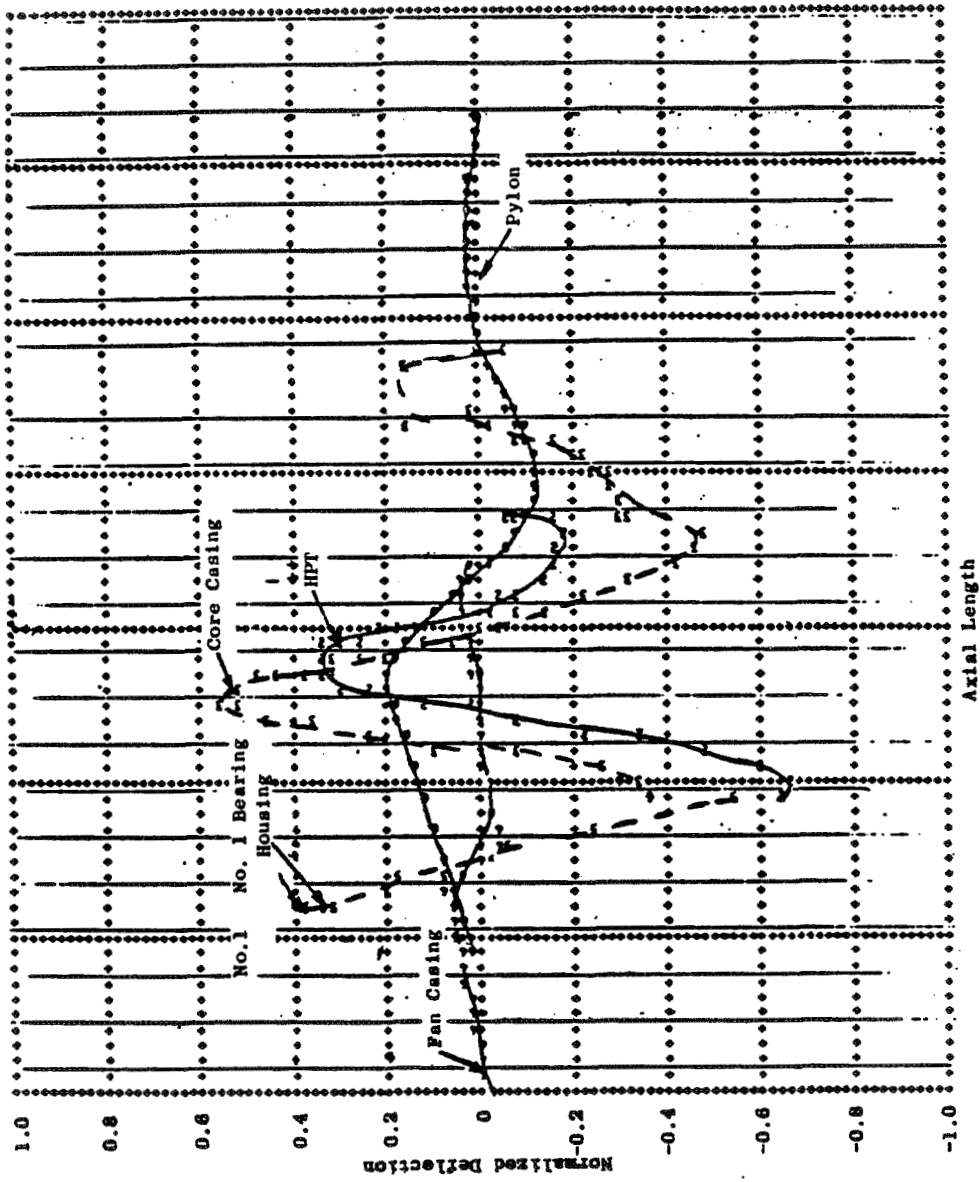


Figure 140. Subsystem 1 (Casing) Normalized Mode Shapes at 15,130 rpm.

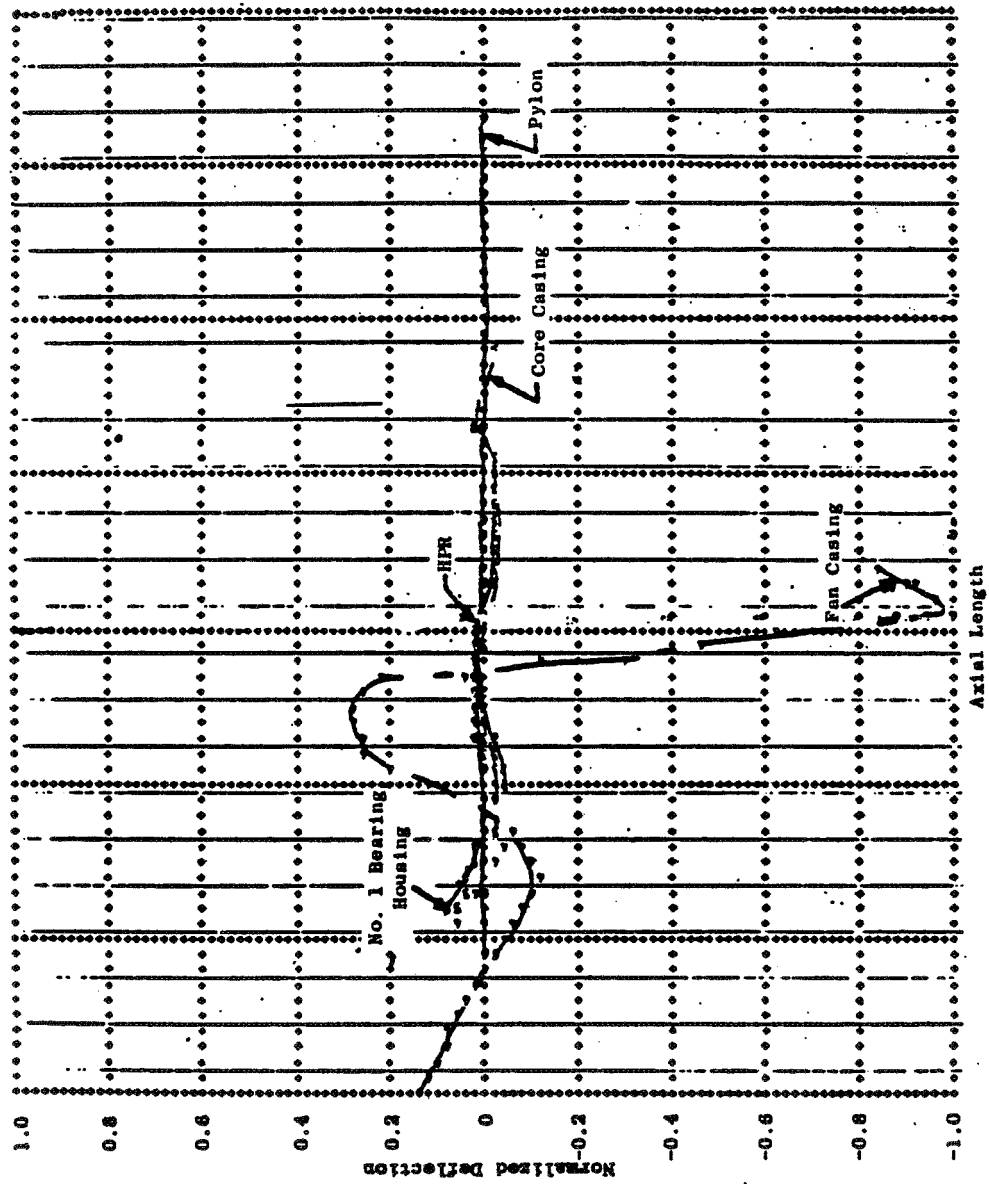


Figure 141. Subsystem 1 (Casing) Normalized Mode Shapes at 15,469 rpm.

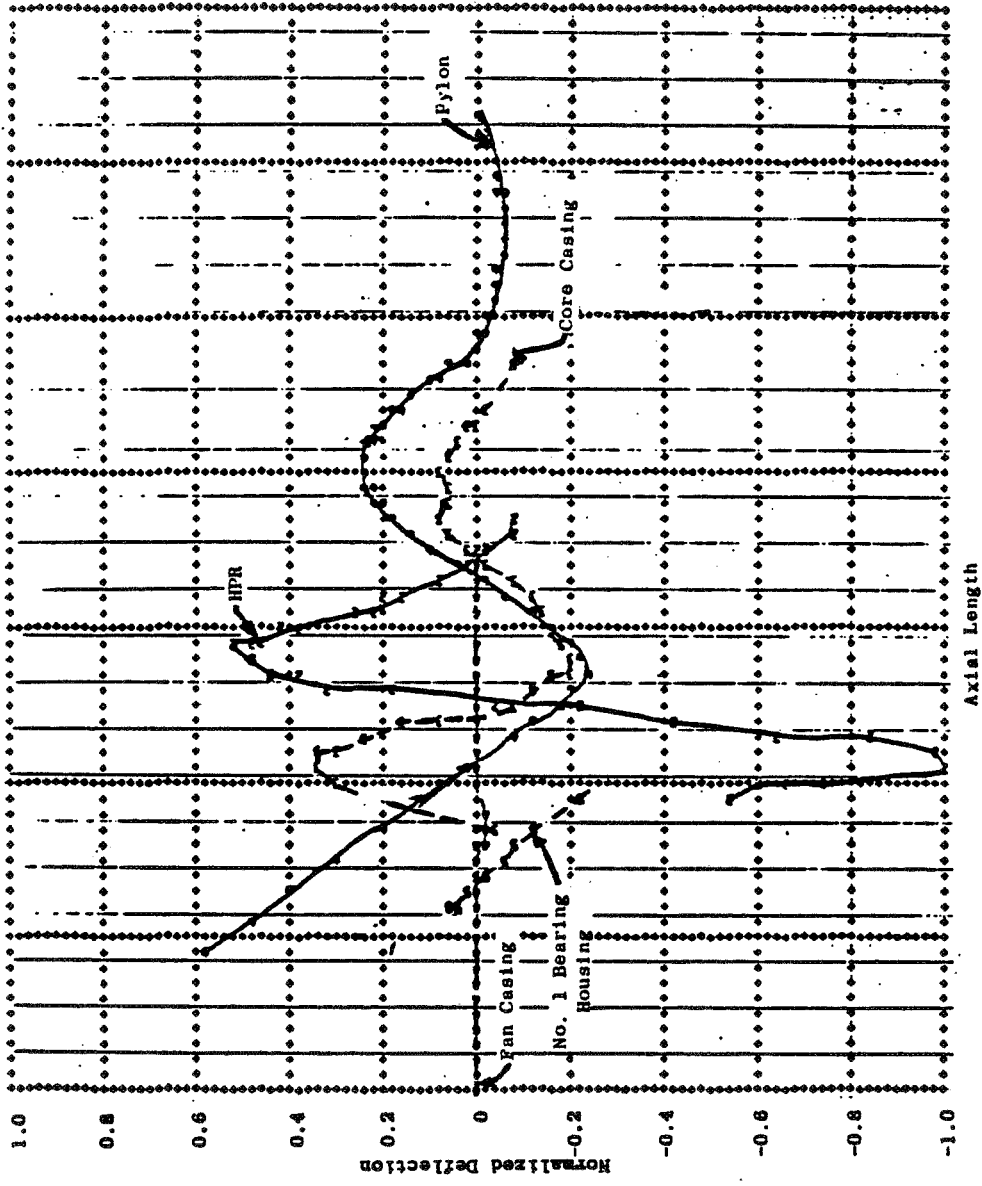


Figure 142. Subsystem 1 (Casing) Normalized Mode Shapes at 18,172 rpm.

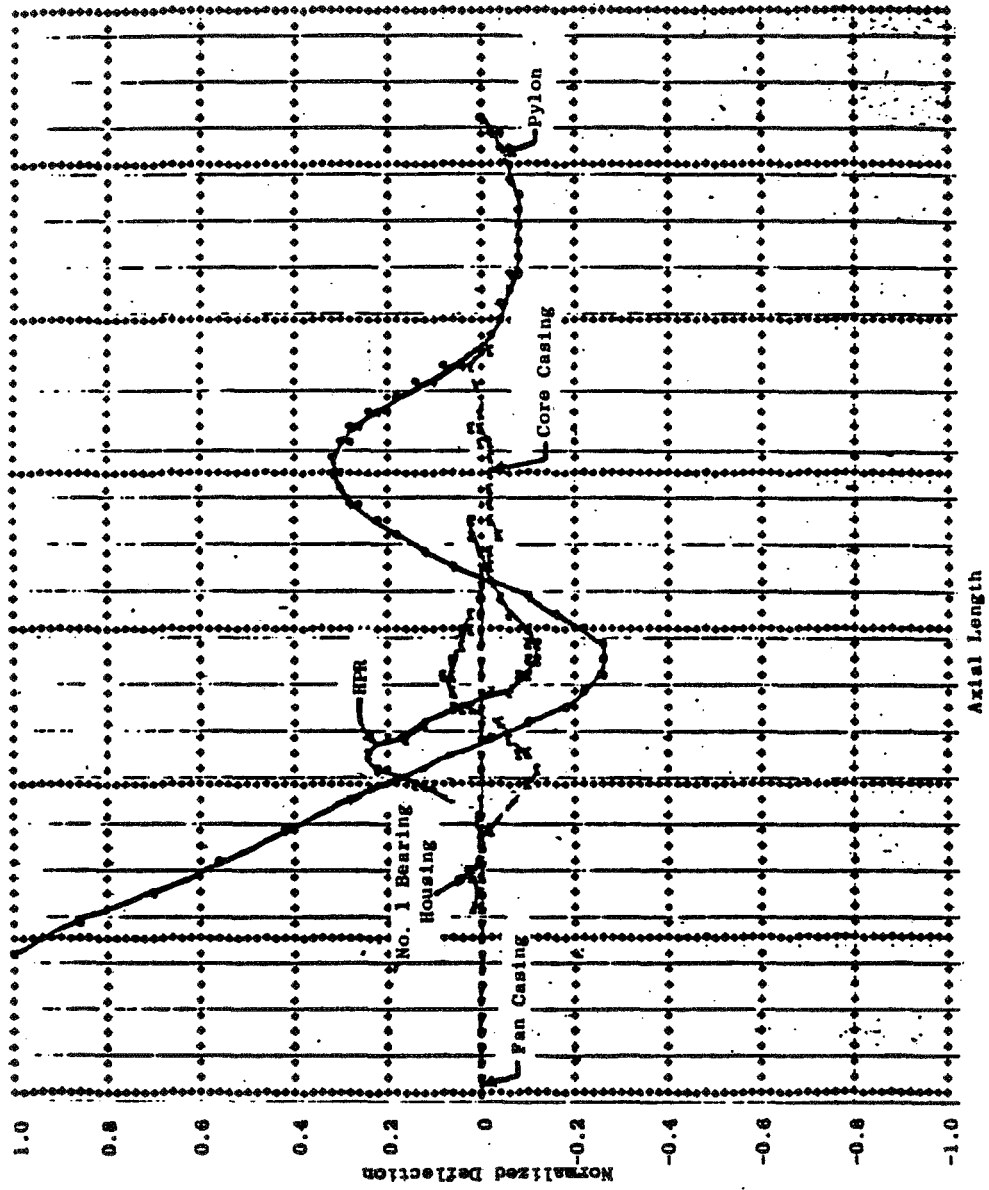


Figure 143. Subsystem 1 (Casing) Normalized Mode Shapes at 18,845 rpm.

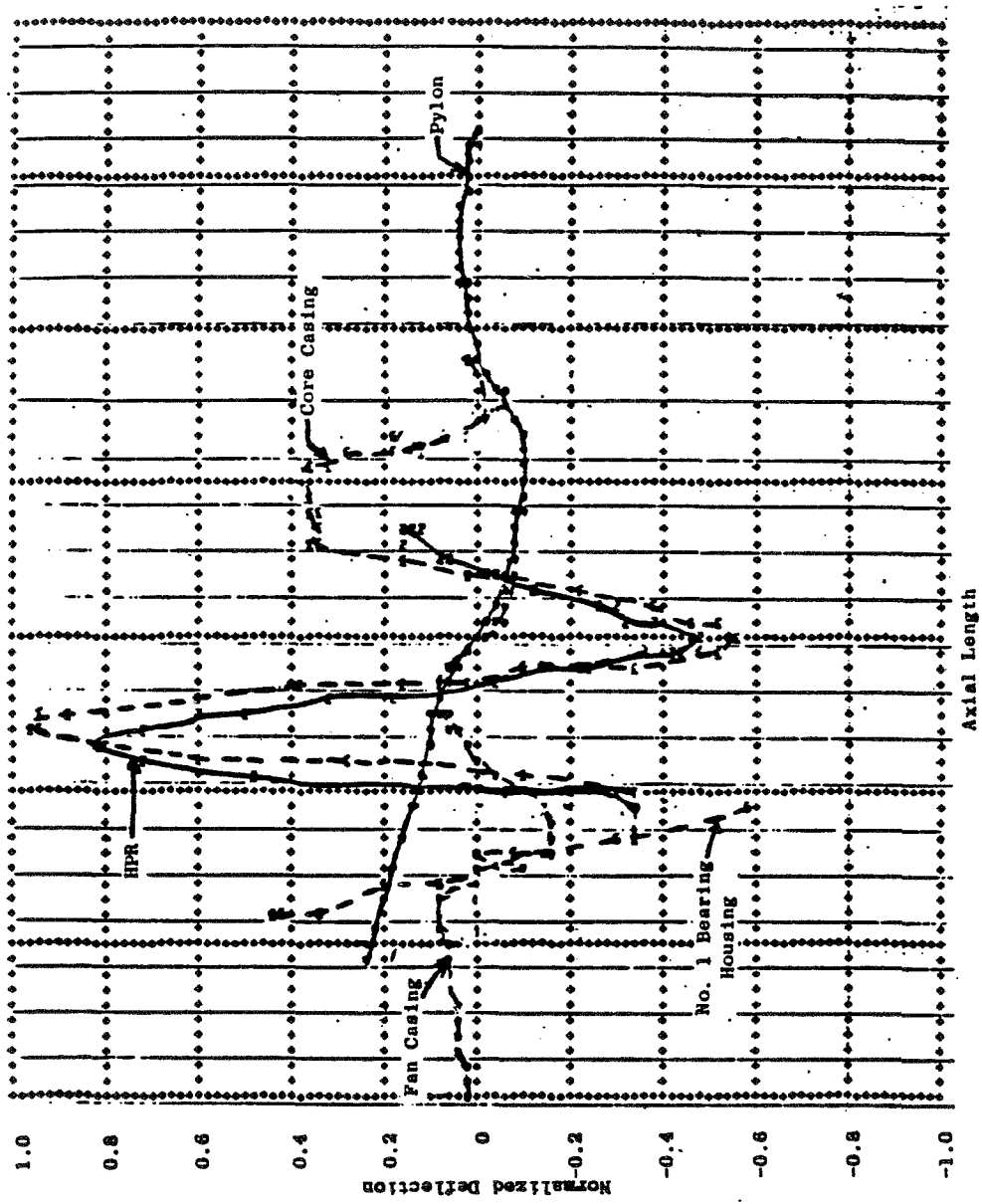


Figure 144. Subsystem 1 (Casing) Normalized Mode Shapes at 19,480 rpm.

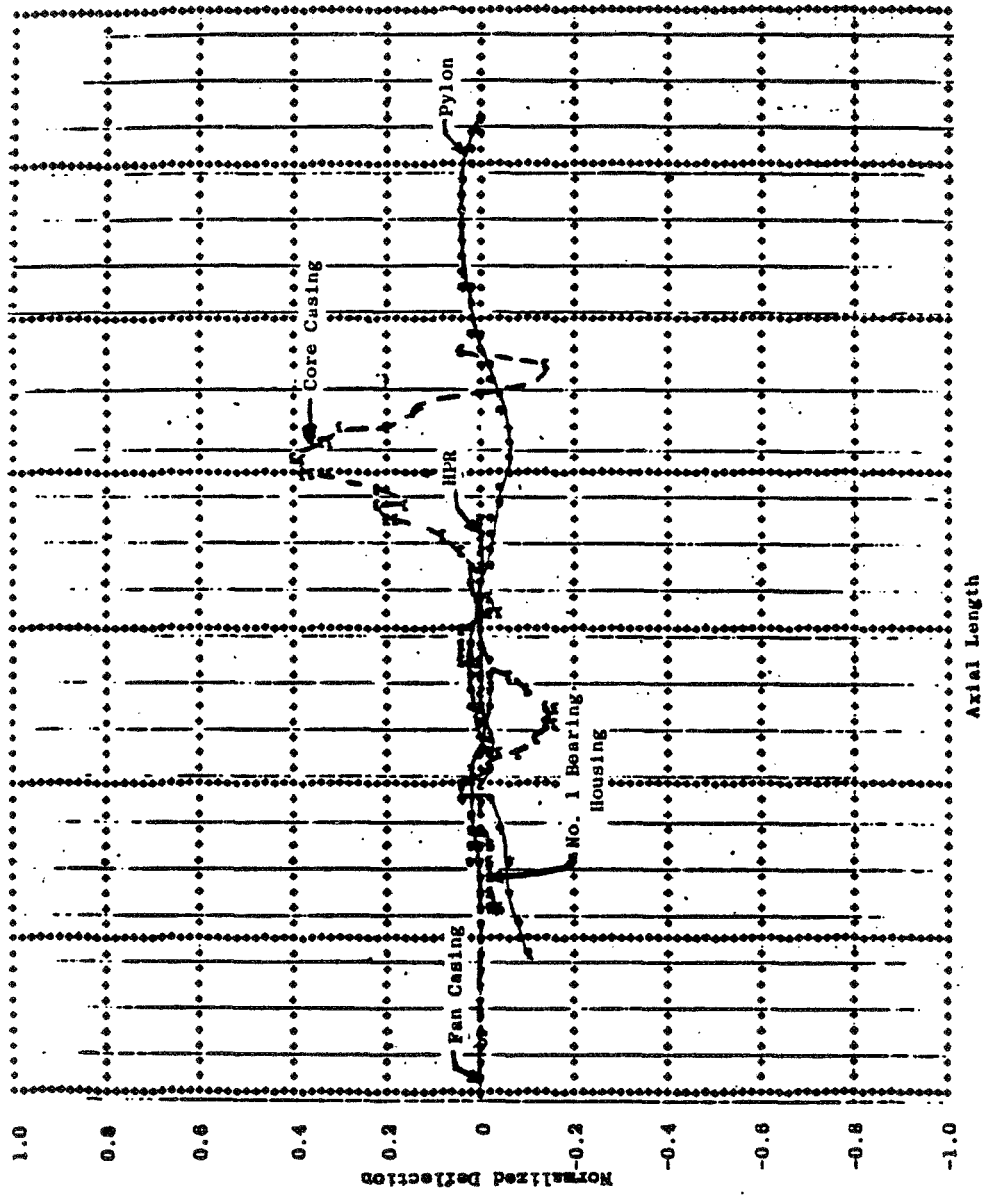


Figure 145. Subsystem 1 (Casing) Normalized Mode Shapes at 21,616 rpm.

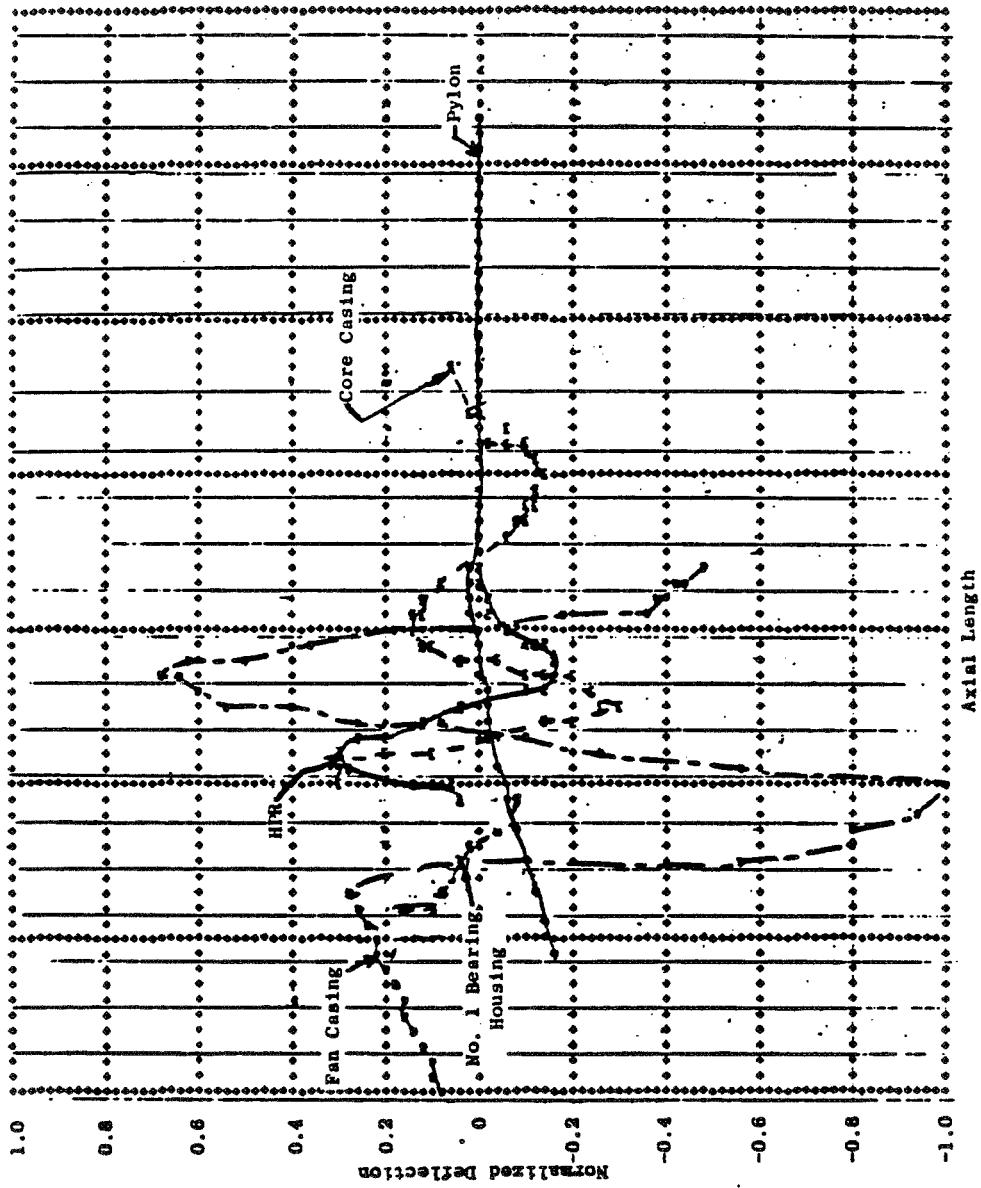


Figure 146. Subsystem 1 (Casing) Normalized Mode Shapes at 22,085 rpm.

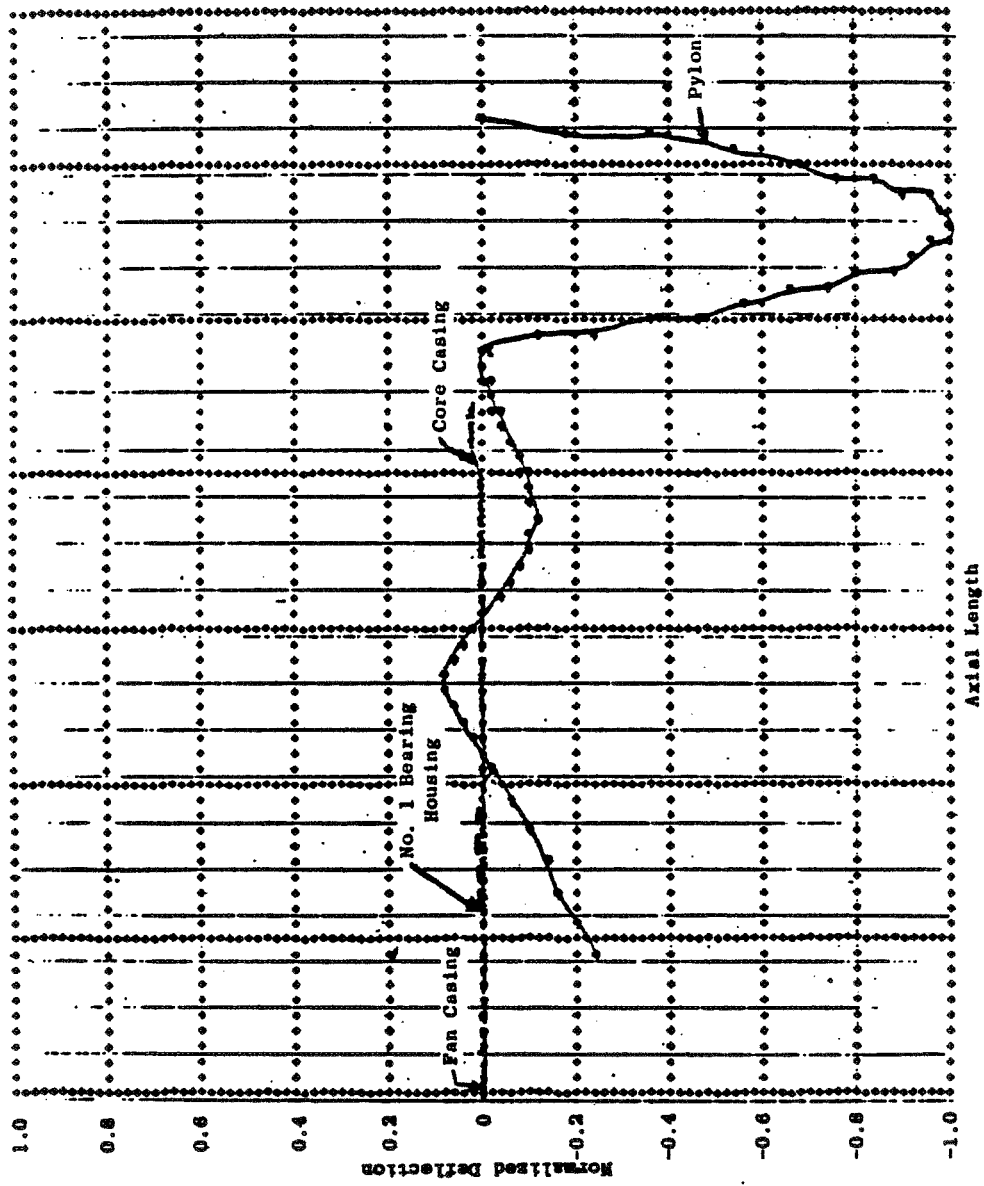


Figure 147. Subsystem 1 (Casing) Normalized Mode Shapes at 23,181 rpm.



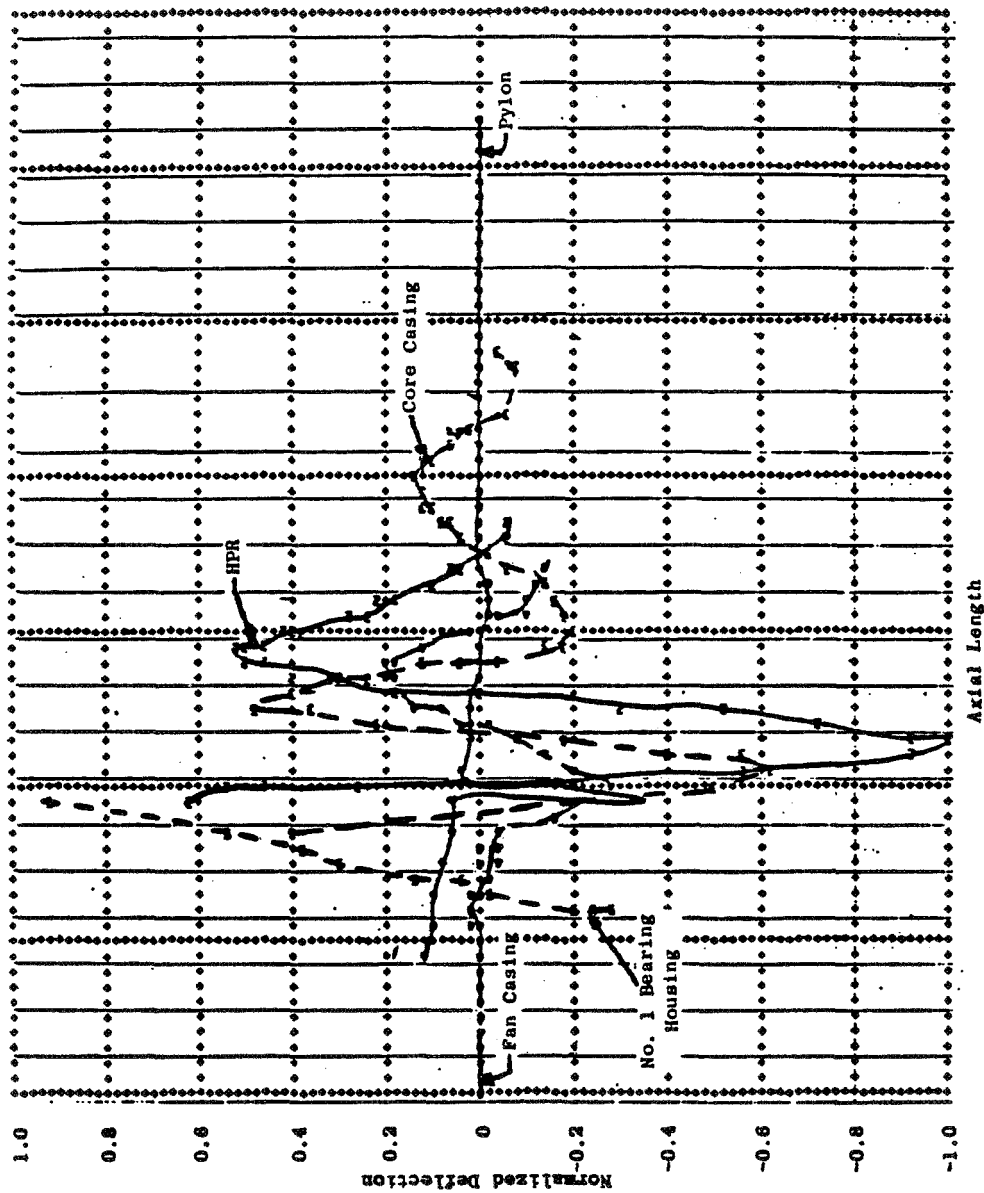


Figure 148. Subsystem 1 (Casing) Normalized Mode Shapes at 24,268 rpm.

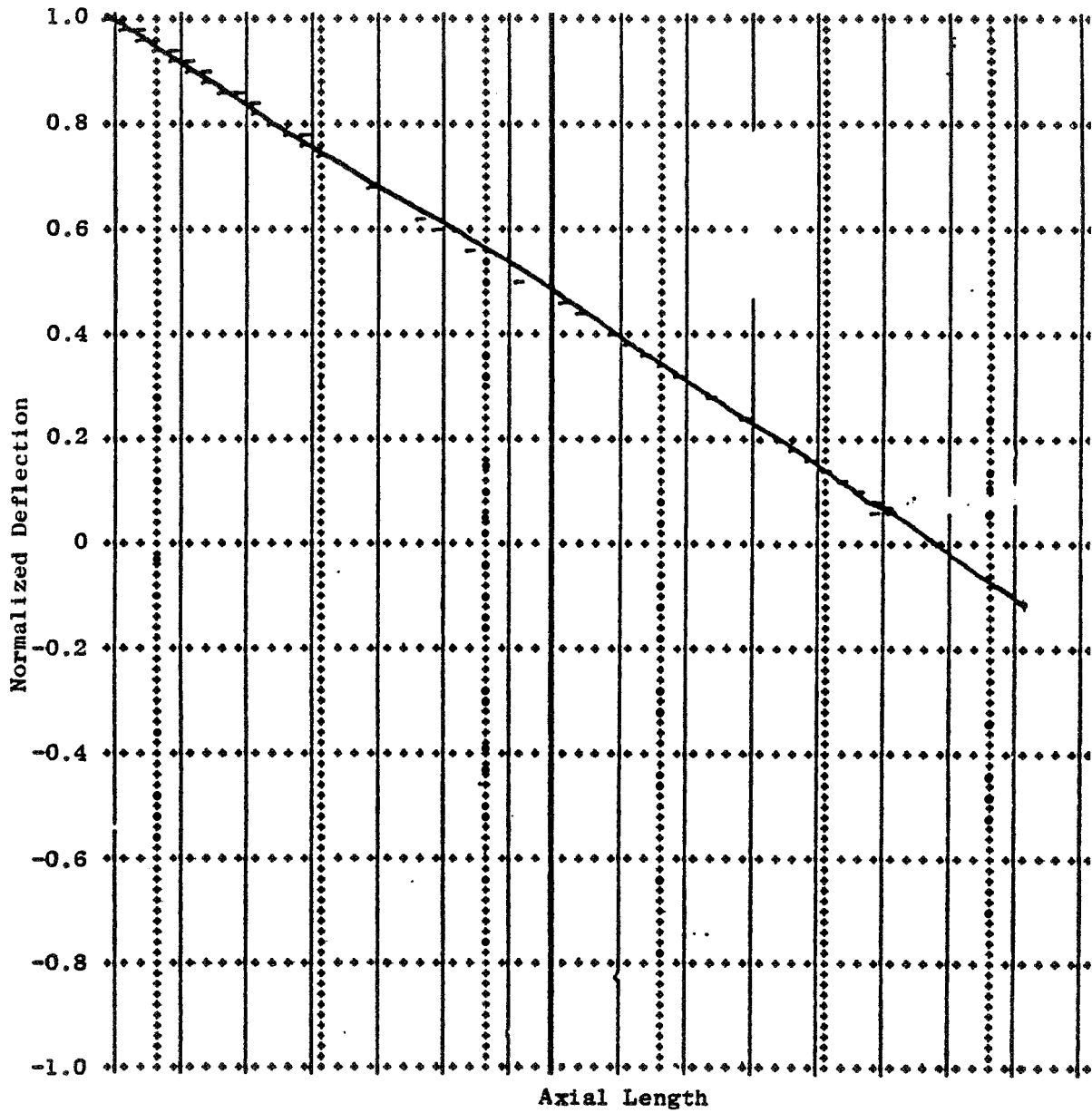


Figure 149. Subsystem 2 (Rotor) Normalized Mode Shapes at 55 rpm.

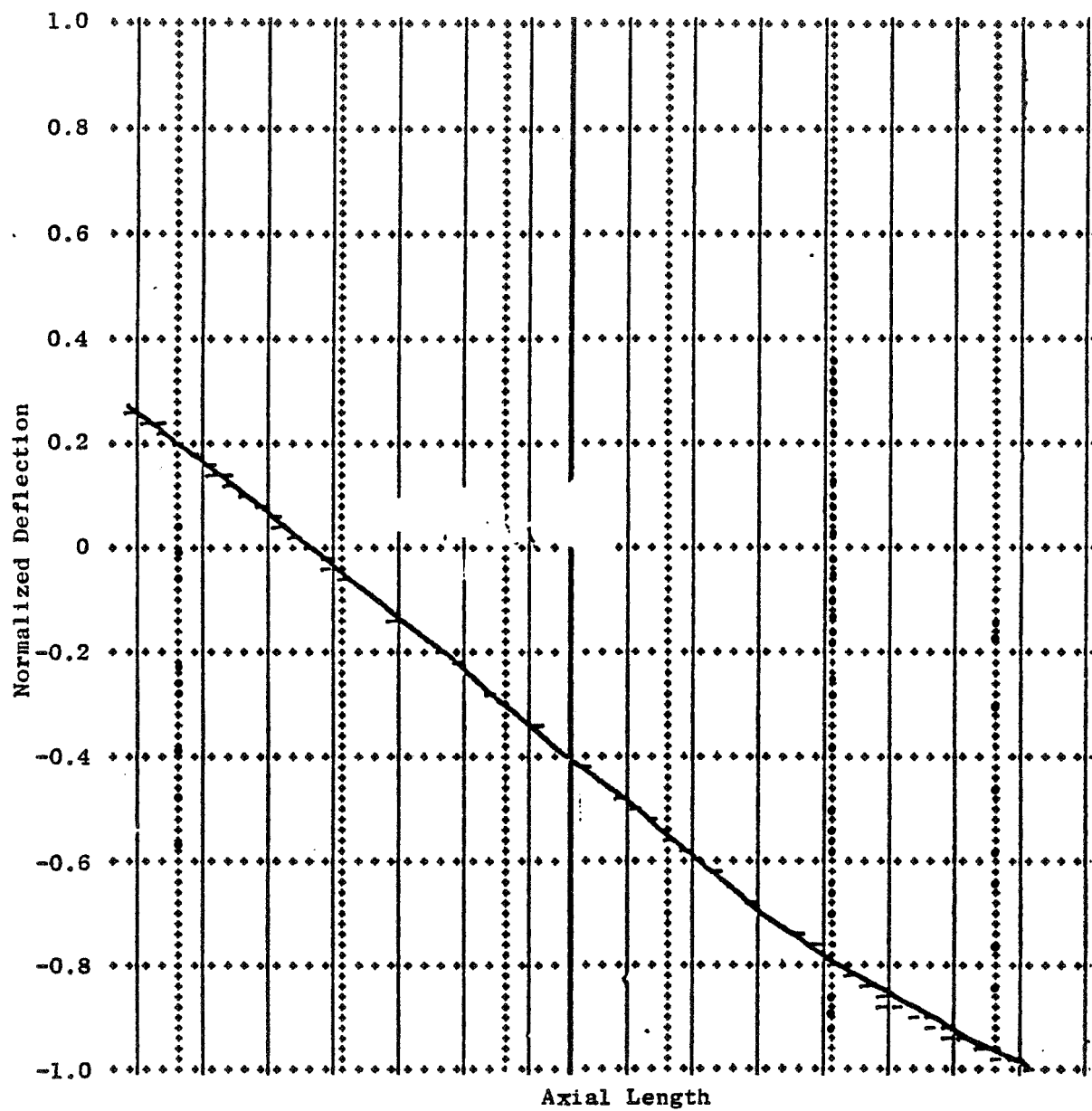


Figure 150. Subsystem 2 (Rotor) Normalized Mode Shapes at 73 rpm.

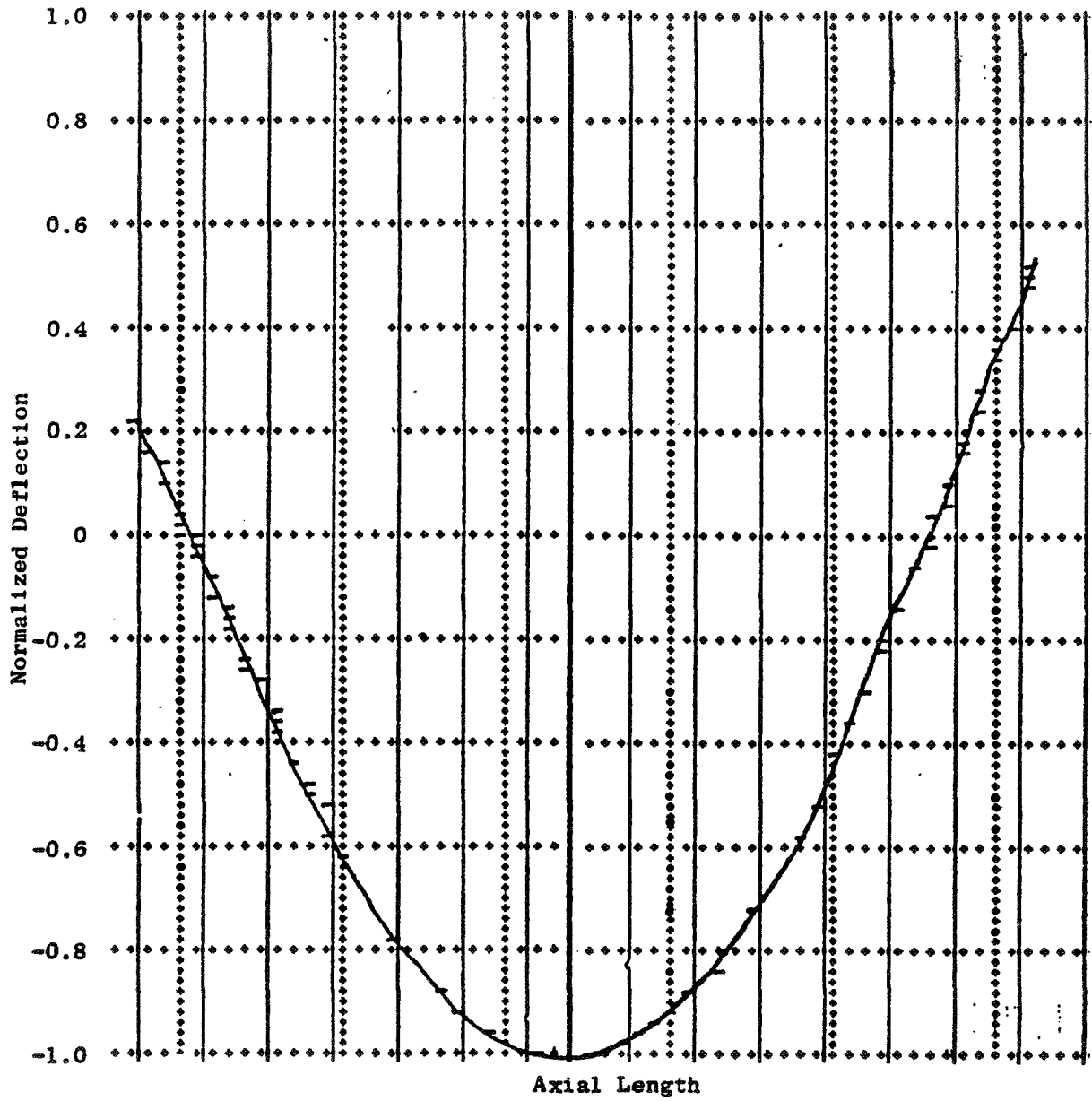


Figure 151. Subsystem 2 (Rotor) Normalized Mode Shapes at 972 rpm.

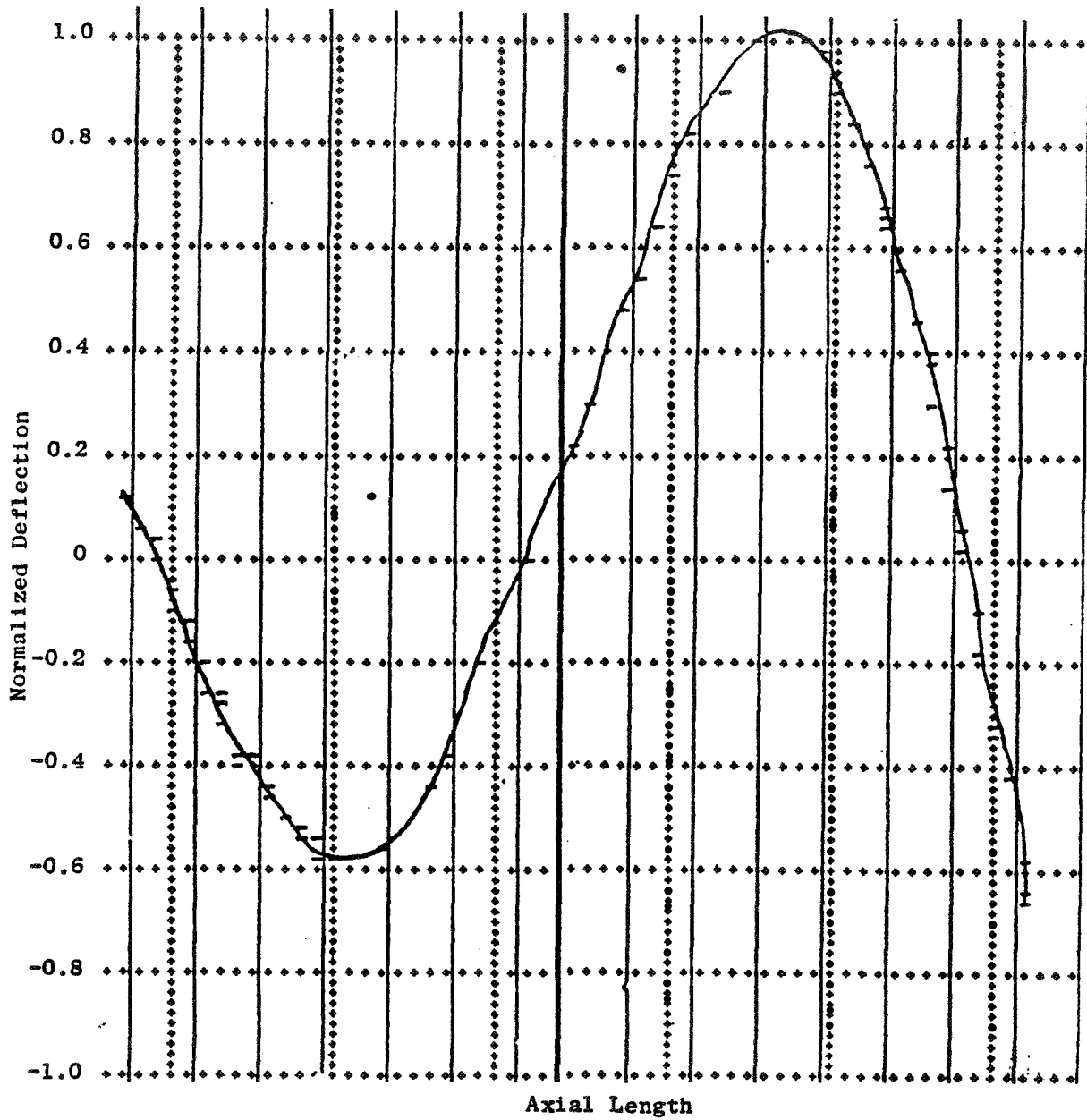


Figure 152. Subsystem 2 (Rotor) Normalized Mode Shapes at 2421 rpm.

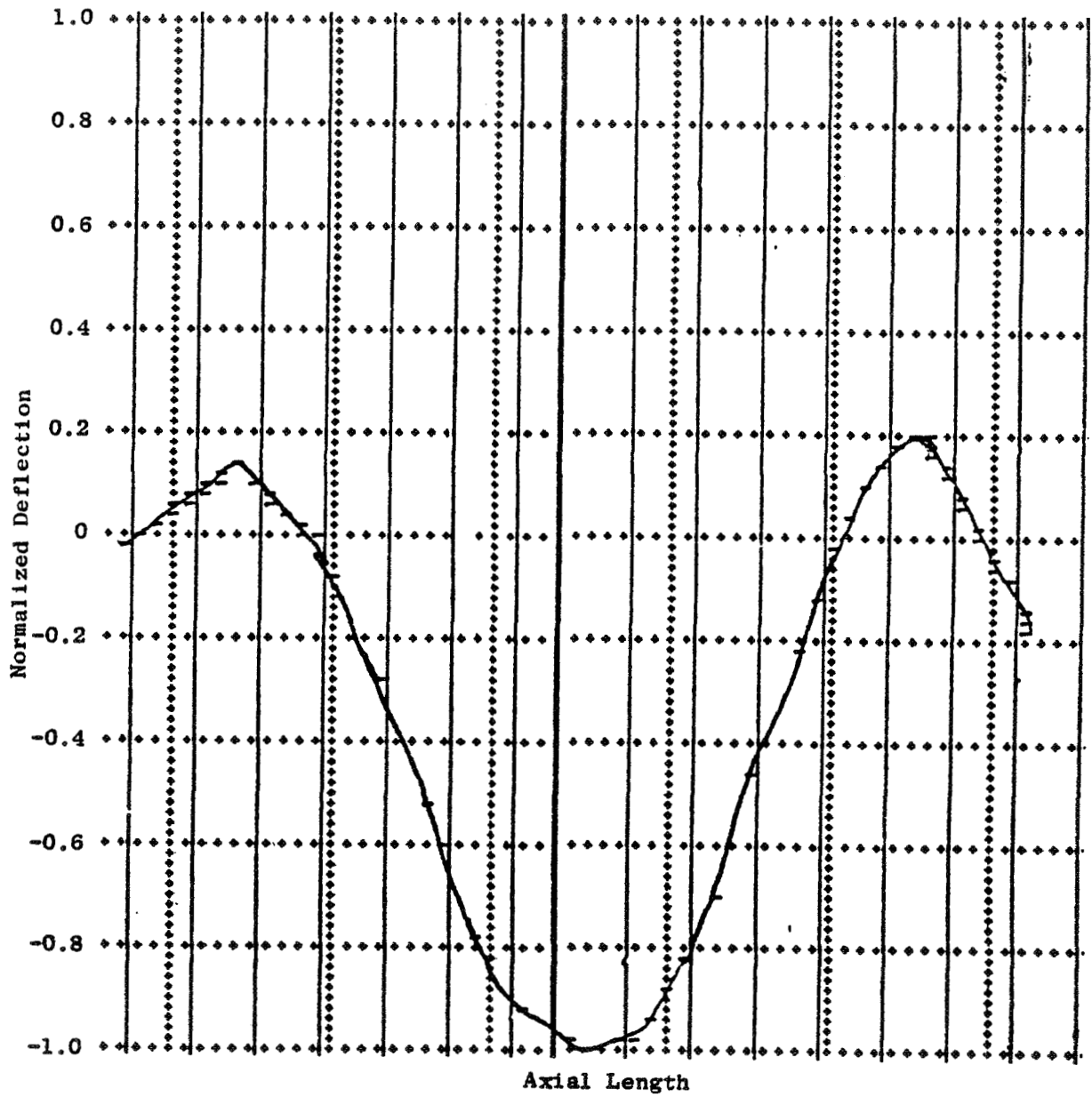


Figure 153. Subsystem 2 (Rotor) Normalized Mode Shapes at 5627 rpm.

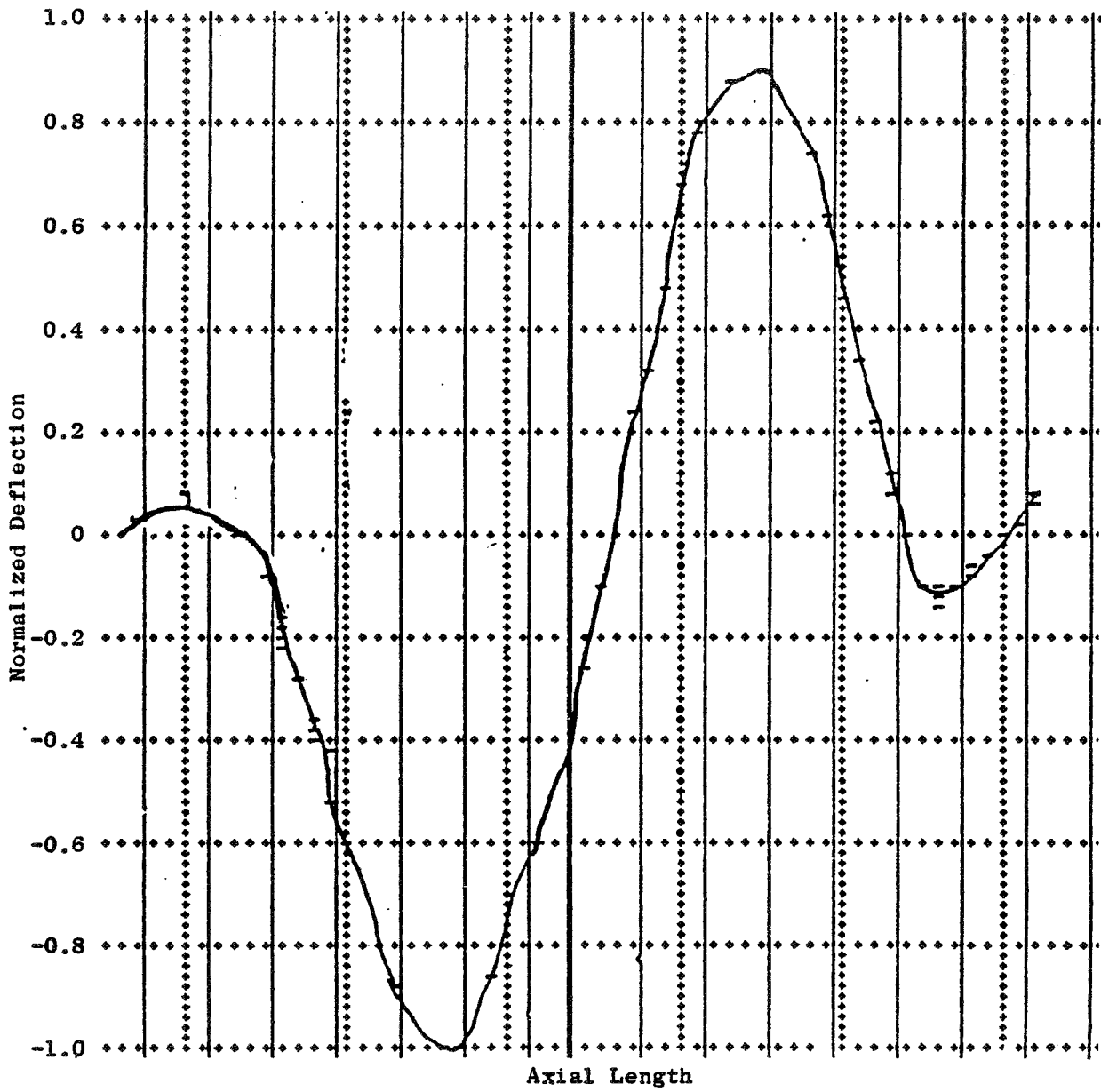


Figure 154. Subsystem 2 (Rotor) Normalized Mode Shapes at 11,081 rpm.

APPENDIX F

TETRA DATA FILE FOR THE BLADE-OUT ENGINE LINEAR ANALYSIS

Figure 155 is a listing of the TETRA data file for the engine. List 1 calls in the casing and rotor subsystems from previously created (VAST) data files. List 2 defines the four connecting elements, and List 3 is the command section.



```

120 $LIST1
130 NAME=60HBACH-GALLARDO DATE 8-80 CHARGE 19510
140 ADDRESS=602H 500 BSMT MAIL DROP K71 EXT 4279
150 IDENT1=60H CF6-50 WING ENGINE TETRA CHECKOUT
160 IDENT2=60HCHECK CASE VERT AND HORIZ MODEL ONLY
170 SS(1,1)=
180 7,0,0,0,15.0,15,
185 8,0,0,0,15.0,15,
190 1,0,0,0,0,18,
195 2,0,0,0,0,18,
200 $
210 $LIST2
220 ITYPE=5,
230 ILEN=1,
240 JT=2,10,
245 YS=4.0E6,
250 ZS=4.0E6,
260 IDAMP=1,
270 GELEM=15.0,
280 QFREQ=50.5,
290 $
300 $LIST2
310 ITYPE=5,
320 ILEN=2,
330 JT=3,11,
335 YS=3.391E6,
340 ZS=3.391E6,
350 IDAMP=1,
360 GELEM=15.0,
370 QFREQ=50.5,
380 $
390 $LIST2
400 ITYPE=5,
410 ILEN=3,
420 JT=4,17,
425 YS=3.115E6,
430 ZS=3.115E6,
440 IDAMP=1,
450 GELEM=15.0,
460 QFREQ=50.5,
470 $
480 $LIST2
490 ITYPE=5,
500 ILEN=4,
510 JT=5,18,
515 YS=2.549E6,
520 ZS=2.549E6,
530 IDAMP=1,
540 GELEM=15.0,
550 QFREQ=50.5,
560 $
570 $LIST3
580 ISTART=0,
590 DELTA=.00005,
600 TFINAL=.36,
610 IPRMUL=250,
620 IPLMUL=5,
630 IROTI=1,
640 BEGTIM=0,
650 BEGRPM=3700,
660 TRHIS(1,1)=
670 .36,0,
680 UNDM(1,1)=
690 0.00025,1,
700 CYRO(1,1)=
710 1,320000,
720 7,300000,
730 8,322000,
740 12,273000,
750 13,272000,
760 NPD(1,1)=
770 1,1,
780 2,1,
790 3,1,
800 4,1,
810 5,1,
820 6,1,
830 7,1,
840 8,1,
850 12,1,
860 13,1,
870 10,1,
880 11,1,
890 14,1,
900 15,1,
910 16,1,
920 19,1,
930 20,1,
940 17,1,
950 10,1,
960 23,1,
970 24,1,
980 25,1,
990 21,1,
1000 22,1,
1010 9,1,
1020 NEPD(1,1)=
1030 1,2,1,
1040 2,3,1,
1050 3,4,1,
1060 4,5,1,
1070 $

```

Figure 155. TETRA Data File Listing for Engine.

APPENDIX G

BLADE-OUT ENGINE TETRA RESULTS FOR NOMINAL UNBALANCE

The steady-state response as a function of speed was determined by running a succession of solutions initiated at discrete rpm's to cover the speed range of interest. Moderate unbalance levels were used to assure a linear (no rub) solution. The resulting time histories at each speed are given in this Appendix. The levels attained after the initial starting transients decayed are used to define the steady-state response as a function of speed. The individual TETRA time histories with moderate unbalance are given in Figures 156 through 163. These plots show the No. 1 bearing loads and deflections (vertical) at each steady-state speed point as a function of time. In each case, the unbalance was initiated at Time = 0.00025 second.

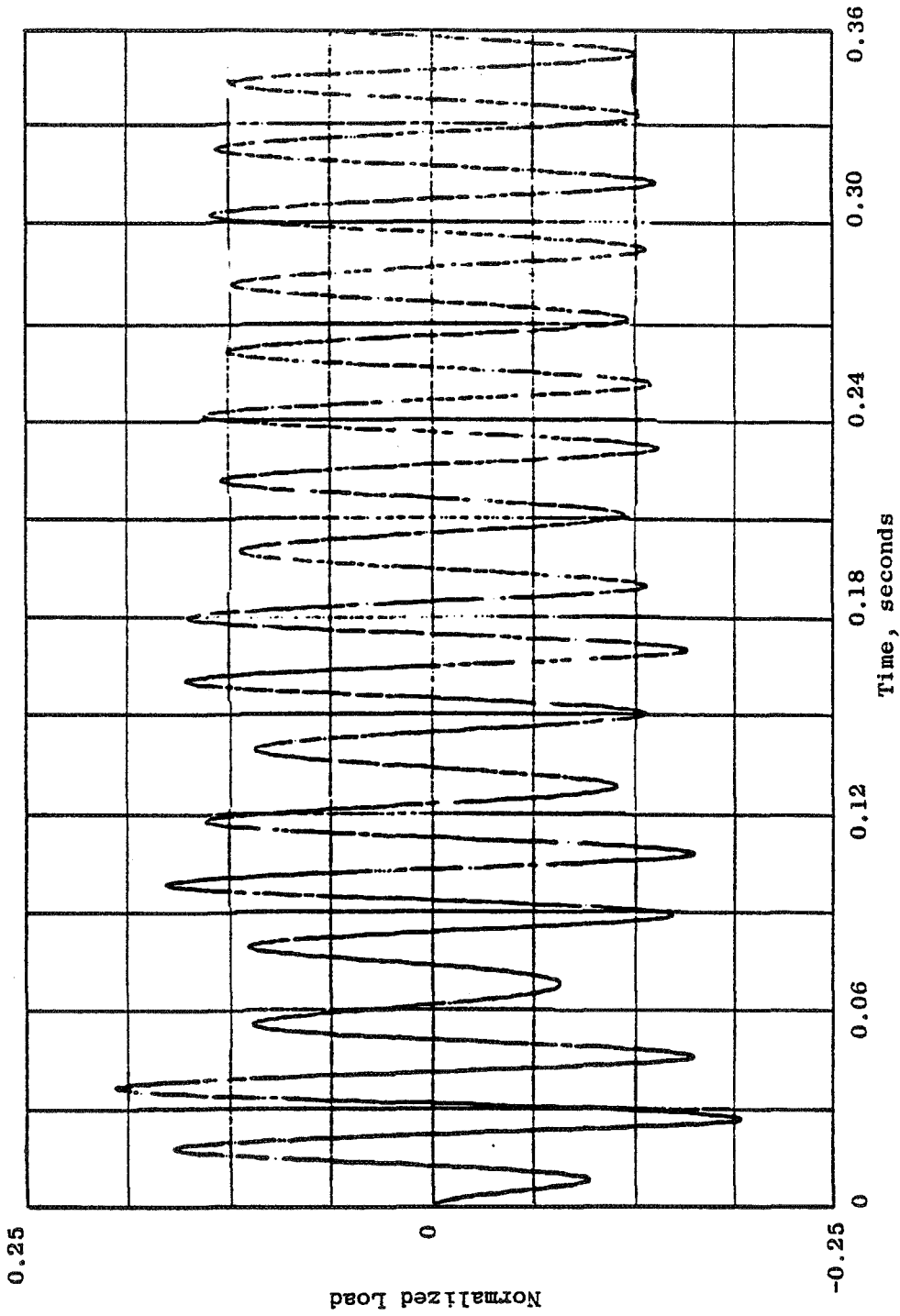


Figure 156. No. 1 Bearing Load at 2950 rpm.

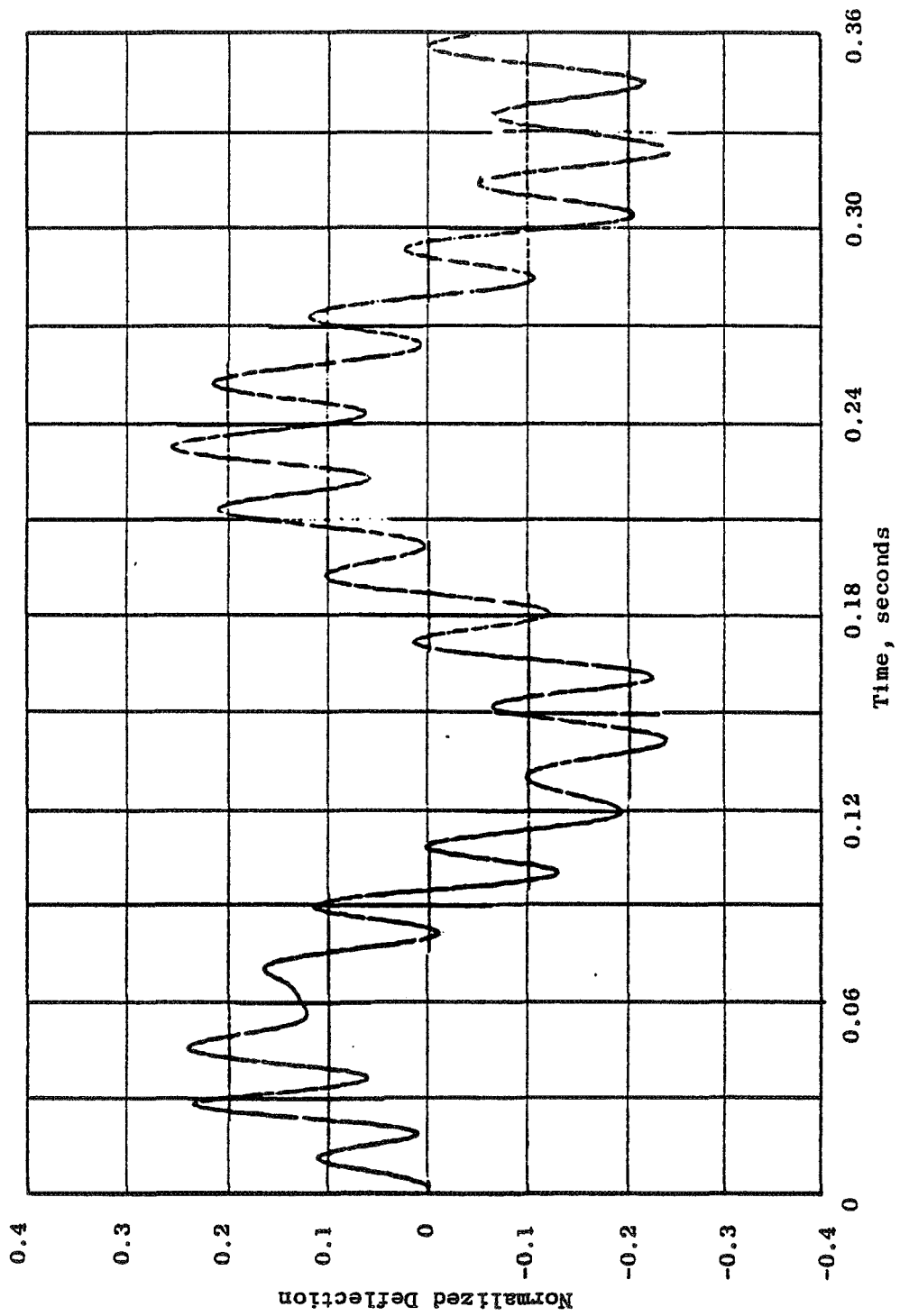


Figure 157. No. 1 Bearing Deflection at 2950 rpm.

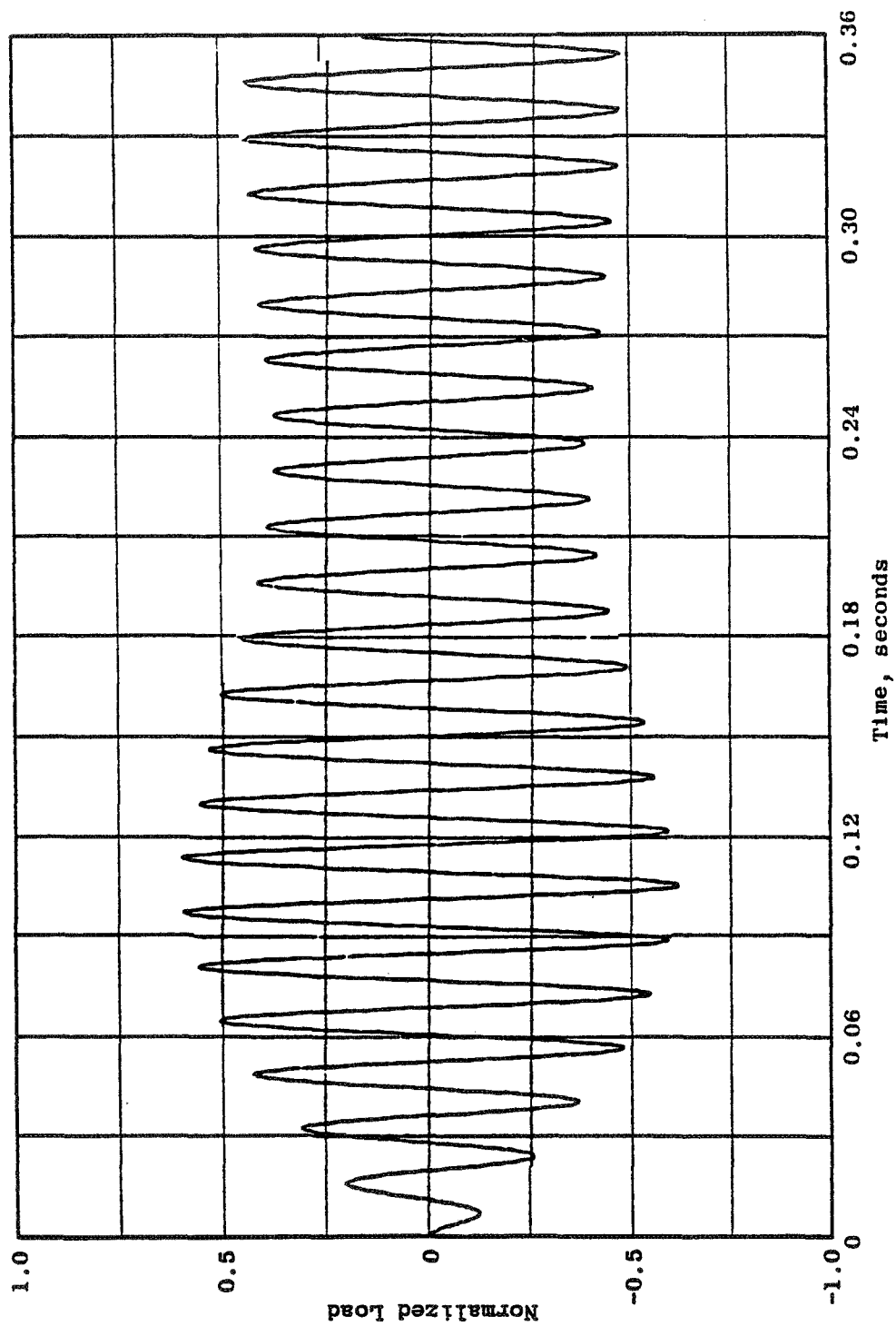


Figure 158. No. 1 Bearing Load at 3600rpm.

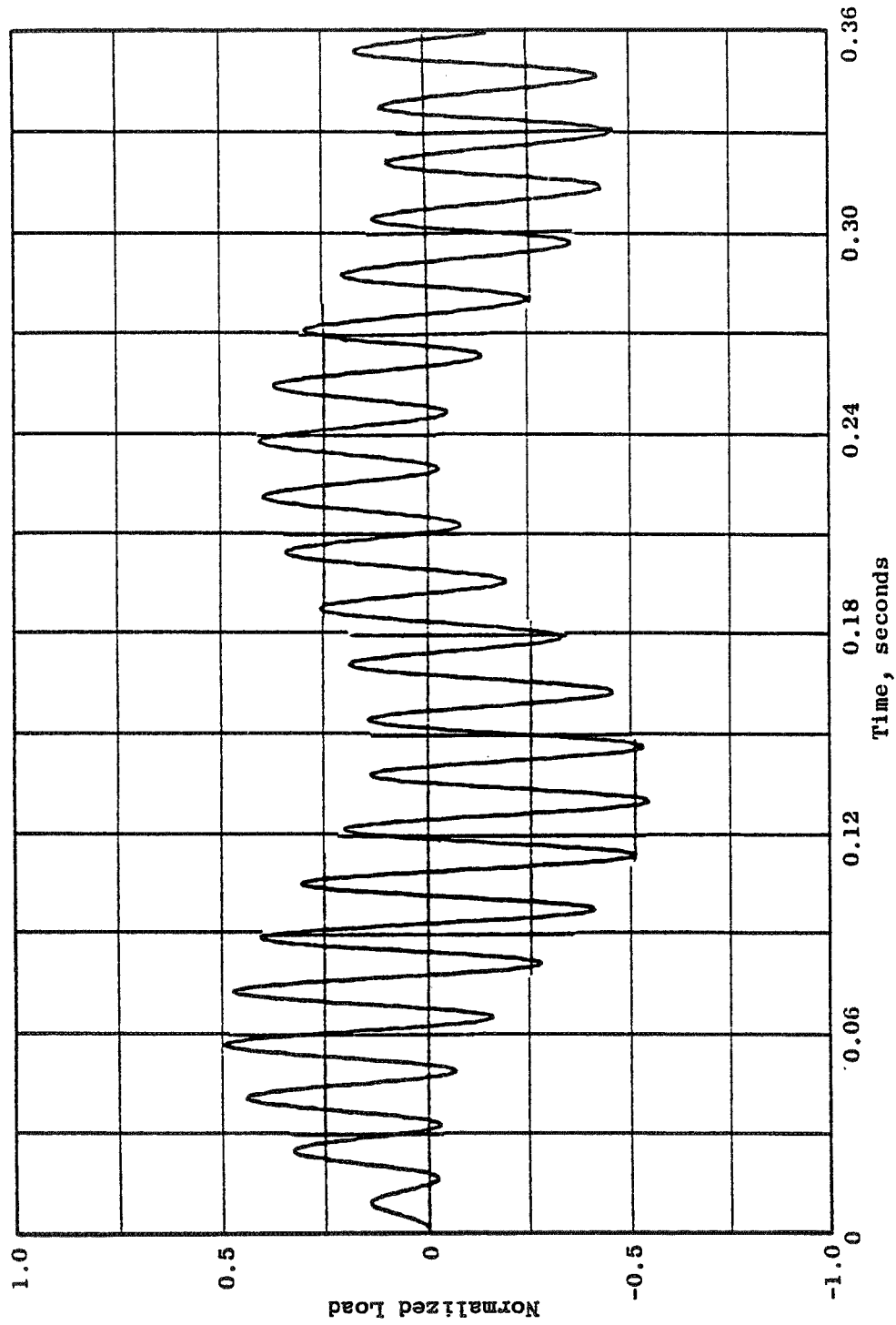


Figure 159. No. 1 Bearing Deflection at 3600 rpm.

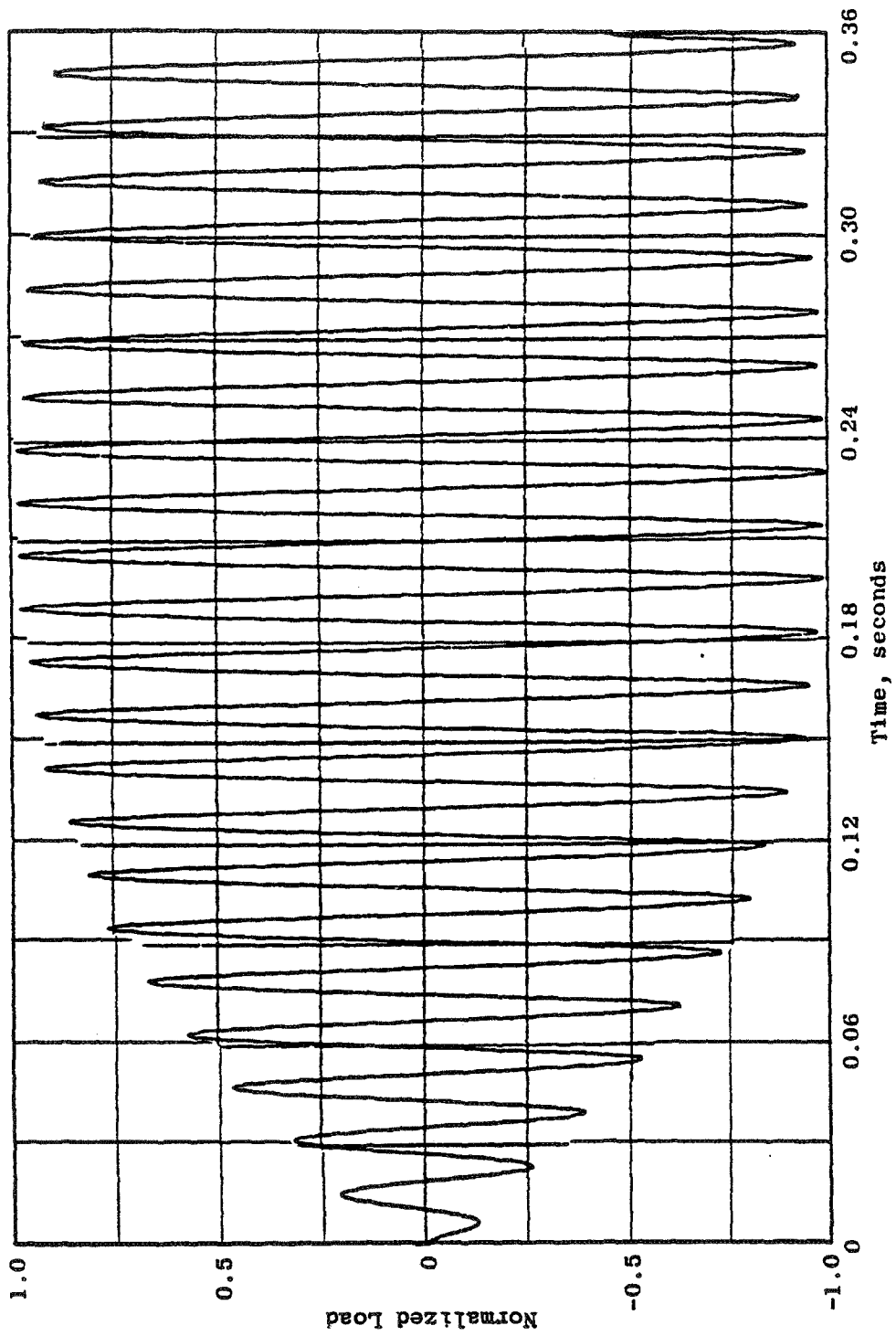


Figure 160. No. 1 Bearing Load at 3750 rpm.

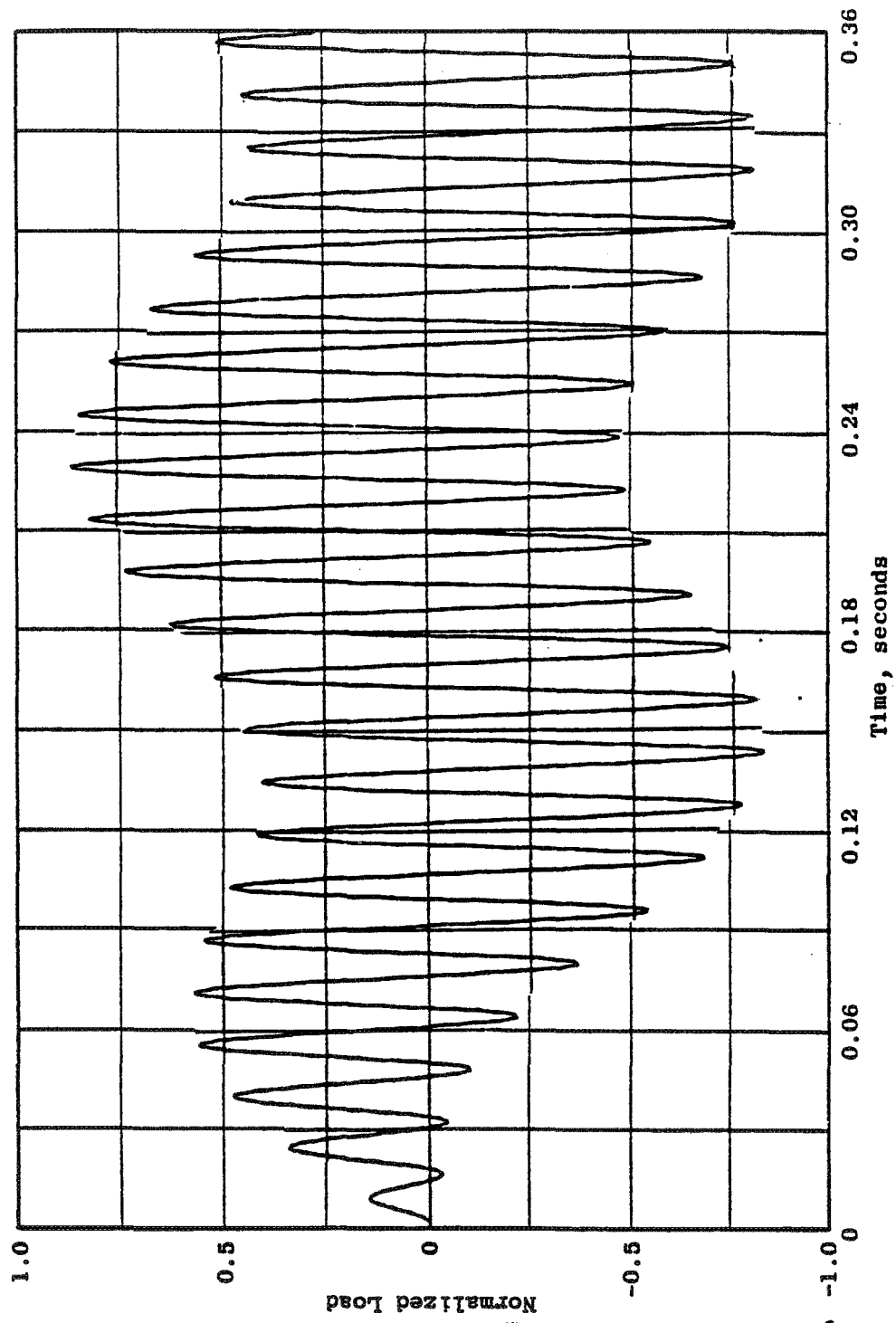


Figure 161. No. 1 Bearing Deflection at 3750 rpm.



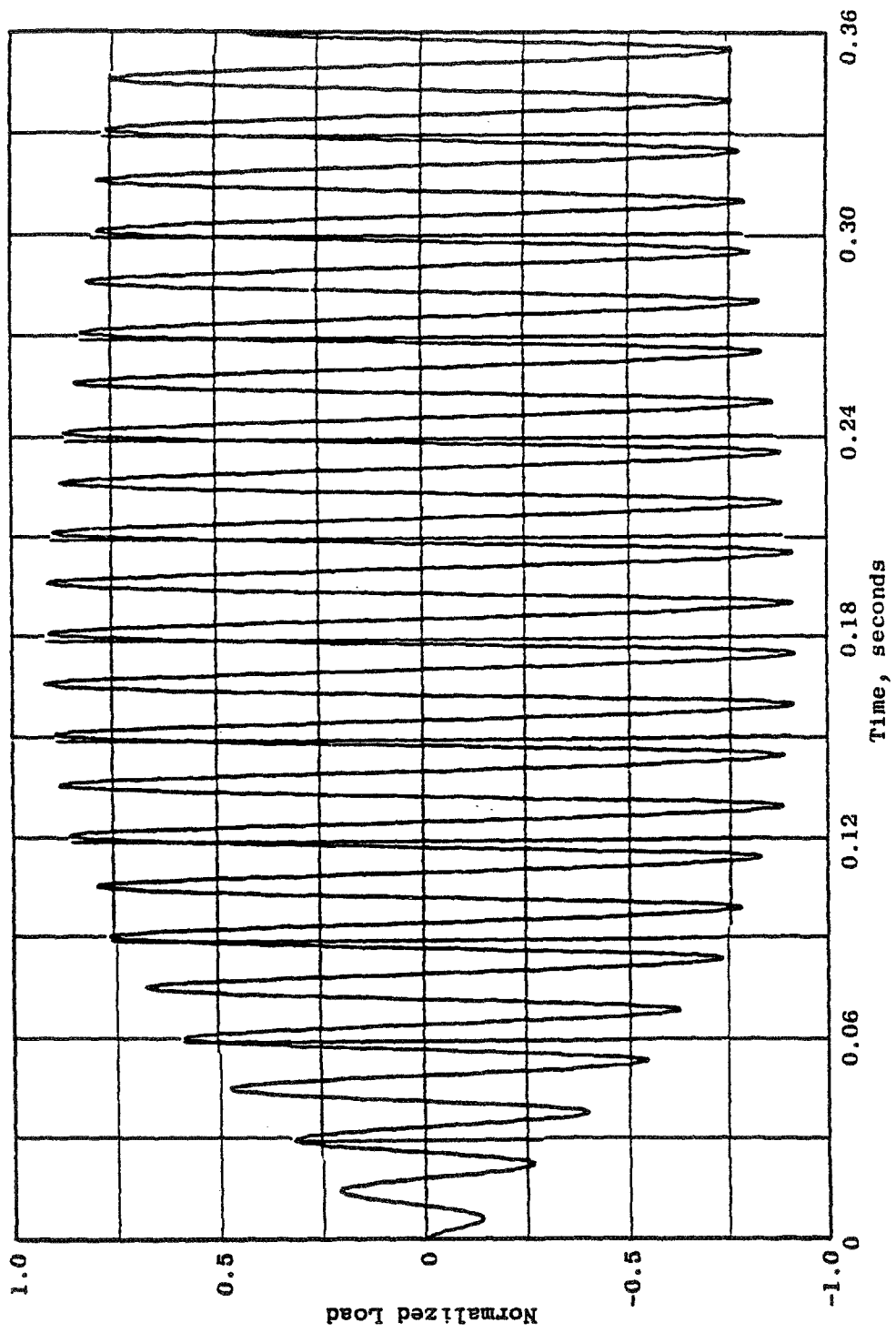


Figure 162. No. 1 Bearing Load at 4000 rpm.

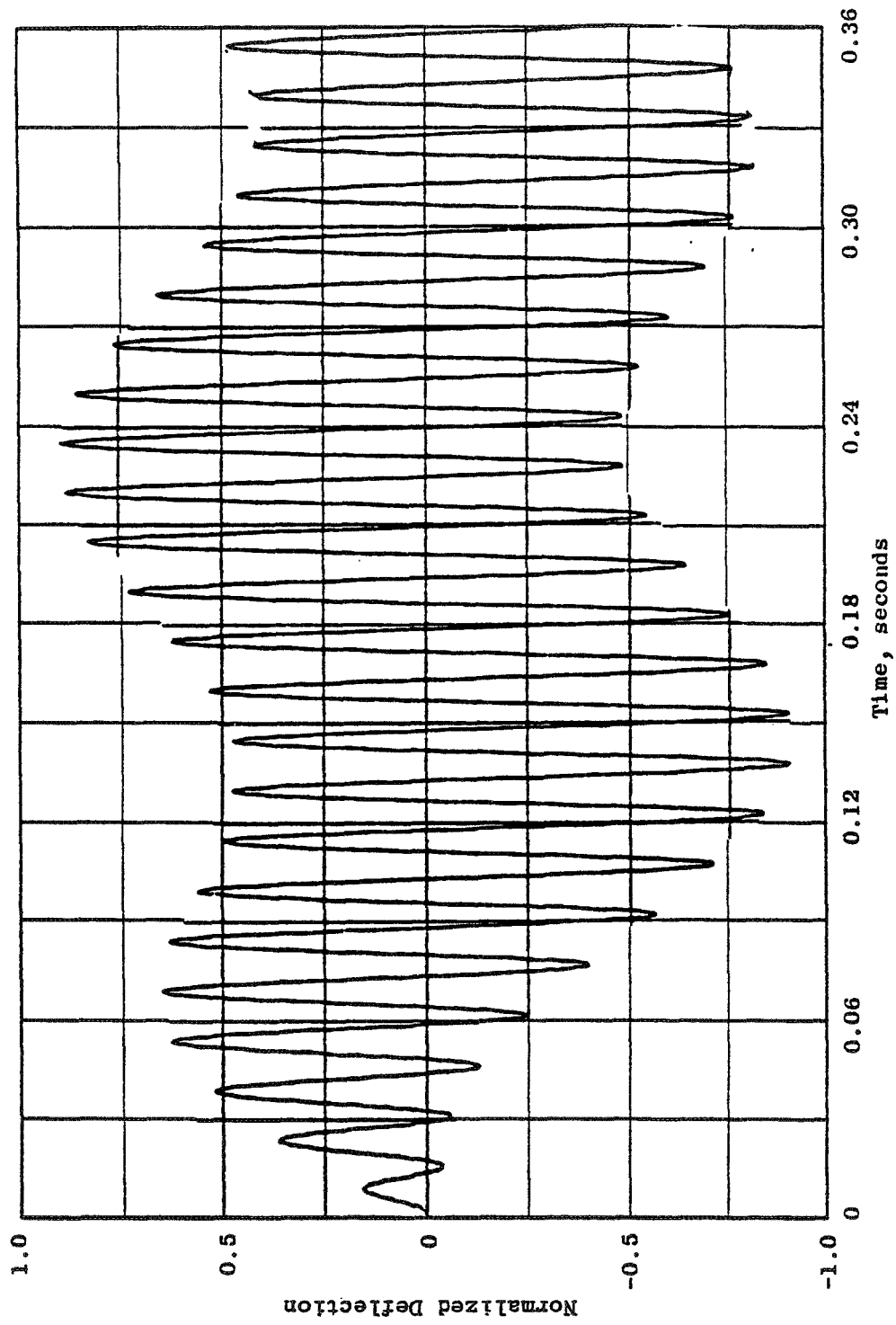


Figure 163. No. 1 Bearing Deflection at 4000 rpm.

#### REFERENCES

1. Scanlan, R.H. and Rosenbaum, R., Introduction to the Study of Aircraft Vibration and Flutter, MacMillan Co., New York, NY, 1951.
2. Craig, R.R. and Bampton, M.C.P., "Coupling of Substructures for Dynamic Analysis," AIAA Journal, Vol. 6, No. 7, July 1968.
3. Hurty, W.C., "Dynamic Analysis of Structural Systems Using Component Modes," AIAA Journal, Vol. 3, No. 4, April 1965.
4. Gallardo, V.C., "A linear Whirl-Flutter Theory for Helicopter Blades with Flapping Axes," M.S. Thesis, Hartford Graduate Center, Rensselaer Polytechnic Institute, 1967.
5. Levy, S. and Wilkinson, J., The Component Element Method, McGraw-Hill Inc., New York, NY, 1976.
6. Meirovitch, L., Analytical Vibrations, MacMillan Co., New York, NY, 1967.
7. Childs, D.W., "A Rotor-Fixed Modal Simulation Model for Flexible Rotating Equipment," ASME Journal of Engineering for Industry, Vol. 96, No. 2, May 1974, pp 659-669.
8. Lund, J.W., "Modal Response of a Flexible Rotor in Fluid-Film Bearings," ASME Journal of Engineering for Industry, Vol. 96, No. 2, May 1974, pp 525-533.
9. Lewis, E.M., "Vibration During Acceleration Through a Critical Speed," Translations of ASME, Vol. 54, 1932, pp 253-261.

